PHYSIK-DEPARTMENT

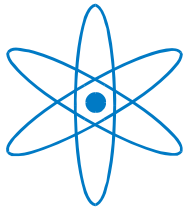

A study of very high energy γ-ray emission from AGNs and constraints on the extragalactic background light

Dissertation

von

Daniel Mazin

TECHNISCHE UNIVERSITÄT

MÜNCHEN

Technische Universität München

Max-Planck-Institut für Physik
(Werner-Heisenberg-Institut)

A study of very high energy γ-ray emission from AGNs and constraints on the extragalactic background light

Daniel Mazin

Vollständiger Abdruck der von der Fakultät für Physik der Technischen Universität München zur Erlangung des akademischen Grades eines
Doktors der Naturwissenschaften
genehmigten Dissertation.

Vorsitzender: Univ.-Prof. Dr. A. J. Buras
Prüfer der Dissertation:
1. Hon.-Prof. Dr. S. Bethke
2. Univ.-Prof. Dr. F. von Feilitzsch

Die Dissertation wurde am 27.11.2007 bei der Technischen Universität München eingereicht und durch die Fakultät für Physik am 27.11.2007 angenommen.

Abstract

This thesis studies very high energy (VHE) γ-radiation from active galactic nuclei (AGNs) using the novel Major Atmospheric Gamma-ray Imaging Cherenkov (MAGIC) telescope on La Palma. A significant part of the thesis is devoted to the development of the analysis tools and the analysis of MAGIC data taken on AGNs. New precision results on the well known AGN Markarian 421 as well as the discovery of VHE γ-ray emission from the AGNs Markarian 180 and 1ES 1011+496 are presented. These data are used to investigate the violent processes within AGNs, the most prominent extragalactic objects of non-thermal radiation. Furthermore, all available VHE γ-ray spectra of AGNs are used to derive constraints on the density of the extragalactic background light (EBL), which represents the integrated light emitted during the entire star and galaxy evolution of the Universe.

The well known AGN Markarian 421 (redshift $z = 0.030$) was measured with MAGIC from December 2004 to April 2005. For the first time an energy spectrum of the source has been derived down to 100 GeV. The spectral domain between 100 GeV and 500 GeV was not accessible prior to these MAGIC observations. The flux of Markarian 421 is found to vary between 0.5 – 2 Crab units (integrated above 200 GeV), a rather low state when compared to previously published data. Although the flux varies on a day-by-day basis, no short-term variability is observed. A clear correlation is observed between γ-rays and X-rays fluxes, whereas no significant correlation between γ-rays and optical data is seen. The spectral energy distribution between 100 GeV and 3 TeV shows a clear deviation from a power law. The deviation persists after correcting for the effect of attenuation by the extragalactic background light, and most likely is source–inherent. There is a rather clear indication of an inverse Compton peak around 100 GeV. The spectral energy distribution of Markarian 421 can be fitted by a one-zone synchrotron self-Compton model suggesting once again a leptonic origin of the very high energy γ-ray emission from this blazar. Within this model physics parameters of the jet of Markarian 421 are constrained using reasonable assumptions on the shape of the X-ray spectrum.

The AGN Markarian 180 (redshift $z = 0.045$) was observed to have an optical outburst in 2006 March, triggering a Target of Opportunity observation with the MAGIC telescope. The source was observed for a total of 12.4 hours, and VHE

γ-ray emission was detected with a significance of 5.5 σ. An integral flux above 200 GeV of $(2.3 \pm 0.7) \times 10^{-11}\,\mathrm{cm}^{-2}\,\mathrm{s}^{-1}$ is measured, corresponding to 11% of the Crab Nebula flux. A rather soft spectrum with a photon index of -3.3 ± 0.7 is determined. No significant flux variation is found. It is the first time that VHE γ-rays are detected from the direction of Markarian 180.

Also the discovery of VHE γ-ray emission from the AGN 1ES 1011+496 was triggered by an optical outburst in March 2007. 1ES 1011+496 was observed with the MAGIC telescope from March to May 2007 for a total of 18.7 hours. The analysis of the data results in an excess of $6.2\,\sigma$ with an integrated flux above 200 GeV of $(1.58 \pm 0.32) \cdot 10^{-11}$ photons cm^{-2} s^{-1}. Previous MAGIC observations in March–April 2006 during a lower optical state resulted in upper limits only, which suggests that the VHE emission state is related to the optical emission state. The redshift of $z = 0.212$ makes 1ES 1011+496 the most distant source observed to emit VHE γ-rays up to date.

In the second part of the thesis, VHE γ-ray spectra of AGNs are used to derive limits on the EBL density. The EBL consists of the light produced by galaxies during the entire history of the Universe. This radiation, redshifted according to its emission epoch, extends from the ultraviolet to the far-infrared range. VHE γ-rays are attenuated by the photons of the EBL via pair production, which leaves an imprint in the measured spectra from distant sources. A new method to derive constraints on the EBL is presented. The method does not rely on a predefined EBL model but uses rather a large number of generic shapes constructed from a grid in EBL density vs. wavelength. Spectral data from all known TeV blazars are utilized, making this the most complete study so far. Limits on the EBL are derived for three TeV blazar spectra (Markarian 501, H 1426+428, 1ES 1101-232) individually and for all spectra combined. The latter leads to significantly stronger constraints over a wide wavelength range from the optical ($\sim$ 1 micron) to the far-infrared ($\sim$ 80 microns). The limits are only a factor of 2 to 3 above the absolute lower limits derived from source counts. In the mid-infrared our limits are the strongest constraints derived from TeV blazar spectra so far. A high density of the EBL around 1 micron, reported by direct detection experiments, can be excluded. The results can be interpreted in two ways: (i) The sources resolved by galaxy counts account for the large fraction of the EBL, leaving only little room for additional components by e.g. the first stars or (ii) the assumptions about the underlying physics are not valid, which would require substantial changes in the standard emission models of TeV blazars.

Using the knowledge of the minimum EBL level one can deduce an upper limit for the distance of AGNs observed at VHE γ-rays. The method uses the argument that the intrinsic photon index after deconvoluting the EBL absorption cannot be harder than $\Gamma = 1.5$. PG 1553+113 is a BL Lac object of unknown redshift, newly detected in the GeV-TeV energy range by H.E.S.S. and MAGIC. Here we apply the above method to the combined H.E.S.S. and MAGIC spectrum and derive an upper limit on the redshift of $z < 0.69$. Moreover, we find that a

redshift above $z = 0.42$ implies a possible break of the intrinsic spectrum at about 200 GeV. Assuming that such a break is absent, we derive a much stronger upper limit of $z < 0.42$. Alternatively, this break might be attributed to an additional emission component in the jet of PG 1553+113. This would be the first evidence for a second component is detected in the VHE spectrum of a blazar.

Zusammenfassung

Diese Doktorarbeit untersucht sehr hochenergetische (VHE) Gammastrahlung von aktiven galaktischen Kernen (AGN) unter Verwendung des neuartigen Major Atmospheric Gamma-ray Imaging Cherenkov (MAGIC) Teleskops auf der Insel La Palma. Ein Teil der Arbeit ist der Entwicklung von Analysemethoden und der Analyse von AGN Beobachtungen mit MAGIC gewidmet. Es werden neue Präzisionsmessungen des etablierten AGNs Markarian 421 sowie die Entdeckung von VHE Gammastrahlung aus der Richtung der AGNs Markarian 180 und 1ES 1011+496 vorgestellt. Diese Daten werden verwendet, um die physikalischen Prozesse innerhalb der Jets von AGNs zu studieren. Des weiteren werden alle vorhandenen VHE Gamma-Spektren von AGNs verwendet, um die Dichte des extragalaktischen Hintergrundlichtes (EHL) einzuschränken, welches das über alle Epochen ausgestrahlte Licht der gesamten Sterne und Galaxien des Universums darstellt.

Der bekannte AGN Markarian 421 (Rotverschiebung $z = 0.030$) wurde mit MAGIC von Dezember 2004 bis April 2005 beobachtet. Hiermit konnte das Quellenspektrum zum ersten mal runter bis 100 GeV gemessen werden. Der Spektralbereich zwischen 100 GeV and 500 GeV war vor den MAGIC Beobachtungen nicht zugänglich. Der mit MAGIC gemessene Fluss von Markarian 421 variiert zwischen 0,5 – 2 Krebsnebel Einheiten (integriert über 200 GeV), was einem eher niedrigen Flusszustand entspricht, verglichen mit vorherig publizierten Messungen. vergleicht. Obwohl der Fluss von Tag zu Tag variiert, konnte keine signifikante Änderung des Flusses innerhalb einzelner Nächte beobachtet werden. Eine klare Korrelation wurde zwischen den Flüssen im VHE γ–Bereich und im Röntgen–Bereich festgestellt, allerdings wurde keine Korrelation zwischen den Flüssen im VHE γ–Bereich und dem optischen Bereich gefunden. Das Energiespektrum erstreckt sich von 100 GeV bis 3 TeV und zeigt eine klare Abweichung von einem Potenzgesetz. Die Abweichung verbleibt auch nach der Korrektur des Spektrums für den Effekt der extragalaktischen Absorption und hat wahrscheinlich einen intrinsischen Ursprung. Es gibt ein klares Anzeichnen dafür, dass das Maximum der Inverse-Compton Emission um 100 GeV herum liegt. Die spektrale Energieverteilung von Markarian 421 kann durch ein einfaches Synchrotron-Self-Compton-Modell erklärt werden, was einen leptonischen Ursprung der VHE Gammastrahlung vermuten lässt. Innerhalb dieses Modelles und unter Verwendung

sinnvoler Annahmen über das Röntgenspektrum, konnten physikalische Parameter des Jets von Markarian 421 eingeschränkt werden.

Ein erhöhter Fluss im optischen Bereich wurde beim AGN Markarian 180 (Rotverschiebung $z = 0.045$) im März 2006 beobeachtet, woraufhin MAGIC Beobachtungen (Target of Opportunity) durchgeführt wurden. Die Quelle wurde insgesamt 12,4 Stunden lang beobachtet, und eine VHE γ-Emission wurde mit einer Signifikanz von 5,5 σ registriert. Es wurde ein integraler Fluss von $(2.3 \pm 0.7) \times 10^{-11}$ Photonen $\mathrm{cm}^{-2}\,\mathrm{s}^{-1}$ oberhalb 200 GeV gemessen, was 11% des Krebsnebelflusses entspricht. Das abgeleitete Energiespektrum ist eher weich und hat einen Photonenindex von -3.3 ± 0.7. Keine signifikanten Flussänderungen wurden festgestellt. Das ist das erste mal, dass VHE Gammastrahlung aus der Richtung von Markarian 180 gemessen werden konnte.

Die Entdeckung von VHE Gammastrahlung vom AGN 1ES 1011+496 wurde ebenfalls durch einen optischen Ausbruch der Quelle im März 2007 ausgelöst. 1ES 1011+496 wurde mit dem MAGIC Teleskop zwischen März und May 2007 insgesamt 18,7 Stunden lang beobachtet. Die Analyse der Daten ergab einen Überschuss von γ-Ereignissen mit einer Signifikanz von $6{,}2\,\sigma$, was einem Fluss oberhalb von 200 GeV von $(1.58 \pm 0.32) \cdot 10^{-11}$ Photonen $\mathrm{cm}^{-2}\ \mathrm{s}^{-1}$ entspricht. Während früherer MAGIC Beobachtungen im März–April 2006 konnte kein signifikanter Fluss gemessen werden. Die Quelle befand sich zu diesem Zeitpunkt in einem niedrigen optischen Zustand. Das lässt eine Korrelation zwischen dem Niveau der VHE Gammastrahlung und dem Zustand der optischen Emission vermuten. Die Rotverschiebung von $z = 0.212$ macht 1ES 1011+496 zu der bislang am weitesten entfernten Quelle, von welcher VHE Gammastrahlung nachgewiesen worden ist.

Im zweiten Teil der Arbeit werden Gammaspektren von AGNs verwendet, um die Dichte des EHLs einzuschränken. Das EHL besteht aus dem Galaxienlicht, das während der gasamten Geschichte des Universums ausgestrahlt wurde. Diese Strahlung, je nach Zeitpunkt der Emission rotverschoben, erstreckt sich von Ultraviolet bis Fern-Infrarot. VHE Gammastrahlen werden durch den Prozess der Paarerzeugung mit den Photonen des EHLs teilweise absorbiert, was eine merkliche Veränderung der gemessenen Spektren von entfernten Quellen bewirkt. Eine neue Methode wird vorgestellt, um das EHL einzuschränken. Die Methode benutzt keine vordefinierten EHL Modelle, sondern verwendet eine grosse Schar analytischer Kurven, die auf einem Punkteraster im Phasenraum von EHL Dichte und Wellenlänge konstruiert werden. Spektren aller bekannten TeV Blazare wurden verwendet, was diese Studie zu der bis lang umfangreichsten Untersuchung dieser Art macht. Obere Grenzen auf das EHL werden für drei TeV Blazarspektren (Markarian 501, H 1426+428, 1ES 1101-232) einzeln abgeleitet und dann auch für alle Spektren kombiniert. Die letzteren Grenzen führen zu deutlich stärkeren Einschränkungen über einen weiten Wellenlängenbereich von optischem ($\sim 1\ \mu$m) bis zu Fern-Infrarot ($\sim 80\ \mu$m). Die oberen Grenzen sind nur um den Faktor 2 bis 3 oberhalb der absoluten unteren Grenzen, die von Galaxienzählungen stam-

men. Im Mittel-Infrarot sind die oberen Grenzen die stärksten Einschränkungen, die bislang publiziert worden sind. Eine hohe Dichte des EHLs um 1 μm herum, die durch eine direkte Messung eines japanischen Experiments erzielt worden ist, kann ausgeschlossen werden. Die Ergebnisse können auf zwei Arten interpretiert werden: (i) Die während der Galaxienzählungen aufgelösten Quellen entsprechen einem Grossteil des EHLs, und es gibt wenig Raum für zusätzliche Komponente wie z.B. von früheren Sternen. Oder (ii): Die verwendeten Annahmen über die zugrundeliegende Physik sind nicht richtig, was erhebliche Änderungen in den standard Emissionsmodellen der AGNs erfordert.

Mit Hilfe der Kenntnis über das minimale EHL-Niveau, kann man eine obere Grenze auf die Enfernung von AGNs ableiten. Die Methode verwendet das Argument, dass der intrinsische Photonenindex nach der Entfaltung der EHL Absorption nicht härter als $\Gamma = 1.5$ sein kann. PG 1553+113 ist ein BL Lac Objekt mit einer unbekannten Rotverschiebung. Die Quelle wurde kürzlich von H.E.S.S. und MAGIC im GeV-TeV Enrgiebereich nachgewiesen. Es wird die oben beschriebene Methode auf das kombinierte H.E.S.S. und MAGIC Energiespektrum angewendet und eine obere Grenze der Rotverschiebung von $z < 0.69$ abgeleitet. Des weiteren wird festgestellt, dass eine Rotverschiebung von $z > 0.42$ einen möglichen Knick im intrinsischen Spektrum um 200 GeV mit sich bringt. Angenommen, dass es keinen Knick im Spektrum gibt, leiten wir eine viel stärkere obere Grenze von $z < 0.42$. Alternativ kann der Knick durch eine zusätzliche Emissionskomponente im Jet von PG 1553+113 erklärt werden. Das wäre der erste Nachweis für eine zweite Komponente in einem gemessenen VHE Blazarspektrum.

Contents

List of Figures

List of Acronyms and Abbreviations

1ES	First Einstein survey [catalogue]
2MASS	Two micron all sky survey
AGASA	Akeno giant air shower array
AGN	Active galactic nucleus
AMC	Active mirror control
ASM	All-sky monitor (detector on board RXTE)
a.s.l.	Above sea level
Az	Azimuth
BeppoSAX	Satellite per astronomia X
CANGAROO	Collaboration of Australia and Nippon (Japan) for a gamma-ray observatory in the outback
CAT	Cherenkov array at Themis
CCD	Charged coupled device
CELESTE	Cherenkov low energy sampling and timing experiment
CGRO	Compton gamma-ray observatory
CMB	Cosmic microwave background
CORSIKA	Cosmic ray simulations for KASCADE
CR	Cosmic ray(s)
CT	Cherenkov telescope
DAQ	Data acquisition
DEC	Declination
EAS	Extended air shower
EBL	Extragalactic background light
EGRET	Energetic gamma-ray experiment telescope
EM	Electromagnetic
FADC	Flash analog to digital converter
FIR	Far-infrared
FOV	Field of view
FSRQ	Flat spectrum radio quasar
FWHM	Full width at half maximum
GLAST	Gamma-ray large area space telescope

GMRT	Giant meterwave radio telescope	
GNCT	Global network of Cherenkov telescopes	sect. A.6
GRB	Gamma-ray burst	
GZK	Greisen–Zatsepin–Kuz'min	
H.E.S.S.	High energy stereoscopic system	
HE	High energy	
HEGRA	High energy gamma-ray astronomy	
HST	Hubble space telescope	
IACT	Imaging atmospheric Cherenkov telescope	
IC	Inverse Compton	
IR	Infrared	
ISM	Interstellar medium	
KASCADE	Karlsruhe shower core and array detector	
KVA	Kungliga Vetenskapsakademien [telescope]	
LBL	Low–frequency peaked BL Lac	
LED	Light emitting diode	
LONS	Light of the night sky	
M	Messier [catalogue]	
MAGIC	Major atmospheric gamma-ray imaging Cherenkov	
MARS	MAGIC analysis and reconstruction software	
MC	Monte Carlo [simulations]	
MJD	Modified Julian day	
Mrk	Markarian	
NSB	Night–sky background	
PG	Palomar–Green catalog of UV-excess stellar objects	
ph.e.	photoelectrons	
PiN	Positive intrinsic negative [diode]	
PKS	Parkes catalogue of radio sources	
PMT	Photomultiplier tube	
PSF	Point spread function	
PWN	Pulsar wind nebula	
QE	Quantum efficiency	
RA	Right ascension	
RF	Random forest^{TM}	
RMS	Root mean square	
ROOT	An object–oriented data analysis framework	
ROSAT	Röntgen satellite	
RXTE	Rossi X-ray timing explorer	
SED	Spectral energy distribution	
SNR	Supernova remnant	
SSC	Synchrotron–self Compton	

Swift	Swift gamma-ray burst explorer
UV	Ultraviolet
VCSEL	Vertical cavity surface emitting laser
VERITAS	Very energetic radiation imaging telescope array system
VHE	Very high energy ($> 50\,\mathrm{GeV}$)
XMM	XMM-Newton satellite mission
Zd	Zenith distance

Useful units definitions

This section provides a small collection of units definitions that are commonly used in astrophysics. In addition, the conversion to SI units (International System of Units) is given.

- **Electronvolt (eV):** The electronvolt is the unit of energy. It is the amount of energy equivalent to that gained by a single unbound electron when it is accelerated through an electrostatic potential difference of one volt, in vacuum.
  Conversion to the SI units: 1 eV = 1.602 176 53(14)$\times 10^{19}$ J.

- **Erg:** The erg is the unit of energy and mechanical work. Its name is derived from the Greek word meaning "work".
  Conversion to the SI units: 1 erg = 10^{-7} J.

- **Gauss (G):** The gauss, abbreviated as G, is the unit of magnetic field (B), named after the German mathematician and physicist Carl Friedrich Gauss. One gauss is defined as one maxwell per square centimetre.
  Conversion to the SI units: 1 G = 10^{-4} T.

- **Light year:** The light year is a common unit of distance in astrophysics.
  Conversion to the SI units: 1 light year = 9.4607$\times 10^{15}$ m.

- **Jansky (Jy):** The jansky is the unit of electromagnetic flux density and is named after the pioneering radio astronomer Karl Jansky.
  Conversion to the SI units: 1 Jy = $10^{-4} \frac{\mathrm{W}}{\mathrm{m}^2 \cdot \mathrm{Hz}}$

- **MJD:** The Modified Julian Date (MJD) is the number of days (with decimal fraction of the day) that have elapsed since midnight at the beginning of Wednesday November 17, 1858. In terms of the Julian day (JD): MJD = JD - 2,400,000.5. JD 0 is defined as January 1, -4712 (=4713 BC) 12:00 noon Greenwitch mean time.

Introduction

Very high energy (VHE) astrophysics is one of the youngest fields of modern physics. The first celestial source emitting VHE γ-rays (i.e. photon energies $100\,\mathrm{GeV} < E < 100\,\mathrm{TeV}$) was only found in 1989 opening a new window to the Universe. The low fluxes in the VHE γ-ray regime require ground based detectors. The most successful technique uses Imaging Atmospheric Cherenkov Telescopes (IACT), which measure the Cherenkov light emitted by the air showers induced by VHE γ-rays impinging on the atmosphere. In less than two decades the field has evolved very dynamically leading to several exciting discoveries of VHE γ-ray sources providing fascinating insights into the non-thermal Universe. Most of the results have been obtained just recently after the H.E.S.S. IACT system in Namibia and the MAGIC telescope on La Palma became operational. The MAGIC telescope is currently the largest single dish IACT featuring a 17 m diameter reflector. The technological key elements of the MAGIC telescope result in an unprecedented low energy threshold allowing the reconstruction of γ-rays with energies even below 100 GeV. A large part of my work was committed to the development and commissioning of the analysis tools for the MAGIC data with the goal to achieve a high flux sensitivity in the full accessible energy range.

My scientific work was devoted to the study of extragalactic sources of this radiation. When I started this work in 2004, only six extragalactic objects emitting VHE γ-rays had been established. All of them are so-called active galactic nuclei (AGNs) harboring a supermassive black hole in the center and emitting powerful collimated plasma jets, which extend to distances much larger than the dimension of the galaxies themselves. The AGNs are believed to accelerate charged particles to the highest known energies and thus are one of the major factories of the non-thermal radiation in the Universe. The study of the high energy processes within the AGN jets using new precision data taken on the well established AGN Markarian 421 and the discovery of two distant AGNs never seen before to emit VHE γ-rays is the first major topic of this thesis. One of the discovered AGNs is currently the most distant VHE γ-ray source.

The second topic deals with a diffuse low energy radiation originating from the entire history of star formation and evolution in the Universe. This so-called extragalactic background light (EBL) is the second largest background radiation after the cosmic microwave radiation extending from the ultraviolet to the far

infrared range. The EBL is difficult to measure directly due to strong foregrounds from our solar system and the Galaxy. The observation of distant AGNs emitting VHE γ-rays provides an unique indirect measurement of the EBL. This indirect measurement is based on the fact that VHE γ-rays from the AGNs interact with the EBL photon field via pair-production causing an energy-dependent absorption of the AGN energy spectra. The imprint of the EBL on the AGN spectra can then be used to constrain the level and the shape of the EBL density. A detailed study of the possibilities to constrain the EBL using all available VHE γ-ray spectra from AGNs resulted not only in the strongest upper limits on the EBL up to date but has also cosmological implications in constraining the abundance of the first stars in the Universe.

The thesis is structured as follows. An introduction to VHE γ-ray astrophysics is given in Chapter 1. TeV blazars and theoretical models of VHE γ-ray production are introduced in Chapter 2. Chapter 3 describes the extragalactic background light (EBL), including the status of EBL measurements and EBL models. Details on the imaging Cherenkov technique and the MAGIC telescope are presented in Chapter 4. The analysis chain of the MAGIC data and the analysis performance are demonstrated in Chapter 5 using a Crab Nebula data set. Chapter 6 deals with the results of MAGIC observations of Markarian 421. Correlation studies between different energy bands and different flux states are presented as well as a modeling of the relevant physics processes inside of the jet. The discovery of two new blazars emitting VHE γ-rays, Markarian 180 and 1ES 1011+496, are presented in Chapter 7 and Chapter 8, respectively. A generic study of the EBL using available VHE spectra of TeV blazars and the resulting constraints are described in Chapter 9. Chapter 10 presents a new method to derive an upper limit on the redshift of the blazar PG 1553+113, which was newly detected in the GeV-TeV energy range by H.E.S.S. and MAGIC. Conclusions and a short outlook can be found in Chapter 11.

In the Appendix, technical studies and results are presented. Appendix A deals with strategies for the MAGIC telescope to more effectively observe extragalactic objects. An alternative data analysis technique, the model analysis, is presented in Appendix B. The model analysis aims to decrease significantly the energy threshold of MAGIC and improve the sensitivity of the experiment at low energies.

Chapter 1

Introduction to very high energy γ-ray astrophysics

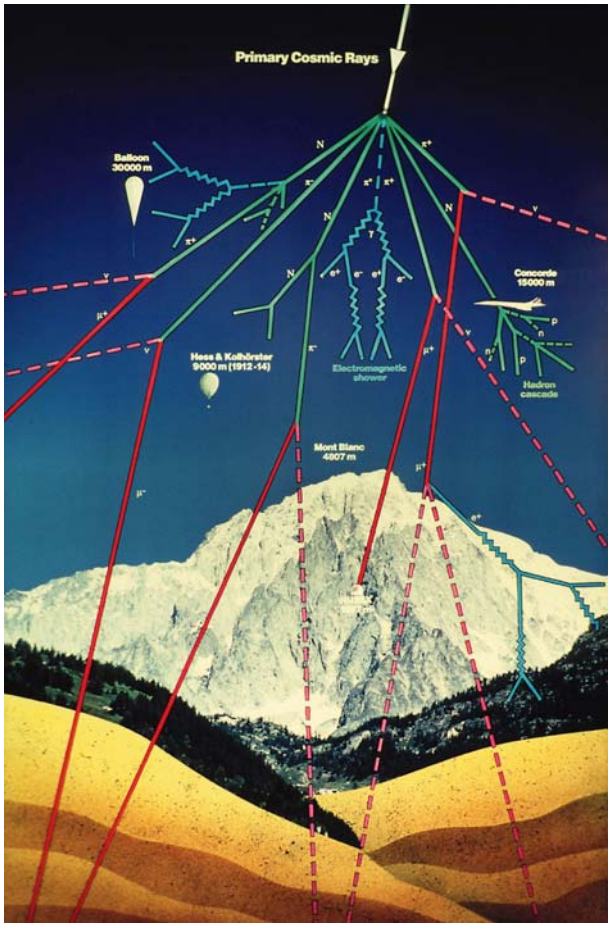

Figure 1.1: Astroparticle physics with Cosmic rays.

1.1 Astroparticle Physics

Astroparticle physics is a branch of particle physics that studies elementary particles of astronomical origin, and their relation to astrophysics and cosmology. It is a quite new field of research emerging at the intersection of particle physics, astronomy, and cosmology.

The astroparticle physics aims to answer fundamental questions about the contents and history of the Universe, nature of the dark matter, properties of neutrinos, origin of Cosmic rays, and nature of gravity. The rapid development of the astroparticle physics has led to the design of new detection techniques and construction of new experiments. In underground laboratories or with specially designed telescopes, antennas and satellite experiments, astroparticle physicists search for and study a wide range of cosmic particles including neutrinos, γ-rays and Cosmic rays at the highest energies. They are also searching for dark matter and gravitational waves.

The most active topics in astroparticle physics are:

- Search for dark matter, its nature, origin, and its distribution in the Universe
- Detailed studies of Cosmic rays and their chemical composition
- Gamma-ray astronomy
- Neutrino physics and neutrino astronomy
- Search for gravitational waves

This thesis is devoted to the Gamma-ray (γ-ray) astronomy, which is historically closely connected to the search of the origin of Cosmic rays. Therefore, I start with a short introduction on Cosmic rays before I concentrate on γ-rays.

1.2 Cosmic Rays

What are Cosmic rays? Ever since in 1912 the Austrian physicist Viktor Hess announced the first experimental evidence that an ionizing radiation constantly impinges on the Earth's atmosphere (Hess, 1912), the then newly discovered Cosmic rays have been puzzling physicists and astrophysicists. The spectrum of Cosmic rays is a remarkable power law extending over 13 orders of magnitude (Fig. 1.2). Due to the power law spectral behavior, Cosmic rays must have been emitted by objects which did not have time to thermalize. Cosmic rays are considered messengers from the non-thermal part of the universe, containing similar amount of energy as the thermal radiation, which is dominated by the cosmic microwave background (CMB). It is yet not clear where and how Cosmic

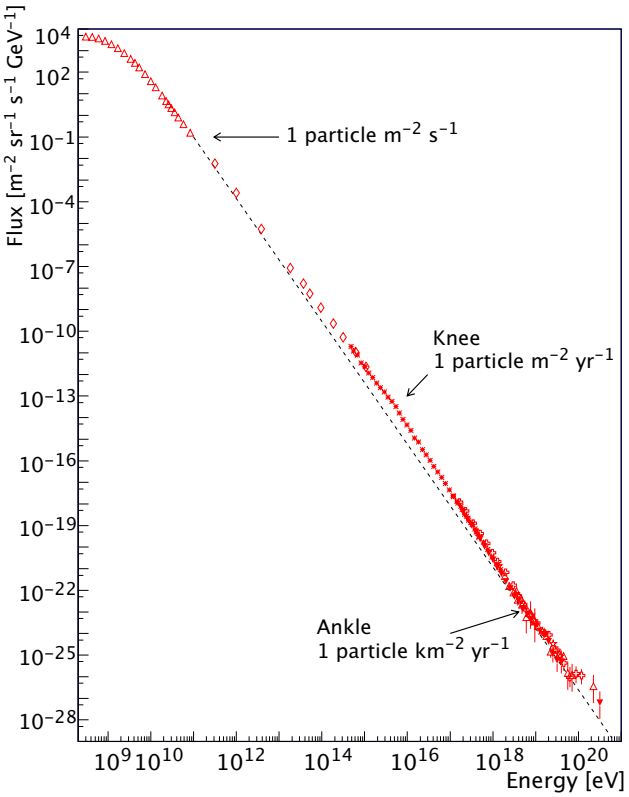

Figure 1.2: All particle energy spectrum of Cosmic rays.

rays are produced, what their composition is over the whole observed energy range and how far they propagate in space.

What are the features of Cosmic rays? The measured Cosmic ray spectrum (Fig. 1.2) spans an energy range extending over more than 13 orders of magnitude with fluxes dropping from 1 particle/(cm^2 s) at around 100 MeV to less than 0.01 particles/(km^2 century) for the highest observed energies. In the region of the energy spectrum which is unaffected by the Earth magnetic field and the propagation of particles to the Earth through the solar wind (at energies E greater than 1 GeV), the differential flux, dN/dE, follows a power law, $dN/dE \propto E^{-\alpha}$. The index $\alpha = 2.7$ is valid for energies below the knee (located at ≈4-5 PeV[1]), $\alpha = 3.0$ from the knee to the ankle (at ≈3 EeV[2]), $\alpha = 2.6$ from the ankle up to ≈30 EeV. At the highest energies with $E > 10^{20}$ eV, a cut-off (known as the Greisen-Zatsepin-Kuzmin (GZK) cut-off (Greisen, 1966; Zatsepin and Kuz'min, 1966)) in the spectrum is expected due to interaction of the charged particles with the CMB photons. The newest results above $E > 3 \cdot 10^{19}$ eV from the HiRes collaboration and the Auger observatory seem to confirm the expected steepening

[1]PeV= 10^{15}eV
[2]EeV= 10^{18}eV

of the energy spectrum (Teshima, 2007).

What is the composition of Cosmic rays? Up to the knee, the chemical composition has been measured directly: About 79% of the primary nucleons consist of protons, the remainder consist of helium nuclei and only a small fraction of nuclei of heavier elements (Longair, 1992). Less than 1% of the Cosmic rays consist of electrons and positrons, the spectrum of which is steeper than the one of protons and nuclei. Only a tiny fraction of the Cosmic rays is made up of γ-rays. While the origin of a significant part of the low-energy Cosmic rays (below 10 GeV) can be traced back to the Sun, the high-energy part ranging up to the knee is believed to originate from mostly galactic accelerators. The region between the knee and the ankle is under debate, while at higher energies the particles are usually explained by an extragalactic origin. Cosmic rays up to about 1 EeV are isotropic, while a claim on anisotropy at higher energies is still under debate (Teshima, 2007). It is believed that Cosmic rays are confined in the magnetic field of our Galaxy up to the knee. Still, some particles escape the galaxy (leaky box), in particular the giro radius is proportional to the energy of the particles and thus the escape rate out of the galaxy is energy dependent. As a result, the intrinsic source spectrum is harder ($\alpha \approx 2.1$) than the locally observed Cosmic ray spectrum.

What are the possible sources of Cosmic rays? There are only a few features in the energy spectrum of the Cosmic rays. This can be an evidence that the same mechanism and the same class of sources are responsible for the bulk of Cosmic rays. A general consideration can be made for a bottom-up scenario, e.g. particles are accelerated via magnetic shocks (Fermi acceleration I and II, Longair (1994)) and have to cross several times the shock region. This means that the particles' giro radius should not exceed the radius of the shock region. In the well-known Hillas plot (Fig.1.3) a number of possible sites, able to provide conditions to accelerate particles up to 1 ZeV[3], is shown. One can see that only a few object classes fulfill this criteria, which simplifies the search of the origin of Cosmic rays. However, for Cosmic rays with energies below the knee, more sources have to be considered as potential candidates. Following is a list of best known possible cites:

Galactic sources of Cosmic rays:

- Supernova Remnants, shell type
- Plerions
- Pulsars
- Microquasars, X-ray binary systems
- Young stars and young open star clusters

[3]ZeV= 10^{21}eV

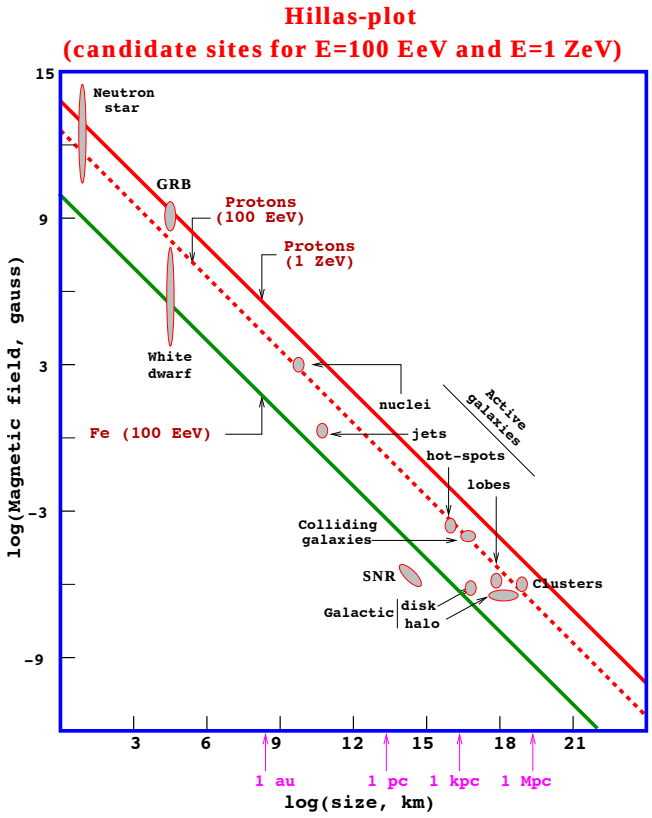

Figure 1.3: Hillas-Plot. Candidate sites to produce Cosmic rays with highest energies in the Universe.

Extragalactic sources of Cosmic rays:

- Active Galactic Nuclei (in the beamed regions, jet)
- Gamma-Ray-Bursts
- Starburst galaxies
- Clusters of Galaxies

How can one find the sources of Cosmic rays?
Gamma-rays and neutrinos are possible tracers of the sources because they are not deflected by magnetic fields, thus, they point directly to the places of their creation.

How transparent is the Universe to γ-rays?
The highest energy γ-rays are absorbed by pair creation with low energy photons (see Section 1.5). The transparency of the Universe for very high energy γ-rays is shown in Fig. 1.4 as a function of the redshift of a source. The transparency (or opacity) of a medium to radiation is characterised by the optical depth τ. If the number of γ-rays (or particles in general) is N_0 at a time t_0 then for

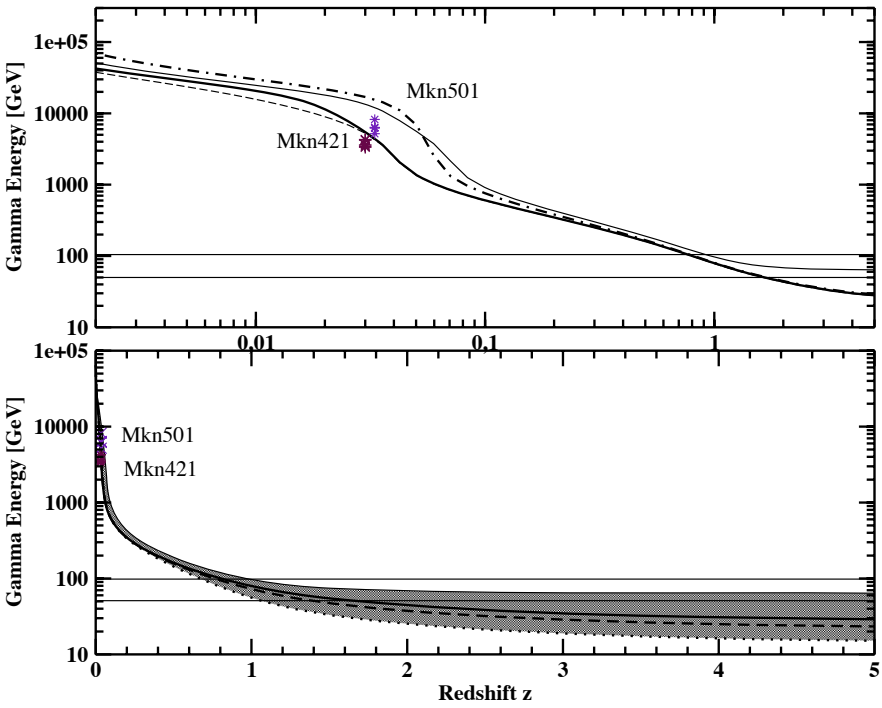

Figure 1.4: Gamma-ray horizon plot. The Gamma-ray horizon is defined as a function of the redshift, at which the optical depth τ for γ-rays with energy E is equal unity (see text for details). Curves correspond to different model predictions reflecting uncertainties in the knowledge of the absorbing medium (Kneiske et al., 2004). Points correspond to reported measurements of the cut-off energy which might be attributed to the absorption. The upper panel emphasizes differences between possible models for a nearby Universe (z $<$ 0.1), whereas the lower panel shows the opacity up to z = 5. The horizontal lines represent the energy thresholds of H.E.S.S. (100 GeV) and MAGIC (50 GeV).

a later time t the number of remaining γ-rays in an homogeneous medium is $N(t) = N_0 \exp(-\tau' \cdot (t - t_0))$. τ' depends on the properties of the medium. Throughout the thesis the optical depth $\tau = \tau' \cdot (t - t_0)$ is used so that for $\tau = 1$ the photon flux is e-fold, i.e. $N = N_0/e$ and e is the Euler's number. The so-called γ-ray horizon (Fazio and Stecker, 1970) is shown in Fig. 1.4 by plotting the energy of γ-rays at which $\tau = 1$ as a function of the redshift. The shown curves correspond to different model predictions for the density of the low-energy background radiation (Kneiske et al., 2004). For 200 GeV photons, the Universe is transparent up to a redshift of z = 0.5, whereas at 1 TeV only sources below z = 0.1 can be detected.

What are the experimental approaches? Experimentally, several approaches have been followed to detect Cosmic rays and γ-rays. Cosmic rays can be detected directly by:

- satellite experiment carrying a compact particle detector

- balloon experiments carrying a compact particle detector
- array of particle detectors on the ground

Cosmic rays can be detected indirectly by measuring:

- air shower particles using detectors (or arrays of detectors) on the ground;
- air shower Cherenkov light using cameras on the ground;
- air shower fluorescence light using cameras on the ground;
- acoustic waves of air showers using antennas on the ground or on balloons;
- radio emission of air showers using antennas on the ground.

Gamma rays can be detected by:

- satellite telescopes and detectors (directly);
- ground based imaging atmospheric Cherenkov telescopes, IACTs (indirectly, used in this thesis);
- water Cherenkov tanks (indirectly).

1.3 Very high energy gamma rays as messengers of cosmic processes

Gamma rays are electromagnetic radiation of very short wavelength of $\lambda < 10^{11}$m. The definition of the different energy/wavelength bands of the electromagnetic spectrum is shown in Fig.1.5. In this thesis, we are dealing with γ-rays in the so-called Very High Energy (VHE) band, i.e. with $E > 100\,\mathrm{GeV}$. Presently many VHE γ-rays sources have been discovered: from stars in an advanced stage of evolution (including pulsars and X-ray binaries) to energetic sources outside our Milky Way (active galaxies).

VHE γ-rays are of interest to astronomers because they can provide information about objects producing energetic charged particles, the Cosmic rays, which are the progenitors of gamma rays. Therefore, VHE γ-rays are messengers of violent, non-thermal processes happening at the location of the sources or close to it.

Another good reason for studying VHE γ-rays is to determine the origin of Cosmic rays. γ-rays are produced where Cosmic rays interact with matter, which usually happens close to the acceleration place. Therefore, γ-rays are generally indicating the origins of Cosmic rays. However, there are also alternative hypotheses of γ-ray production, which means that a γ-ray source is not necessarily a Cosmic ray accelerator.

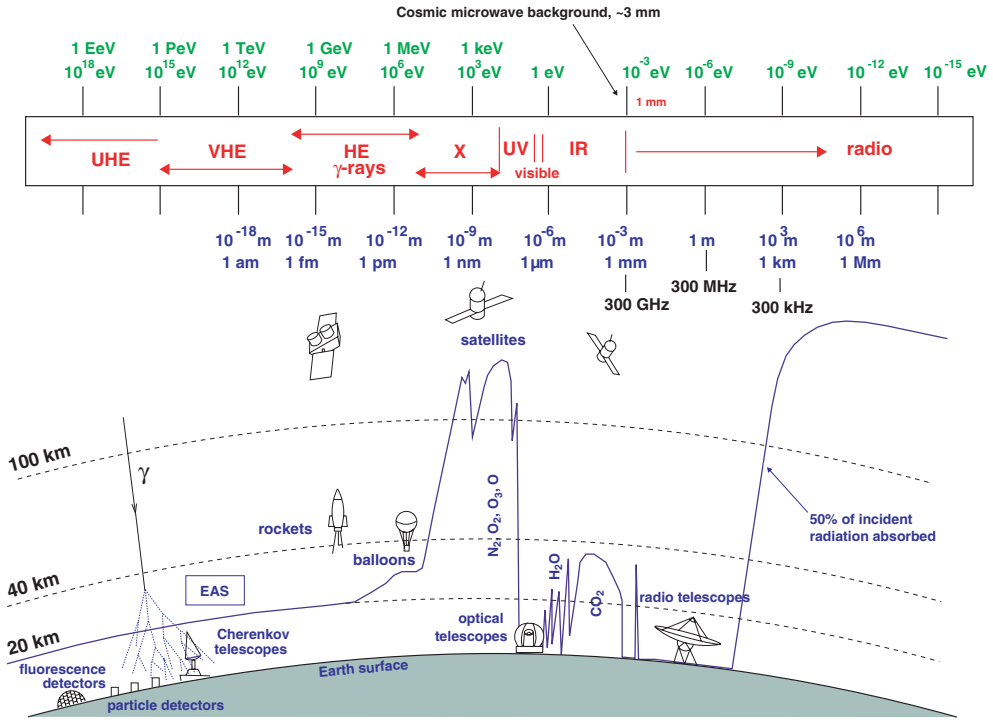

Figure 1.5: Atmospheric windows for electromagnetic radiation to observe the Universe (Longair, 1992). Common definitions of the energy bands are written in red. The continuous blue line corresponds to the height, at which a detector can receive half of the total incoming radiation at a given wavelength.

1.4 Production mechanisms of γ-rays

Astronomical objects emit energy in different types of processes. Most of the radiation energy is emitted thermally, which can be described in first approximation by a blackbody radiation (Planck's formula). The effective temperatures range from typically 3.000 K (red stars) to 150.000 K (X-ray binaries, white dwarfs). The hottest objects thermally radiate X-rays up to a few keV energy band. Gamma-rays with even higher energies are produced by non-thermal processes, i.e. from thermally not equalized systems. The most relevant non-thermal γ-ray production processes are summarized in Longair (1992):

- π^0 **decay**: Pions are the lightest mesons ($m_{\pi^0} = 135$ MeV, $m_{\pi^\pm} = 140$ MeV) and therefore are among end products of nucleonic cascades involving strong interactions. Charged (π^+, π^-) and neutral (π^0) pions are produced with the same probability. Neutral pions have a short life time of 10^{-16} s and electromagnetically decay into:

$$\pi^0 \longrightarrow \gamma\,\gamma \quad (99\%) \tag{1.1}$$
$$\pi^0 \longrightarrow e^+\,e^-\,\gamma \quad (1\%) \tag{1.2}$$

Charged pions, due to their relatively long life time $\approx 2.6 \cdot 10^{-8}$ s, undergo either collisions of strong interactions or depending on the gas density decay into:

$$\begin{aligned} \pi^{\pm} \longrightarrow \quad & \mu^{\pm} \quad \overline{\nu}_{\mu} \\ & \mu^{\pm} \quad \longrightarrow e^{\pm}\, \nu_{\mu}\, \overline{\nu_e} \end{aligned} \tag{1.3}$$

- **Bremsstrahlung.** When charged particles are deflected in electric fields they radiate bremsstrahlung. The emitted photon spectrum has a power law form with the same spectral index as the one of the accelerated particles. Bremsstrahlung of UHE Cosmic rays can reach TeV energies.

- **Synchrotron radiation.** In the presence of magnetic fields, relativistic charged particles emit Synchrotron radiation. For electrons, the peak emission energy is given by $E_{peak} = 5 \cdot 10^{-9} B_{\perp,\mathrm{G}} \gamma_e^2 \mathrm{eV}$ with the transverse component of the magnetic field $B_{\perp,\mathrm{G}}$ given in units of Gauss and the electron Lorentz factor γ_e. Synchrotron radiation of accelerated electrons is one of the most important processes in the non-thermal Universe. In the contest of VHE γ-rays, synchrotron radiation is the usual process for the generation of seed photons for Inverse Compton scattering. However, UHE Cosmic rays (electrons or protons) can emit Synchrotron radiation directly in the VHE domain.

- **Inverse Compton scattering**: Relativistic electrons (and positrons) scatter off low energy photons and transfer part of their energy to these photons. Depending on the electron-photon energy ration, one distinguishes three cases to specify the cross-section for the Inverse Compton scattering:

$$E_e E_\gamma \ll m_e^2 c^4 : \quad \sigma_{\mathrm{T}} = \frac{8}{3}\pi r_e^2 \quad (\mathrm{Thomson\ cross-section}) \tag{1.4}$$

$$E_e E_\gamma \approx m_e^2 c^4 : \quad \sigma_{\mathrm{KN}} \quad \mathrm{exact\ Klein-Nishina\ cross-section} \tag{1.5}$$

$$E_e E_\gamma \gg m_e^2 c^4 : \quad \sigma_{\mathrm{KN}} = \pi r_e^2 \frac{1}{\epsilon}\left(\ln 2\epsilon + \frac{1}{2}\right), \quad \epsilon = \frac{E_\gamma}{m_e c^2} \tag{1.6}$$

$$(\mathrm{Klein-Nishina\ approximation})$$

It can be shown that in the latter case the maximum energy gain for the photons is described by:

$$E_{\max} \approx 4\gamma^2 E_\gamma,$$

with Lorentz factors γ. In the Thomson regime, the emitted photons follow the spectral shape of the seed photons. In the Klein-Nishina regime, the resulting spectrum has a sharp cut-off, which is determined by the maximum energy of the participating electrons.

The hadronic process of π^0 decay and IC scattering are the most important sources of VHE γ-rays. In fact, it is a highly debated issue, which of the two processes is the dominant one. In case of the π^0 decay, this would point to hadronic accelerators and thus explain at least part of the origin of the Cosmic rays. Observation of VHE neutrinos from the same source would be the unambiguous proof of hadronic production. In case of IC scattering, leptonic accelerators would be favored, leaving the origin of Cosmic rays an open issue. I will go into some details of the acceleration models in the next Chapter. But at first, I discuss propagation losses of VHE γ-rays (following Section), as well as introduce object classes emitting this radiation (Section 1.6).

1.5 Absorption of VHE γ-rays in the Universe

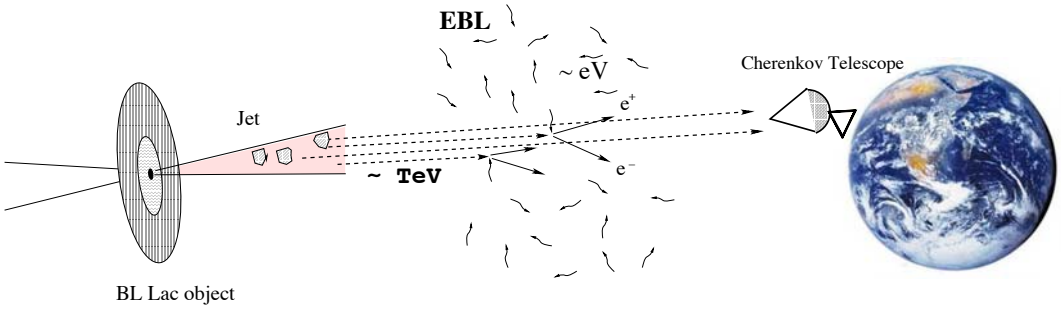

Figure 1.6: Sketch to illustrate absorption of losses extragalactic VHE γ-rays on the way to Earth by low energy photons of the extragalactic background light.

On the way from the source to the observer (Fig. 1.6), VHE γ-rays can suffer absorption losses by interaction with the low energy photon fields. The low energy photons belong to the evolving extragalactic background light (EBL), which is the topic of Chapter 3. The corresponding reaction is the pair-production of an electron-positron pair:

$$\gamma_{\rm VHE} + \gamma_{\rm EBL} \longrightarrow e^+ + e^- \quad \text{with} \;\; E_{\gamma\,\rm VHE} \cdot E_{\gamma\,\rm EBL} > (m_e c^2)^2 \tag{1.7}$$

The cross section for pair production $\sigma_{\gamma\gamma}$ can be analytically calculated in quantum electrodynamics (e.g. Heitler (1960)):

$$\sigma_{\gamma\gamma}(E,\epsilon,\theta) \;\; = \;\; \frac{3\,\sigma_{\rm T}}{16}\,(1-\beta^2)\,\left[2\beta\,(\beta^2-2) + (3-\beta^4)\ln\frac{1+\beta}{1-\beta}\right] \tag{1.8}$$

$$\text{with} \;\; \beta \;\; := \;\; \left(1 - \frac{2\,m_e^2\,c^4}{E\,\epsilon\,(1-\cos\theta)}\right)^{1/2}$$

E is the energy of the VHE γ-ray photon, ϵ is the energy of the low energy photon, $\sigma_{\rm T}$ is the Thomson cross section[4], and θ is the angle between the two photons

[4] $\sigma_{\rm T} \;=\; 6.6524 \;\cdot\; 10^{-25} \;\; {\rm cm}^2$

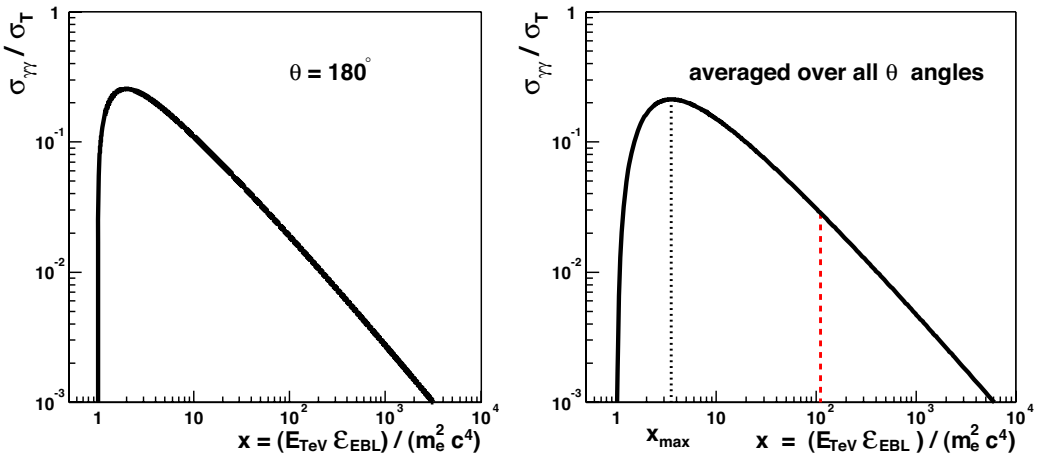

Figure 1.7: Cross section of the pair creation process $\gamma\,\gamma \longrightarrow e^+\,e^-$ in units of σ_T (see Eq. 1.8). *On the left:* the differential cross section for head-on collisions $\theta = 180°$. *On the right:* the cross section when integrating over an isotropic photon distribution in the angle θ. The maximum is at $x_{\rm max} \approx 3.6$ (marked by the vertical dotted line). The vertical dashed line marks the place where the cross section decreased by $1/e^2$ of the maximum value.

in the center of mass system. In Fig. 1.7, the cross section for pair creation is shown in units of $\sigma_{\rm T}$. The X-axis is chosen to have units of the threshold of pair creation: $x = (E\,\epsilon)\,/\,(m_e^2\,c^4)$. On the left, the cross section for head-on collision of two photons is shown ($\theta = 180°$), whereas on the right the averaged cross section over an isotropic photon distribution can be seen. The steep rise of the cross section close the threshold is clearly visible. The energy of EBL photons, for which the cross section has its maximum, can be expressed (for convenience reasons) in terms of the corresponding γ-ray energy as:

$$\epsilon_{EBL} \approx \frac{1}{E_{\rm TeV}}\,{\rm eV} \quad \text{or} \quad \lambda_{EBL} \approx 1.24\,\frac{E_{\rm TeV}}{1}\,\mu{\rm m} \tag{1.9}$$

$E_{\rm TeV}$ is energy of the VHE γ-rays in units of TeV. Note that the wavelength range of EBL photons responsible for absorption of a single energy of VHE γ-rays is quite large: it extends over about two magnitudes. The red dotted line in Fig. 1.7 is at the place where the cross section decreased by $1/e^2$ of its maximum value. Note that the influence of the 2.7 K cosmic microwave background ($\lambda > 300\,\mu$m) can be neglected for energies up to ≈30 TeV: The threshold of γ-rays of $E = 20$ TeV is at $\lambda \approx 100\,\mu$m.

The optical depth of the VHE γ-rays, $\tau(E)$, emitted at the redshift z, can be then calculated solving the three-fold integral (see also Dwek and Krennrich

(2005)):

$$\tau(E_\gamma,\, z) = \int_0^z \mathrm{d}\ell(\mathrm{z}') \int_{-1}^{1} d\mu \, \frac{1-\mu}{2} \int_{\epsilon'_{th}}^{\infty} d\epsilon' \, n(\epsilon', z') \, \sigma_{\gamma\gamma}(\epsilon', E', \mu) \quad (1.10)$$

$$\begin{aligned} \mu &:= \cos\theta \\ n\,(\epsilon\,) &:= \text{EBL energy density} \\ \mathrm{d}\ell(\mathrm{z}) &:= \text{distance element} \end{aligned}$$

A computer program has been developed to calculate $\tau(E)$ for a given distance and a given density profile of the EBL photons, i.e. to solve Eq. 1.10 (Mazin, 2003). The program was refined during this Thesis and made available for the MAGIC collaboration.

Throughout the Thesis I adopt a Hubble constant of $H_0 = 72\,\mathrm{km\,s^{-1}Mpc^{-1}}$ and a flat universe cosmology with a matter density normalized to the critical density of $\Omega_m = 0.3$ and $\Omega_\lambda = 0.7$.

Whereas the distance to the source is generally known (see Chapter 10 for an exception), the density of the EBL is uncertain. Recent model predictions differ by a factor of 2 in the expected EBL density. The direct measurements of the EBL are very difficult due to strong foreground emissions in our Solar system (see Chapter 3 for more details and Chapter 9 for new constraints on the EBL density).

The expected optical depth for sources at different redshifts is shown in Fig. 1.8. Hereby, the "best fit" model from Kneiske et al. (2002) is used to estimate the EBL density. One can see that the optical depth is not only redshift but also energy dependent. According to a common definition of the optical opacity we say that for $\tau < 1$ the medium is transparent, whereas for $\tau > 1$ the medium is opaque. The crossing points of the horizontal dotted line in Fig. 1.8 ($\tau = 1$) with the attenuation lines define then the energy for the different redshifts, at which the Universe becomes opaque. It is evident that a low threshold of a VHE γ-ray detector is essential to observe distant sources. For example, no VHE γ-ray emission is expected to be detected above 1 TeV for a source at $z = 0.2$.

There are two major aspects concerning the interconnection between VHE γ-rays and the EBL:

1. The EBL leaves a unique imprint on the VHE spectra. This imprint can be used to study the EBL.

2. The impact of EBL onto VHE spectra is fundamental. We need to understand EBL in order to study intrinsic properties of the VHE γ-ray sources.

Concerning point (1): From a single observed energy spectrum of a VHE γ-ray source, it is rather difficult if not impossible to distinguish between the imprint of the EBL and intrinsic features of the source. Observed features can be source

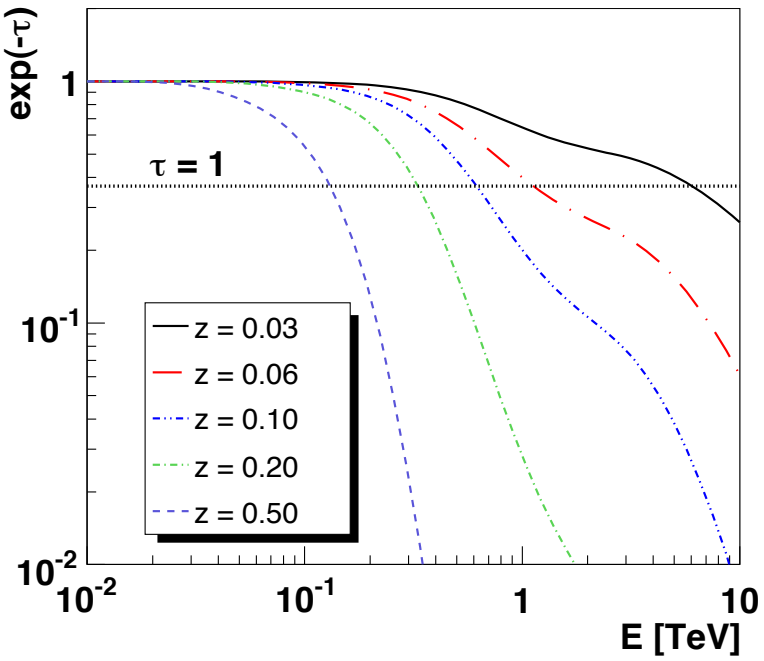

Figure 1.8: Attenuation coefficients $\exp(-\tau)$ as a function of γ-ray energy. The "best fit" model from Kneiske et al. (2002) is used for the EBL density. The curves represent the expected attenuation of the VHE γ-ray spectra for different source distances. The horizontal dotted line corresponds to the optical depth $\tau = 1$, i.e. it crosses the attenuation curves at the energy, above which the Universe becomes opaque.

inherit due to an intrinsic absorption or due to a source, which does not provide necessary conditions for acceleration of charged particles to high enough energy. A way to pin-point the EBL impact is to use population studies of many extragalactic sources: whereas the intrinsic features might be different, the imprint of the EBL is the same (at a given redshift). With the current population of VHE γ-ray sources, it is only possible to set limits on the EBL, arguing that the observed spectra contain at least the imprint of the EBL.

Note that only distant extragalactic VHE γ-ray emitters suffer from the absorption by the EBL. For the galactic sources, the effect is negligible up to energies of about 100 TeV. For higher energies, the absorption on the photon field of the Cosmic Microwave Background (CMB) starts to be important.

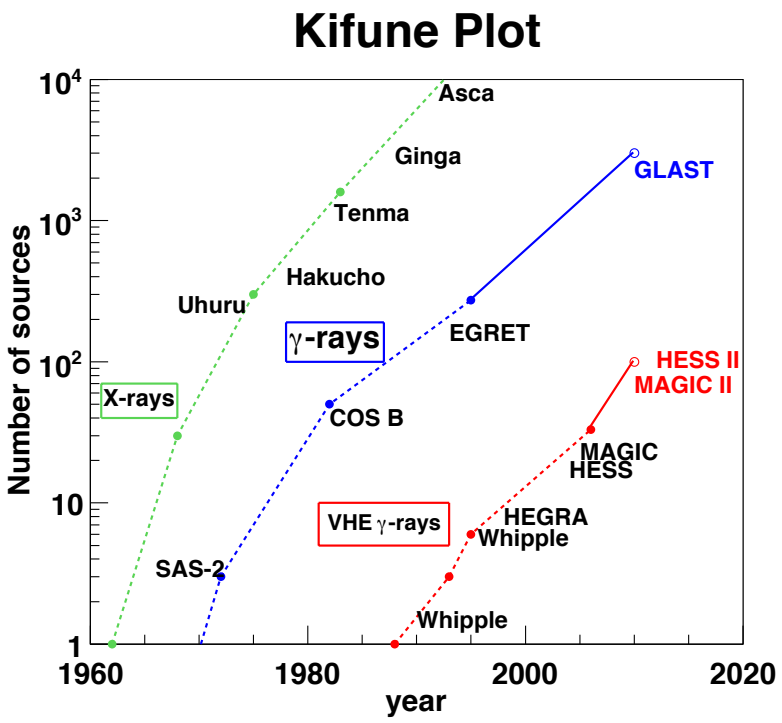

Figure 1.9: Diagram of the number of detected sources versus time for three energy bands: X-rays, γ-rays, and VHE γ-rays. One can clearly see that the number of detected sources depends on the age of the field (related to the sensitivity of the instruments). The kind of plot is called after his inventor "Kifune plot".

1.6 Sources of VHE γ-rays

In the following, I am briefly summarizing major classes of VHE γ-ray emitters. Objects of some of these classes are already detected to emit VHE γ-rays, some others are still very good candidates. Due to the fact that the field of the VHE γ-ray astrophysics is quite young, a detection of a source is quite often a matter of a long observation time (order of 100 hours) and a sensitivity of the instrument. The sensitivity for IACTs is usually defined as a flux level, which can be detected after 50 h of observation with a significance of $5\,\sigma$. The relatively small field of view of IACTs (maximum 5 degrees) does normally not allow to observe several sources together. For variable sources, often only a flaring (high flux) state can be detected. Guidance for source searches from observations in lower energy bands is of limited use because correlations between lower and higher energy emission are far from being understood. A detection of a flaring state of an object is often a matter of luck. This in turn means that many flares (and sources) remain undetected although the sensitivity of the current instruments would make a detection possible if one observes in the right moment. Note, however, that a

proposed optical–VHE γ-ray correlation used for the search for new sources in this thesis resulted in a detection of two new VHE γ-ray emitters (see Chapters 7 and 8). The current number of detected sources is about 55 and continuously growing. In Fig. 1.9, a time diagram for the detected sources is shown. Solid lines represent extrapolations of the experiments going online in the year 2008/9: GLAST, MAGIC II, and H.E.S.S II.

The VHE γ-ray sources are naturally divided into galactic and extragalactic sources. There are about 40 detected galactic sources and 15 extragalactic ones. The current sky map of VHE γ-ray sources is shown in Fig. 1.10.

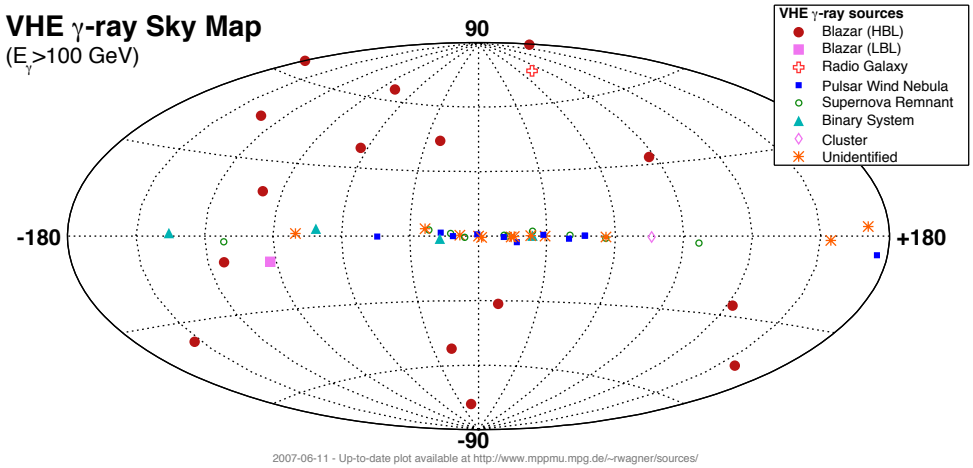

Figure 1.10: A sky map of VHE γ-ray sources in galactic coordinates as of May 2007.

Galactic sources:

- **Supernova remnants: shell type.** A supernova remnant is the left-over of a supernova explosion of a star. The supernova remnant is expanding into the interstellar medium of a lower density building a shock wave. The remnant consists of ejected material expanding from the explosion, and the interstellar material it sweeps up and shocks along the way. Particles are accelerated in these shocks by means of collisionless interaction of the particles with magnetic clouds in the interstellar medium (Fermi acceleration, Longair (1994)). Supernova remnants have long been suspected to be the main source of Cosmic rays and hence also to produce VHE γ-rays; they seem to be the dominant sources capable of supplying the energy required to feed the bulk of the Cosmic rays in our Galaxy. The mechanism of particle acceleration in the expanding supernova remnant shocks is thought to be well understood. However, clear evidence for the production of high-energy hadronic particles in supernova shells has proven to be remarkably hard to find. It seems that only observation of VHE neutrinos from the direction of the supernova shells would unambiguously prove the theory.

Prominent detected supernova remnants emitting VHE γ-rays are: Cas A, RX J1713.7-3946, HESS J1813-178, and RX J0852.0-4622.

- **Pulsar wind nebulae.** Pulsar wind nebulae - PWNe or plerions - are systems created in supernova explosion, in which a fast rotating magnetized neutron star (pulsar) is the central object surrounded by the sweeped up material. Plerions are amongst the most abundant sources of VHE γ-rays in our Galaxy. The rotational energy of the neutron star is converted, by some not fully understood mechanism, into a relativistic stream of particles, presumably mostly electrons and positrons generated near the pulsar. This pulsar wind terminates in a shock when it encounters the ambient medium, which is often composed of ejecta from the supernova explosion. The accelerated electrons of the pulsar wind nebula are an efficient source of VHE γ-rays, by IC upscattering of ambient photons, for example those of the microwave background. Compared to the case of supernova remnants, the upscattering process is very efficient in generating γ-rays, which explains the abundance of pulsar wind nebulae detected in high energy gamma rays. The prototypical pulsar wind nebula is the Crab Nebula, which is the brightest known steady VHE γ-ray emitter in the sky. Currently (July 1007), 18 PWN have been detected to emit VHE γ-rays (Hinton, 2007).

- **Pulsars.** Pulsars are rotating magnetized (magnetic fields $\approx 10^6\,\mathrm{G}$[5]) neutron stars with the rotation cycle of the neutron star linked to the pulse period. The accelerated particles near the pulsar are beamed forming outflowing jets. Since the rotation and magnetic axes of the pulsar are misaligned, the observer only sees an emission from a pulsar when the beam crosses his line of sight. The emission mechanism is not yet completely understood: It can be Synchrotron emission near the polar caps of the pulsar. Or it can be IC scattering in the outer regions (outer gaps) of the magnetosphere. The emission can be also a mixture of both mechanisms. Pulsars are ones of the best known clocks in the Universe with periods down to milliseconds and have been found to emit electromagnetic radiation in radio through hard X-ray energy band. Five pulsars have been detected by EGRET in γ-rays with energies up to 10 GeV but searches for pulsed VHE γ-ray signals resulted in upper limits only.

- **X-ray binary systems.** In our Galaxy, more than 80% of stars are members of multiple systems made up of several stars (double, triple...) orbiting around each other. The X-rays are produced by matter falling from one component (usually a relatively normal star) to the other component, which is often a neutron star or a black hole. Three of these objects have recently been found to emit VHE γ-rays: LS 5039 (Aharonian et al., 2005b),

[5] $1\ \mathrm{G} = 10^{-4}\ \mathrm{T}$

LS I +61 302 (Albert et al., 2006e), and PSRB 1259-63 (Aharonian et al., 2005a). The likely emission mechanism is that relativistic particles, very likely electrons, are injected into the surrounding medium. The particles are further accelerated when they enter a shock region created between winds of the two objects. VHE γ-rays are then created via IC scattering of the cosmic microwave background. All three sources are found to be variable with a period coinciding with the orbital cycle.

- **Microquasars.** Microquasars are stellar objects named after their similarity to quasars. They have many common characteristics: strong and variable radio emission, often resolved as a pair of radio jets, and an accretion disk surrounding a black hole or neutron star. In quasars, the black hole is supermassive (millions of solar masses); in microquasars, the black hole mass is a few solar masses. Since blazars (quasars with jets pointing towards observer) are known VHE γ-ray emitters, it was suggested that also some microquasars would emit VHE γ-rays. In fact, during the write-up of this Thesis, the first evidence of a VHE γ-ray signal form a bright microquasar Cygnus X-1 has been reported (Albert et al., 2007h).

- **Young open star clusters.** It has been suggested that winds of young massive stars collide with each other and create shocks, which can accelerate particles to extreme energies. First evidence of such a process was reported by HEGRA in the vicinity of Cygnus OB2 region (Aharonian et al., 2002e) and confirmed by MAGIC (Oña-Wilhelmi et al., 2007). Shortly afterwards, a VHE γ-ray signal associated with extremely massive stars, known as Wolf-Rayet (WR) stars, has been detected by H.E.S.S. (Aharonian et al., 2007c) establishing a new class of galactic VHE γ-ray emitters.

- **Galactic center.** The Galactic center has been found to emit steady VHE γ-ray signal up to 10 TeV as reported by the CANGAROO (Tsuchiya et al., 2004), H.E.S.S. (Aharonian et al., 2004c), VERITAS (Kosack and VERITAS Collaboration, 2004), and the MAGIC (Albert et al., 2006c) collaborations. However, the interpretation of the emission mechanism is difficult since the region is packed with different potential sources, and the angular resolution of the current instruments is insufficient to disentangle the exact location of the VHE γ-ray emission. Most probable scenarios involve emission due to a pulsar wind nebula or a close by supernova remnant. More exotic scenarios include the black hole as an accelerator or even dark matter particles annihilation to reproduce the observed signal (Horns, 2005).

- **Unidentified sources.** Unlike above described sources, some of the detected galactic VHE γ-ray emitters do not have any obvious other wavelength counterparts, which spatially coincide with the location of the observed excess. It might be that the sources are to dim to have been detected

by EGRET. This hypothesis will be clarified by GLAST with a 20 times better sensitivity than EGRET.

- Diffuse emission. Furthermore, the H.E.S.S collaboration reported a diffuse VHE γ-ray emission along the galactic plane after subtracting point sources (Aharonian et al., 2006c). The most likely scenario is a hadronic collision of Cosmic rays with dense molecular clouds and dust in the galactic plane creating among other particles π^0s with a subsequent decay into VHE γ-rays. A spacial agreement between the observed VHE γ-ray excess and distribution of molecular clouds supports this hypothesis. Noteworthy, EGRET also observed a diffuse HE γ-ray excess in the galactic plane region.

Extragalactic sources:

- **Active Galactic Nuclei.** Active galactic nuclei (AGNs) are galaxies with an active core, i.e. being brighter and more energetic than the ones of usual galaxies. AGNs are believed to be the most powerful sources of non-thermal energy in the Universe. They host a very compact (order of big planets) supermassive black hole (SMBH) in the central region with a mass around 10^6 to 10^{10} solar masses. In the unified scheme of AGNs, the SMBH is surrounded by a disc of material being accreting by the SMBH. Perpendicular to the disc, two plasma jets are created carrying out part of the angular momentum of accreted material. The jets extend up to several kpc distance scale from the central SMBH and seem to harbor conditions adequate for very efficient cosmic particle acceleration. Non-thermal emission from the jets has been measured to be highly variable at all wavelength from radio through γ-rays. In case, the jet points towards the observer, the object is classified as blazar. Currently all but one extragalactic object detected in VHE γ-rays are blazars. The only exception is M87, the largest known radio galaxy at a distance of $z = 0.0047$. The production process of VHE γ-rays is under debate: both leptonic and hadronic models seem to be able to describe the observational data well. More details on AGNs and their emission mechanisms can be found in Section 2.

- **Starburst galaxies.** A starburst galaxy is a galaxy with an exceptionally high star formation rate, compared to the usual star formation rate in most galaxies. Such galaxies are often observed to have a burst of star formation after a collision or close encounter between two galaxies. It is believed that a high supernova rate is associated with the high star formation rate, providing shocks strong enough to accelerate charged particles up to highest energies. However, presumably due to a relatively low flux level, starburst galaxies have not been detected so far in VHE γ-rays.

- **Gamma Ray Bursts.** Gamma Ray Bursts (GRBs) are short (seconds to minutes) but very violent and quite frequent (1-2 per day) phenomena

in the Universe. During their bursts mostly in γ-rays they outshine all other sources in the Universe. The origin of the enigmatic GRBs is still three decades after their discovery under debate (see Meszaros (2006), for a recent review). The currently most accepted model is that these highly transient bursts are asymmetric supernova or hypernova explosions. In the fireball model (Rees and Meszaros, 1992), the explosion produces an ultrarelativistic outflow of an optically thick plasma shell, which emits the GRB as soon as it becomes optically thin. An alternative model of GRBs has been developed by Dar and de Rújula (2004). The short duration of GRBs (milliseconds to a few hundred seconds) hints at very compact progenitors. The mean distance of GRBs is about $z = 2.8$, which means that in most cases the VHE γ-rays will be absorbed by the EBL and only HE γ-rays can reach the Earth. However, few GRBs occur at redshifts much closer than $z = 1$, may be even in our Galaxy (1 per 10-100 My) which makes a detection possible. To search for the short burst durations of the isotropically distributed GRBs on the sky, the MAGIC telescope is equipped with a drive system allowing a fast repositioning to a GRB location provided by satellite detectors. The repositioning times range from 0 to 40 sec depending on the angular distance the telescope has to slew, whereas the mean slewing time is about 30 seconds. In the first two years of operation of the MAGIC telescope about 10 GRBs were observed seconds after the alert was given but no VHE γ-ray signal was found so far.

Exotic sources: connection to fundamental physics In the following, rather uncertain and speculative candidates of VHE γ-ray emission are presented. Though observations of these sources normally result in upper limits on a VHE γ-ray flux, they probe fundamental physics of the Universe and have a potential of great discoveries.

- **Dark matter candidates.** One of the main questions of cosmology is the nature of dark matter (DM). In 1933, F. Zwicky used the kinematic movement of galaxy clusters to estimate the total mass needed to keep the clusters together. The visible mass appeared to be far too low and he postulated a different kind of matter (invisible or dark matter). The dark matter particles interact only by gravitational forces with hadronic matter, otherwise they would have been discovered before. Since then the search for the nature of these particles is ongoing. So far one of the best theoretical candidates is the neutralino – the lightest supersymmetric weakly interacting massive particle. The neutralino has a property to be the anti-particle of itself so that neutralinos can undergo a self-annihilation, converting into quarks or into two γ-rays. The quarks convert into baryons and muons, among them π^0s, which in turn decay by emitting γ-rays. These γ-rays can be then detected confirming the existence of the neutralino in case other γ-ray production mechanisms can be ruled out. The energy of the expected

γ-rays is uncertain as the rest mass of the neutralino is uncertain. However, popular models predict a rest mass above 50 GeV, which allows for VHE γ-ray signals. Several sources with an enhanced probability to enrich DM were observed with the MAGIC telescope in the first two years of operation but only upper limits could be derived.

- **Lorentz invariance violation (LIV) to be possibly observed in short duration γ-ray flares.** Lorentz Invariance (LI) is postulated by Special Relativity and by extension of General Relativity. Any experimental evidence for a violation of the LI will be a clear signature of new physics beyond General Relativity. MAGIC has a possibility to test the LIV by measuring time differences as function of energy when observing short flares from distant sources. If LI is conserved, the VHE γ-rays emitted at the same time should also arrive at the same time on the Earth. If the arrival time is the same, one can put constraints on the level at which the LI is conserved. In case there is a delay in arrival times depending on the energy of γ-rays, a possible LIV can be claimed. However, the delay can be source intrinsic, i.e. VHE γ-rays are emitted at different times or different locations in the source.

Chapter 2

TeV blazars

Figure 2.1: Artistic view on a blazar. Image by J. J. van Ellinckhuijzen.

TeV blazars and especially their emission of very high energy γ-rays are the main topic of this thesis. The emission can not only be used to study non-thermal processes in the Universe but also to constrain the extragalactic background light of low energy photons. In the following, I will briefly describe observational properties of blazars, models of the VHE γ-ray emission, and the sources found so far.

2.1 Active Galactic Nuclei

In some galaxies, known as active galactic nuclei (AGNs), the nucleus (or central core) produces more radiation than the entire rest of the galaxy. This core is often highly variable in flux. Currently accepted AGN models are based on supermassive black holes (SMBH) which lie in the center of the galaxies. The energy spectra of AGNs differ very much from blackbody emission, which is normally observed from stars. The AGN emission is observed to be bright at all wavelengths, suggesting, therefore, that the emission is mainly non-thermal. The high energy luminosity varies on very short time-scales, less than a day, and this means that the size of the central region (or, in general, the size of the high energy emission region) is less than one light-day across (six times the distance from the Sun to Neptune). At lower energies (radio and visible bands), variations in the luminosity are also found, but they are weaker and slower than at high energies. Usually, sources spend most of the time in a low flux state, accompanied by short (hours-days) or long (months-year) outbursts, which are called "flares". The most efficient conversion of matter into energy is the accretion by a black hole. By this mechanism about 10% of the matter can be transformed into kinetic energy, and so models of AGNs infer that it is a SMBH, which is the engine behind the emission.

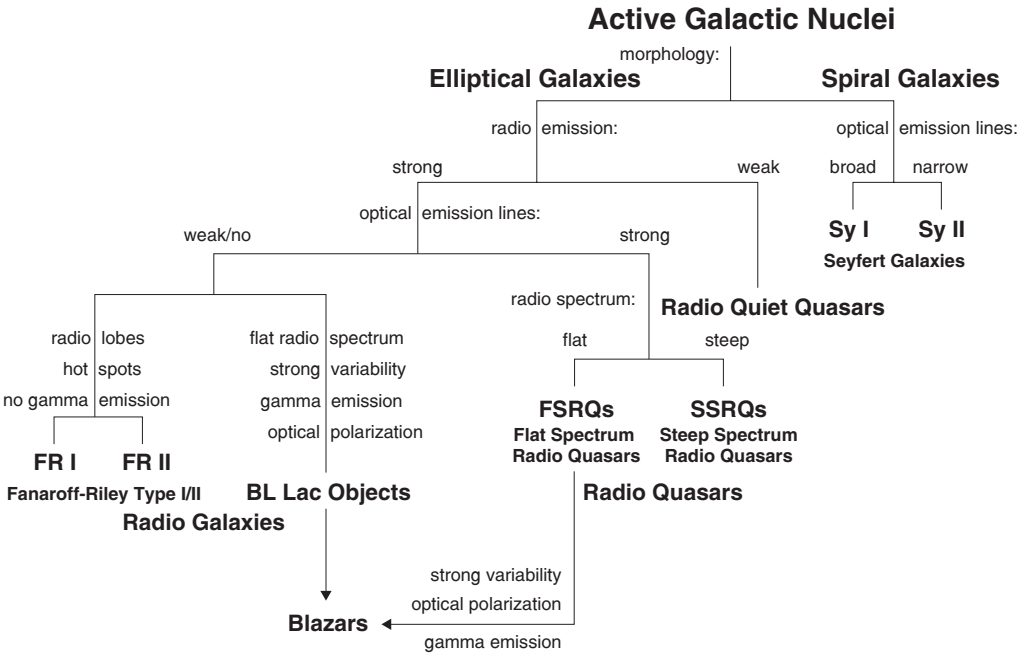

Figure 2.2: Classification scheme for AGNs (adapted from Wagner (2006))

In the unified AGN scheme (Blandford and Konigl, 1979; Urry and Padovani, 1995), the observed properties of the AGNs mainly depend on the viewing angle

of the observer, the accretion rate and the mass of the central SMBH (Fig.2.3 and Fig.2.4). The SMBH is located in the central region and accretes surrounding material, which forms a disc of hot plasma. Due to friction and turbulent processes caused by magnetic instabilities in the accretion disc, gravitational energy is transformed into thermal radiation. This in turn heats up (ionizes) atoms in the rapidly moving gas clouds close to the SMBH. These clouds form broad-line regions, observed by the Doppler-broadened emission lines. Molecular gas clouds further away from the SMBH move slower and produce narrow line absorption and emission spectrum. The whole system is surrounded by a dust torus, which obscures the view to the central part of the AGN along the equatorial plane. In case the accretion rate is high enough, two strongly collimated ultra-relativistic plasma outflows (jets) are observed.

Different AGN names (Fig.2.3) originate from optical and radio observations. Most ($\sim$90%) of AGNs are radio quiet and many are also obscured. This means that they have large amounts of gas and dust around them which blocks large amounts of the light they emit. The low optical luminosity AGNs are called Seyfert Galaxies (there are two types) and Radio Galaxies. The more powerful AGNs in the optical band are called quasars (from Quasi-Stellar Objects or QSO as they looked like stars in early telescopes) and BL Lacs. Flat Spectrum Radio Quasars (FSRQ) and BL Lacs have their jet aligned close to the line of sight of the observer. The two subclasses are jointly called "blazars". Quasars are so bright in the optical band that they can be seen across the Universe and are a useful cosmological tool to measure the evolution of the Universe. I will show in Chapter 3 that blazars (not bright in the optical band in general), due to their brightness in the VHE γ-rays, can be used to test the evolution of the Universe, too.

In the following, I will concentrate on the AGN subclass of blazars because all but one detected extragalactic VHE γ-ray emitters belong to this subclass.

2.2 Blazars

2.2.1 General Properties

Blazars are AGNs with a jet, which is aligned close to the line of sight of the observer. The observer looks, so to say, inside the jet. The name *blazar* goes back to the astronomer Ed Spiegel, who originally used it to denote a combination of Optically Violently Variable (OVV) quasars, Flat Spectrum Radio Quasars (FSRQs), and BL Lacertae objects ("BL Lac objects" or simply "BL Lacs"). The blazar types have differences in the optical emission: OVV and FSRQs have strong optical emission lines; BL Lacs have weak or no optical lines. The difference seems to lie in the amount of cold molecular clouds along of the observer's line of sight.

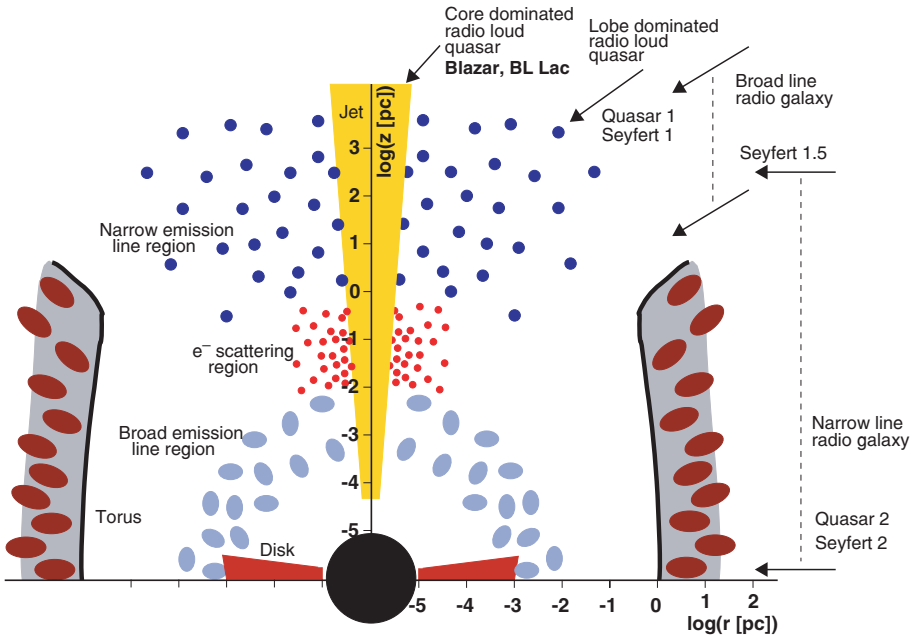

Figure 2.3: Artist's view of the unified AGN scheme. The classification is based on the viewing angle. The different regions around the black hole are illustrated. Due to symmetry the lower half is omitted. Note that the scale is logarithmic. Adapted from Biermann et al. (2002).

It is widely believed that the relativistic jet is the key element of the observed blazar emission. Acceleration processes in the jet generate non-thermal highly variable emission over an energy range spanning up to 20 orders in magnitude, i.e. from radio to VHE γ-ray domain. The jets are beamed by strong magnetic fields and oriented perpendicular to the accretion disc. The jets themselves seem to be stable up to kpc scales being a strong source of non-thermal radiation from radio to VHE γ-rays. The jets are often characterized by a highly polarized radiation, short variability time scales and an apparent superluminal motion. It is believed that the twisting of magnetic fields in the accretion disk collimates the outflow along the rotation axis of the central object, so when conditions are suitable, a jet will emerge perpendicular to the plane of the accretion disk.

The physical conditions inside of the jet are currently mainly unknown. The general popular believe is that detailed magnetohydrodynamic models should be able to reproduce jet collimation and particle acceleration mechanisms in the accretion framework (see e.g. Meier et al. (2001)). The magnetic field is frozen (i.e. bound to) in the outflowing plasma, allowing particles to escape along the magnetic field lines. At the beginning, the jets as a total are magnetically driven (Poynting flux dominates over the kinetic matter flux) and collimated due to a

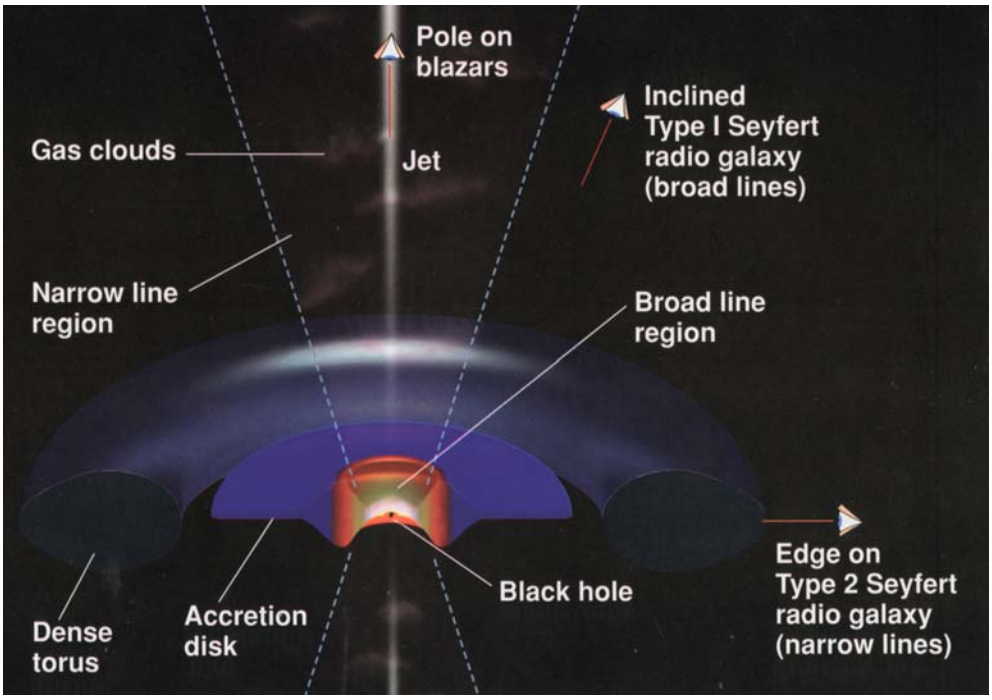

Figure 2.4: Another artist's view of the unified AGN scheme to better illustrate the geometry of the system.

toroidal component of the magnetic field (Sikora et al., 2005). Further down the jet, on sub-parsec scales, the energy density of non-thermal particles is much higher than the energy density of the magnetic field. However, the strength of the magnetic field as well as the composition of the jets are still uncertain. In order to explain the observed electromagnetic spectrum, most models assume that a relativistic population of electrons or of protons or of both is somehow accelerated within the jet. The acceleration mechanism is indeed a matter of debate, and I will go into more details below. The geometry of the emission region is unknown as well as the number of the emission regions in the jet. In simplest models, one single spherical region is assumed (one-zone models).

From the observational point of view, the spectral energy distribution (SED) of blazars exhibits a two-bump structure with the first peak in the infrared up to keV energy range and the second maximum at MeV up to GeV-TeV energies. A typical example is shown in Fig.2.5 for the blazar Mrk 421 (closest known blazar with $z = 0.030$, and the first one discovered to emit at TeV energies, Punch et al. (1992)). The historical data from 1994 to 1998 show variability at all wavelengths.

2.2.2 The blazar sequence

The statistics of blazars found so far allows to make several phenomenological studies about their properties. So combining 126 blazars and binning their SEDs

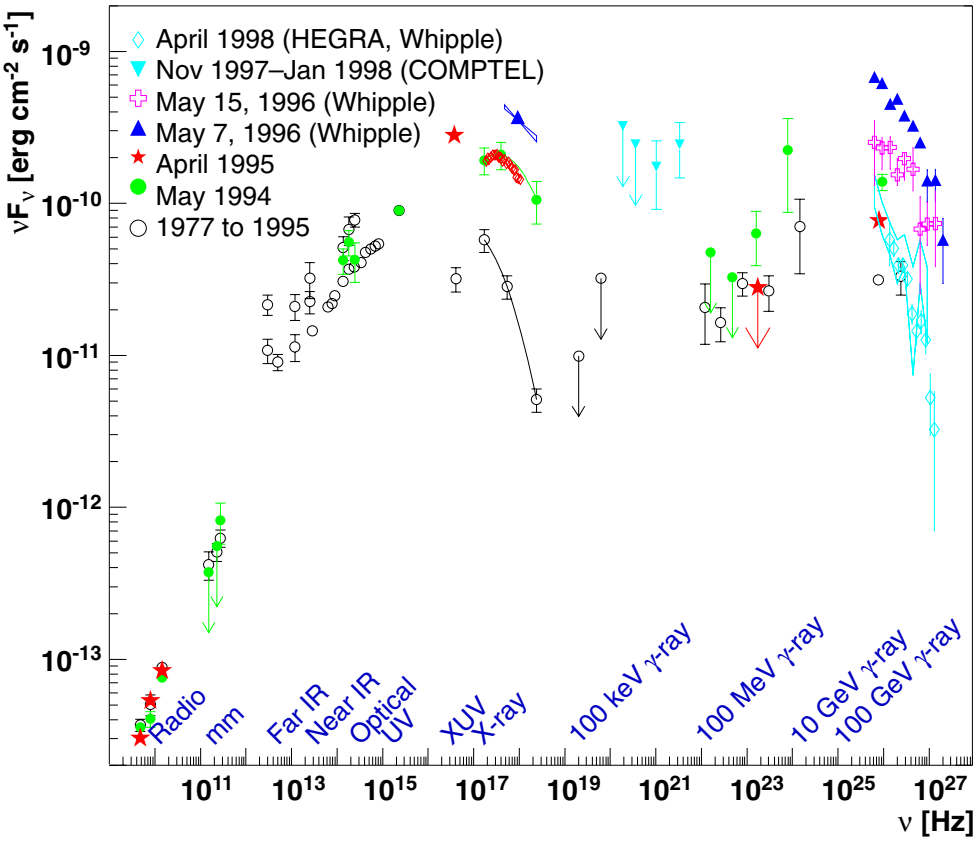

Figure 2.5: Spectral energy density distribution of the TeV blazar Mrk 421 showing the typical two-bump structure observed in many blazars. Data from observations in the time 1994–1998 show a strong coupling of both bumps in case of source flaring. (Adapted from Wagner (2006).)

according to the mean radio flux, Fossati et al. (1998) drew the following conclusions:

- The first peak occurs in different frequency ranges for different samples/luminosity classes, with the most luminous sources peaking at lower frequencies;
- the peak frequency of the γ-ray component correlates with the peak frequency of the lower energy one;
- the luminosity ratio between the high and low frequency components increases with bolometric luminosity.

This so-called *blazar sequence* found a wide popularity because just a single parameter, related to luminosity, seems to govern the physical properties and radiation mechanisms in the relativistic jets present in blazars. The blazar sequence is shown in Fig.2.6. According to its simplest form, one distinguishes low peaked and high peaked BL Lac objects (LBLs and HBLs). LBLs are more luminous

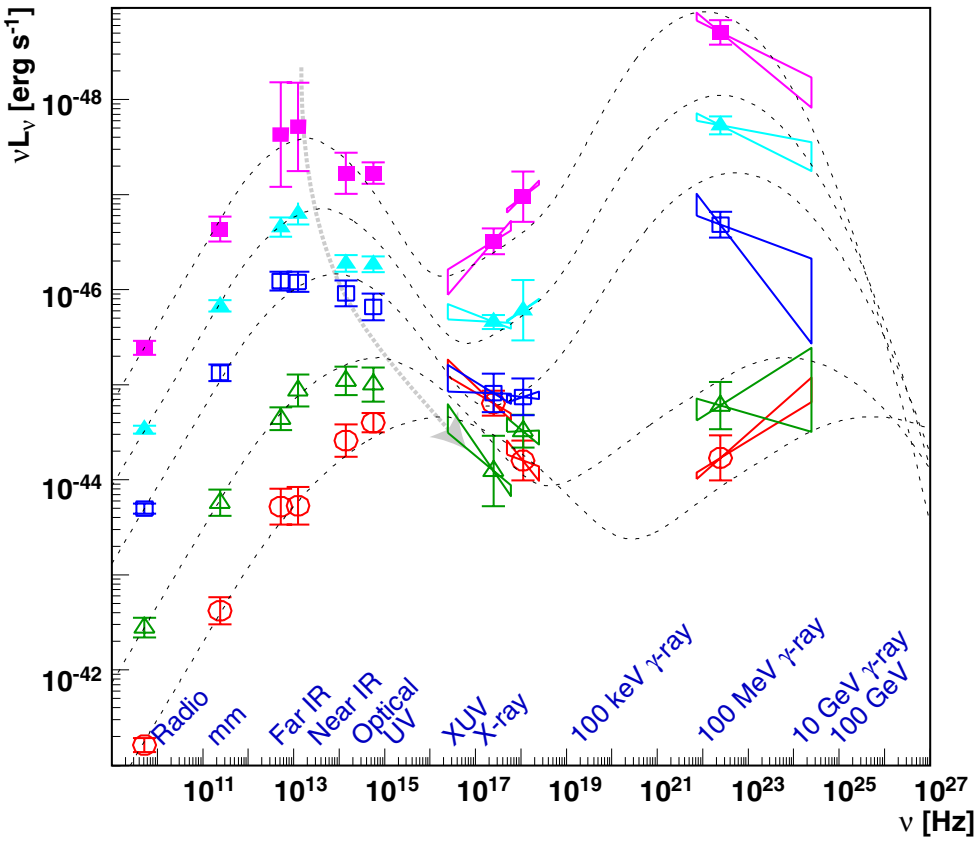

Figure 2.6: Average differential luminosity for a sample of 126 blazars, showing the LBL–HBL transition (Fossati et al., 1998). The thin lines represent a simple leptonic model proposed by Ghisellini et al. (1998).

and have their first peak in the infrared – optical band and the second one in the keV–MeV regime. The energy emitted in the second peak dominates the one released in the first one. In HBLs, the first peak arises at higher energies (in UV – X-rays) and dominates over the second peak at GeV-TeV energies. A simple one-zone leptonic model (Ghisellini et al. (1998), see below) describes the results satisfactory well by opposing that the differences between the sources can be accounted by requiring different maximum energy of accelerated electrons.

The model of Ghisellini et al. (1998) was used to predict sources with detectable VHE emission by Costamante et al. (2001). The authors proposed to look at sources (at moderate redshifts) of highest combination between the radio flux at 5 GHz and the X-ray flux at 1 keV. Indeed, in the 6 years after the publications, 10 new extragalactic TeV γ-ray emitters were discovered and (almost) all of them fulfill the proposed criteria. This supports the major predictions of the blazar sequence. However, the proposed sources were primary extragalactic targets for the Cherenkov telescopes in the last years, i.e. there is no proof that there are no VHE γ-ray emitters outside of the selected criteria.

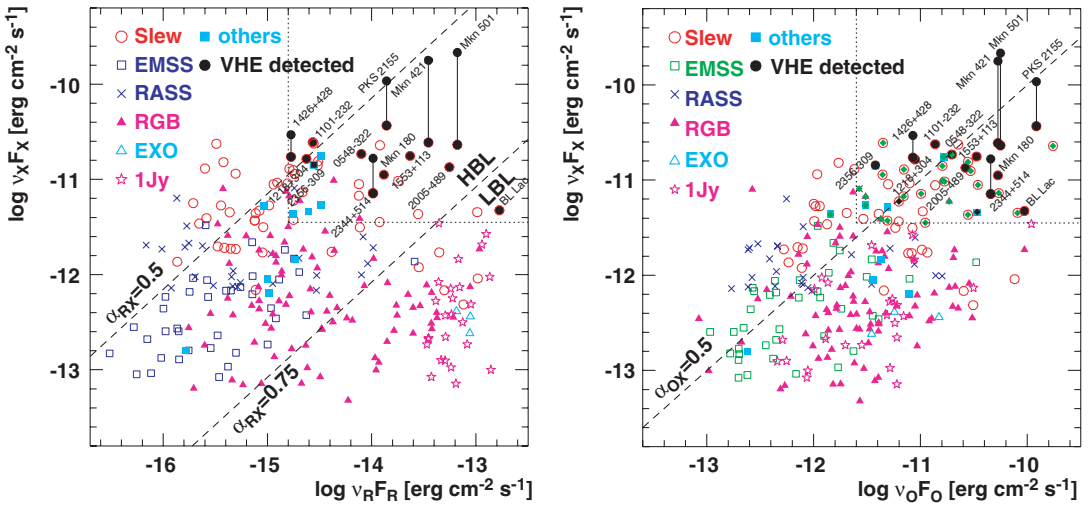

Figure 2.7: Blazars from the blazar catalog set up by Costamante et al. (2001). The authors proposed that the sources located in the upper right corner of the plots (marked by the dashed line) would be good candidates for VHE γ-ray emitters. Detected VHE sources are marked. When appropriate, different flux states are shown. *Left figure:* radio – X-ray plane. *Right figure:* Optical – X-ray plane.

The blazar sequence was examined lately with different tests taking an advantage of a higher statistics of detected blazars. Padovani (2007) concluded that the blazar sequence in its simplest form (Fig. 2.6) is an artifact of a selection effect. However, the connection between the two bumps in the SED for LBLs and HBLs is confirmed. It is not clear why the maximum synchrotron peak of FSRQ appears to be lower than in the BL Lacs. It even can still be a selection effect due to the fact that for really high-power–high-$\nu_{\rm peak}$ blazars it might be hard to get a redshift estimate. This question could be answered by the detection of high-power, moderately high-redshift TeV blazars.

2.3 Detected TeV blazars

The detected extragalactic VHE γ-ray emitters are shown in Fig 2.8 and in Table 2.1. Since 1992 as the first extragalactic source, Mkn 421, was discovered by the Whipple telescope (Punch et al., 1992), all but one detected sources are TeV blazars, i.e. the blazars emitting γ-rays at VHE. The exception is M 87, the largest known radio galaxy at a redshift of $z = 0.0044$, discovered to emit TeV γ-rays by HEGRA (Aharonian et al., 2003c) and confirmed by HESS (Aharonian et al., 2006e).

When M 87 is the closest extragalactic TeV source, the farthest TeV source is

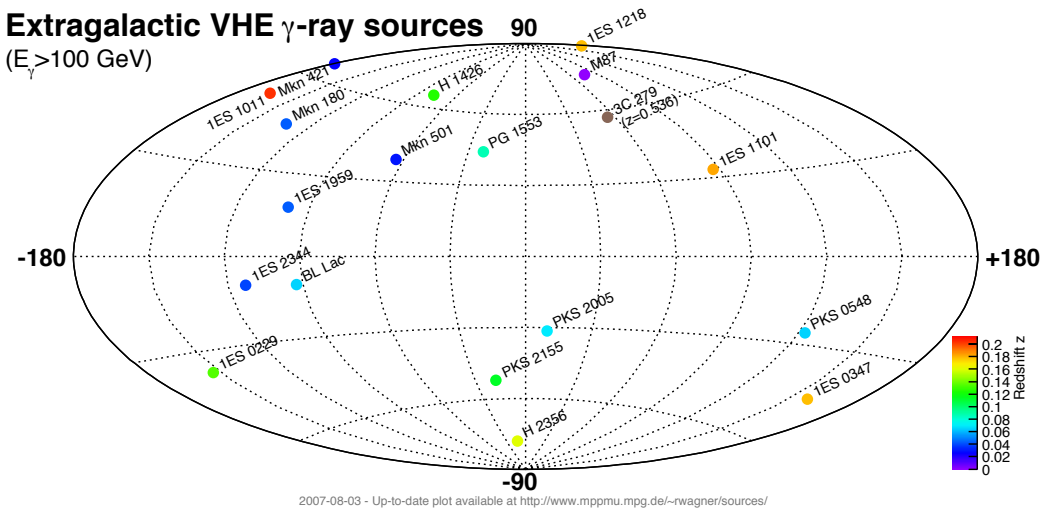

Figure 2.8: Sky map with 19 detected extragalactic TeV sources above 100 GeV using different IACT experiments. Colors correspond to the redshift of the sources.

1ES 1011+496 ($z = 0.212$), which was discovered during writing of this thesis[1]. As a consequence of a better sensitivity of the experiments, the number of extragalactic sources detected above 100 GeV tripled in the last three years (from 6 to 18 sources), after HESS and MAGIC came online.

2.3.1 Correlations and variabilities found for TeV blazars

The known VHE γ-ray–emitting AGNs are variable in flux in all wave bands (see e.g. Fig. 2.9). Most of the detected sources show a flux variability in the TeV band except of some newly detected sources. The lack of variability for the latter ones can be explained by a low significance of the detection, at which a possible variability is below the statistical fluctuations. As well the newly detected sources have to be monitored over years in order to detect possible variabilities at longer time scales (months to years). Spectral shape variability has been established for the strong TeV blazars Mrk 421, Mrk 501, H 1426+428 (Aharonian et al., 2003d), and 1ES 1959+650 (Aharonian et al., 2003b; Albert et al., 2006d). However, during a very strong outburst of PKS 2155-304 in July – August 2006 no spectral change was found (Aharonian et al., 2007b). Modeling of simultaneously taken X-ray and γ-ray data with well measured spectral changes in both bands has not yet been performed but such an analysis has the potential of breaking most of the model degeneracies.

Several extensive multiwavelength campaigns have already been carried out.

[1]In August 2007, a preliminary analysis of MAGIC data from 3c279 ($z = 0.536$), a source which was one of the brightest AGNs in the EGRET data above 100 MeV, revealed a significant signal above 80 GeV (Kranich et al., 2007).

Table 2.1: detected extragalactic TeV sources, ordered by their redshift. The last column indicates if a flux variability was found in the VHE γ-ray band.

source name	redshift z	type	discovery	confirmation	variab. in TeV band
M 87	0.0044	radio	HEGRA (Aharonian et al., 2003c)	HESS, VERITAS	yes
Mkn 421	0.030	HBL	Whipple (Punch et al., 1992)	many	yes
Mkn 501	0.034	HBL	Whipple (Quinn et al., 1996)	many	yes
1ES 2344+514	0.044	HBL	Whipple (Catanese et al., 1998)	MAGIC	yes
Mkn 180	0.045	HBL	MAGIC, this work (Albert et al., 2006b)		possible
1ES 1959+650	0.047	HBL	7 Tel. Array (Nishiyama et al., 1999)	many	yes
BL Lac	0.069	LBL	MAGIC (Albert et al., 2007b)		yes
PKS0548-322	0.069	HBL	HESS (Superina et al., 2007)		no
PKS 2005-489	0.071	HBL	HESS (Aharonian et al., 2005c)		no
PKS 2155-304	0.116	HBL	Durham Mark6 (Chadwick et al., 1999)	many	yes
H 1426+428	0.129	HBL	Whipple (Horan et al., 2002)	HEGRA	yes
1ES 0229+200	0.140	HBL	HESS (Raue et al., 2007)		no
H 2356-309	0.165	HBL	HESS (Aharonian et al., 2006b)		no
1ES 1218+304	0.182	HBL	MAGIC (Albert et al., 2006a)	VERITAS	no
1ES 1101-232	0.186	HBL	HESS (Aharonian et al., 2007d)		no
1ES 0347-121	0.188	HBL	HESS (Aharonian et al., 2007a)		no
1ES 1011-496	0.212	HBL	MAGIC, this work (Albert et al., 2007c)		possible
PG 1553+113	> 0.09	HBL	HESS/MAGIC (Aharonian et al., 2006d; Albert et al., 2007a)		possible

The correlation of X-ray and TeV γ-ray fluxes had first been seen in Mrk 421 data (Buckley et al., 1996; Takahashi et al., 1996). Since then, correlations with high statistical significances have been observed in data from Mrk 501 (Petry et al., 2000; Krawczynski et al., 2000; Sambruna et al., 2000; Albert et al., 2007g), Mrk 421 (Takahashi et al., 2000; Fossati et al., 2004; Albert et al., 2007e)[2], and PKS 2155-304 (Aharonian et al., 2007b). However, a campaign on the TeV blazar 1ES1959+650 has shown an orphan γ-ray flare without an X-ray or optical counterpart (Whipple: Holder et al. (2003), HEGRA: Krawczynski et al. (2003)). On the other hand, for Mkn 421 an orphan flare in X-rays was found without a TeV γ-ray counterpart (Rebillot and VERITAS Collaboration, 2003).

Optical–TeV correlations have yet to be studied, but the optical–GeV correlations seen in 3C 279 (Hartman et al., 2001) suggest that at least in some sources, such correlations exist. Likely candidates are LBLs and intermediate HBLs with the first bump in the optical. The optical radiation of blazars consists of usually two components: the synchrotron emission of the electrons and the thermal emission of the host galaxy. In order to look for the optical–TeV correlations, the latter component has to be measured and subtracted from the total flux, which is sometimes difficult. Recent discoveries of TeV γ-ray emission from the HBLs Mkn 180 (see Chapter 7, Albert et al. (2006b)) and 1ES 1011+496 (see Chapter 8, Albert et al. (2007c)) during an optical outburst make it very tempting to speculate about the connection between optical activity and increased VHE emission. This connection is also supported by the observations of the LBL object BL Lac

[2]also as a part of this Thesis, Chapter 6

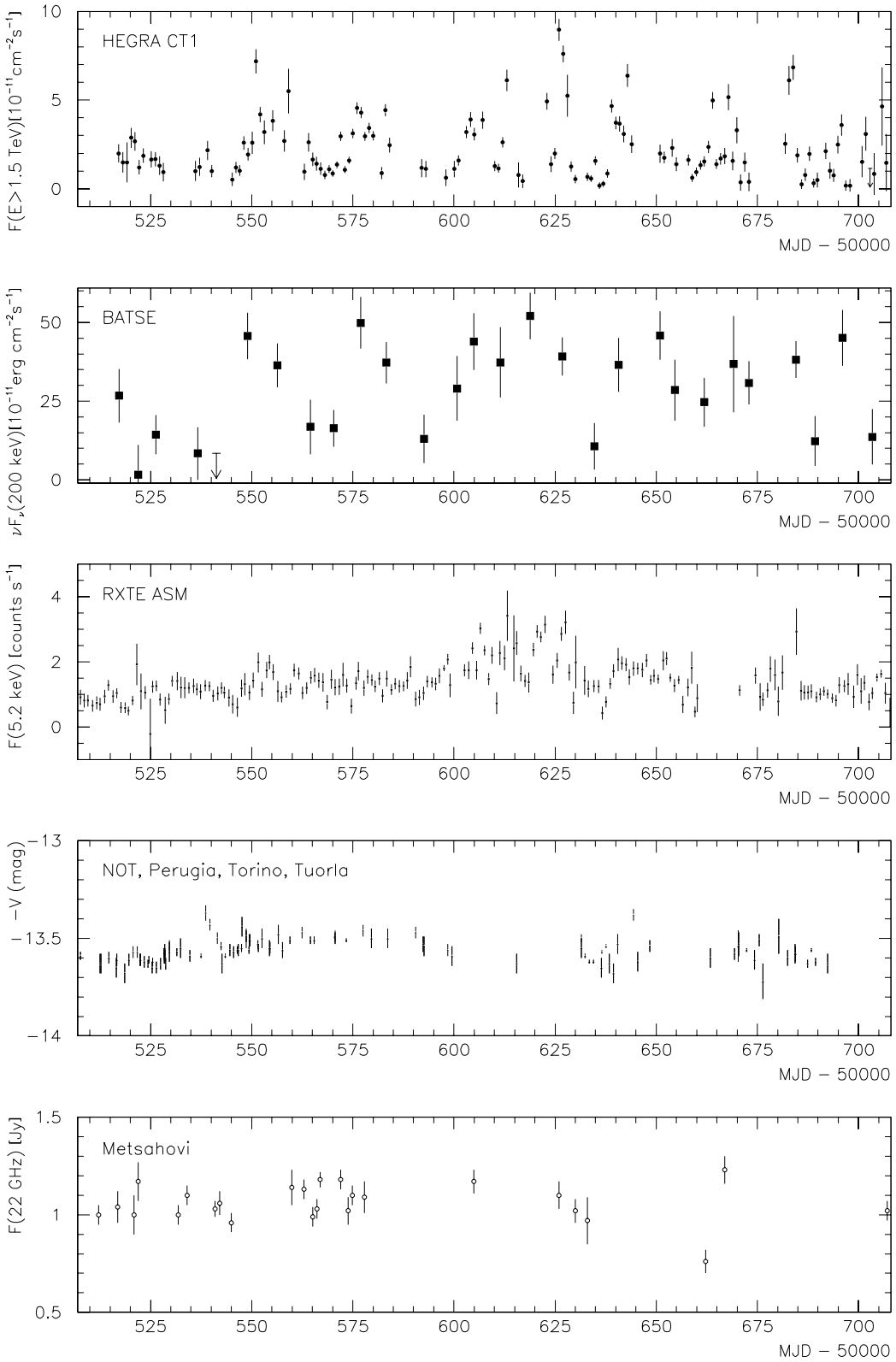

Figure 2.9: Light curve from the blazar Mkn 501 showing clear variability at all energy bands (Petry et al., 2000).

(Albert et al., 2007b), where the observations during the lower optical state failed to detect any VHE γ-rays.

The rapid variability of blazars measured at TeV energies put new constraints on the emission models. Soon after its discovery Mkn 421 was found to have flux doubling times as fast as 15 minutes (Gaidos et al., 1996). Recently, Mkn 501 and PKS 2155-304 showed a variability on time scales below 3 minutes (Albert et al., 2007g; Aharonian et al., 2007b). Large amplitude flux variability at these time scales implies that the TeV emission originates from a small region very near the SMBH. The generally more pronounced variability at high energies, in particular in X-rays and above, also points to an origin close to the central engine. Therefore, the VHE γ-rays observations offer an unique opportunity to study the close vicinity of the central black holes.

2.4 VHE γ-ray production mechanisms

I will briefly summarize popular models to explain VHE γ-ray emission from blazars. The models usually aim not only at reproducing the observational data but also at constraining the jet parameters, like the strength of the magnetic field, the geometry of the emission region and the Lorentz boost factor of the jet. Since the accelerated particles, responsible for the VHE γ-ray emission, can be either electrons (positrons) or hadrons (mostly protons), the models are divided into *leptonic* and *hadronic* ones. After this, I will discuss the currently preferred models for particle acceleration. The model review is based on the recent article by Krawczynski (2004).

2.4.1 Leptonic models

In Synchrotron Compton (SC) models of TeV blazars the radio to X-ray emission is produced as synchrotron radiation from a population of non-thermal electrons (and possibly positrons) in the presence of a magnetic field. In so-called Synchrotron Self-Compton (SSC) models (Coppi, 1992; Ghisellini et al., 1998), the same electron population emits γ-rays through Inverse Compton processes by electrons scattering synchrotron photons.[3] In so-called External Compton (EC) models (see Sikora and Madejski (2001) and references therein), the electrons upscatter "external" photons that originate outside the jet. A third mechanism has been proposed, which increases the efficiency of the IC scattering. In these synchrotron mirror models synchrotron photons are back-scattered by the ambient matter and interact with the parent electron population head-on. In case of BL Lac objects, the lack of strong emission lines is commonly taken as evidence

[3] In the simplest SSC models there are 6 free parameters: the size of the emitting blob, the Doppler factor of the blob, the magnetic field strength in the blob, the spectral index of the injected electron spectrum, and the lowest and the highest energy of the injected electrons.

that ambient photon fields are not so important, and that SSC models rather than EC or mirror models are more likely to explain the data.

TeV blazar data have been modeled intensively with a variety of codes. The more simpler ones assume 1-zone homogeneous emission volumes and use phenomenological electron energy spectra to fit the broadband data (e.g. Inoue and Takahara (1996); Bednarek and Protheroe (1999); Takahashi et al. (2000); Tavecchio et al. (2001)). Modeling with time-dependent self-consistently evolved codes (e.g. Coppi (1992); Mastichiadis and Kirk (1997); Krawczynski et al. (2002); Böttcher and Chiang (2002)) assures that the energy spectra are physically realizable from initial acceleration energy spectra. Time dependent modeling has to be used whenever the flare duration is short. By short it means that the flare is comparable to or shorter than micro-processes that modify the electron energy spectra (e.g. acceleration energy gains, radiative energy gains and losses).

Several conclusions can be drawn from the SSC and EC modeling performed by various authors:

- relatively simple 1-zone and 2-zone SSC models are able to explain most multiwavelength data;
- in some models, the preferred jet Doppler factors are rather high: between 50 and 100 (Mastichiadis and Kirk, 1997; Krawczynski et al., 2001); in other models, the assumed Doppler factor is between 10 and 20, which is confirmed for some objects through VLBI observations of the superluminal jet motion;
- in the jet frame the energy density of non-thermal particles is much higher than the energy density of the magnetic field;
- only a small fraction ($< 10^{-2}$) of the energy transported by the jet is converted into radiation (e.g. Kino et al. (2002); Krawczynski et al. (2002)).

Noteworthy, leptonic models have two important features: (i) electrons can be readily accelerated to TeV energies, e.g. through the well-understood shock acceleration mechanism, and (ii) they can radiate X-rays and TeV γ-rays with very high efficiency via synchrotron and inverse Compton scattering. Hadronic models are generally lacking these virtues.

2.4.2 Hadronic models

In hadronic models the continuum γ-ray emission is explained by shock acceleration of protons and their interaction with other hadrons. The latter reaction leads to production of π^0s, which eventually decay into γ-rays. The models usually require high magnetic fields (B $>>$ 10G), have a smaller acceleration efficiency and have much longer acceleration and cooling times than the leptonic models (due to the higher mass of protons compared to electrons). All these features make

the hadronic models less attractive. Once the hadrons are accelerated, one of the following mechanisms leads to the VHE γ-ray emission:

- hadronic interactions of a highly relativistic baryonic outflow which sweeps up ambient matter (Pohl and Schlickeiser, 2000);
- interactions of high-energy protons with gas clouds moving across the jet (Dar and Laor, 1997);
- interactions of Ultra High Energy (UHE) protons with ambient photons (Mannheim, 1993, 1998), or with the jet magnetic field (Aharonian, 2000), or with both (Mücke et al., 2003).

The latter models predict UHE proton initiated cascades. The cascade is initiated by injecting UHE γ-rays from π^0 decays, followed by a sequential photon-photon pair production, synchrotron radiation, photon-photon pair production, etc. down to γ-rays with TeV energies.

The observational data challenge the hadronic models harder than they challenge the leptonic models: hadronic models have difficulties to explain the good X-ray/TeV γ-ray flux correlations found for Mrk 421 and Mrk 501 during flares. Due to relatively long cooling time of protons, hadronic models have also difficulties to reproduce the very fast variability found in TeV blazars. Furthermore, little work has yet been done to see if proton models can explain more than single snapshots of data. On the other hand, some hadronic models involve Ultra High Energy Cosmic Ray acceleration, which opens an attractive possibility of explaining cosmic rays up to 10^{20} eV.

In summary, hadronic models are far from being ruled out. Hadronic processes can be also an admixture to the leptonic processes, being for instance responsible for the quiescent state emission at VHE band. A detection of a neutrino emission from the decay of charged pions would unambiguously prove hadronic models. However, the sensitivity of the neutrino detectors is not yet good enough and no extragalactic neutrinos from any source have been detected yet.

2.4.3 Particle Acceleration

Independent of the production mechanism, the only way to emit TeV γ-rays is to accelerate charged particles (electrons or protons or both) to very high energies. Among the many particle acceleration mechanisms that are discussed, Fermi acceleration at strong Magnetohydrodynamic (MHD) shocks has received most attention. Indeed, the data are largely consistent with an electron acceleration energy spectrum $dN/dE \propto E^{-p}$ with p between 2 and 2.23, expected for non-relativistic and ultra-relativistic shocks, respectively (see Kirk and Duffy (1999) and references therein). Based on a time-dependent SC code Kirk and Mastichiadis (1999) have shown that energy gains through Fermi acceleration

and radiative energy losses can result in characteristic hardness–intensity correlations during individual flares. X-ray and recently also TeV γ-ray data do show the predicted signatures: during flares the sources seem to go through clockwise and anti-clockwise loops in the X-ray or γ-ray hardness–intensity planes (e.g. Takahashi et al. (1996)). However, the same sources show a wide range of different signatures (e.g. Takahashi et al. (2000)), indicating that the relative length of the characteristic time scales of particle acceleration and radiative cooling change from flare to flare. The lack of a prevailing signature has cast doubts on whether "cooling loops" and "particle acceleration loops" have really been observed.

Most SC models of TeV blazars invoke a minimum Lorentz factor $\gamma_{\rm min}$ of accelerated particles on the order of 10^5 to account for the data (e.g. Krawczynski et al. (2002) and references therein). Such high $\gamma_{\rm min}$-values could either result from a yet unknown pre-acceleration mechanism, or, from an upstream bulk Lorentz factor on the order of 10^5. A low-entropy, extremely relativistic upstream plasma could be detectable by its Inverse Compton emission if exposed to a suitable external radiation field (Krawczynski, 2004).

2.4.4 Hardness of the VHE γ-ray spectrum

One of the hotly discussed issues in the field is the maximum hardness of the VHE γ-ray spectrum. The hardness of intrinsic spectra became one of the major criteria to constrain the EBL (see Chapters 3, 9 and 10). The argumentation goes as follows: if the deabsorbed (i.e. corrected for the effect of the EBL absorption) VHE γ-ray spectrum is harder than theoretically possible, then the assumed EBL level is too high and the corresponding EBL model can be rejected. So, how "hard" can an intrinsic VHE γ-ray spectrum be?

If the γ-rays are emitted close to the acceleration region and Fermi acceleration is at work, the following scenario should be valid:
The electrons are Fermi-accelerated with a resulting power law spectrum of $dN/dE \sim E^{-\alpha}$, with a slope α of about 2. Due to a faster cooling of high energy electrons compared to lower energies, the slope α can be larger than 2 but there is no simple theoretical possibility to produce an electron spectrum with a harder spectrum. Given an electron spectrum, one can calculate the slope of the synchrotron energy spectrum: it is $dN/dE \sim E^{-\Gamma}$ with a photon index $\Gamma = \frac{\alpha+1}{2} = 1.5$. The energy spectrum of Inverse-Compton photons, independent of the origin of the target photons, has approximately the same photon index as the synchrotron energy spectrum if the scattering occurs in the Thomson regime. In case of the Klein-Nishima regime, the index is even larger. Thus, the photon index of the energy spectrum of VHE photons originating from an IC scattering has to be $\Gamma = 1.5$ or larger. In case of hadronic origin, the spectrum is more complicated. Yet, the resulting VHE photons, which originate from pion decays, are generally leading to a photon spectrum of $\Gamma \geq 2$, which is softer than a hardest possible photon spectrum with a leptonic origin. In conclusion, one can assume

that the photon index Γ of the intrinsic TeV blazar spectrum must be at least 1.5 or larger. These arguments were recently used in Aharonian et al. (2003d, 2006a,d); Albert et al. (2007a).

However, the possibility to obtain even harder photon spectra is not fully excluded. For instance, though in contrast to a wide acceptance of above given general arguments, Katarzyński et al. (2006) argued that synchrotron emission as well as IC scattering of relativistic electrons does not necessarily occur close to the region of electron acceleration. If so, due to propagation effects, the electron spectrum can become truncated, i.e. the minimum energy of electrons can be as high as several GeV. In an extreme case, we would deal with a nearly monoenergetic spectrum of VHE relativistic electrons. Then, and this is the most extreme case, a resulting IC photon index can be as small as $\Gamma = 2/3$.

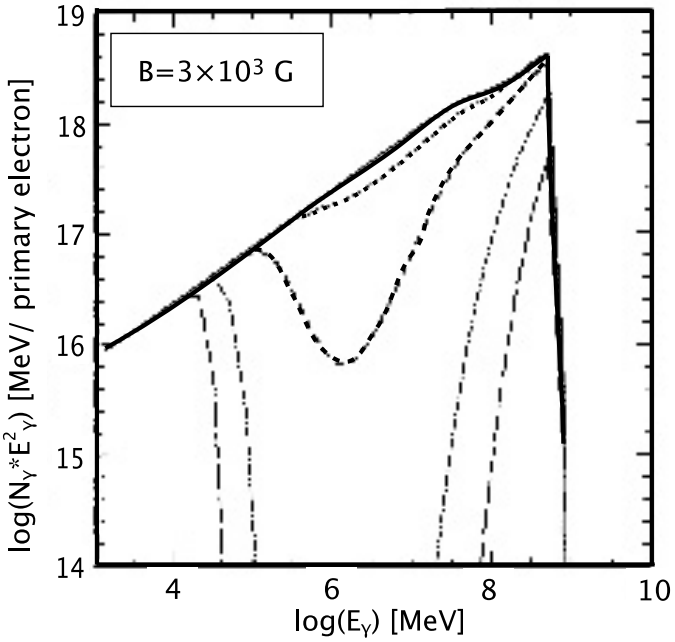

Figure 2.10: Possible modifications of the intrinsic photon spectrum due to the γ-γ-absorption with low energy photons of the accretion disc. The unabsorbed photon spectrum is shown by the solid line, whereas the dashed lines represent the photon spectrum after the absorption depending on the temperature of the disc (adapted from Bednarek (1997)).

Another possibility to measure a very hard γ-ray spectrum was mentioned by Bednarek (1997): if the VHE γ-ray emission takes place in the vicinity of the central engine (which is realistic), the emitted photons may suffer an internal absorption by the thermal photons of the accretion disc. Depending on the temperature of the accretion disc, only distinct energies of the GeV-TeV photons will be absorbed, leaving a kind of a broad absorption line in the VHE γ-ray spectrum

(see Fig. 2.10). If the energy threshold of the measurement would coincide with this absorption feature, the intrinsic spectrum would appear to be much harder than argued above. However, this coincidence is unlikely, especially the implied fact that the internal absorption feature compensates the intergalactic absorption by the EBL such that the measured spectra can be well approximated by a simple power law.

2.5 Short Summary

In this Chapter I briefly described TeV blazars as a subclass of AGNs and possible production mechanisms of VHE γ-rays in these sources. The sources detected so far and their phenomenology suggest that many more extragalactic VHE sources exist and will be detected with an increasing sensitivity of the instruments and longer observation times. The physics behind the VHE γ-ray emission can only be understood by detailed measurements of many sources, simultaneous observations of the sources at all energy bands, especially during strong flares. Strategies to determine best VHE γ-ray candidates and strategies to obtain a maximum scientific output from MAGIC observation of known sources are presented in Appendix 1.

In addition to the origin of VHE γ-rays and to the study of the jet physics, observations of distant extragalactic sources can probe the cosmology of the Universe. For instance, the transparency of the Universe to VHE γ-rays can help to distinguish between different evolution scenarios of the star and galaxy formations. The history of this formation is composed into the extragalactic background light (EBL), which is the topic of the next Chapter.

Chapter 3

The Extragalactic Background Light

Figure 3.1: Deep Universe as seen by the *Spitzer* telescope in infrared. Image credit: NASA/JPL-Caltech/C. Lonsdale (Caltech/IPAC) and the SWIRE Team.

During the star and galaxy formation history a diffuse extragalactic radiation field has been accumulated in the ultraviolet to far infrared wavelength regime. This radiation field, commonly referred to as the extragalactic background light (EBL), is the second largest, in terms of the contained energy, background after the Cosmic Microwave Background of 2.7 K (CMB). While the CMB conserves the structure of the Universe at the moment of the decoupling of matter and radiation following the Big Bang (at redshift $z \approx 1000$), the EBL is a measure of the entire radiant energy released by processes of structure formation that have occurred since the decoupling. The EBL is difficult to measure directly due to strong foregrounds from our solar system and the Galaxy. The observation of distant sources of VHE γ-rays using Imaging Air Cherenkov Telescopes (IACTs, such as MAGIC) provides a unique indirect measurement of the EBL. The precision of

the EBL constraints set by the IACT improved remarkably in the last 3 years. Contemporaneously with the IACT constraints, there has been rapid progress in resolving a significant fraction of this background with the deep galaxy counts at infrared wavelengths from the Infrared Space Observatory (*ISO*) and from the *Spitzer* satellite as well as at sub-millimeter wavelengths from the Submillimeter Common User Bolometer Array (SCUBA) instrument.

In this Chapter, I will emphasize briefly the cosmological importance of the extragalactic background light, review the status of the direct measurements and indirect constraints, and discuss our current understanding of this background. An attempt to constrain the EBL density is part of this thesis and will be presented in Chapter 9.

3.1 Cosmological importance

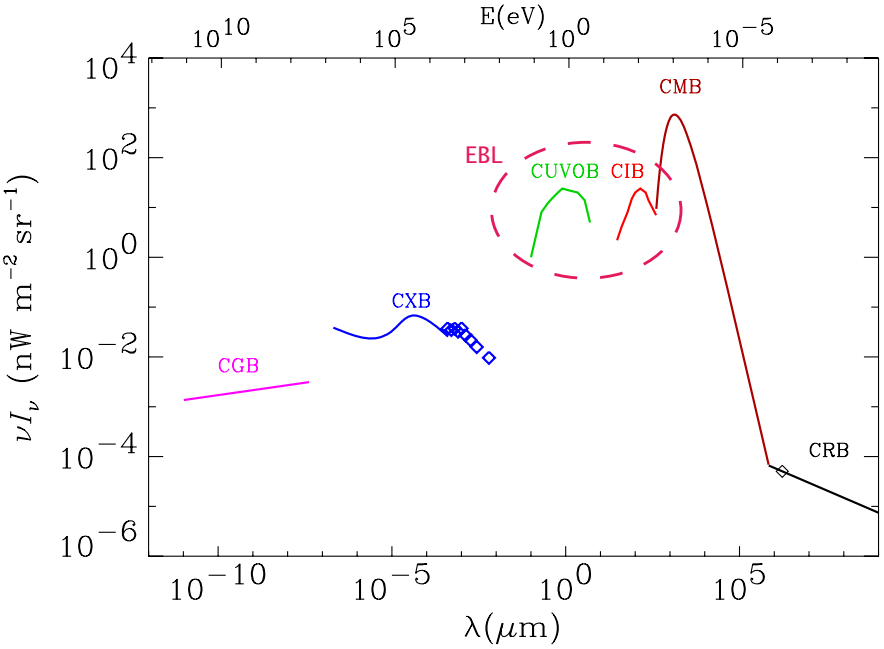

Figure 3.2: Spectrum of the cosmic background radiations. The cosmic radio background (CRB) is represented by a $\nu I_\nu \propto \nu^{0.3}$ spectrum, normalized to the Bridle (1967) value at 170 cm. The cosmic microwave background (CMB) is a blackbody spectrum at 2.725 K. The UV-optical (CUVOB) and infrared (CIB) backgrounds form the EBL. The data for the X-ray background (CXB) are taken from Wu et al (1991), and the curves are analytical representations summarized by Fabian and Barcons (1992). The γ-ray background (CGB) is represented by the power law given by Sreekumar et al. (1998). Figure adapted from Hauser and Dwek (2001).

One of the outstanding challenges in modern cosmology is to explain the formation of structure in the Universe. The formation of stars and galaxies from

matter and the following evolution of such systems is accompanied by the release of radiant energy powered by gravitational and nuclear processes (interactions, decays and thermal fusion). Most of radiant energy is emitted by stars in the ultraviolet (UV) and the optical wavelength range. However, cosmic expansion and the absorption of short wavelength radiation by dust and re-emission at long wavelengths will shift a significant part of this radiation energy into the infrared range. The cosmic infrared radiation background is therefore a unique tracer of structure formation processes, and its measurement provides new and important insight into those processes. Until 10 years ago, there had been no definite measurements of the infrared background radiation.

To stress the importance of the EBL, I show in Figure 3.2 the spectrum of the extragalactic background radiation over ∼20 decades of energy, i.e. from radio waves (10^{-7} eV) to high energy γ-ray photons of a few hundred GeV. The cosmic microwave background (CMB), the fossil blackbody radiation from the Big Bang, contains the highest amount of electromagnetic energy among different backgrounds. Figure 3.2 gives only a schematic representation of the spectrum at wavelengths from the UV to the far infrared, roughly based on the energy released by nuclear fusion in stars. This background light from UV to far infrared wavelengths, commonly called *Extragalactic Background Light* (EBL). The EBL is likely the second largest, in terms of the contained energy, background after the CMB.

A closer look to the UV – infrared backgrounds is given in Figure 3.3. From right to left, the spectral energy distributions of the three major components are shown: the cosmic microwave background (CMB), the cosmic infrared background (CIB), and the cosmic optical background (COB). The numbers inside the boxes in Figure 3.3 refer to the approximate integrated brightness in nW m^{-2} sr^{-1} of these backgrounds. Whereas the CIB and the COB share the energy density almost equally, the CMB dominates both of them by a factor of ∼20. The COB, peaking at around 1 μm is believed to originate directly from stars. The CIB, having its peak at ∼100 μm, results mostly from starlight that has been absorbed by dust inside galaxies and reemitted at higher wavelengths. Other contributions, like emission from AGN and quasars are expected to produce no more than 5 to 20% of the total EBL density in the mid IR (see e.g. Matute et al. (2006) and references therein). Throughout this thesis, I will refer to COB and CIB together as *EBL*.

The diffuse EBL, as it is seen today, consists of the integrated electromagnetic radiation from all epochs, which is redshifted, corresponding to the formation epoch, at which the radiation was produced. The evolution of the EBL in time is extremely important to develop and to test star formation and galaxy evolution models. In turn, the valid cosmological models must explain the current EBL.

The EBL is also the opacity source for GeV - TeV photons (see Section 1.5). In order to reconstruct intrinsic spectra of GeV–TeV sources, the knowledge of the EBL is indispensable.

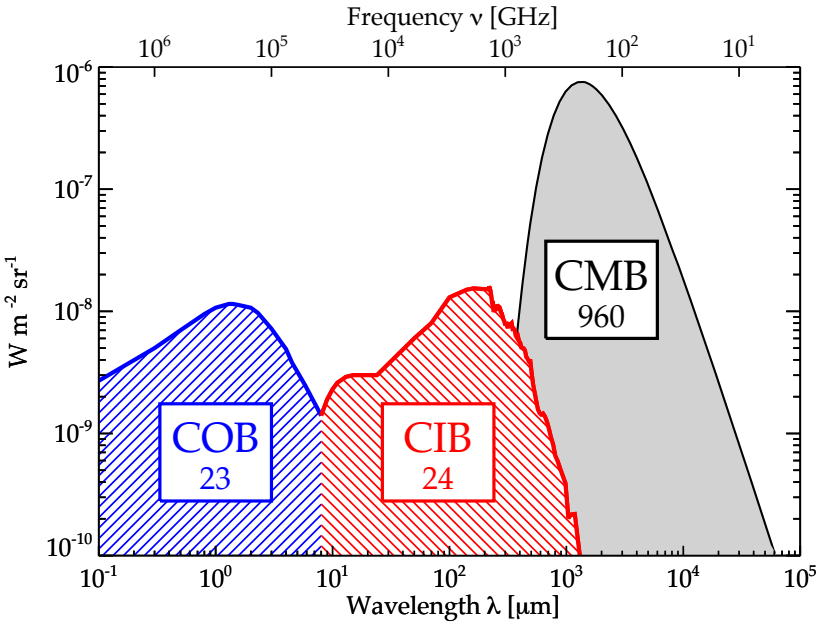

Figure 3.3: Schematic Spectral Energy Distributions of the most important (by intensity) backgrounds in the universe, and their approximate brightness in nW m^{-2} sr^{-1} (written in the boxes). From right to left: the cosmic microwave background (CMB), the cosmic infrared background (CIB) and the cosmic optical background (COB). The last two components together are called EBL. Plot adopted from Dole et al. (2006).

3.2 Status of the EBL measurements

In the last 10 years, several measurements and limits of the EBL could be obtained. Solid lower limits for the EBL level are derived from source counts (e.g. Madau and Pozzetti, 2000; Fazio et al., 2004; Frayer et al., 2006) and their extrapolation via stacking (Dole et al., 2006). Direct measurements of the EBL have proven to be a difficult task due to dominant foreground radiation mainly from inter-planetary dust (zodiacal light) (e.g. Hauser et al., 1998), and it is not expected that the sensitivity of measurements will greatly improve over the next years. Several upper limits were reported from direct observations (e.g. Hauser et al., 1998) and from fluctuation analyses (e.g. Kashlinsky and Odenwald, 2000). In total, the collective limits on the EBL between the UV and far-IR confirm the expected two peak structure, although the absolute level of the EBL density remains uncertain by a factor of 2 to 10 (see Fig. 3.4). In addition to these upper limits, several direct measurements have also been reported, which do not contradict the limits but lie significantly above the lower limits (see Hauser and Dwek (2001) and Kashlinsky (2005) for recent reviews). In particular, a significant excess of the EBL in the near IR (1 to 4 μm), exceeding the expectations from source counts, was reported by the IRTS satellite (Matsumoto et al., 2005), which lead to a controversial discussion about its origin. If this claimed excess of the

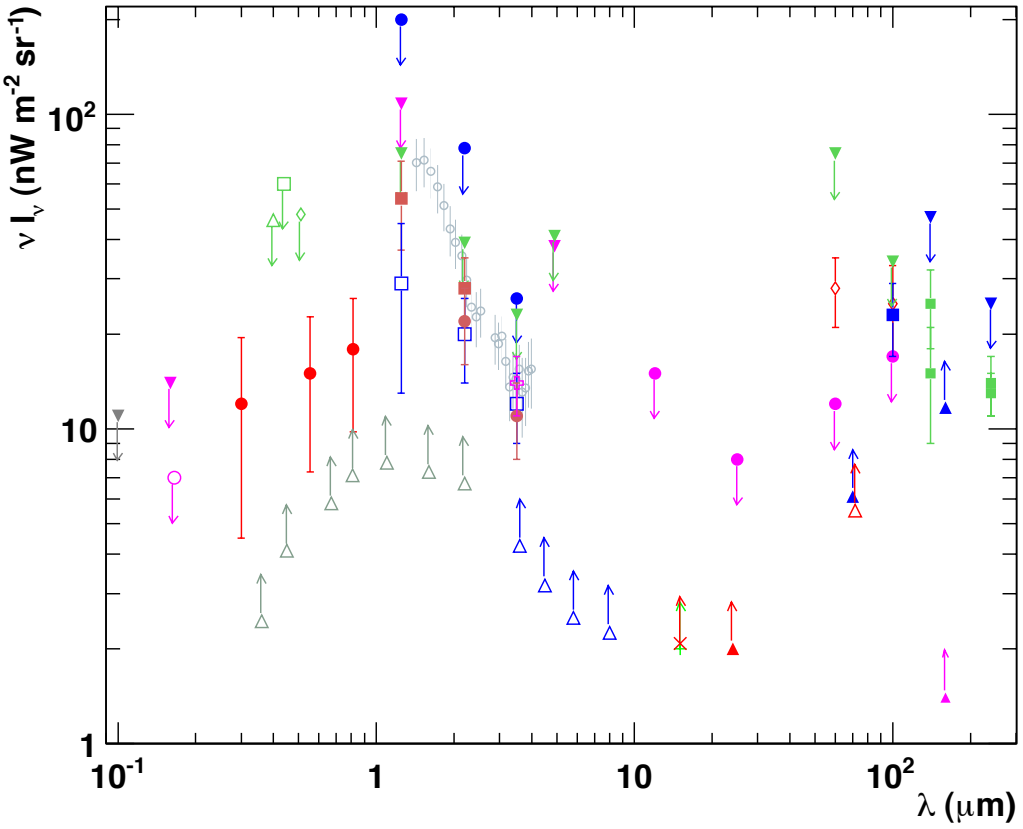

Figure 3.4: EBL measurements and limits (status end 2006). Upper limits in the UV to optical: Edelstein et al. (2000) (grey filled triangle), Martin et al. (1991) (open pink circle), Brown et al. (2000) (filled pink triangle), Mattila (1990) (open green triangle), Toller (1983) / Leinert et al. (1998) (open green square), Dube et al. (1979) / Leinert et al. (1998) (open green diamond); Tentative detection in the UV/optical: Bernstein et al. (2002, 2005) (filled red circle); Lower limits from galaxy counts: Madau and Pozzetti (2000) (open grey triangles), Fazio et al. (2004) (open blue triangles), Elbaz et al. (2002) (green cross), Metcalfe et al. (2003) (red x), Papovich et al. (2004) (filled red triangle), Dole et al. (2006) (filled pink triangles), Frayer et al. (2006) (open red triangle); Detections in the near IR: Dwek and Arendt (1998) (open pink cross), Gorjian et al. (2000) (filled brown circle), Wright and Reese (2000) (open blue squares), Cambrésy et al. (2001) (filled brown squares), Matsumoto et al. (2005) (small open grey circles); Upper limits from direct measurements: Hauser et al. (1998) (filled green triangles), Dwek and Arendt (1998) (filled pink triangles), Lagache and Puget (2000) (filled blue triangles); Upper limits from fluctuation analysis: Kashlinsky et al. (1996) (filled blue circles), Kashlinsky and Odenwald (2000) (filled pink circles); Lower limits from stacking analysis in the far-IR: Dole et al. (2006) (blue triangles); Detections in the far-IR: Hauser et al. (1998) (filled green squares), Lagache and Puget (2000) (filled blue square), Finkbeiner et al. (2000) (open red diamonds).

EBL is real, it might be attributed to emissions by the first stars in the history of the universe. These so-called Population III stars are believed to be heavy stars with a very low metallicity. I will give more on the Population III stars in Section 3.5.

The study of the evolving EBL is only indirectly possible. One possibility is through observing galaxy populations in redshift intervals. The observed distant galaxies might, however, be not representative for all types of galaxy populations. The reason is that the observed sky region might not be representative for the whole Universe. Another reason can be that the spectral templates used to extrapolate from the observed wavelength to another one are wrong due to differences in galaxy composition, which are not taken into account. A different possibility to measure the evolving EBL is the study of TeV γ-spectra of distant sources. The EBL causes a distinct absorption of the spectra (see Section 1.5), resulting in a unique imprint on the spectra observed from Earth. Through observing absorption features in the TeV spectra of blazars located at different redshifts, one attains access to the EBL density distribution. However, the intrinsic spectra are not known *precisely*, thus making any conclusion about the EBL density model dependent. It is important to stress that for a single observed energy spectrum of a VHE gamma-ray source it is rather difficult, if not impossible, to distinguish between the imprint of the EBL and intrinsic features of the source. Observed features (especially cut-offs at high energy) can be source-inherited due to intrinsic absorption or a source, which does not provide necessary conditions for acceleration of charged particles to high enough energy. It is, therefore, only possible to set limits on the EBL, arguing that the observed spectra contain at least the imprint of the EBL.

3.3 Status of the TeV constraints

A different approach to derive constraints on the EBL (labeled "clever" by Dwek and Slavin (1994)) became available with the detection of VHE γ-rays from distant sources. As mentioned above, these VHE γ-rays are attenuated via pair production with low energy photons from the EBL (Gould and Schréder, 1967). It was soon realized that the measured spectra can be used to test the transparency of the universe to VHE γ-rays and thus to derive constraints on the EBL density (Fazio and Stecker, 1970). With reasonable assumptions about the intrinsic spectrum emitted at the source, limits on the EBL density can be inferred. The method is, however, not straightforward. It is in principle not possible to distinguish between source inherent effects (such as absorption in the source, intrinsic cut-offs in the particle acceleration processes, magnetic field strength, etc.) and an imprint of the EBL on a measured VHE spectrum. The emission processes in the detected extragalactic VHE γ-ray emitters are far from being fully understood, which makes it more difficult to use robust assumptions on the shape

of the intrinsic spectrum. Different EBL shapes can lead to the same attenuation imprint in the measured spectra, thus a reconstructed attenuation imprint cannot uniquely be identified with one specific EBL shape. A further uncertainty arises due to the unknown evolution of the EBL with time, which becomes more important for distant sources. In a pioneering work conducted by Stecker et al. (1996), the first limits on the EBL were derived with this method.

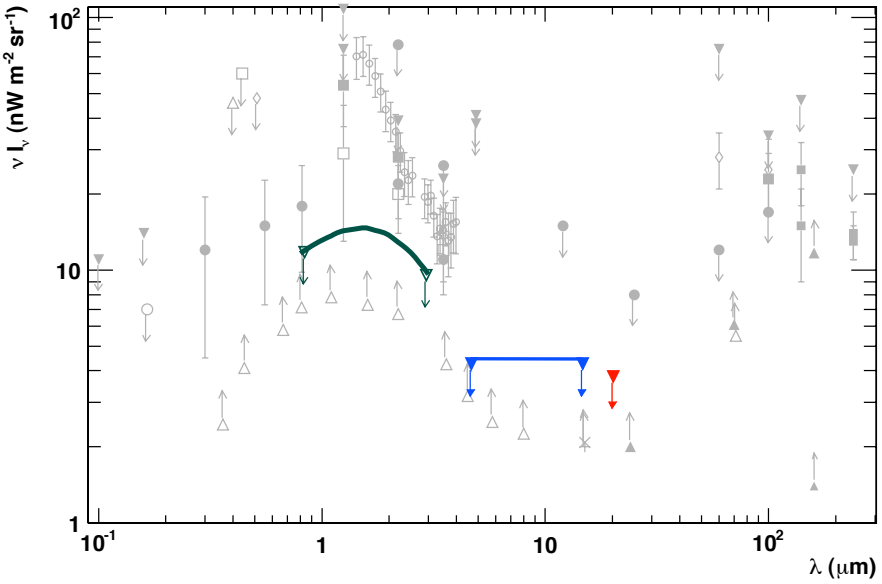

Figure 3.5: Previous constraints from TeV spectra. The EBL measurements and limits are printed in grey, see Fig. 3.4 for symbols. TeV upper limits are marked in color. *Red arrow*: limit at 20 μ by Stecker and de Jager (1997) on Mrk 421. *Blue bar and arrows*: Renault et al. (2001) limits from 5 to 15 μm using the CAT and HEGRA measurements of VHE γ-rays from Mrk 501. *Green bar and arrows*: Aharonian et al. (2006a) limit derived using H.E.S.S. data on 1ES 1101-232 and H 2356-309.

Nevertheless, measured VHE γ-ray spectra can provide robust upper limits on the density and spectral distribution of the EBL, if conservative assumptions about the emission mechanisms of γ-rays are considered. A review of the various efforts to detect the EBL or to derive upper limits via the observation of extragalactic VHE γ-ray sources up to the year 2001 can be found in Hauser and Dwek (2001). Assuming that Mrk 421 (redshift $z = 0.030$, the only known extragalactic TeV γ-ray source at that time) has intrinsically a pure power law spectrum in TeV energies, Stecker et al. (1996); Stecker and de Jager (1997) derived first EBL upper limits at 20 μm (red arrow in Fig. 3.5). The measured spectrum of the TeV blazar H 1426+428 at a redshift of $z = 0.129$ (Aharonian et al., 2002d) led to a first tentative detection of an imprint of the EBL in a VHE spectrum (Aharonian et al., 2002d, 2003d). Using the H 1426+428 spectrum together with the spectra of previously detected TeV blazars, limits on the EBL were derived (Costamante et al., 2003; Kneiske et al., 2004). Later, Dwek and Krennrich (2005) utilized a

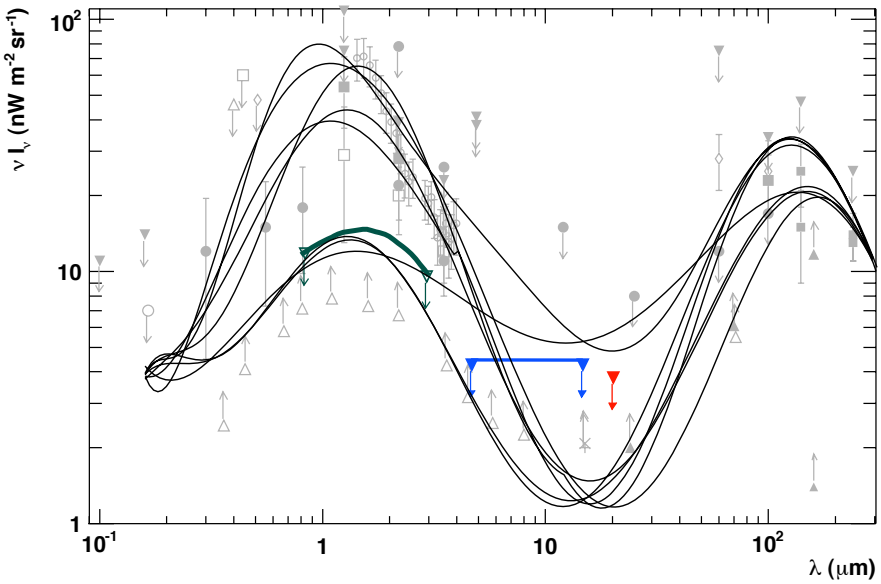

Figure 3.6: Previous constraints from TeV spectra. The same as Fig. 3.5 but with eight allowed EBL shapes from Dwek and Krennrich (2005).

large sample of TeV blazars spectra and solid statistical methods to test a set of twelve EBL shapes on their physical feasibility. EBL shapes were considered forbidden, when, under the most conservative assumptions, the intrinsic spectra showed a significant exponential rise at high energies.[1] The result was that eight of these shapes, shown in Fig. 3.6, were allowed, whereas 4 others could be rejected. Recently, the detection of the two distant TeV blazars H 2356-309 and 1ES 1101-232 by the H.E.S.S. experiment has been used to derive strong limits on the EBL density around 2 μm (Aharonian et al., 2006a). The method is based on the hypothesis that the intrinsic TeV blazar spectrum cannot be harder than a theoretical limit and that the spectrum of the EBL follows a certain shape (Primack et al., 1999). To derive limits on the EBL density, the shape is scaled until the de-absorbed TeV blazar spectrum meets the exclusion criteria. The derived upper limits are only a factor of two above the lower limits from the integrated light of resolved galaxies (galaxy counts). A similar technique using scaling of a certain shape until the de-absorbed spectrum reaches an exclusion criteria was previously adapted by Renault et al. (2001). The authors derived limits on the EBL from the Mrk 501 spectrum measured by the CAT experiment during a flare in 1997. The TeV limits are shown in Fig. 3.5.

An important criticism to all previous EBL limits derived from the TeV measurements is that these limits are obtained under assumption of a certain predefined EBL shape. Relying on a predefined EBL shape, the TeV limits become

[1] It was noted by Protheroe and Meyer (2000) for the first time that a too high level of the EBL in the mid- and far-infrared leads to an exponential rise of the intrinsic blazar spectra.

very much EBL model dependent, from which the shape is taken. Ironically, scaling of a model shape is, in the majority of cases, not a model parameter, thus making the scaling to an arbitrary procedure. Therefore, the TeV limits were not considered robust. Noteworthy, in case of the H.E.S.S. limit (Aharonian et al., 2006a), in addition to the fixed shape several other possible EBL components like a bump in the UV were examined. This made the derived limit less model dependent and more reliable.

Another aspect of the derived limits is that the studies were made with only a small number (typically one or two per study) of detected TeV sources. This limitation resulted in EBL limits, which did not extend over a wide wavelength range. When H.E.S.S. and MAGIC came online, the number of extragalactic TeV sources grew and new studies became feasible. In Chapter 9, I will present a study using all 15 detected TeV sources[2] and a new method, which is mostly independent from any EBL shape. The constraints, which will be derived there, are the strongest so far and extend in wavelength from the optical ($\sim 1\,\mu$m) to the far-infrared ($\sim 80\,\mu$m).

In the following Section, I will briefly present state-of-the-art EBL models.

3.4 Status of the EBL models

Numerous models have been developed for calculating the typical spectral luminosity density of galaxies as a function of redshift, and thus for calculating the evolving EBL (Calzetti et al., 1995). In the review paper of Hauser and Dwek (2001), the various models are grouped into three categories: backward evolution (BE), forward evolution (FE), and semianalytical (SA) models. The models differ in their degree of complexity, physical realism, and ability to account for observations or to make predictions. In principle, all models should be consistent with global observational constraints such as galaxy spectral energy distributions, galaxy counts, luminosity functions and morphology, as well as their intrinsic properties such as the star formation rate, metallicity, dust abundance etc. In practice, all models contain many free parameters that are adjusted to conform with observational constraints. Here I give a brief description of the main models in each category, based on the review by Hauser and Dwek (2001) and the references therein.

Backward evolution models. Backward evolution (BE) models extrapolate the spectral properties of local galaxies to higher redshifts using some parametric form for their evolution. The EBL is then obtained by integrating the local luminosity density up to a maximum redshift, z_{max}, the epoch when galaxies are assumed to have first formed (Lonsdale (1995) and references therein; Rowan-Robinson and Crawford (1989); Malkan and Stecker (2001); Stecker et al. (2006); Kneiske et al. (2002)). The main advantage of BE models is that they are simple

[2]In the time of this study, 15 extragalactic sources have been detected above 100 GeV.

and offer a quick comparison of observations with predicted galaxy magnitude, redshift, color-magnitude, and other relations. Their main disadvantage is that they are not constrained by the physical processes, such as star and metal formation, or radiative transfer processes that go on in the galaxies they represent.

Forward evolution models. Some of the shortcomings of BE models are corrected in forward evolution models. At the heart of these models is a spectral evolution code that describes the evolving stellar populations and calculates the stellar, gas, and metallicity content and SED of a galaxy as a function of time starting with the onset of star formation. These models were pioneered by Tinsley (1973), and are now widely used to model the SED of globular clusters and various galaxy types (Leitherer et al. (1996) and references therein; Fioc and Rocca-Volmerange (1997); Jimenez and Kashlinsky (1999)). Model input parameters include a prescription for the star formation rate, the stellar initial mass function (IMF), and the chemical evolution. Forward evolution models are successful in fitting the SEDs of individual galaxies, galaxy counts in select bands, and the general characteristics of the EBL. However, a serious disadvantage of FE models is the assumption of monolithic star formation. In these models, galaxies form at the same time and evolve quiescently. The models do not provide prescriptions for galaxy interactions, stochastic changes in the star formation rate, or morphological evolution of galaxies. In particular, these models fail to match the 850 μm galaxy counts without including a new population of ultraluminous infrared galaxies. Such galaxies must be introduced in an ad hoc fashion in these models.

Semianalytical models. The next steps in complexity and detailed simulations are incorporated in the semianalytical (SA) models. SA models work like FE models but instead of a simple parametrization of the galaxy evolution they include semianalytical codes to model numerous physical processes in order to reproduce observable galaxy properties. These include the cooling of the gas that falls into the halos, a prescription for the formation of stars, a feedback mechanism that modulates the star formation efficiency, a stellar IMF, and a star formation efficiency during merger events. In addition, SA models require the standard stellar spectral evolution and chemical evolution models that are used in FE models. The models contain several adjustable parameters to match the observed properties of galaxies in the local universe (White and Frenk, 1991; Kauffmann et al., 1993; Somerville and Primack, 1999). In spite of the successes of the SA models, there remain some discrepancies between model predictions and observations. The origin of these discrepancies is often difficult to trace because of the inherent complexity of the models. Approximations used in describing the physical processes, uncertainties in the input data, and possible fundamental shortcomings of the approach could all contribute to the discrepancies.

Summary of model predictions. Most popular, state-of-the-art EBL models are presented in Fig. 3.7. Stecker et al. (2006) developed a backward evolution model up to a maximum redshift of $z_{max} = 6$. The differences between the fast

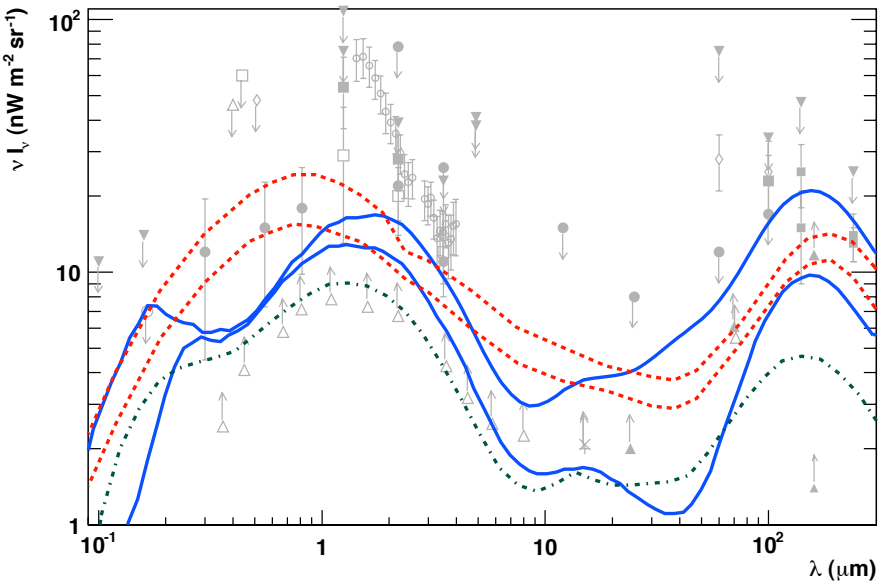

Figure 3.7: EBL models compared to the EBL measurements. Symbols are same as in Fig. 3.5. *Red dashed line*: Stecker et al. (2006), baseline (low) and fast evolution (high) model. *Blue solid line*: Kneiske et al. (2002), high and low as limits for possible EBL realizations. *Green dot-dashed line*: Primack et al. (2005), best prediction of the EBL.

evolution model (upper red dashed curve) and the baseline model (lower red dashed line) are in the assumed galaxy evolution scenarios. Kneiske et al. (2002) developed another backward evolution model by considering exploiting free model parameters of the galaxy and star evolution available in year 2002. The upper solid blue curve shows the maximum possible EBL model and the lower solid blue curve shows the minimum possible EBL model. The result of the semi-analytic model by Primack et al. (1999) (updated by Somerville et al. (2001); Primack et al. (2005)) is presented by the green dot-dashed curve. The model is the most complete and complex EBL model, aiming to make very accurate predictions on the EBL evolution and its current level. The model, however, underpredicts the observed EBL level in far infrared (FIR) band. The reason lies in an underestimation of the number of ultra luminous infrared galaxies, which have only recently been discovered. Taking these galaxies into account, the model fits also the FIR measurements well without changing its level in UV-optical (J. Primack, private communication).

None of the presented models takes into account (or predicts) a possible high contribution of the Population III stars to the current EBL. The reported diffuse residual excess in the near IR by (Matsumoto et al., 2005) has lead to a controversial discussion about the origin of this excess, which is briefly summarized in the next Section.

3.5 Possible Population III Star Contribution to the NIR

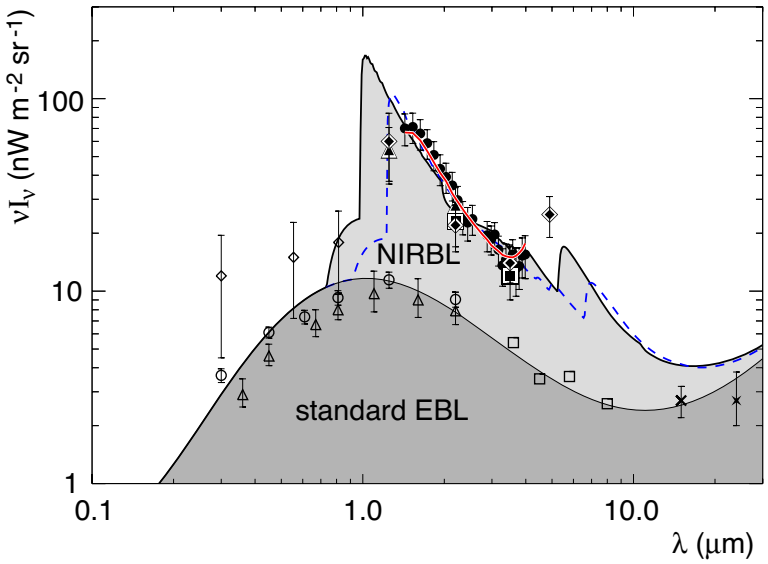

Figure 3.8: Comparison of current limits and detections of the EBL to the spectrum generated by normal star forming galaxies (marked "standard EBL", dark shaded area), and the excess near–IR background light (marked "NIRBL", lightly shaded area). The red curve depicts the spectrum of the zodiacal light (Matsumoto et al., 2005), scaled by a factor of 0.23 to provide a fit to the NIRS data. The plot adapted from Dwek et al. (2005).

A diffuse residual excess in the near IR (NIRBL, 1 to 4 μm) was reported by the IRTS satellite (Matsumoto et al., 2005). The excess is significantly higher than the EBL density expected from galaxy counts. If the excess would be of extragalactic origin (i.e. associated with the EBL), it might be attributed to emissions by the first stars in the history of the universe (Population III) and would make the EBL and its structure a unique probe for the epoch of Population III formation and evolution (e.g. Salvaterra and Ferrara (2003); Kashlinsky et al. (2005)). The Population III stars started to form somewhere in the redshift interval $30 > z > 15$ and continued to exist until $9 > z > 7$. A possible modeling of the NIRBL, including a strong Population III contribution, is shown in Fig. 3.8. The light emitted by the Population III stars is absorbed by surrounding cold dust (neutral hydrogen). The relaxation of excited hydrogen leads to a dominant Ly-α emission line with a wavelength of $\lambda = 0.12\,\mu$m in the lab frame. For an observer today, the line is redshifted by the Doppler law by a factor (1+z) such that the strong feature at $\lambda \approx 1\,\mu$m (Fig. 3.8) can be attributed to Ly-α emission from the last (latest) Population III stars at a redshift of z $\approx$ 9.

Such a luminous Population III star generation, however, over-predicts the

number of Ly-α emitters in ultra-deep field searches (Salvaterra and Ferrara, 2006) and violates common assumptions on baryon consumption and star formation rates (Dwek et al., 2005). In addition, Dwek et al. (2005) and Matsumoto et al. (2005) have pointed out that the NIR excess could be attributed to zodiacal light. This possibility is also supported by the shape of the reported excess being identical to the spectrum of the zodiacal light (upscaled red curve in Fig. 3.8).

Chapter 4

The MAGIC Telescope

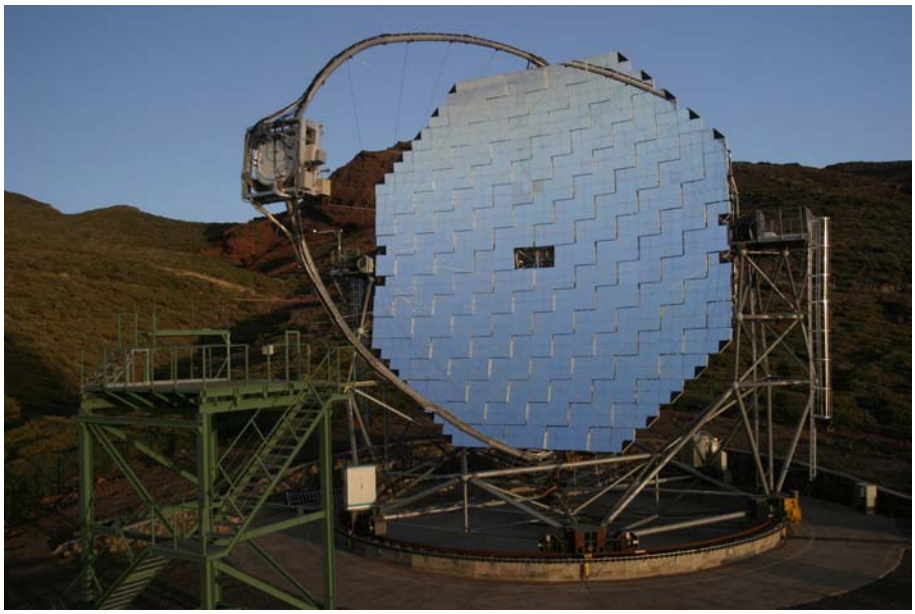

Figure 4.1: Photograph of the MAGIC telescope.

The MAGIC telescope (**M**ajor **A**tmospheric **G**amma **I**maging **C**herenkov telescope) is designed to detect VHE γ-rays in the energy range from 50 GeV to tens of TeV. In Section 4.1 I will briefly describe principles and experimental challenges of the imaging technique for the γ-ray telescopes. In Section 4.2 I will then introduce the MAGIC telescope, which is the largest single dish atmospheric imaging Cherenkov telescope in the world. Section 4.3 gives a short overview of the MAGIC II telescope, which is being built in order to increase the sensitivity of the MAGIC project.

4.1 Imaging Air Cherenkov Telescopes

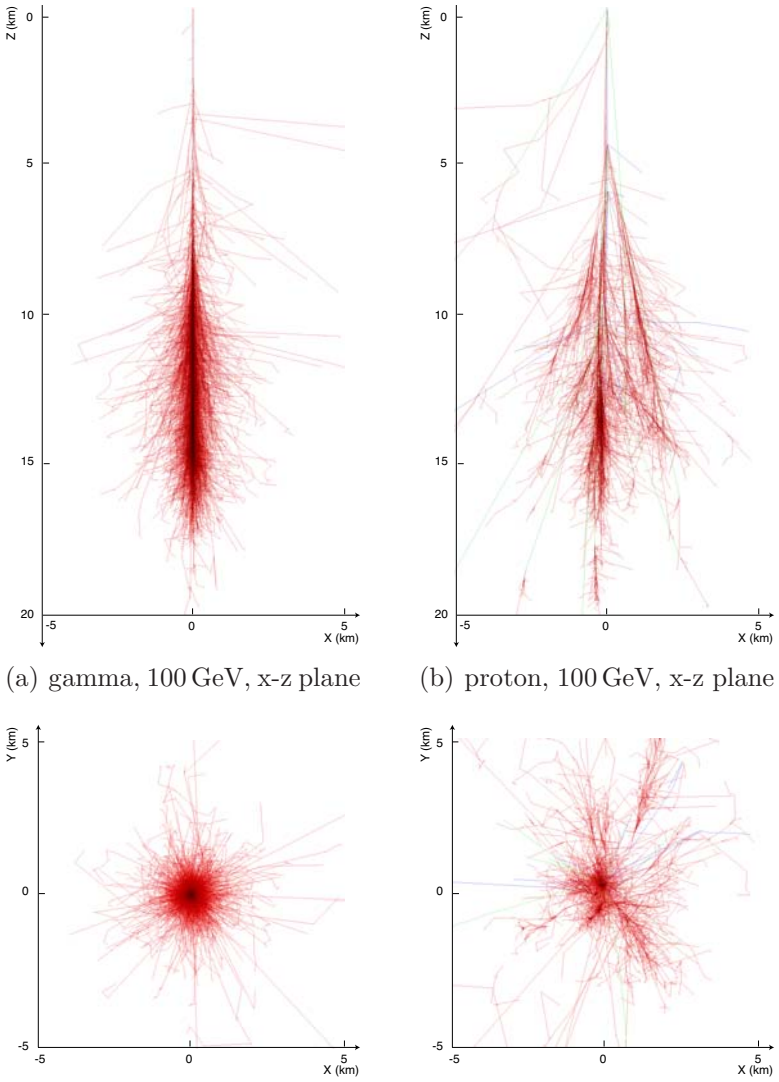

(a) gamma, 100 GeV, x-z plane (b) proton, 100 GeV, x-z plane

(c) gamma, 100 GeV, x-y plane (d) proton, 100 GeV, x-y plane

Figure 4.2: Monte-Carlo simulated extended air showers. *Left plots:* vertical γ-ray shower, E = 100 GeV; *Right plots:* a vertical proton induced shower, E = 100 GeV. Plots adapted from Schmidt (2007).

4.1.1 Extended Atmospheric Showers

The cosmic γ-ray flux above 100 GeV is generally very low and requires big detection areas to detect even strong point-like γ-ray sources as the Crab Nebula in a reasonable time. The EGRET satellite experiment on board of the Compton Gamma Ray Observatory (operating in the years 1991–2000 (Hartman et al., 1999)) was able to measure γ-rays with energies up to 30 GeV. The upper energy bound is due to the small detector area, which was 0.1 m^2 in the case of EGRET. The new generation of satellite experiments AGILE (launched May 2007) and GLAST (launch is planned to be at the end of 2007) has more sensitive instruments and larger detector areas. With the new satellites, it will be possible to measure γ-rays from 100 MeV up to an energy of 300 GeV. Still, even GLAST will need several years of observation to deliver a γ-ray spectrum of the Crab Nebula above 50 GeV. Instruments with a larger sensitive area can be built on the ground. The Earth atmosphere is not transparent for Cosmic rays and VHE γ-rays. Cosmic rays as well as VHE γ-rays react with molecules of the atmosphere and loose their entire energy in a particle shower (extended atmospheric showers (EAS), see Fig. 4.2). Proton-induced (in general hadron-induced) showers are much more numerous than γ-induced. Even for the Crab Nebula, the ratio between γ-induced to hadron-induced showers is about 1:1000, making hadron-induced showers the main source of the background for the VHE γ-ray measurements.

In the last 40 years, several techniques have been developed to detect Cosmic rays and VHE γ-rays through secondary processes. Following effects and processes occur in the atmospheric particle shower and can lead to indirect detection of the incident particles from the ground:

- **Shower particle detection.** Shower particles can be directly detected with particle counters on ground (as e.g. in AGASA (Chiba et al., 1992), AUGER (Mantsch, 2005), HEGRA (Lindner, 1997), KASKADE (Antoni et al., 2003)). The technique works well for energies above 10^{14} eV. In case of lower energies shower particles do not reach the ground level. The energy threshold of an experiment can be then lowered by building detectors at high altitudes (mountains).

- **Cherenkov light detection.** Charged particles emit Cherenkov light when their speed in a medium (e.g. the atmosphere, ice, water) is higher than the light speed in this medium (Cherenkov effect, Cherenkov (1934)). Due to the low refraction index of the atmosphere the Cherenkov light is highly focussed and illuminates typically an area of radius of about 120 m on the ground at the MAGIC site. Cherenkov light for air showers above 15 TeV can be detected directly by placing light detectors with a large field of view ($\approx$1 sr) in the light pool (e.g. AIROBICC, Aharonian et al. (2002b)). **Imaging Atmospheric Cherenkov Telescopes** (IACTs), instead, have a smaller field of view (3–5 deg) and focus the Cherenkov light of a shower

into a pixelized camera. The combination of a smaller field of view per pixel, which suppresses accidental triggers, and a much larger photon collection area allows to reduce in the energy threshold. In fact, the trigger threshold of the MAGIC telescope is as low as 50-60 GeV for observations at low zenith angles.

- **Fluorescence light.** A small fraction of the energy of the shower particles is transferred to atmospheric nitrogen molecules and excites them. During the de-excinction, a distinct line spectrum (amongst other lines the well known 337 nm N_2-line) is isotropically emitted in the near UV. Only showers with energy above 10^{15} eV produce a detectable amount of fluorescence light. The showers are usually observed from the side as in HiRes (Abbasi et al., 2005) or AUGER (Mantsch, 2005) experiments. It has been also proposed to detect from space fluorescence light emitted by showers (e.g. EUSO (Catalano et al., 2005) and OWL (Monnet and D'Odorico, 2006)), which would increase the detection area by two orders of magnitude. So far these projects are in the design phase.

- **Radio Emission.** In the 1950's the possibility to detect radio emission from atmospheric showers was investigated. At that time the technique was discarded because of inefficient detectors. In the last few years, the technique was explored again because better antennas were developed and a better understanding of the radio wave emission was achieved. Recently, the feasibility of shower detection in radio was shown (Falcke et al., 2005). Radio detection of Cosmic rays becomes feasible for energies above 10^{17} eV.

The techniques mentioned above aim to detect air showers and reconstruct their energy and direction. It is, however, very difficult to reveal the nature of the primary particle. One of the possibilities is a precise reconstruction of the shower maximum. Since a lighter mass particle (say proton) penetrates deeper into the atmosphere than a heavier particle (say iron)[1] the corresponding shower maximum will be closer to the ground. However, the difference in cross section between protons and γ-rays is small, and only a precise measurement of the shower maximum can help to determine the kind of primary particle. At the moment, the most powerful technique to separate between γ-ray- and hadron-induced showers is the imaging Cherenkov technique. In the thesis, I concentrate on this technique. This imaging Cherenkov technique does not rely on the shower maximum reconstruction but on the differences between images of electromagnetic and hadronic showers. In the following, I will explain the reason for this difference.

[1] due to a higher cross section of heavier particle, the penetration depth is smaller

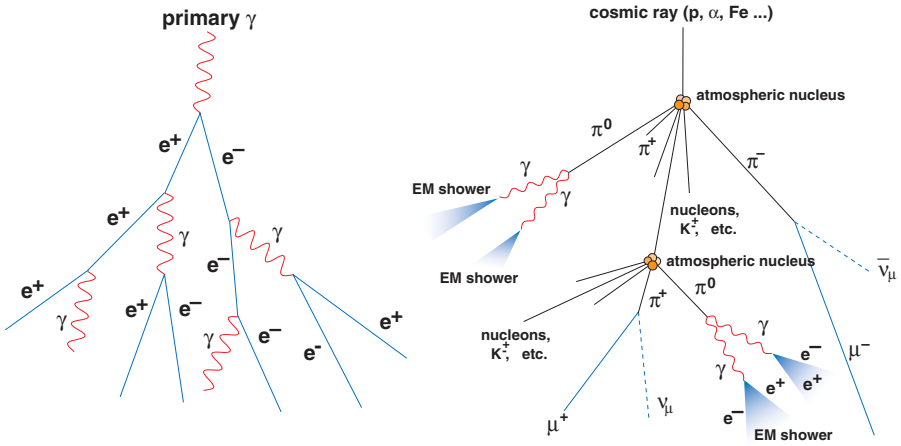

Figure 4.3: Schematic view of the development of a γ-ray induced atmospheric shower (left) and an atmospheric shower induced by a hadron (right).

Electromagnetic showers

High energy photons (or electrons) enter the atmosphere and interact with nuclei of the air molecules. Thereby an extended air shower (EAS) starts to evolve. Two processes contribute mainly to the shower development: the bremsstrahlung, which leads to radiation of new photons, and the pair creation, in which a pair of an electron and a positron is produced (see left sketch in Fig 4.3). Both processes are very similar: the radiation length of an electron or positron for the bremsstrahlung is $X_0^e = 37$ g/cm^2 (in air), and the mean free path of the photon before pair creation is $X_0^\gamma = 7/9\, X_0^e$. Therefore, the structure of an electromagnetic shower is quite simple and symmetric in respect to the main shower axis (left plots in Fig. 4.2 and left sketch in Fig. 4.3). The cross section of VHE γ-rays with air is weakly energy dependent so that the first interaction point is similar for different γ-ray energies and is at about 20 to 30 km above sea level. In each step of the cascade the number of particles doubles and the energy per particle is reduced accordingly. At some point the energy per particle reaches a critical energy, at which the energy losses of electrons and positrons by ionization and by bremsstrahlung are equal. In air, the critical energy is 86 MeV (Berger and Seltzer, 1964). At lower energies the losses by the ionization become dominant and the shower dies out. The height above the sea level where the number of particles in the shower is highest, is defined as the shower maximum. The higher the energy of the primary particle, the deeper is the shower maximum due to a longer cascade until the critical energy is reached[2]. The shower maximum is at about 13 to 7 km above sea level for energies of primary γ-rays between 50 GeV and 10 TeV.

[2]The depth of the shower maximum is proportional to the logarithm of the primary energy: $h_{\max} \propto \ln(E)$.

Hadronic showers

In case the primary particle is a hadron (usually a proton), the primary collides with a nucleus in the atmosphere. Thereby mostly pions are created ($\pi^+ : \pi^- : \pi^0$ with proportion 1:1:1) as well as kaons and further nucleons (their number is much less than the one of pions). Hadrons and pions initialize a hadronic cascade through further collisions. Furthermore, pions decay (see below) and the resulting photons, electrons and positrons build electromagnetic sub-showers, whereas resulting muons form a muonic component of the shower. A hadronic shower grows until the energy per nucleon is below the pion production threshold of about 1 GeV. A hadronic shower with a proton of E = 100 GeV as the primary particle is shown in Fig. 4.2, right panels. A schematic view of a hadronic shower is shown in the right sketch in Fig. 4.3. The following processes mainly form a hadronic shower:

$$\begin{aligned} \pi^0 &\longrightarrow 2\,\gamma \\ \pi^- &\longrightarrow \mu^- \overline{\nu}_\mu \\ \pi^+ &\longrightarrow \mu^+ \nu_\mu \\ \mu^- &\longrightarrow e^- \overline{\nu}_e \nu_\mu \\ \mu^+ &\longrightarrow e^+ \nu_e \overline{\nu}_\mu \end{aligned} \tag{4.1}$$

Strong interactions are different from the electromagnetic ones, and as an effect pions and kaons receive on average a higher transversal momentum than electrons and positrons. In addition, a hadronic EAS has, in general, several subcascades. Therefore, hadronic EAS are much wider and irregular than electromagnetic EAS (compare plots in Fig. 4.2). This feature is used to separate γ-ray induced EAS from hadronic ones. However, subcascades of hadronic EAS, if only the electromagnetic subcascade is detected, can mimic γ-ray induced EAS making them to an almost irreducible background.

4.1.2 Cherenkov light emission from EAS

Within an EAS electrons and positrons are mostly ultrarelativistic, and Cherenkov radiation is emitted (Cherenkov, 1934). The Cherenkov effect works as follows (Tamm and Frank, 1937): An ultrarelativistic charged particle polarizes the medium. The polarized medium (atmosphere) with a refraction index n emits spherical electromagnetic waves along the track of relativistic particles (Fig. 4.4). If a relativistic particle moves with a speed v, which is faster than the speed of light in medium $c' = c/n$ (c is vacuum speed of light, n is the refractive index of the medium), then the particle moves faster than the spherical waves are propagating. As illustrated in Fig. 4.4 the individual waves experience an interference

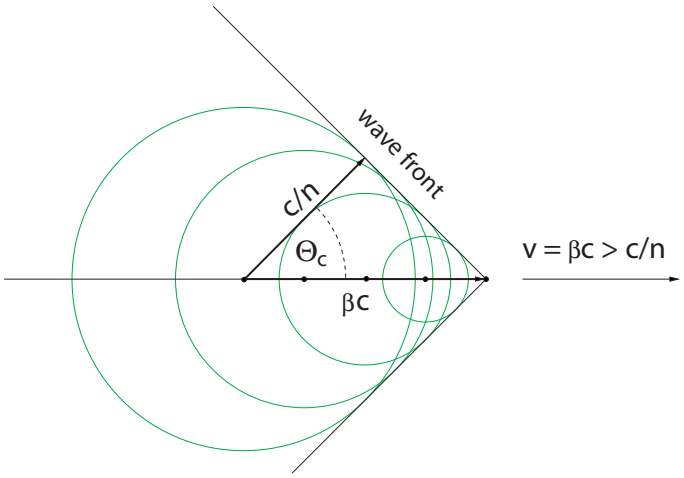

Figure 4.4: Schematic view on Cherenkov emission of a charged particle, which is moving with ultrarelativistic speed in a medium. The speed of light in a medium with a refraction index n is $c' = c/n$. In the polarized air the emitted spherical electromagnetic waves superimpose to a cone with an opening angle of $\Theta_C \sim 1°$. This emission is called Cherenkov light.

at an angle Θ_C, which is also called the Cherenkov angle. It is easy to show that:

$$\begin{aligned} \cos(\Theta_C) &= \frac{c'}{v} = \frac{c/n}{\beta\, c} = \frac{1}{\beta\, n} \\ \text{with} \quad \beta &:= v/c \end{aligned} \tag{4.2}$$

Following the condition above, an electromagnetic radiation will be emitted in a cone at the angle Θ_C and cancel out in all other directions. This radiation (called Cherenkov light in the following) has an analogy in acoustics in the form of the shock waves produced by a projectile or an airplane traveling at an ultra-sonic velocity (Mach waves).

The mean value of Θ_C is about 1° in air. The Cherenkov radiation from a finite track of an ultrarelativistic charged particle illuminates a "donut ring" on the ground. The donut becomes thicker and finally merges to a circle as the track is longer and reaches the ground. The circle is, however, not illuminated uniformly because the air density is increasing towards the ground, which leads to an increase of the refraction index n and the opening angle Θ_C.

The Cherenkov radiation of an EAS consists of a cumulative Cherenkov light emitted by shower particles. In case of an electromagnetic shower, Cherenkov light illuminates typically a circle[3], called "Cherenkov light pool", with a radius of 120 m if measured at 2000 m above the sea level. An example of a simulated Cherenkov light distribution on this altitude coming from a vertical electromagnetic EAS is shown in Fig. 4.5, left plot. The resulting Cherenkov light pool is a

[3]A circle forms in case of a vertical air shower. In case the EAS is inclined, the overlapping Cherenkov light illuminates an ellipse on the ground.

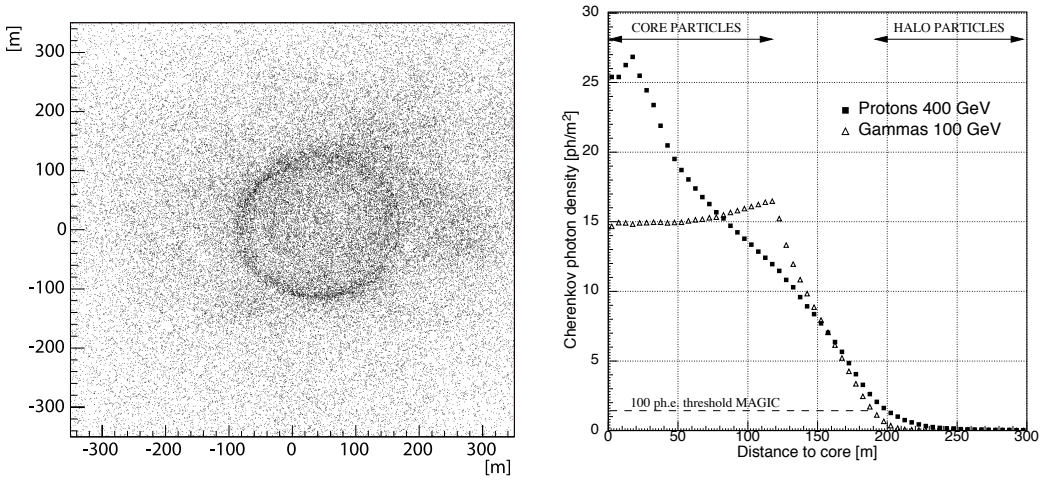

(a) Cherenkov photon distribution for an atmospheric shower induced by a 50 GeV γ ray

(b) Lateral distribution of Cherenkov photon densities for 100 GeV γ-ray and 400 GeV proton induced showers (from Barrio et al. (1998))

Figure 4.5: Simulated Cherenkov photon distribution at 2200 m altitude above sea level. The majority of photons arrive within a radius of 120 m from the impact point. Due to the increasing Cherenkov angle with increasing shower depth a maximum in the photon distribution is seen at ≈ 120 m. This is often referred to as the "hump".

superposition of individual donuts from charged shower particles moving under small random angles to the shower axis. The photon density is almost constant from the center to the rim at about 120 m radius. The rim has a higher density and is usually known as the "hump". The hump is a consequence of the increasing opening angle Θ_C of the Cherenkov photons as the light emitting particles penetrate deeper into the atmosphere. At distances larger than the "hump" the photon density is decreasing rapidly. Still, there is light emission even beyond 200 m impact distance, caused by the shower halo particles. A profile of the light yield of Cherenkov photons as a function of the radius is shown in Fig. 4.5, right plot. Not shown are fluctuations of the mean value. These are much stronger for hadronic showers and, thus, the Cherenkov light can be even detected up to 400 m from the shower core.

The number of emitted Cherenkov photons per unit track length for a particle with one elementary charge and per wavelength of the photon is (Yao et al., 2006):

$$\frac{d^2N}{dxd\lambda} = \frac{2\pi\alpha}{\lambda^2}\left(1-\frac{c^2}{v^2n^2(\lambda)}\right), \quad \alpha \text{ is the fine-structure constant} \quad (4.3)$$

$$\frac{d^2N}{dxdE} \approx 370\sin^2\theta_c(E)\,\mathrm{eV}^{-1}\mathrm{cm}^{-1}$$

The spectral intensity has a strong, λ^{-2}, dependency of the photon wavelength λ. As one can see from Fig. 4.6, most of the photons are emitted in the UV

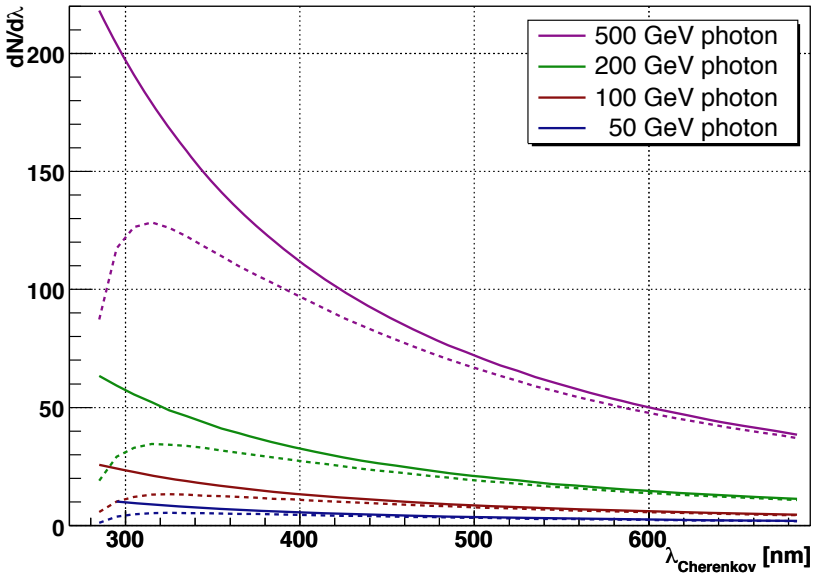

Figure 4.6: Spectra of Cherenkov light by vertical γ-ray showers of different primary energy at 10 km height (solid lines) and the corresponding spectra at 2200 m a.s.l (dashed curves) affected by absorption, Rayleigh and Mie scattering as described in the text (plot taken from Wagner (2006)).

range. The emitted photons suffer, however, transmission losses in the atmosphere. The transmission losses in air are mainly caused by Rayleigh scattering off air molecules, which has a λ^{-4} dependency. At wavelengths below 300 nm an additional strong absorption caused by ozone molecules takes place. Most of the hard UV photons are therefore absorbed. A more complex Mie-scattering off aerosols (also water droplets, dust) occurs without strong dependence on the photon wavelength $\propto \lambda^{-(1...1.5)}$. The measured Cherenkov photon spectrum is shown in Fig. 4.6 and mainly ranges from 300 nm to 500 nm with a peak at roughly 320 nm. The Cherenkov spectrum is zenith angle dependent with a shift of the peak position towards larger wavelengths for an increasing zenith angle of atmospheric showers.

The light yield of EAS initiated by different incident particle species is shown in Fig. 4.7. For an electromagnetic shower, the summed track length of all charged shower particles is in first order proportional to the energy of the primary particle. The number of emitted Cherenkov photons is proportional to the number of shower particles. Therefore, the total Cherenkov light yield is proportional in first order to the energy of the primary particle. This means that the atmosphere behaves almost like an ideal calorimeter for γ-ray-initiated showers.

The time needed for an EAS development is of the order of several 10's of microseconds. Cherenkov light emitted earlier during the shower development is slower than the particle movement in the shower. However, Cherenkov light

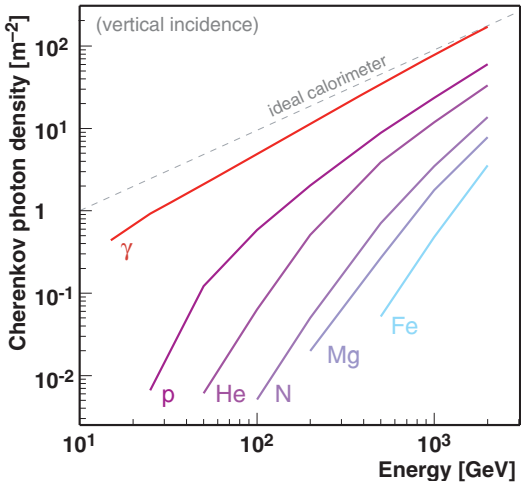

Figure 4.7: Cherenkov photon yields for different incident particles. The plot shows the mean Cherenkov photon density within a radius of 125 m from the shower core for vertical showers (Oser et al., 2001; Wagner, 2006). The atmosphere behaves almost like an ideal calorimeter for γ-ray-initiated showers.

emitted later and closer to the ground has an overall longer way (including the tracks of the parent particles) to the observer than the former photons. Du to these two effects, differences in propagation times of the photons cancel out the development of the shower in time. Therefore, the duration of the Cherenkov light flash seen at ground is just of the order of 4 – 10 ns. The extremely short flashes are very difficult to measure due to a high background of the night sky. The light of the night sky (LONS, see Roach and Gordon (1973) for details) consists of light of bright and faint stars, diffuse light of the galactic plane, zodiacal light , airglow, polar light, and artificial light. The LONS is not isotropically distributed and is higher towards e.g. Galactic plane than for a typical extragalactic field of view. In order to discriminate between the light of EAS and LONS, an integration time of the device should be not much longer than the duration of the EAS. This makes an usage of CCD cameras impossible because they need milliseconds for readout. The usage of photomultiplier tubes (PMTs) to measure Cherenkov light of atmospheric showers has been proven to be efficient. The PMT are light sensitive detectors with a very fast (few nanoseconds) response time. Though their peak quantum efficiency (at $\approx$ 300-350 nm) is currently just about 25% and they can be easily damaged when they are exposed to a strong light source, PMTs are currently the best light sensors for this purpose. Taking into account that for an analysis of the shower images at least 100 ph.e. are needed (corresponding to roughly 600 photons), the threshold of the MAGIC telescope is shown by the dashed line in Fig. 4.5, right. Several novel techniques using silicon avalanche photodiodes or hybrid photosensors to detect Cherenkov light of the EAS are under development and appear to be very promising (see Otte (2007) for an

overview). In the following I will describe the imaging technique to measure EAS.

4.1.3 The imaging technique

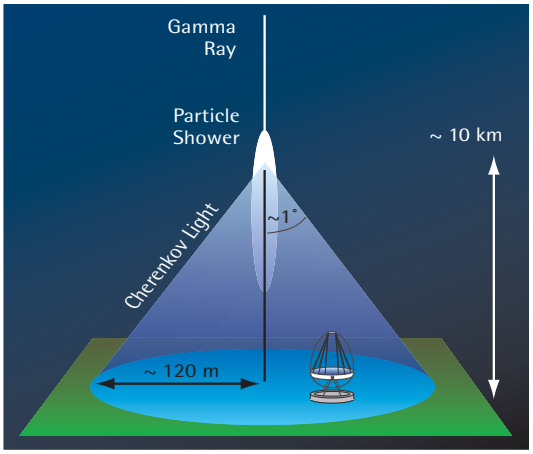

Figure 4.8: The picture shows the basic principle of the imaging atmospheric shower Cherenkov technique. A telescope within the light pool of an atmospheric shower (light blue cone) can record an image of the shower provided the primary energy is high enough.

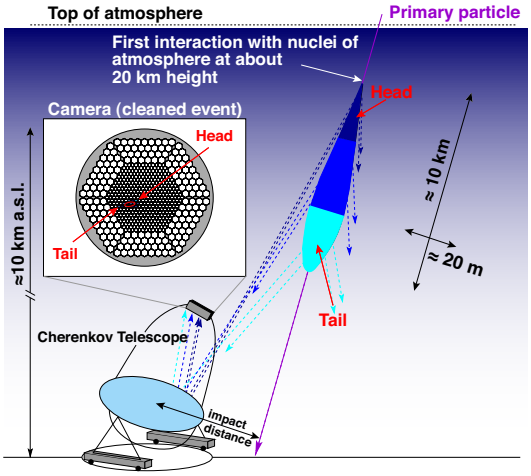

Figure 4.9: A schematic view on the isogonal image of an extended air shower by using its Cherenkov light. The air shower is approximated by a light cylinder. The image in the camera has an elliptical shape of a certain Length and Width. The so-called "head" and "tail" of the shower are mapped into the camera image.

One of the possibilities to measure an EAS is making a photography of it in Cherenkov light against the night-sky. It was suggested that the high resolution of the image should be able to provide detailed information both on the true direction of the shower and on the type of the primary particle (Jelley and Porter, 1963). However, due to technical difficulties and thus a low sensitivity of the early instruments (see Weekes (2006) for a historical review), it was not until 1989 as with the Whipple telescope a γ-ray signal from the Crab nebula was detected (Weekes, 1989). The detection motivated continuing operation of the existing and building better instruments. It finally lead to many great discoveries using the Imaging Atmospheric Cherenkov Telescopes (IACTs). The principle of the IACT is shown in Fig. 4.9.

In order to achieve a high sensitivity of an IACT, a large light collection area, high QE fast photo detectors, and a fine pixelized camera are required. The bigger the reflector, the more photons can be collected from a single shower and,

hence, the better image of the EAS can be recorded. The camera is placed in the focal point of the reflector, where parallel light rays are focussed to the same point (see Fig. 4.9). A symmetrical ellipsoid in the atmosphere causes an elliptical image in the camera. Three types of recorded events / images with the MAGIC telescope are shown in Fig. 4.10. From Fig. 4.10 one can recognize differences between hadron-, muon- and γ-induced images.

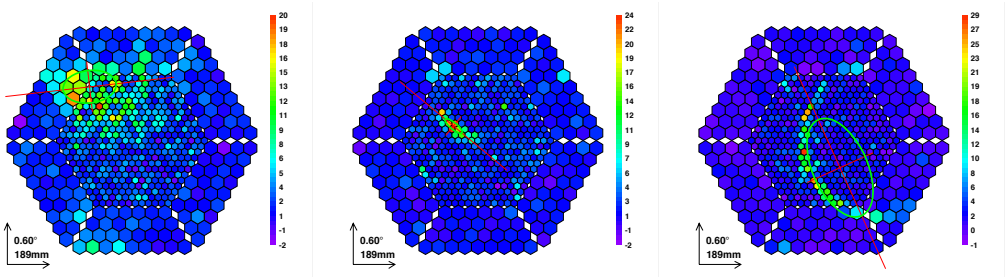

(a) hadron (b) gamma (c) muon

Figure 4.10: Examples of recorded images with the MAGIC Telescope. *Left:* hadron candidate; *Middle:* γ-ray candidate; *Right:* muon ring.

Differences in the image shape between electromagnetic and hadronic showers are used to select γ-ray induced images. In addition, the arrival direction of hadronic showers is isotropically distributed in the sky. In contrary, the arrival direction of an EAS originating from γ-rays of a (usually) point source is a well defined position in the sky. This means that a high accuracy in reconstruction of the arrival direction of the measured showers has a high potential in the signal to background discrimination. The pixelization of the camera thereby is of major importance. Fine pixels of the camera, i.e. pixels with a small field of view, improve shower reconstruction, in particular reconstruction of the shower arrival direction. Also the γ/hadron separation and night sky background rejection can be improved with finer camera pixels. However, it does not make sense to have smaller pixels than $\approx 1/2$ of the optical point spread function[4] of the telescope.

In case of electromagnetic showers, the main shower axis is easily recognized in the recorded image as the main axis of the elliptical image (γ-image in Fig. 4.10). The main axis points to the arrival direction of the shower. However, two quantities are difficult to access with a single telescope:

1. The absolute position of shower in the sky. The shower is seen as an elliptic image in the camera (see Fig. 4.9). The distance between the image and the source position in the camera corresponds to the angle between the optical axis of the telescope and the shower in the atmosphere. This angle, however, can correspond to A) a high impact distance of the shower combined with

[4]The optical spread function is defined as an angular distance between images of two point sources, which are separated by 1 full width at half maximum (FWHM) of the image intensities.

a high position of the shower maximum or to B) a low impact distance combined with a low position of the shower maximum.

2. The sky direction[5] of the incident particle. This direction lies on (or close to) the main axis of the elliptical image. There is, however, an ambiguity in the solution and one has to guess on which side of the image the incident direction is located. For images with a high charge content, one can often distinguish between the *head* and the *tail* of a shower using the asymmetry of the image along its main axis. The *head* of the image points towards the incident particle direction.

4.1.4 Backgrounds

The aim of IACTs is to measure physical properties of primary VHE γ-rays (arrival direction, energy) by means of the Cherenkov light produced in the EAS induced by these γ-rays. Once sensitive measurements are made, most of the underlying physics information, such as origin of the source, its extension, its spectral and temporal properties etc, can be extracted from the data. Strong backgrounds, however, reduce the sensitivity of the measurement. The most important sources of the background are:

- **Light of the night sky (LONS).** As mentioned before, main background source is LONS: light coming from planets, stars, airglow, and zodiacal light (Roach and Gordon, 1973). The energy threshold of an IACT is determined by the level of LONS, reflector area and its reflectivity, and the sensitivity of the used light detectors. LONS depends on the sky region, zenith angle of observation, and on the location on Earth. The LONS is always contaminating the Cherenkov light of EAS and is one of the limiting factors at trigger level. In the following, I will use the notation "Night sky background (NSB)" when referring to the light recorded by the telescope due to LONS.

- **Hadrons.** Hadron induced showers are the main background of the measurement. Even for a strong γ-ray source like the Crab Nebula, the ratio between hadron triggers and γ-ray triggers is roughly 1000/1 at 1 TeV. The energy distribution of the hadron background follows a power law distribution $dN/dE = E^{-\Gamma}$ with photon index $\Gamma = 2.7$.

- **Muons.** Close by single muons are easily recognized by the ring or arc image in the camera. Cherenkov light from single high altitude muons, which have their impact point far away from the IACT (50 – 120 m), can mimic γ-ray images of low energies and are often difficult to reject. A typical

[5] also called arrival direction, which is described by the celestial coordinates right ascension and declination

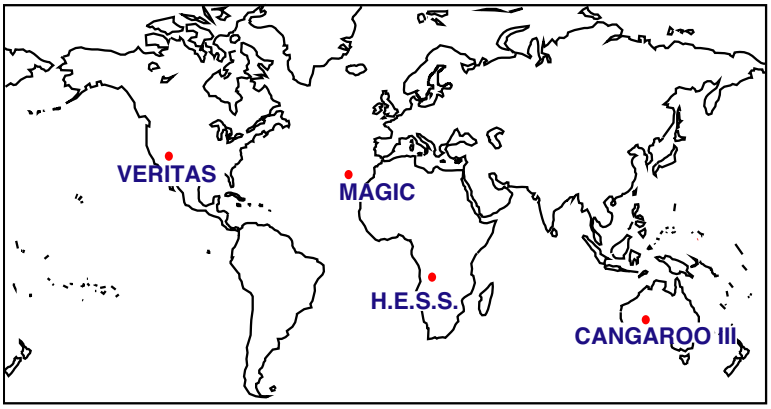

Figure 4.11: Locations of the 4 major IACT experiments.

rate of such events is hard to estimate since the muons can originate even from hadronic showers with their impact point of larger than 500 m from the telescope.

- **Cosmic electrons.** At energies below about a few 100 GeV cosmic electrons become a non-negligible background. VHE electrons produce electromagnetic EAS, which look exactly like electromagnetic EAS from VHE γ-rays. It is an irreducible but isotropic background.

- **Diffuse γ-rays.** It is believed that there exist diffuse VHE γ-rays coming from unresolved galactic and extragalactic sources. The H.E.S.S. collaboration has indeed recently measured a diffuse galactic component Aharonian et al. (2006c). The diffuse extragalactic γ-ray background is believed to be smaller by several orders of magnitude than the galactic one. Diffuse γ-rays represent another source of an irreducible background when searching for γ-ray emitting point sources. Fortunately, this background is very weak even in the galactic plane where its level seems to be highest.

Even if the image properties are very similar between γ-ray induced showers and images due to various backgrounds, one property remains unique for γ-rays: γ-images point to the source direction whereas reconstructed directions of background induced images are isotropically distributed. This is why a precise reconstruction of the arrival direction of the shower will significantly increase the sensitivity of the measurement.

4.2 MAGIC I

Currently, four big collaborations operate world-wide four IACTs of the third generation: The Australian-Japanese CANGAROO-III collaboration has built four 10 m telescopes in Australia; the largely European H.E.S.S. collaboration has

built an array of four 12 m telescopes in Namibia; the Irish-British-USA collaboration that has also built recently an array of four 12 m telescopes in Arizona, USA (VERITAS); and the largely German-Spanish-Italian MAGIC collaboration[6], which has built a stand alone 17 m telescope in La Palma (Canary Islands, Spain). The locations of the experiments are illustrated in Fig. 4.11. The MAGIC telescope is the subject of this section. While CANGAROO-III experienced some financial problems and VERITAS just finished the construction phase, H.E.S.S. and MAGIC started observations in 2003 and 2004, respectively, which lead to a number of discoveries and important publications.

The MAGIC collaboration currently consists of 20 groups (institutes) from 8 European countries and the USA. Altogether, there are about 150 scientists and roughly 100 technicians working at least partially for the experiment. First ideas of the project were formulated back in the early 1990's and an extensive design report was published in 1998 (Barrio et al., 1998). The site was chosen to be on the area of the Observatorio de Astrofisico of the Canary Island La Palma on the Roque de los Muchachos (2200 m asl, 28°45′N, 17°54′W). The site is well known for its very good atmospheric conditions for most of the year, and it was previously used for the Cosmic ray experiment AEROBICC (Karle et al., 1995), HEGRA array (Aharonian et al., 2002a), HEGRA CT1 (Mirzoyan et al., 1994), and the HEGRA CT system (five IACTs with 5 m diameter each, Daum et al. (1997)). Construction of MAGIC in La Palma was started in 2001, and the official inauguration of the telescope was celebrated in October 2003.

Several novel technologies were used for the design of the MAGIC telescope. With a 17 m diameter tessellated dish it has the largest reflector of all operating IACTs. Light weight carbon fiber tubes, the active mirror control, a 577-pixel PMT (photomultiplier tubes) camera with a 3.5° field of view, analog optical transport of the signal from the camera, a fully programmable two-level trigger, and 300 MHz signal digitizers are the key technological elements of the telescope. The aim of the project was to achieve the lowest energy threshold among all IACTs of the third generation (down to 30 GeV) and the possibility to move the telescope within seconds to any sky position. The latter is needed to quickly react on Gamma Ray Burst alerts and point the telescope as fast as possible to the sky position of a burst. The key elements of the MAGIC telescope are described in the next subsection.

4.2.1 The hardware components of the telescope

The major hardware components of the telescope are:

- Alt-Azimuth frame mount on a circular rail;

[6]The MAGIC Collaboration currently has about 150 members from nine countries: Armenia, Bulgaria, Germany, Finland, Italy, Poland, Spain, the Switzerland, and the USA.

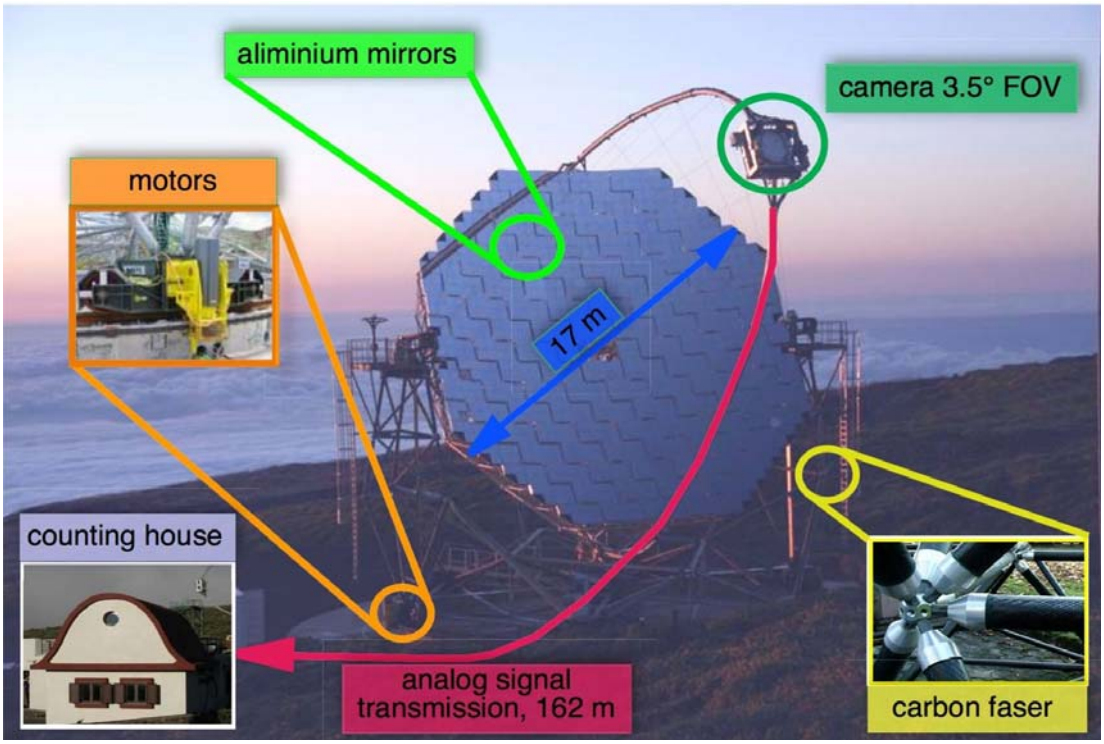

Figure 4.12: The MAGIC telescope and its major hardware components.

- Drive system;
- Parabolic 17 m diameter reflector dish;
- Lightweight aluminum mirrors;
- Active Mirror Control;
- Starguider system;
- Photomultiplier camera with 577 channels
- Signal transmission over 162 m to the counting house via optical fibers;
- Signal receivers;
- 3-Level trigger system;
- Data acquisition system (DAQ);
- Calibration;

Fig. 4.12 illustrates several of the major elements. In the following I will give some details on the hardware components.

The telescope frame and the drive system

The telescope mirror support frame is made of robust, light weight carbon fiber tubes. The frame of the telescope, including mirrors and the camera support weighs less than 20 tons while the whole structure plus the undercarriage amounts to about 65 tons. The assembly of the whole frame took only one month thanks to a construction based on the so-called tube and knot system by the MERO company.

The telescope has an alt-azimuth mount. This means that in order to track a source in the sky, the telescope has to be moved around two axes (azimuth and elevation). The azimuth axis is equipped with two 11 kW motors, while the elevation axis has a single motor of the same power. The angular position of the telescope is measured by three absolute 14-bit shaft encoders. One of them is in azimuth axis and two in the declination to control twists of the mirror dish. With this configuration it is possible to measure the telescope position with an accuracy of about 0.02°. The optical axis of the telescope (also called pointing) is then calibrated by taking pictures of stars at different azimuth and zenith angles using a CCD camera in the middle of the dish (T-Point camera, see Fig. 4.13). Measurements of about 150 different stars are necessary to produce an accurate bending model for the telescope. Together with the shaft encoders, a tracking accuracy of 0.01° (1/10 of a PMT camera pixel size) can be achieved (Riegel et al., 2005b). This accuracy does not include a possible irregular bending of the telescope structure or changes in the bending with time. The positioning of the telescope is therefore constantly monitored using another CCD camera mounted on the reflector frame (starguider camera, see below). The maximum repositioning time of the telescope is about 100 s, whereas the average repositioning time is ≈40 s, a bit worse than the 30 s that were set as a target for Gamma Ray Burst (GRB) follow-ups. The reason is that the telescope cannot be currently operated in the so-called *reverse* mode, i.e. moving over zenith such that the MAGIC camera is upside-down. Still, the MAGIC telescope has by far the fastest response among the operating IACTs for GRB alerts (Albert et al., 2007d). This is a merit of the light weight of the reflector and the PMT camera.

The reflector dish and the mirrors

The reflector has a parabolic shape with f (focal length) = D (diameter) = 17 m. Parabolic mirrors are isochronous. This is necessary for such a large telescope, otherwise time differences between photons reflected at different points of the reflector become too large.[7] The side effect of the parabolic dish is the coma

[7]For a spherical dish, arrival time differences increase. In particular this means that the trigger has to open a gate for a longer time, which would result in an integration of more NSB noise. Since the duration of a Cherenkov flash is just in order of few nsec, an integration time in the same order of magnitude has a large advantage of the NSB suppression.

aberration, which makes the images to look extended (blurred) if looking off-axis. The effect has a radial symmetry to the camera center resulting in an image stretching, which is in first order directly proportional to the angle, under which the shower is seen by the telescope. In case of the MAGIC reflector the coma aberration effect amounts to 7%, i.e. a image point which should have a distance d from the camera center, has an effective distance of $1.07 \cdot d$. The value of f/D = 1 is one of the smallest among the currently operating IACTs (the smaller the f/D value the larger the coma aberration) and it is a consequence of the light structure of the telescope and the limited cost. A larger f/D value would mean that the camera has to be larger and placed further away from the reflector than 17 m, which would necessitate both a much heavier PMT camera and supporting structure. The reflector itself consists of 956 square mirror elements of 49.5 cm×49.5 cm size, each of spherical shape but with different radii to match the parabolic structure. The mirrors are made of 5 mm thick AlMgSi alloy plates glued on aluminum honeycomb inside a thin Al-box. The reflectivity of the mirrors ranges between 80 and 90% depending on the wavelength, whereas the average reflectivity is about 85%. Groups of 4 mirrors each (few at edges with 3 mirrors) are mounted onto a $1 \times 1\,\mathrm{m}^2$ support panel. Due to an originally too tight mount between the panels, a staggering, called *chessboard structure*, of the panels (by about 6 cm) was introduced in summer 2005, which lead to a small difference in the photon arrival times at the PMT camera of up to 0.6 ns, which is still below a possible signal resolution of the PMTs (1-2 ns).

The active mirror control (AMC)

In order to correct for distortions of the telescope frame and the mirror panels by varying gravity when tracking a source, an active mirror control (AMC) is implemented. The system consists of two actuators per mirror panel and a red (635 nm) laser pointer installed in the center of each panel. On demand by the control software the laser is switched on projecting a red spot on the PMT camera cover, which is viewed by a CCD camera (AMC camera, see Fig. 4.13). The AMC camera determines the laser spot w.r.t. some reference marker and, accordingly to the deviation to the nominal position, steers the mirror panels with the actuators. The reference marker positions are defined in respect to several LEDs mounted on the PMT camera cover. This makes sure that the optical axis of the reflector points towards the center of the MAGIC camera even if the camera sinks due to gravity for large zenith angles. The alignment can be also done with stars: the AMC camera can identify reflected star light of each panel. A control software uses the image of the star on the PMT camera cover to adjust the panels such that the spot is focussed in the PMT camera center. The corresponding actuator positions are stored as a function of the zenith angle of the pointing in look-up-tables (LUTs). In this procedure, absolute actuator positions are stored. During normal operation (data taking), two different approaches can be used to adjust

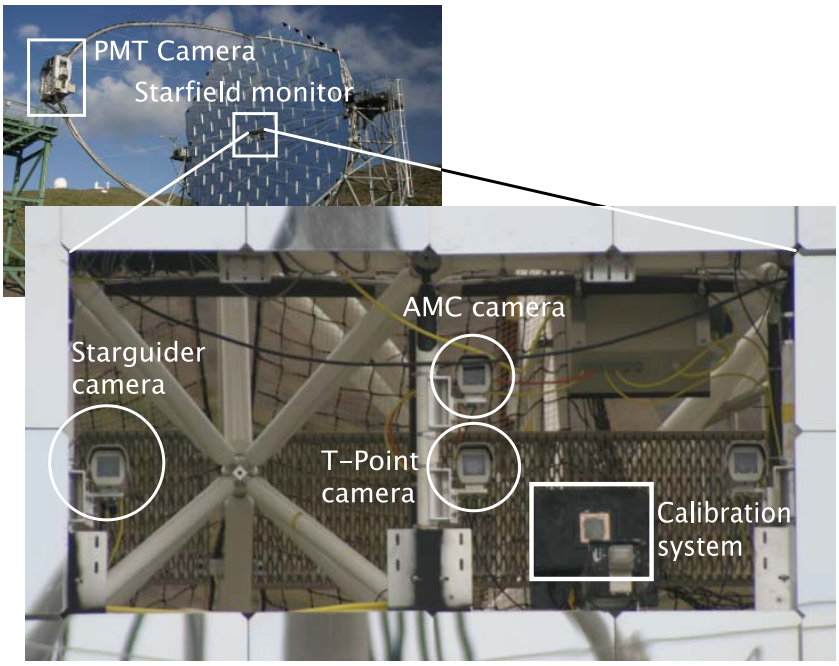

Figure 4.13: The CCD cameras in the middle of the reflector of the MAGIC telescope. The starguider CCD camera and the calibration system are indicated. Pictures adapted from Wagner (2006).

the mirrors. The first one is to use the LUTs, i.e. move the motors to the stored positions according to the zenith angle of observation. It is a very fast procedure and can be done during the repositioning or even tracking of the telescopes. The second method is to use the laser pointers switching them on and adjusting the panels according to the corresponding markers. In this case, the PMT camera has to be closed for each readjustment because the laser pointers can damage the PMTs. It was finally shown in summer 2006 that a usage of the LUTs is more stable over the time than an adjustment with the laser pointers. It seems that the pointing direction of the lasers inside the boxes is changing with time. For more details see Garczarczyk (2007).

Starguider

In order to monitor the tracking system and correct for a possible mispointing,[8] a starguider system is installed. In the center of the mirror dish (see Fig. 4.13), a sensitive CCD camera is installed, having a $4.6° \times 4.6°$ field of view. A part of the PMT camera is inside the field of view of this camera as shown in Fig. 4.14. The position of the PMT camera is recognized by the starguider software using 6 LEDs mounted on the border of the PMT camera. The starguider identifies the

[8]mispointing means that the desired sky direction is focussed to a position, which has an offset w.r.t. the camera center

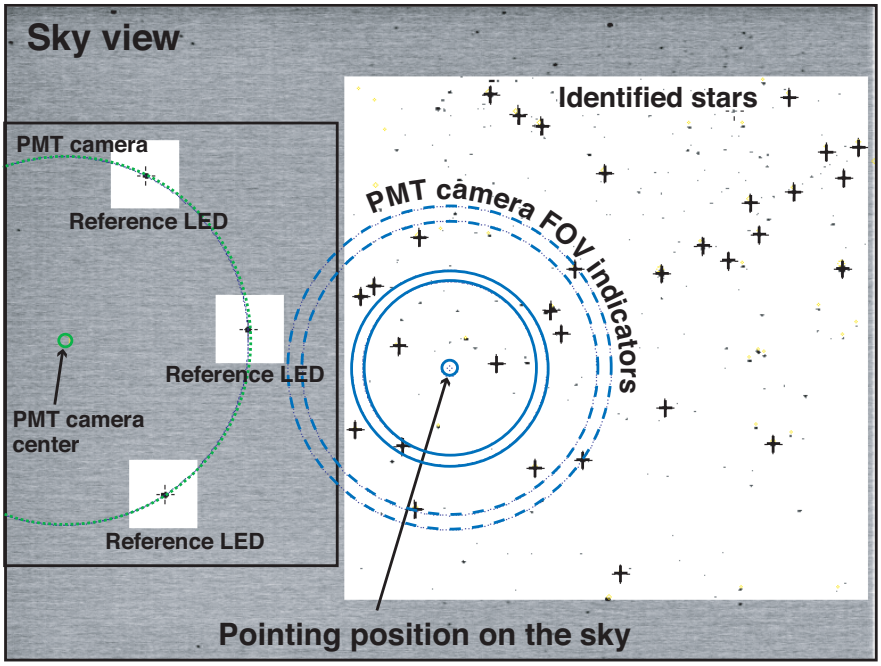

Figure 4.14: Field of view of the starguider camera. The colors are inverted for clarity. On the left part, 3 references LEDs are visible, which are used to determine the position of the PMT camera center. The white field on the right is a part of the sky, which is used to identify stars and determine the pointing of the telescope. The identified stars are marked by a cross. The MAGIC FOV is marked by blue circles: inner camera (solid blue circles) and outer camera (dashed blue circles). Picture adapted from Wagner (2006).

pointing direction of the telescope by comparing star positions in the field of view (FoV) with a starfield catalog. This makes sure that, together with the AMC, the actual pointing of the telescope is known. The starguider information is used offline in the data analysis after the commissioning phase. Currently, the typical residual telescope mispointing is about 0.02°. An important positive side effect of the starguider is that one can compare the number of identified stars with an expected number of stars and in such a way judge about weather conditions, in particular about the atmospheric transmission, for a given observation.

The PMT camera

The PMT camera (Fig. 4.15) is designed to record the Cherenkov light from the atmospheric showers with help of photomultiplier tubes (PMTs), amplify the signal, reconvert it again into an intense light flash, and transmit it to the counting house via optical fibers. The collection area of the MAGIC PMT camera is augmented by hexagonal light catchers (Winston cones) in order to minimize light losses in the camera. The inner part of the camera is equipped by 397 PMTs

Figure 4.15: Photograph of the camera of the MAGIC telescope with opened lids. while the Winston cones are being installed. The inner part of the camera consists of 397 PMTs of 1" that are surrounded by 180 PMTs of 1.5" diameter.

of type ET9116 with a 0.1° FoV each. The PMTs are combined into a hexagonal arrangement to a total of roughly 2° FoV. The inner PMTs are surrounded by 180 outer PMTs of type ET9117 with a 0.2° FoV each. The hemispherical entrance window of the PMTs is coated by a diffuse lacquer doped with a wavelength shifter to enhance the sensitivity for UV photons (Paneque et al., 2004). For protection purposes the camera is covered by UV transmitting plexiglas window. The camera has a 3.5° FoV. A detailed description of the camera can be found in Paneque (2005); Gaug (2006).

Signal processing in the camera and transmission

The MAGIC readout chain is schematically shown in Fig. 4.16. The PMTs are operated with negative high voltage at a gain of roughly 30,000 (inner PMTs) and 20,000 (outer PMTs). At the PMT base the signal is AC coupled to an ultra-fast preamplifier with a gain of about 6. The pre-amplified PMT signals are converted into light again using fast current driver amplifiers coupled to vertical cavity surface emitting laser diodes (VCSELs). The analog optical signal is then transmitted from the camera over 162m long optical fibers to the counting house. The conversion of the electrical signal back into an optical one has some advantages such as: a) minimizing the dispersion of the signal during the transmission over 162 m; b) no electromagnetic pickup; c) almost no signal at-

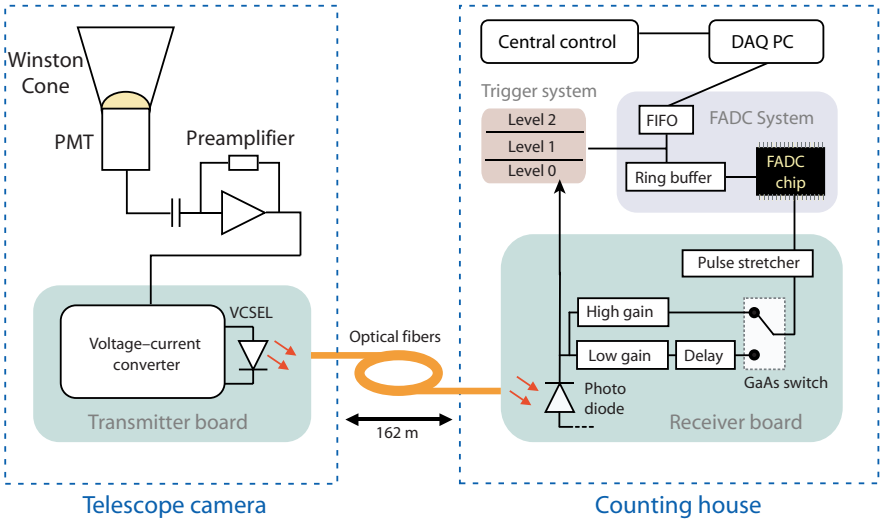

Figure 4.16: A flow diagram of the MAGIC readout chain. PMT signals are reconverted into optical pulses, sent to the counting house, where the pulses are digitized and, in case a trigger condition is fulfilled, recorded on disc.

tenuation; d) much lower weight than coaxial cables. The characteristics of the optical transmission system has been studied in detail by Paneque (2005).

A fast photodetector is one of the key elements to suppress NSB contribution to the measured signal. The PMTs are very well suited for this task [9] because of a low intrinsic noise and a possibility to provide analog signals with a duration of just ≈1–2 ns (FWHM). To make use of the fast PMT signals an equally fast digitalization system is required. The trigger and the digitalization are the next topic.

The signal receiver in the counting house, the trigger and the signal digitalization

The receiver. In the counting house, the optical signals are received and converted back to electrical ones by fast GaAs PIN diodes in the receiver board. After a further amplification, the electrical signals are split into two. One part of the signal routed to the trigger branch and the other part is routed to the amplitude digitalization system (see Fig. 4.16).

The trigger. The trigger decision is made based on three consecutive levels. Currently, only first two are in use.

[9] A disadvantage of the PMTs is a high rate of afterpulsing. An afterpulsing signal occurs in a PMT when an ion gets detached (from a PMT dynode or from restgas), travels back to the photocathode. There it kicks out many electrons through the photo-effect. The electrons then produce a huge signal, which is called afterpulsing. The effect is random and has a mean rate of 0.3 – 0.4% of the pixel rate. For a MAGIC pixel rate of 250 MHz (usual individual rate due to NSB) it corresponds to a rate of 1 MHz of big signals.

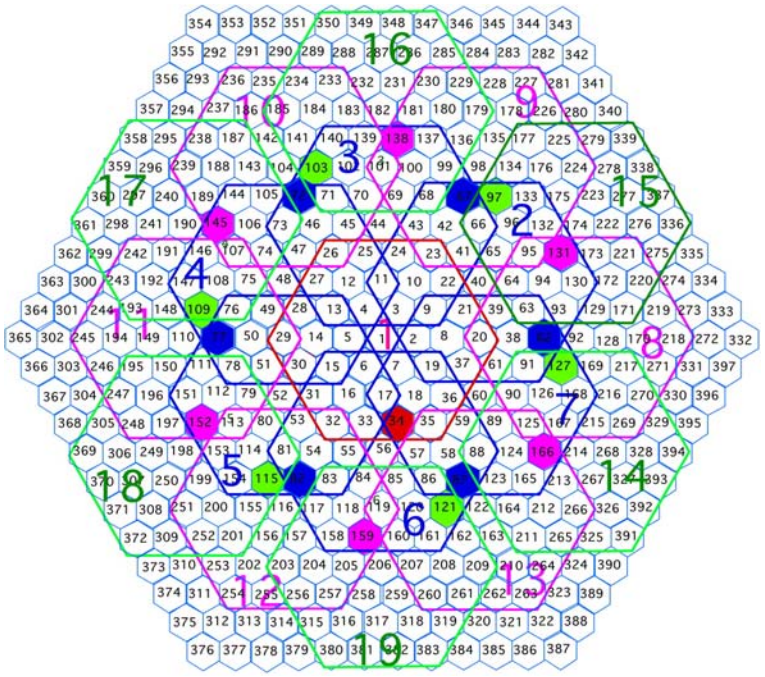

Figure 4.17: Sketch of the trigger topology in the MAGIC camera

- **Level 0:** discriminator level for individual pixels. A part of the analog signal from a camera pixel goes into a discriminator, which issues an approximately 6 ns long digital signal as soon as the amplitude of the input signal exceeds a certain level. The threshold is computer adjustable for each pixel individually in order to take into account different FoVs (in particular, pixels containing bright stars require a higher threshold) and different levels of the night sky brightness. A typical individual pixel rate is kept between 100 and 500 MHz. The effective trigger window is about 7 ns. The Level-0 trigger is restricted to only 325 inner pixels, which is about 1 degree radius from the camera center (pixels in the cells, see below, as shown in Fig. 4.17). Most images from the γ-ray-induced showers are within 1 degree radius from the sources position, thus the efficiency to trigger a γ-induced shower is above 90%. In the same time, those light flashes, which are mostly contained in the outer part of the camera and are not likely to be γ-ray induced, will not be triggered. In this way one can already separate γ-ray induced showers from background (hadron induced and NSB) triggers. However, this does not hold for extended γ-ray sources or for a γ-ray source, which is off center. This is the reason why the trigger region of the MAGIC II camera will be increased.

- **Level-1:** next neighbor coincidence. Since images from electromagnetic showers are compact, the next-neighbor coincidence is used. All signals

from the Level-0 are grouped into 19 overlapping cells of 36 pixels (see Fig. 4.17). Level-1 gives a trigger signal if for at least one of the cells a logical condition is fulfilled. Implemented logical conditions request a number of next neighbors (NN) in a close compact configuration to be above a threshold after the Level-0. Several options are available: 2NN, 3NN, 4NN, and 5NN. During normal operation, the 4NN condition is used leading to a trigger rate of about 200-250 Hz depending on the zenith angle in moonless nights.

- **Level-2:** higher level topological trigger. A further widely programmable logical trigger is based on the topology of an event that passed the Level-1 trigger. For example, one could discriminate images pointing to the source position from the ones pointing perpendicular to it. Up to now, the Level-2 trigger has not been used. There are no conclusive plans to use it either.

Digitalization of the fast signals. The PMT signals are digitized by a custom-made system of 8-bit, 300 MHz Flash-Analog-to-Digital-Converters (FADC). In order to increase the dynamical range of the system, the part of the signal going from the receiver to the FADCs is split again into two (see Fig. 4.16). One signal branch is amplified by a factor of ten, so-called "high-gain" signal. The other signal branch, so-called "low-gain" signal is delayed by roughly 55 ns. If the high-gain signal exceeds a certain amplitude (i.e. it is likely saturating the dynamical range), a GaAs switch is activated and the delayed low-gain signal is digitized. In this case the first half of the recorded information contains the clipped high-gain signal and the second half contains the low-gain signal. In case the high-gain signal does not exceed the threshold, all recorded information comes from the high-gain part.

Just before the digitalization the signal is shaped with a time constant of about 6 ns. The reason is that the FADC system is too slow to handle signals of 2 ns width coming from the camera. A typical duration of a signal in a given pixel after the shaper is about 6-7 ns. The shaped signals are sampled by the FADCs at a rate of 300 Ms/sec[10] and the digitized information is written to a ring buffer. After a trigger has been generated the digitalization is stopped and the corresponding part of the ring buffer is written to disk. 30 samples (slides) per event and per pixel are written to disk to ensure that even events with duration up to 10 ns are not truncated during the digitalization. The dead time introduced by the readout is about 25 μs. This is negligible compared to an averaged trigger rate of 250 Hz which corresponds to an event every 4 ms.

The rather low sampling rate of 300 Ms/sec requires additional pulse stretching to ensure proper sampling of the signal. The stretching in turn smoothes differences between the shapes of PMT signals coming from γ-rays, Cosmic rays, and NSB fluctuations. In order to better suppress the NSB contribution and to

[10]Ms/sec is mega sample per second, i.e. 10^6 samples per second

increase the sensitivity to the timing structure of the signals, an upgrade of the digitizing system by a 2 GigaSamples/sec MUX FADCs was performed in 2007. See Section 4.2.3 for more details.

Limitations of the trigger rate. The trigger rate of the MAGIC telescope is kept between 200 and 250 Hz, which corresponds to an energy threshold of ≈60 GeV for γ-rays at low zenith angle. Lowering individual Level-0 thresholds would enable to trigger on lower energies and, therefore, decrease the energy threshold. However, the trigger rate becomes unstable, and therefore, the performance of the telescope, too. The limiting factors are:

- Level of NSB. Lowering Level-0 thresholds increases probabilities that the 4NN condition is fulfilled just due to a NSB fluctuation. The trigger rate becomes very much weather, zenith angle, and sky field dependent. Setting the Level-0 thresholds to an even lower level causes an explosion of the rate to several kHz, i.e. more than 99% of the recorded events are just fluctuations of NSB. One solution to avoid it is a clever use of the topological trigger (Level-2) but there are no conclusive studies yet.

- Afterpulsing of the PMTs. Here the same applies as for the NSB level: lower Level-0 thresholds enable more triggers due to afterpulses. Experts even tend to believe that the afterpulsing has a major limitation power for the MAGIC performance.

- Data acquisition system. In principle, the DAQ can handle a rate up to 600 Hz. A higher rate causes instabilities, dead time, and crashes. For the DAQ, the main limitation is the writing speed to the disc. However, rates above 400-500 Hz are not desirable due to the first two limitations.

Each of the 577 PMTs provides photon information, which is used to reconstruct air showers. When talking about signals of PMTs it is common to use the term *pixel* instead of *channel* because it better describes imaging properties of the technique. It must be noted that the central pixel, which contains the signal from the PMT in the very center of the camera, is not included in the standard readout and analysis because it is reserved to perform optical observations. Such observations are very useful for a search for pulsed γ-ray emission from objects, which have a corresponding optical pulsation (Crab Nebula). The central pixel is used then to simultaneously determine the optical periodogram of a source (Lucarelli et al., 2007).

The calibration system

The electronic chain of the MAGIC telescope (from PMT to the FADC readout) has to be calibrated, i.e. one has to obtain calibration constants from the measured FADC counts to the physical quantity of photoelectrons as well as

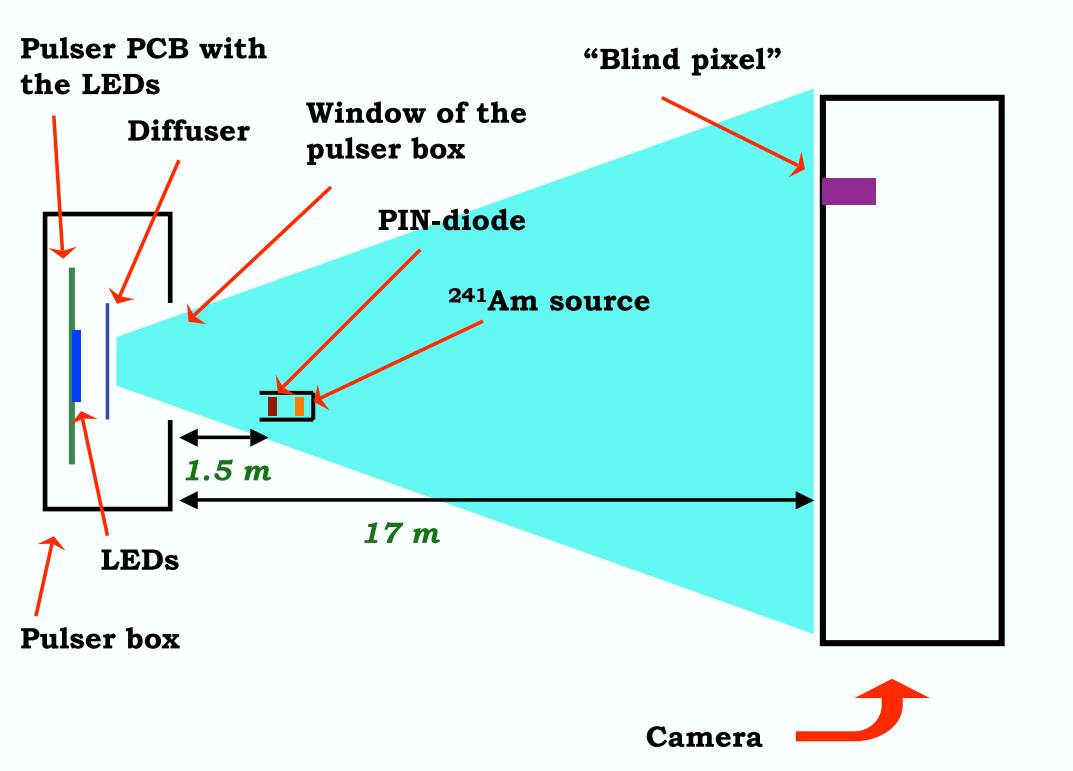

Figure 4.18: Components of the calibration system used in the MAGIC telescope.

conversion factors from the FADC timing into an absolute signal timing. The calibration system (Schweizer, 2002) for the MAGIC telescope is illustrated in Fig. 4.18. The main components of the calibration system are: a pulser box mounted in the middle of the mirror dish, a PIN diode mounted between the pulser box and the camera, and three blinded pixels in the camera. The pulser box houses LEDs, which provide fast light pulses in different wavelengths, different intensities and different frequencies of pulses, which can be controlled from the counting house. The pulsed light is used to make a relative calibration of the data chain using the F-factor method (described in Section 5.2). In addition, the pulser box has a continuos light source in four different colors to simulate star and moon light. The PIN diode and the three blinded pixels are used for absolute calibration of the MAGIC camera. The PIN diode is calibrated using a natural radioactivity of ^{241}Am. Details on the calibration system and used algorithms are described in Gaug (2006).

4.2.2 The data taking modes

Data taking with MAGIC is carried out during dark nights and favorable atmospheric conditions. It is not possible to take data with very bright optical objects in the FoV. Bright optical objects could be stars or planets with apparent magnitudes below 3. Bright objects cause high currents in the PMTs and would

damage them if the anode current is $> 100\,\mu$A. The duty cycle of MAGIC in dark nights is about 1000 h per year. This number is an average taking into account technical problems and bad weather periods. For an ideal case of perfect weather and no losses due to technical issues, the maximum would be 1600 h per year.

In addition to dark nights, MAGIC can take data during moderate moon shine avoiding direct moon light hitting directly or focussed by the reflector into the camera. MAGIC is currently the only operating IACT in the world, which takes data during moon shine. This currently increases the duty cycle of MAGIC by about 300 h per year[11]. It has to be noted, that the energy threshold is higher by up to a factor of 2 since the discriminator thresholds have to be increased to avoid too high trigger rate from NSB.

In order to ensure that none of the subsystems of the telescope is in danger, the following criteria must be fulfilled for any data taking procedure:

- Wind speed $< 40\,$km/h
- Humidity $< 90\%$
- Average PMT current $< 7\,\mu$A (mainly moon observations)
- Individual PMT current $< 20\,\mu$A
- Zenith angle $> 1.5°$

In addition, the weather is checked regularly for adverse atmospheric conditions like haze, dust, and clouds to ensure that the data are useful for analysis. Currently, two early warnings provide the tool to decide that the atmosphere is not clear enough in the FoV: i) the trigger rate is lower than expected and ii) the number of recognized stars by the starguider is lower than expected. In addition, the analyzers are encouraged to cross-check the optical transmission measurement of the atmosphere provided by the Carlsberg Meridian Telescope on a night-by-night basis[12], which is situated just a few 100 m from the MAGIC site.

In case the conditions are good and the above criteria are fulfilled, a standard data taking procedure is performed. It includes pedestal run, calibration run, and data runs as described below:

- **Pedestal runs (P).** These runs contain usually 1000 events, taken with random trigger and used to calculate the pedestal offsets for the calibration runs.
- **Calibration runs (C).** These runs contain usually 4096 events, taken with the standard calibration light pulses from 10 UV LEDs and the calibration

[11] theoretically, it should be possible to gain up to 500 to 600 h per year
[12] available online at http://www.ast.cam.ac.uk/∼ dwe/SRF/camc_extinction.html

trigger. It is used to calculate the conversion factors from FADC counts into the number of photo-electrons and the arrival time offsets.

- **Data runs (D).** These run contain usually 53521 events corresponding to a size of 1 GB disk space size. After the size of 1GB is reached, the next data run is started automatically with no dead time (FADC buffers are usually not emptied, which means dead time losses are avoided). The events are taken with the trigger criteria from the Level-1 as described above. In addition to cosmic events, interlaced calibration pulses, again 10 UV LEDs, are fired and recorded with a rate of 50 Hz. These calibration events are used to update the conversion factors and the arrival time offsets, which are initially calculated from the Calibration run.

For each source or a sky region, which is observed in a given night, the following sequence of runs is executed: P-C-D-D-...-D. The duration of the sequence is either as long as the sky direction is observed for or 1 h, whatever comes first.

MAGIC observation data are taken in one of the three following modes:

- So-called **ON mode**. The source is tracked by the telescope such that the source position is in the camera center.

- So-called **OFF mode**. In case ON-data are taken for a given source, usually dedicated OFF data are taken in addition in order to obtain reliable background data. For the OFF data, a sky region is selected and observed, which should have very similar stars in FoV and NSB brightness as the ON region. It is also important that the zenith and azimuth angle distributions are the same for the OFF and the ON data.

- So-called **WOBBLE mode**. Following good experience from the HEGRA CT system (Daum et al., 1997), MAGIC also accommodated the so-called WOBBLE tracking mode. In this mode, first proposed by Fomin et al. (1994) (illustrated in Fig. 4.19), two directions on opposite sides 0.4° away from the source, are tracked alternately for 20 minutes each, which provides a simultaneous measurement of signal and background. There is then *a priori* no need for additional OFF data. Details on the extraction of the background events from the Wobble mode data are described later in Section 5.10.

Currently, most MAGIC data are taken in WOBBLE mode. The advantages of the WOBBLE mode are:

- No extra time for observations in the OFF-mode.

- Optimal time coverage of the source activity, which is important for variable sources.

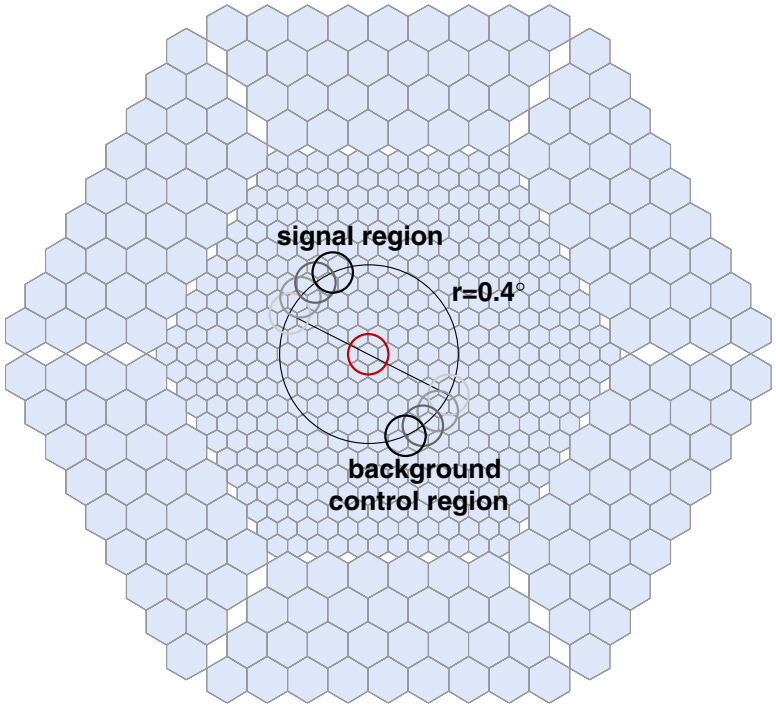

Figure 4.19: Observation modes. During ON-mode observations, the source is positioned in the center of the camera (red circle). For OFF-mode observation, a sky region is tracked without a γ-ray source in the field of view. During WOBBLE-mode observations, the source is placed at 0.4° off center (marked as "signal region"), rotating around the center following the apparent rotation of a sky field of view with time. In the WOBBLE mode, a background region can be defined at the opposite side of the signal region (marked as "background control region"), providing a simultaneous measurement of the background. Every 20 minutes the wobble position is changed, usually placing the γ-ray source on the opposite side of the camera center. More control regions can be defined along the circle around the camera center increasing the statistics of background data. Plot adapted from Wagner (2006).

- Simultaneous measurement of the background. This is considered to be the most important advantage compared to the ON-OFF mode because of:
  - Reduction of systematic effects due to different weather conditions (as this happens for the ON–OFF observations);
  - Reduction of systematic effects due to different NSB levels;
  - Averaging over systematic effects in the camera acceptance due to frequent wobbling between the wobble positions. See more details on the camera acceptance below;

There are as well some disadvantages of the WOBBLE mode:

- Because of the offset of the γ-ray source γ-ray trigger acceptance is reduced by 15–20% depending on the energy;
- In case of a variable source, some additional systematic flux uncertainty is introduced by changing the source position in the camera;
- In case the γ-ray signal extraction is needed for a short data sample (i.e. a data sample with only one WOBBLE pointing), the background determination has an additional uncertainty. The uncertainty is due to a hardware problem of the telescope: see below.

Camera inhomogeneity. The main critics about the WOBBLE mode observations emerges from the fact that the PMT camera has a high inhomogeneity: the event acceptance is not just a smooth function of the camera geometry and the trigger region. In Fig. 4.20 top panel, the distribution of triggered events from a Crab Nebula sample is shown. The distribution is clearly asymmetric and several deeps / holes are visible. On the right plot, the azimuth distribution of the same events is shown quantifying the inhomogeneity to be up to 30%. The inhomogeneity is thought to emerge from several effects:

- Dead pixels in the camera. Several pixels in the camera are dead: either the PMT is broken or the optical link is bad or the corresponding FADC channel is defect.
- Inefficiency of the trigger. Individual trigger cells (each consisting of 36 pixels) have different trigger rates, which might point to trigger inefficiencies.
- Insufficient flatfielding of the camera. Due to differences in PMTs (gain, quantum efficiency) and differences in the readout chain (optical transmitters, splitters, etc.) the HV setting has to be adjusted for each pixel individually to obtain the same signal at the trigger level.

However, the effect of the inhomogeneity is much less for the events after γ/hadron separation cuts (Fig. 4.20, bottom panel). The number and the strength of the deeps / holes is reduced, suggesting losses on a level of at most 20%. These losses have to be taken into account when calculating systematic uncertainties of the flux level for a γ-ray source.

A problem related to the camera inhomogeneity is that a background level determined for a camera region, which is different from the source region, might lead to an overestimation or an underestimation of the signal. In case of the ON–OFF data, the signal and background regions have the same camera coordinates, which avoids this problem. However, it is only true if the inhomogeneity pattern does not change in time between ON and OFF data samples. A possible workaround for the WOBBLE data is not to determine the background from a simultaneous data but from the next / previous WOBBLE position, thus using the

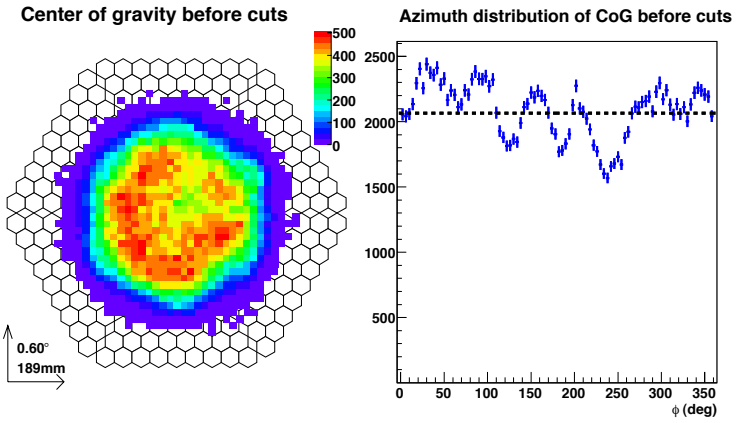

(a) events before cuts

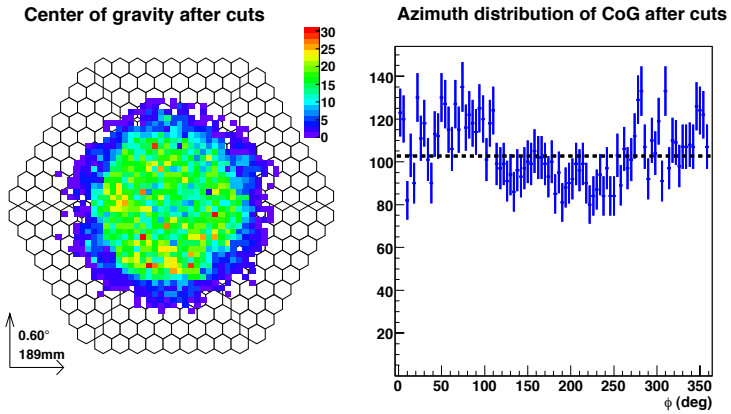

(b) events after cuts

Figure 4.20: The inhomogeneity of the MAGIC camera. *Top:* distribution of the triggered events before cuts. On the left: the distribution of the center of gravity of the events in camera coordinates. On the right: the same events as a function of an azimuth angle ϕ around the camera. The dashed line is a fit by a constant. Deviations up to 30% are clearly visible. *Bottom:* distribution of the events from the same sample after γ/hadron separation cuts. The deviations from the mean are reduced but are still on the level of 15–20%. A Crab Nebula sample is used for this study (Chapter 5), a minimum SIZE cut of 150 photoelectrons per event is applied.

same camera region for determining source events and background events. The averaging over the inhomogeneities also naturally happens for a long data sample in WOBBLE mode (several hours), for which the source and the background regions spend the same amount of time in the same camera regions.

My opinion is that using WOBBLE mode reduces the main systematic uncertainty, which emerges through differences in an ON-OFF sample due to i)weather conditions (high clouds, transparency of the atmosphere, etc.) and ii) telescope

performance. My experience in analysis of the data also showed that the match in image parameters for the WOBBLE data (comparing source and background regions) is usually better than in case of ON-OFF samples. The only serious disadvantage I see is the reduced trigger efficiency for γ-rays (due to a displacement of the source position so that 10-20% γ-rays are outside of the trigger region). The other disadvantage of the WOBBLE mode mentioned above, which arises with a very short data set in case of a high camera inhomogeneity, can be eliminated during the data analysis (software). For the MAGIC II telescope, the trigger area will be larger avoiding these losses. Before coming to a description of MAGIC II, which is being built right now, I will give a short report on the upgrade of the readout system of MAGIC I.

4.2.3 Upgrade of MAGIC I

As already described above, the analog signals are transfered via optical fibers to the trigger and FADC electronics. Until February 2007 a dual gain 300 MSamples/s 8-bit FADC system had been used. This rather low sampling rate required additional pulses stretching to ensure proper sampling of the signal. The γ-ray signals are very short and the PMT response time is very fast resulting in 2 ns pulses. A fast readout therefore allows one to minimize the integration time and thus to reduce the influence of the background from the LONS. In addition a precise measurement of the time structure of the gamma ray signal can help to reduce the background due to hadronic background events. The MAGIC collaboration has thus developed a new, affordable 2 GSamples/s readout system.

Fast FADCs are commercially available, but they are prohibitively expensive and power consuming to read out all the pixels of the MAGIC camera. To reduce the costs a new 2 GSamples/s read-out system has been developed and tested (Mirzoyan et al., 2002; Bartko et al., 2005). It uses a novel fiber-optic multiplexing technique. Multiplexing is possible as the signal duration (few ns) and the trigger frequency (typically 1 kHz) result in a very low duty cycle for the digitizer. The developed fiber-Optic Multiplexing (MUX) readout system uses a single 2 GSamples/s FADC to digitize 16 read-out channels consecutively. The MUX readout results in a cost reduction of about 85% compared to a solution of using one FADC per read-out channel.

Since the installation in February 2007 the MUX FADC system has been taking data smoothly (Goebel et al., 2007). A sustainable data acquisition rate of up to 100MBytes/s corresponding to a trigger rate of 1 kHz has been achieved. First results on the potential and performance of the MUX FADC system showed an increase of the sensitivity of the MAGIC telescope by up to 40% (Tescaro et al., 2007), which also includes a new analysis technique using the timing information. For this thesis, however, mostly older (digitized with 300 M Samples/s) data were used and no use of the MAGIC upgrade could be made.

4.3 MAGIC II

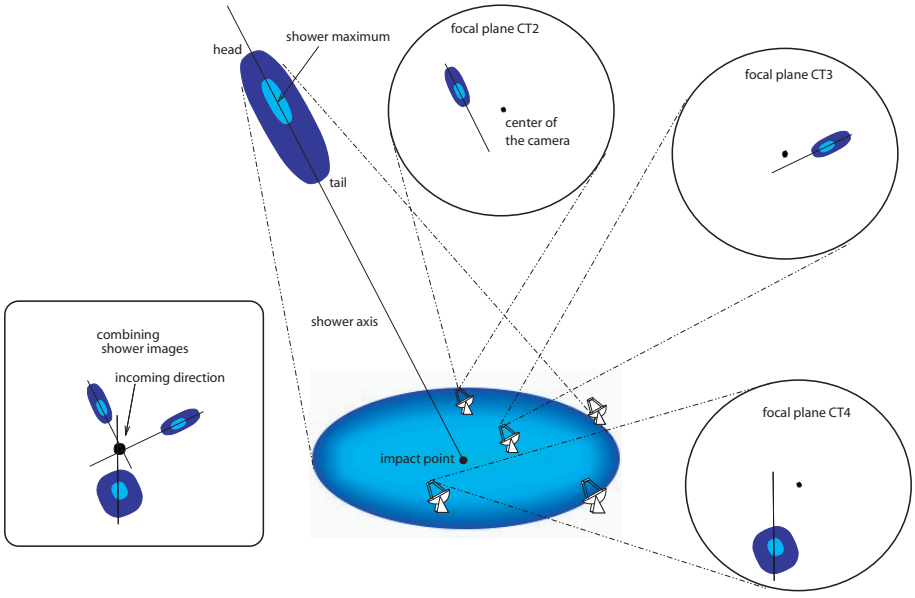

Figure 4.21: Sketch demonstrating a measuring principle of a stereoscopic system of 5 HEGRA telescopes. The orientation of the shower axis in the atmosphere can be unambiguously reconstructed through the intersection point of the main image axes of the images from the individual telescopes. Image adapted from Horns (2001).

The HEGRA collaboration used for the first time successfully imaging *stereo* observation of EAS (Daum et al., 1997). The principle of a stereo observation is to place several imaging telescopes in the light pool of an EAS and operate them as a system. That means e.g. that a trigger will only be created when at least two telescopes of the system have a certain signal over a threshold. In each of the telescopes inside of the light pool a shower image is recorded (see Fig. 4.21). One can then combine the recorded images to reconstruct the impact point of the shower, which improves the energy reconstruction significantly. The energy reconstruction as well as the γ/hadron separation profits from several recorded images of the shower instead of one image for a single telescope: multiple images reduce fluctuations and wrong reconstructions. In addition, the stereo technique helps to reduce the background arising from local muons[13] because the Cherenkov rings of muons would usually trigger just one telescope of the system. The MAGIC collaboration is currently building a second telescope in order to use the advantages of the stereoscopic observation mode (see Fig. 4.22 and Goebel (2007) for the status of the construction in July 2007).

[13]The local muons are usually difficult to reject in the analysis because they mimic γ-ray induced EAS.

Figure 4.22: Picture of MAGIC I (left) and MAGIC II (right) on La Palma in June 2007. Courtesy by Robert Wagner.

The MAGIC II telescope is placed 85 m from the MAGIC I telescope to the South–West (Fig. 4.22). The MAGIC II telescope looks quite similar to the MAGIC I but this is just a visual impression: many main hardware components will be different. To name most prominent upgrades:

- The mirrors will be 1^2 m (four times larger in area);
- The PMT camera will still have a FoV of 3.5° but will contain 1039 pixels, all of them with a small size (0.1°); this would increase sensitivity for sources located off-center as well as make an easier calibration of the PMTs. However, due to the coma aberration resulting from the parabolic mirror, the sensitivity remains reduced for a source located more than 0.5° off center.
- The PMT camera will be built such that it can be upgraded with HPDs (hybrid photodetectors) or silicon PMTs;
- The trigger region will be extended up to 1.2° radius; this is an advantage for the wobble mode observations, for a scan of a sky region with unknown source position as well as for extended sources.
- The readout electronics will use the so-called DOMINO chips, which are based on a switch capacitor array technology, allowing for a very fast readout speed up to 2.5 Gsamples/sec.

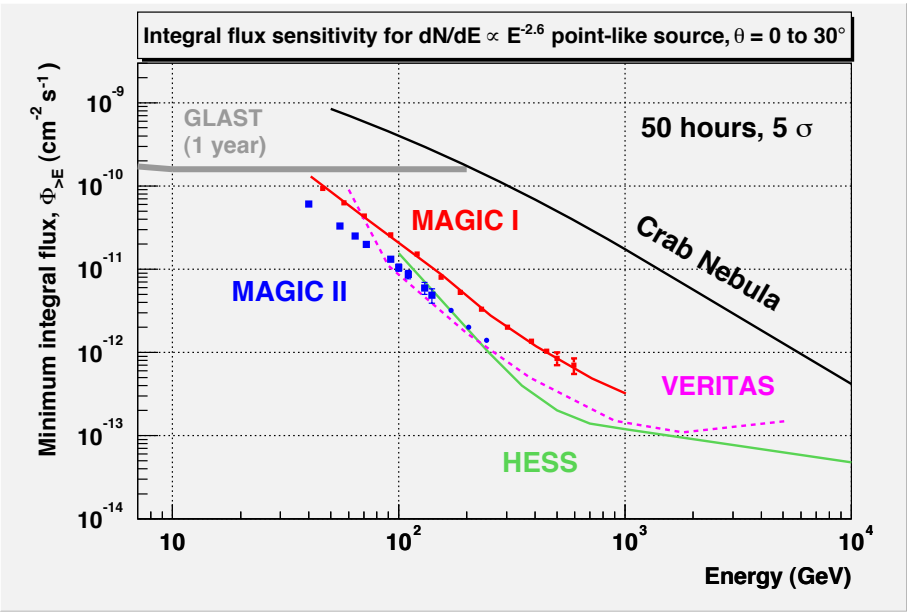

Figure 4.23: Sensitivity plot. Integral flux sensitivity for different experiments is shown at small zenith angles after 50 h of observation. The sensitivity of the GLAST satellite is shown after 1 year of observation. For comparison the Crab Nebula flux is indicated.

The calibration system will also be different from that of MAGIC I. Instead of LEDs as light emitters, a calibration system using a Nd:YAG nano laser is planned. The advantage of the nano laser system is that the width of the light pulses is below 1 ns, i.e. the pulses are shorter than the PMT pulses. The wavelength of the already purchased (from a company ALPHALAS, Goettingen, Germany) and tested Nd:YAG laser is 355 nm (the third harmonic). The lower harmonics (first harmonic with 1064 nm and second harmonic with 532 nm) are shielded to make the laser eye safe. The expected stability of the laser system is also higher than the one of the LED system. It is planned to build a temperature and humidity controlled calibration box with an integrated monitoring of the laser. In front of the laser, a remotely steerable filter wheel will be placed to select calibration pulses of different wavelength and different intensities. The pulse frequency of the laser can be varied remotely from 1 Hz to 200 Hz. In this way, the performance of the PMTs can be monitored much better and the signals can be calibrated with a higher accuracy.

The expected improvement in the sensitivity (compared to the current performance of MAGIC I) can be seen in Fig. 4.23 and is roughly a factor 2 at all energies. This is a consequence of the stereo observations, which become available with MAGIC II. Just to repeat the main advantages of the stereo observation mode: i) joint trigger possible, which would allow to reject local muons, one of the dominant backgrounds; ii) multiple images allowing to improve angular and

energy resolution; iii) direct unique reconstruction of the impact point of the shower. In addition, moon observations with a lower threshold become possible due to the telescope coincidence trigger, which suppresses accidental trigger due to NSB fluctuations.

MAGIC II is expected to see its first light in spring 2008.

Chapter 5

The Standard Analysis of MAGIC data

In this Chapter, I describe the tools and performance of the standard analysis chain for the MAGIC telescope. I contributed actively to the development of the standard analysis in the years 2004-2006, writing parts of the code, debugging and testing almost all of the analysis steps from the calibration of the data up to the calculation of the energy spectrum and light curves. In this Chapter, I present basic structure and the status of the standard analysis as of Summer 2006. At that time, some analysis parts, like producing sky maps, were not yet officially implemented as standard but I am already referring to them as being standard. The analysis of the VHE γ-ray sources, which I present in this thesis, was performed with the standard analysis. However, due to the development of the analysis tools during the time of the thesis, slightly different flavors of the analysis were used for different sources. Therefore, I refer in this Chapter to typical values of the cuts and the used selection criteria.

To demonstrate the techniques and the performance of the standard analysis, a set of Crab Nebula data is chosen. TeV γ-rays from the Crab Nebula were discovered by the Whipple collaboration in 1989 (Weekes, 1989). The Crab Nebula is currently the best studied steady TeV γ-ray emitter. It is located in our Galaxy at a distance of $\approx$2 kpc[1] from the Earth. The Crab Nebula is a supernova remnant with a very powerful pulsar (period of roughly 30 ms) as the central object of the explosion observed in 1054 AD. VHE γ-rays are believed to be produced in the Pulsar Wind Nebula, located at approximately 0.1 pc from the pulsar. The measured γ-ray spectrum extends from 80 GeV (Albert et al., 2007i) up to 80 TeV (Aharonian et al., 2000) and seems to be constant over the years (from 1990 to present). Only steady VHE γ-ray emission was detected so far with the IACTs, whereas a search of a pulsed component (expected to originate from the pulsar itself and measured by EGRET up to 10 GeV, Nolan et al. (1993)) resulted

[1] 1 pc (parsec) = 1 Parsec = 3.262 ly = 3.08610^{18} cm

only in upper limits. The stability and the strength of the measured steady γ-ray emission from the Crab Nebula made it to the "standard candle" of the TeV γ-ray astronomy.

The outline of the Chapter is as follows: After a short general introduction to the MARS software and to the analysis chain (Section 5.1), I will explain the calibration of the data in Section 5.2. The Crab Nebula data set and the corresponding Monte-Carlo data set are presented in Section 5.3 and Section 5.4, respectively. Details on the analysis steps such as image cleaning, γ–hadron separation, signal extraction, energy spectrum calculation, sky map reconstruction, and light curve calculation are given in Sections 5.5 to 5.15. Finally, in Section 5.16, the results of the standard analysis and systematic effects are discussed.

5.1 The MARS software and the analysis chain

There are three primary goals in every analysis for an IACT experiment:

1. Distinguish between γ–like and hadron–like events, the so-called γ–hadron separation.

2. Determine the primary γ-ray energy of the γ–like events, which would allow to derive an energy spectrum of a detected γ-ray source.

3. Precisely determine the incoming direction of the γ-like events. In fact, in case the position of the γ-ray emitter is known and its dimension is a point source for the telescope, the direction information can be used for a better γ–hadron separation and a more accurate energy determination.

The software package MARS (MAGIC Analysis and Reconstruction Software) has been developed to cover all signal processing steps, providing robust tools starting from the reading of uncompressed raw FADC data and extending to the calculation of energy spectra and light curves for detected γ-ray sources. The MARS software is written in C++ language and is based on the ROOT framework[2].

The MAGIC analysis chain is shown in a flow diagram in Fig. 5.1. The main steps of the analysis are:

- Calibration of FADC information for each pixel into number of photoelectrons (ph.e.), including timing information of the signal. The program is called `callisto`.

- Image cleaning removing pixels containing noise. Calculation of image parameters using survived pixels. The program is called `star`.

[2]an object oriented data analysis framework, `http://root.cern.ch`

- Training of γ/hadron matrices and training of energy estimation matrices. For the first one, a subsample of Monte-Carlo γ-events is used vs. a subsample of background events from the data. For the energy estimation, a subsample of Monte-Carlo γ-events is used. The program is called `osteria`.

- The γ/hadron matrices and the energy estimation matrices are applied to a test sample of Monte-Carlo γ-events, to background data, and to signal data. The program is called `melibea`.

- The effective on-time is determined from the data sample. γ/hadron separation cuts are applied to the data (signal and background). The number of excess events is determined. The effective area is determined from the corresponding Monte-Carlo γ-sample. The spectrum and light curves are determined in corresponding bins of estimated energy. The program is called `fluxlc`.

- The energy spectrum is unfolded taking into account the energy resolution of MAGIC and other analysis effects. The energy spectrum is bins of true energy is obtained. The program is called `unfolding`.

The analysis chain relies on Monte-Carlo (MC) simulated γ-ray events to resemble γ-ray excess in the MAGIC data. One has to rely on MC simulations because there is no natural or artificial calibrator of VHE γ-rays in the atmosphere. MC γ-rays are also used to calculate effective areas after all cuts, which is needed for the calculation of the energy spectrum and the light curve of a γ-ray source. Several studies have been done for MC - data comparison (Albert et al., 2007i; Otte and Majumdar, 2006). The agreement between parameter distributions of the excess events in case of a γ-ray source and MC γ-rays proved to be good. However, a reasonable agreement was not shown between MC hadrons and real background. It is widely believed that the disagreement has two reasons: i) not enough statistics of simulated hadronic showers and ii) a possible disagreement between simulated hadronic showers and real hadronic showers at energies below 200 GeV. As I mentioned before, MC hadrons are not used for the data analysis. To represent background, MAGIC data with no γ-ray source in the analyzed region are used. In case the source was observed in WOBBLE-mode, background data are extracted from the same field of view. In case the source was observed in ON-mode, extra OFF-mode data are necessary to represent the background. See Section 4.2.2 for the definition of the observation modes.

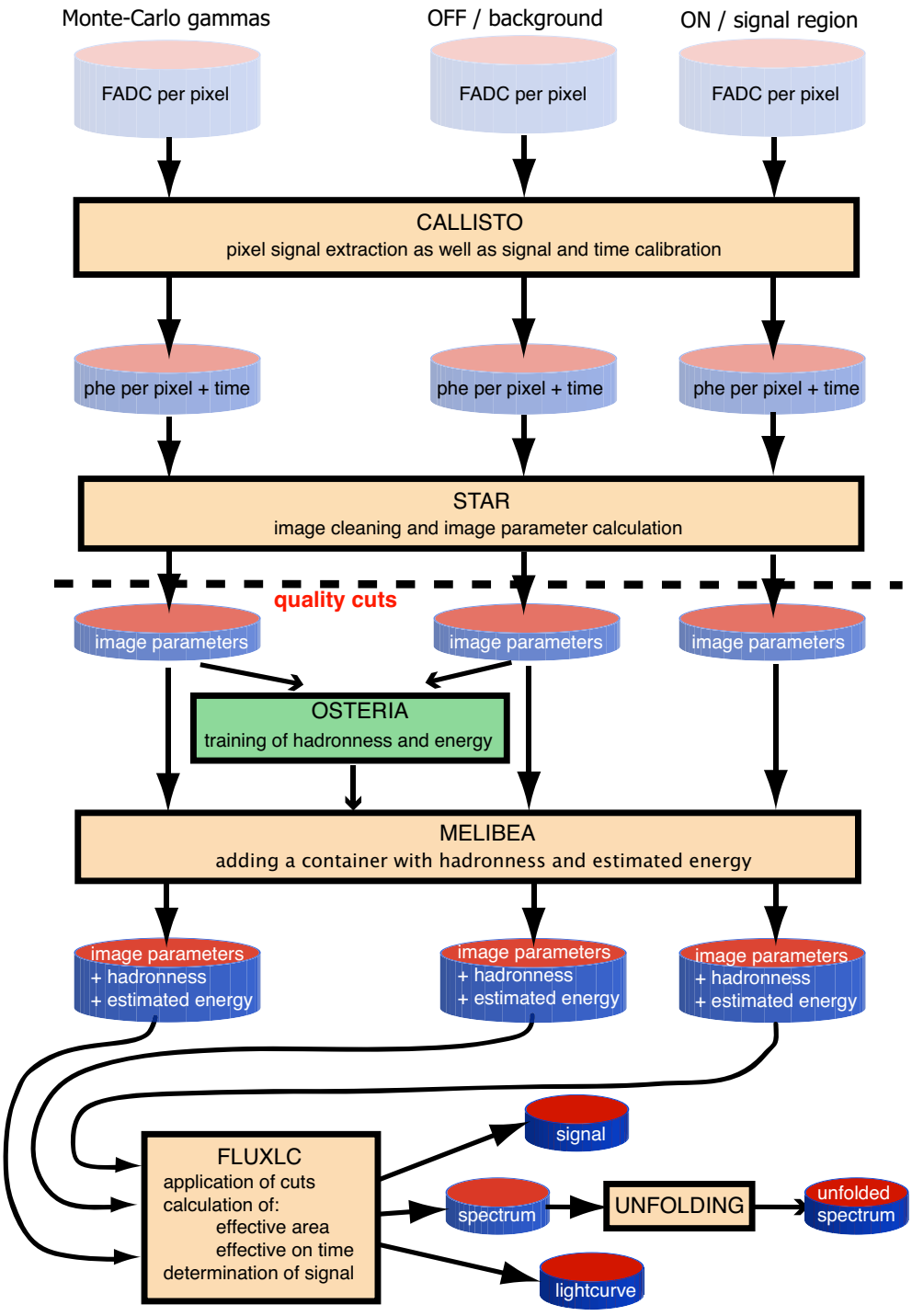

Figure 5.1: MARS analysis chain for data of the MAGIC telescope.

5.2 The calibration software

The signals from the camera pixels are digitized as described in Section 4.2.1. The calibration part of the software takes care to extract signals from the FADC slices and convert the extracted information back into number of photoelectrons (ph.e.). In the following, the signal extraction and the conversion procedure are briefly described.

Signal extraction. In order to discriminate the signals with low intensity from the light of the night sky, the highest possible signal to noise ratio, signal reconstruction resolution, and a small bias are important. After comparison between different extraction algorithms, it was shown that the digital filtering method (Bartko et al., 2005) is suited the best. The method can be used if the following assumptions are true:

- The normalized signal shape has to be always constant.
- The noise properties must be constant, especially independent of the signal amplitude.

The fact that the signals are shaped before the digitization with a large enough time constant of 6 ns makes sure that fluctuations are smoothed out and the first assumption is fulfilled. Also the second assumption is fulfilled: Signal and noise are independent and the measured pulse is the linear superposition of the signal and noise contributions. It was shown by Gaug (2006) that the systematic effect due to different noise levels is about 5%, which is just slightly higher than the statistical precision of the method 3%. See plots in Fig. 5.2 for charge and time resolution of the method.

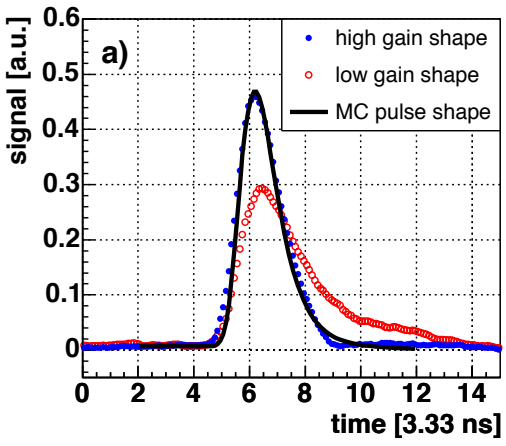

(a) signal shape

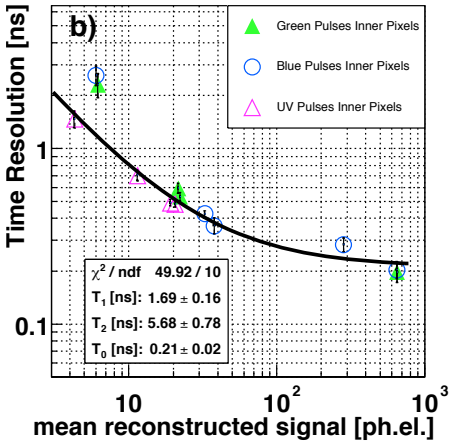

(b) Time resolution with the digital filter

Figure 5.2: Signal extraction with digital filter

Conversion to photoelectrons using the F-factor method The extracted signal amplitude is converted into the number of ph.e. in a pixel by using a proportional relation between both quantities. Several methods exist to extract the conversion factor of each pixel with help of special technical (calibration) runs. For the calibration of the data presented here the so called F-factor method (Mirzoyan and Lorenz, 1997) has been applied. The F-factor method works as follows: The number of generated ph.e. per calibration event is Poisson distributed, i.e. the distribution of the ph.e. has a mean of N ph.e. and a root mean square (RMS) of $\sqrt{N}$. Now, the measured quantity in FADC counts after pedestal subtraction, let us say Q, has a mean of $\overline{Q}$ and a RMS σ. The RMS σ is, however, wider than a pure Poissonian one. That means that the relative widths of the two distributions can be written as:

$$F\frac{1}{\sqrt{N}} = \frac{\sigma}{\overline{Q}} \tag{5.1}$$

The F-factor is introduced in equation 5.1 to account for the additional broadening of the measured distribution. The additional broadening is due to the multiplication process in the PMT and has to be individually quantified for each PMT in the laboratory. In principle, the transmission and amplification chain contributes in addition to the broadening of the measured distribution. This contribution, however, is negligibly small compared to the intrinsic F-factor of a PMT. In case of MAGIC, an averaged F-factor of 1.15 is used for all PMTs.

Since $\overline{Q}$ and σ are extracted quantities from calibration events and the F-factor is known, equation 5.1 can be used to calculate the average number of ph.e. of a calibration event and thus the conversion factor C:

$$C = \frac{N}{\overline{Q}} = F^2\frac{\overline{Q}}{\sigma^2} \tag{5.2}$$

Special calibration runs with 4096 events each are used to calculate the conversion factors. This number of events is enough to keep the relative statistical error of the calculation on a level of 1.5%. During the data taking of cosmic events, additional interlaced calibration light flashes are fired with a rate of 50 Hz in order to update the conversion factors. The derived (and constantly updated) conversion factors are then applied to the data events to obtain the number of ph.e. N_i from the measured number of FADC counts Q_i:

$$N_i = C \cdot Q_i \tag{5.3}$$

For more details on the calibration see (Gaug, 2006).

5.3 The data set of the Crab Nebula

The chosen data set refers to an observation of the Crab Nebula between 5th and 7th December 2005. The data were taken in the WOBBLE mode (see Sec-

tion 4.2.2) placing the source position 0.4° either side off the camera center. The weather conditions were good, which is also confirmed by the extinction measurements of the Carlsberg Meridian Telescope on La Palma[3]. The total observation time for this data set amounts to 1.72 hours, consisting of 53 minutes for one WOBBLE position and 50 minutes for the other WOBBLE position. The WOBBLE positions (pointings of the telescope, marked Wobble 1 and Wobble 2) were chosen to be on two opposite sides of the Crab Nebula location. The zenith angle distribution of the data spans over ∼15 degrees and is shown in Fig 5.3. The source position (Crab Nebula location) movement in camera coordinates is shown in Fig 5.4. Note that the trajectory is relatively short (for each WOBBLE position it spans two small camera pixels) because the source was tracked for just about 30 minutes per WOBBLE position at almost identical times on both nights.

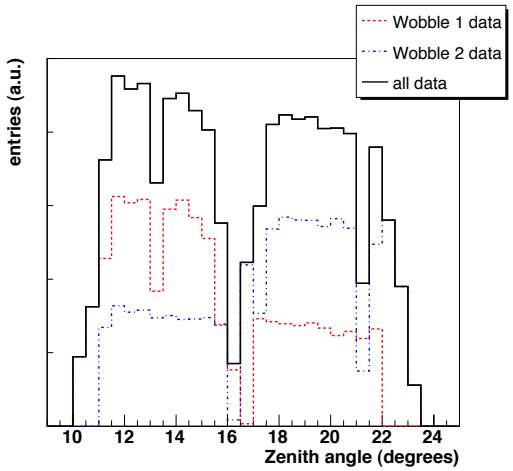

Figure 5.3: Zenith angle distribution of the Crab Nebula data sample.

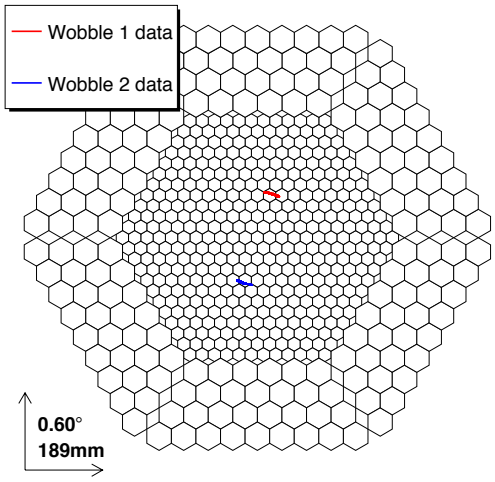

Figure 5.4: Source position during the observations of the Crab Nebula data set, in camera coordinates.

5.4 The Monte-Carlo γ-ray set

The Monte-Carlo (MC) simulation program for the MAGIC telescope is divided into three steps. Step 1: The development of γ-ray initiated air showers is simulated with CORSIKA 6.019 (Heck et al., 1998), using the US standard atmosphere. Cherenkov photons arriving on the ground around the telescope location

[3]extinction coefficients are available on the web: `http://www.ast.cam.ac.uk/~dwe/SRF/camc_extinction.html`

are stored in binary files containing all the relevant parameters (including wavelength). Step 2: The so-called `reflector` program accounts for the Cherenkov light absorption and scattering in the atmosphere (using the US standard atmosphere to compute the Rayleigh scattering as well as Mie-scattering losses using the Elterman model (Elterman, 1964) for the distribution of aerosols and ozone). The `reflector` program calculates then the reflection of the surviving photons on the mirror dish (composed of 964 tiles) to obtain their location and arrival time on the camera plane. Finally in step 3, the `camera` program simulates the behavior of the MAGIC photomultiplier camera, trigger system and data acquisition electronics. Realistic pulse shapes, noise levels and gain fluctuations obtained from the real MAGIC data have been implemented in the simulation. For more details on the `reflector` and the `camera` programs see in Majumdar et al. (2005).

To train γ/hadron separation cuts, both a representative background sample and a γ-ray sample are necessary. Hadron-induced showers are also simulated for the MAGIC telescope but are currently not used in the analysis. The main difficulty is the CPU time consumption to simulate a large number hadron-induced showers up to relatively high impact parameters of above 500 m, since even these showers can sometimes trigger the telescope. On the other hand, data taken with the MAGIC telescope are normally completely dominated by hadron-induced showers, resulting in a very good statistics of the real background data. Thus, instead of hadron-induced MC events, a subset of events from the real data is used in order to represent the background. Usually a randomly chosen subset of the same data is used to create a background sample. Thus one naturally takes into account the proper zenith angle distribution of the events and the actual level of the NSB during observation. In some cases, however, if the γ-ray signal is very strong, the data are too strongly contaminated by γ-events and the subset of the data cannot be used to represent the proper background. In this case, dedicated OFF data has to be taken for the background. OFF data are data taken with the MAGIC telescope on a sky position, where no γ-ray source is expected. For the Crab Nebula analysis, no OFF data have been used since the amount of γ-events in the data before cuts is less than 1%.

The zenith angle distribution of the γ-MC data is chosen to match the one of the recorded data set. For the particular Crab Nebula data, a range from 10 to 24 degrees was chosen. Due to technical reasons (limitation of computer power), the MC sample consists of two parts: The one sample originates from the standard MC production, with a γ-ray energy spectrum simulated according to a power law distribution with a photon index of 2.6, from 10 GeV to 30 TeV. The other sample originates from a so-called "high energy production" with a flat distribution in energy (photon index 0) from 300 GeV to 30TeV in order to compensate the lack of high energy data in the first sample.

5.5 Data selection and quality cuts

Data runs to be used in the analysis have to pass several quality checks. The main quality check is the trigger rate. I require a rate of 250 Hz ±15% at small zenith angles of observations. The trigger rate decreases with increasing zenith angle (ZA) because of the following. On the one hand, the detection area is increasing with increasing ZA of observation because the thickness of the atmosphere increases and a larger atmospheric volume can be see in the FoV of the telescope. On the other hand the fact that the atmosphere becomes thicker means that the showers are generated at larger distances so that less light reaches the telescope site. The combination of the two effects leads to a decreasing trigger rate with increasing ZA following an empirical relation:

$$rate = R_0 \cdot (\cos(ZA))^{0.5}, \tag{5.4}$$

where R_0 is the nominal trigger rate at zenith. A significantly lower trigger rate points to either worse weather conditions or hardware problems of the detector. A significantly higher trigger rate is normally due to an unusual increase of the background light, caused by bright stars in the field of view or by the presence of moon light (predictable), or by passing cars (unpredictable). Especially car light causes some problems by saturating many PMTs for several seconds. On the other hand, trigger rates have been found to vary by 10-15%, even for good and stable conditions due to different star fields being observed and a dynamical adjustment of the individual discriminator thresholds (see Subsection 4.2.1). Therefore, runs having a trigger rate deviating by more than ± 15% from the expected mean are removed from the analysis to assure good data quality.

The telescope performance is monitored by means of standard data quality checks, which are produced during an automatic on site analysis in La Palma on the day after the data was taken. Quantities like the optical point spread function of the telescope, the mean charge per pixel, the mean pedestal level, the mean pedestal RMS, and many other rather technical quantities are monitored and limits for a good data quality are defined (de los Reyes and Oya, 2006).

The weather is monitored by a weather station on site. The data on humidity (most critical), temperature, and wind speed are available and can be used in case some doubts on data quality arise. In addition, the very useful starguider information is added into the data stream, and the number of recognized stars in the field of view of the observation is stored every 10 seconds. The number of recognized stars (depending on a star field, typically about 20) is used to judge the integral transmission of the atmosphere. The atmospheric transmission is also monitored by the Carlsberg Meridian Telescope, which is located less than 1 km from the MAGIC site. However, these high precision data correspond to a single sky direction, which differs normally from the observation direction.

5.6 The pixel interpolation

Several pixels (usually around 10-15) cannot be calibrated. The reasons are usually malfunctioning hardware components like the PMT itself or the corresponding receiver or the FADC. Since signals of those pixels cannot be used in the analysis they are marked as *bad*. In order to minimize holes in the camera response, the following procedure is applied: in case a *bad* pixel has at least three properly working neighbor pixels, their signals are linearly interpolated and the result is used as the signal of the bad pixel.

5.7 The image cleaning

After removal of runs with unsuitable trigger rates and / or recognized hardware problems as well as bad weather, the *image cleaning* procedure is performed on the events. The idea is twofold: i) to remove for each event pixels containing presumably only noise from the NSB; and ii) to remove pixels containing signals from small tracks far outside the shower.

The calibrated data contain basically three numbers for each event per camera pixel:

1. The charge in photoelectrons in each pixel. This number is already pedestal subtracted, which means that the mean contribution of the mean level from the NSB has been subtracted from the measured signals.

2. Relative arrival time of the measured signal in FADC slices.

3. RMS of the NSB fluctuations per pixel. This number is updated every 500 events (corresponding to a frequency of roughly 0.2-0.5 Hz).

These three numbers are used to separate pixels containing signals from air showers from those pixels containing noise (dominated by the NSB fluctuations). This separation algorithm is called *image cleaning*. There are different image cleaning procedures to optimize the separation.

Extensive studies were made to find out the best image cleaning procedure for the MAGIC data (Tonello, 2006; Gaug, 2006; Otte, 2007). As a compromise between a low energy threshold of the analysis and its robustness, the following procedure was made standard. In the standard image cleaning, criteria to keep or reject a given pixel in an event depend only on the charge (in ph.e.) contained in the pixel. It is, therefore, called absolute image cleaning. The chosen selection criteria are: $Q_{core} \geq 10\,\text{ph.e.}$, $Q_{boundary} \geq 5\,\text{ph.e.}$, 1 boundary ring. The selection works as follows:

1. At first, the so-called *core pixels* are determined. These are pixels containing at least 10 ph.e. (i.e. $Q_{core} \geq 10\,\text{ph.e.}$) and have at least one neighboring

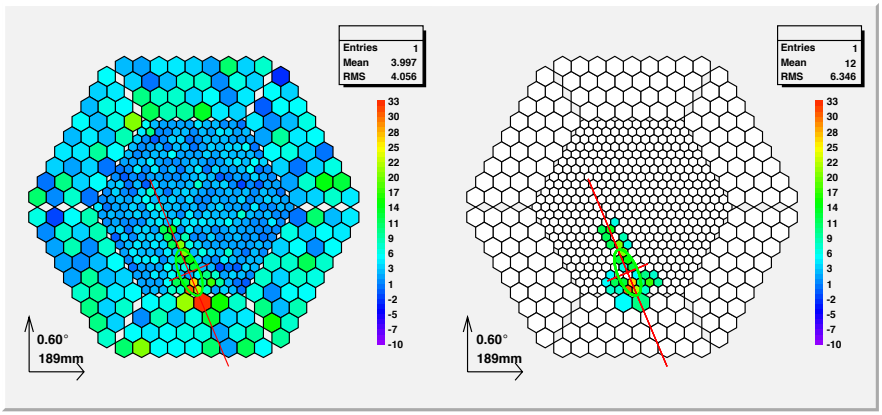

Figure 5.5: An event before (left) and after (right) the image cleaning procedure. An ellipse resulting after the calculation of the image parameters is also shown.

pixel fulfilling this condition, too. One event can have several isolated (spatially not connected) groups of core pixels.

2. In the next step, the so-called *boundary pixels* are determined. These are pixels, containing at least 5 ph.e. (i.e. $Q_{boundary} \geq 5\,\text{ph.e.}$) and have as a neighbor at least one core pixel.

3. The number of boundary rings is set to 1, i.e. all those being neither a core pixel nor a boundary pixel in the first boundary ring are removed from the event. In general, the number of rings n means that all pixels having charge Q, with $Q_{boundary} \leq Q \leq Q_{core}$, are defined as boundary and will survive the image cleaning in case their nth neighbor is a core pixel.

An image before and after image cleaning can be seen in Fig. 5.5. It has to be noted that after the image cleaning it is possible to have several isolated groups of pixels, which are called islands. The number of islands is a characteristics of an event and can be used later in the analysis. By default, the image parameters (next Section) are calculated using all pixels which survived the image cleaning, without taking into account a possible discontinuity between parts of the image.

5.8 The image parameters

The image remaining after the image cleaning should represent the light distribution from an EAS on the camera plane. Most of the classical image parameters (Hillas, 1985; Wittek, 2002) are defined as moments of this distribution, others are quantities suggested by differences in γ-ray- and hadron-induced images. In total, about 25 image parameters are calculated. Here, I present the most important ones, i.e. the ones which are later used for the γ/hadron separation and energy determination:

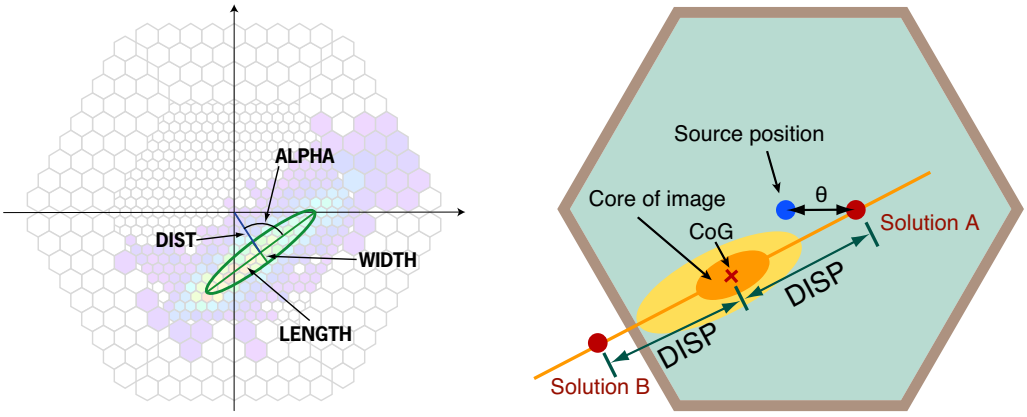

(a) image parameters (b) *Disp* and θ parameters

Figure 5.6: *Left*: Sketch demonstrating the definition of the main image parameters. Note that image parameters calculation is performed after the image cleaning. Sketch adopted from Otte (2007). *Right*: Sketch demonstrating the *Disp* and θ parameters. The *Disp* parameter leads to two estimated sky directions of the event (Solution A and Solution B). This ambiguity can be solved by a measurement of the asymmetry in the image along the main axis, i.e. determining the head and tail of the image. In the case here, Solution A is the correct one. The angle θ is between the estimated source position and the real one. In both sketches, the source position is in the camera center. The source position affects calculation of the parameters *Alpha*, *Dist*, and θ.

- *Size*: The total charge contained in the cleaned image. This parameter is roughly proportional to the energy of the primary γ-ray if the impact point of the shower is <120 m (see Fig. 5.7).
- CoG: the so-called center of gravity of the image. The CoG consists of a pair $(\overline{X}, \overline{Y})$, which is the position in the camera of the weighted mean signal along the X- and Y-axis, respectively. The $(\overline{X}, \overline{Y})$ pair are the 1st moments of the charge distribution in the image.
- *Length*: a 2nd moment, given by the RMS value along the major axis of the photon distribution. At fixed *Size*, the *Length* parameter is on the average smaller for γ-ray induced images than for hadron-induced and provides a strong separation power.
- *Width*[4]: the other 2nd moment, given by the RMS value along the minor axis. At fixed *Size*, the *Width* is also on the average smaller for γ-induced showers than for the major part of the hadron-induced cascades, due to a smaller average transverse momentum in the EAS development. The separation power of *Width* is also strong.

[4]Using *Length* and *Width* as vectors, one usually refers to an ellipse as an approximation for the image of an EAS.

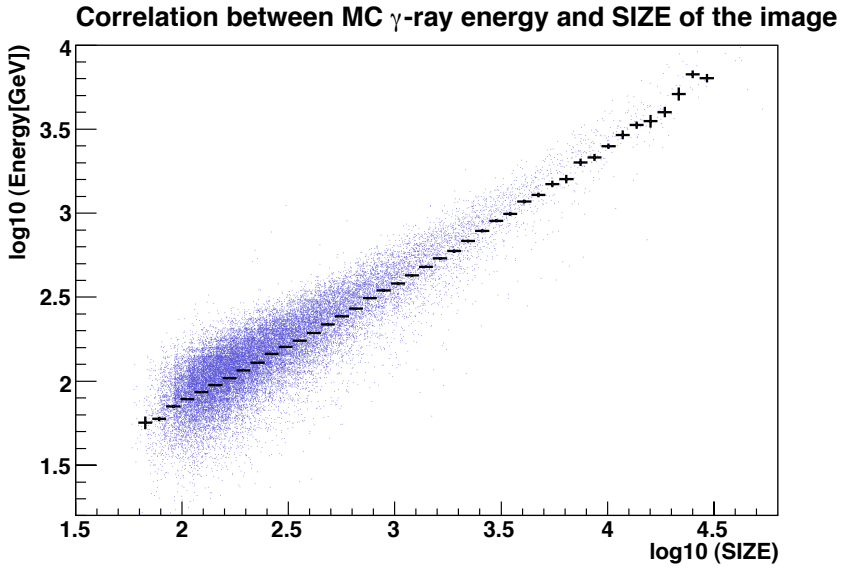

Figure 5.7: Correlation between the energy of the primary γ-rays and the *Size* parameter of the resulting images for MC γ-events. An upper cut of 120 m on the impact point of the showers is applied.

- $Conc(n)$ is a set of concentration parameters. $Conc(n)$ is defined as the ratio between the light contained in the n pixels with the strongest signal and the total light content of the image (*Size*). Images of γ-ray showers tend to be more concentrated than the hadron-induced showers. Thus, the $Conc(n)$ parameters provide an additional rejection power.

- $M3long$: this parameter corresponds to the 3rd moment of the light distribution in the image along its major axis and is a measure of the asymmetry in the signal distribution along this axis. For a typical shower, it is expected that the *head* of the image has a higher charge concentration than the *tail*. Thus, the $M3long$ parameter can be used to assign the side of the image which is closer to the incident particle direction. If the assignment is correct one reduces 50% of the background by keeping almost all γ-rays. For low *Size* values, however, $M3long$ is not well defined, and this parameter is not much of a help.

- LEAKAGE is defined as the fraction of light contained in the image pixels in the outermost ring of the camera. For images with LEAKAGE $> 10\%$, for example, the probability is high that a significant part of the image is outside of the camera and is not recorded. This means that the images are probably truncated. Especially for γ-ray energies above 2–3 TeV the fraction of truncated events is rather large. The energy estimation is unreliable for significantly truncated images and the LEAKAGE parameter is used to

reject these events from the analysis.

- *Dist*: the angular distance between the CoG of the image and the expected source position in the camera. The *Dist* parameter can only be calculated if the source position is known. The *Dist* parameter is correlated with the impact parameter of the EAS. Using *Dist* the accuracy of the energy estimation can be improved.

- *Alpha*: it is the angle between the major axis of the image and the line connecting the CoG of the image with the source position in the camera. Like *Dist*, *Alpha* can only be calculated if the source position is known. For γ-ray showers, their images point to the source location in the camera. Hence, the *Alpha* parameter of γ-rays is expected to have predominantly small values. On the other hand, hadron showers are distributed isotropically in the sky implying a flat *Alpha* distribution.[5] Therefore, *Alpha* is one of the most powerful discrimination parameters.

- θ^2: θ is the angular distance between the real source position and the estimated source position of the event (see the right sketch in Fig. 5.6). The estimated source position is obtained using the *Disp* method (Lessard et al., 2001; Domingo-Santamaría et al., 2005). In the *Disp* method this sky direction is estimated from the image parameters assuming that the source (or the incoming direction of the primary particle) lies on the major image axis. This is plausible because the major axis is a projection of the shower axis onto the camera. The axis coincides in good approximation with the trajectory of the incident γ-ray. The *Disp* algorithm has been optimized using a MC γ-ray sample. A *Disp* parametrization is a function of all image parameters described above except of *Conc* and *Dist*. There is an important degeneracy in the *Disp* method: there are two solutions for a source location along the major image axis (see the right sketch in Fig. 5.6). The *M3long* parameter is used to judge which of these solutions is the correct one placing the source position closer to the *head* of the image. In case of γ-rays, the estimated sky direction of the showers will be close to the direction of the γ-ray source, whereas for hadrons these directions are isotropically distributed. For convenience, one uses the squared quantity θ^2 because the distribution of θ^2 values is flat for background events and has an exponential shape for a γ-ray signal peaking at $\theta^2 = 0\,deg^2$.

The distributions of some of the above parameters are shown in Fig. 5.8. MC γ-ray showers are compared to data events which are mostly hadron showers. *Width*, *Length* and *Alpha* are plotted as a function of *Size* to show the *Size* dependence of these image parameters. While at large *Size* values the differences

[5] Due to the trigger region geometry, the *Alpha* distribution for background is not perfectly flat. This also holds for the background *Alpha* distribution after cuts.

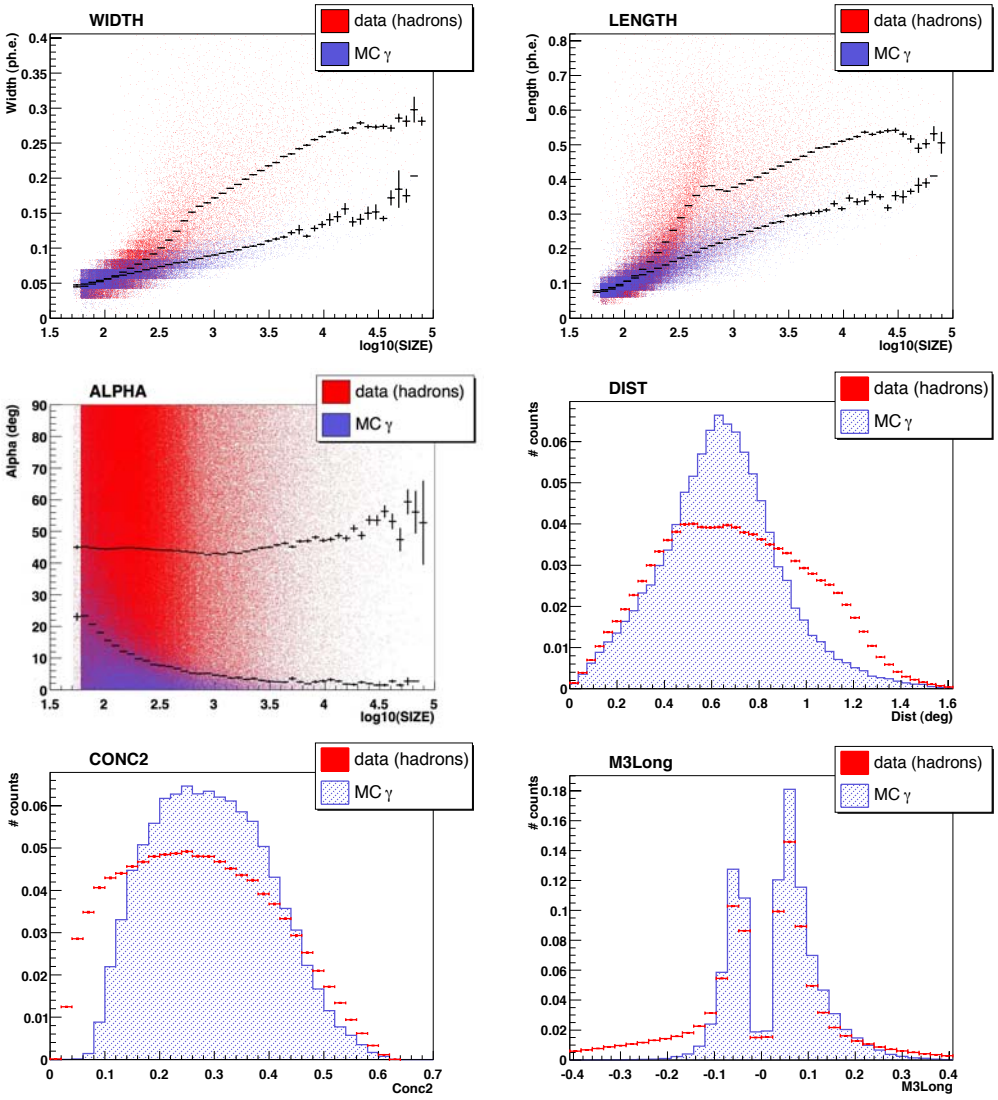

Figure 5.8: Image parameters. In case of *Width*, *Length* and *Alpha*, the dependence of these parameters on *Size* is shown. Black crosses mark the position and error of the mean of the parameter in each *Size* bin. It is also evident that with decreasing *Size* the differences between hadrons and γ-rays vanish.

between the distribution of γ-rays and hadrons are evident, they start to fade away at about 200 ph.e. ($\log10(Size)$=2.3) and finally vanish at about 120 – 150 ph.e. *Alpha* seems the only parameter with a rejection power even below 150 ph.e.

Some cuts (the so-called filter cuts) are applied just after the calculation of the image parameters. Those cuts are called filter cuts and remove images, which are most likely not produced by air showers. In particular, images due to car flashes and the so-called spark events are removed. Spark events are believed to be images originating from a discharge on the PMT surface. The light reflected from the plexiglass can trigger the readout of the camera if seen by a group of pixels. The resulting images contain a lot of light (several pixels are completely saturated) in just a few pixels and are easily distinguished from the usual events. The rate of spark events is 1–2 Hz and is not associated to a particular camera region. The filter cuts have already been applied for the distributions in Fig. 5.8.

5.9 γ-Hadron separation

Data of IACTs are usually dominated by background events. Even for a strong VHE γ-ray emitter such as the Crab Nebula, the ratio before cuts between γ-induced and background events is $\approx$ 1:1000. The signal to noise ratio is so small that a detection of a γ-ray source becomes impossible. In order to obtain a sensitive measurement of a VHE γ-ray source, a very effective hadron suppression in the data is necessary by keeping a large amount of γ-ray events. This suppression is called γ/hadron separation.

For the γ/hadron separation a multidimensional classification technique based on the Random Forest method (Breiman, 2001; Bock et al., 2004; Hengstebeck, 2007) is used. The Random Forest method uses training samples to find a set of classification trees in the space of image parameters. The training sample representing γ-showers are MC generated γ-showers. The training sample representing the background is constructed by selecting randomly events from the experimental data. The final classification, expressed as a number called $Hadronness$, is defined as the mean classification from all trees. The $Hadronness$ values span a range between 0 and 1 and characterize the images being less or more hadron-like, respectively. One can also say that $Hadronness$ is a measure for the probability that the event is a hadron.

The set of the image parameters as input parameters for the Random Forest depends on whether the source dependent or source independent approach is used to extract the signal. I use the so-called *Alpha* approach, i.e. the *Alpha* parameter is used to extract the signal, in combination with the source dependent approach. I use the so-called θ^2 approach, i.e. the θ^2 parameter is used to extract the signal, in combination with the source independent approach. In the case of the *Alpha* approach, the following parameters are used for the training of the

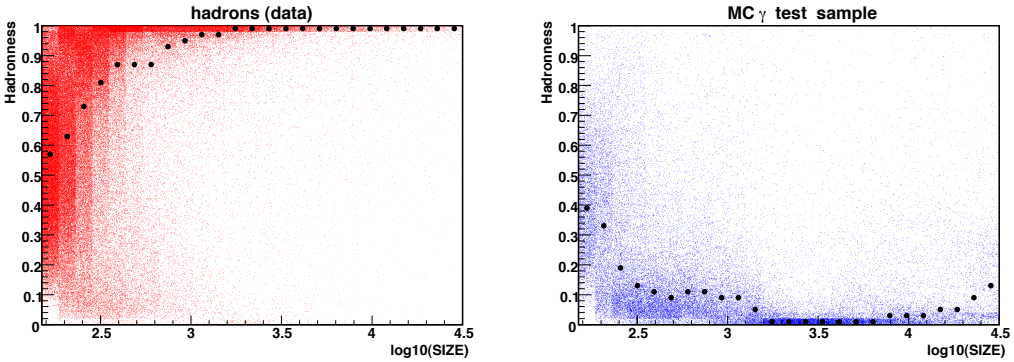

Figure 5.9: *Hadronness* distribution of data, and MC γ-events from the test sample. The *Hadronness* is obtained for the θ^2 approach, i.e. without using source dependent parameters. Overlaid on top are the mean *Hadronness* values for each bin in *Size* (black circles).

Random Forest: *Width*, *Length*, *Dist*, *Conc*2, *M3long*, and *Size*.

In the case of the θ^2 approach, the background level is estimated using different regions of the camera. In this particular implementation, source position dependent parameters (*Alpha*, *Dist*) are not used in the Random Forest. This is done in order to keep the camera acceptance for the background events as flat as possible, i.e. to avoid preferential camera regions. In this analysis, the image shape parameters *Width*, *Length*, *Conc*2, and *Size* are used as input parameters.

The distribution of the *Hadronness* parameter for a sample of experimental data and for MC-γtest sample is shown in Fig. 5.9. The MC-γtest sample is chosen statistically independent from the sample used in the training of the Random Forest. This *Hadronness* distribution is obtained for the θ^2 approach, i.e. without using source dependent parameters. Hadronness values close to 1 mean that an event is hadron-like, *Hadronness* values close to 0 mean that an event is γ-like. Since the data are very much dominated by hadrons, the left plot is representative for a background sample. One can clearly see that above 300 ph.e. ($\log10(Size) > 2.5$) the Random Forest nicely recognizes γ-events as such. However, for *Size* values below 300 ph.e. the identification is not very successful. Still, some separation using the *Hadronness* variable is possible between 150 and 300 ph.e. because most of the hadron events are assigned by *Hadronness* ¿ 0.5 whereas γ-events have lower *Hadronness* values. In fact, the orientation of the image (*Alpha* or θ^2), which is not contained in the *Hadronness*, provides the strongest background suppression at these *Size* values. Below *Size* values of 150 ph.e. the separation breaks down. Thus, an *a priori* lower *Size* cut of 150 ph.e. is applied to the data and MC events.

The *Hadronness* parametrization is optimized for each data set separately. The γ/hadron separation is then performed by applying a cut in the *Hadronness* parameter, while the cut is chosen such that the overall cut efficiency for MC γ

events is not less than about 50%. The corresponding hadron suppression is about 90-99%, improving with increasing *Size* of the events. The performance of the γ-hadron separation can then be judged in the subsequent step of the signal extraction (next Subsection).

Alternative γ/hadron separation methods like a combination of simple cuts on scaled image parameters (Daum et al., 1997; Riegel et al., 2005a), SuperCuts optimization (Reynolds et al., 1993; Kranich, 2002; Paneque et al., 2004) and neural networks (Zimmermann, 2005) were also developed for the analysis and they yield similar results to the ones of the Random Forest. An advantage of the Random Forest is a relatively simple handling and low CPU times. Since the alternative methods developed so far were not found to perform superior to the Random Forest, the latter one is used.

5.10 The signal extraction

After applying *Hadronness* cuts (or any other parameter or parameter combination to select γ-like images), one can extract a possible signal. I am presenting here two different approaches to extract the signal: the so-called *Alpha* and the θ^2 approach. For each of them, the following five-step procedure is applied:

1. Definition of a source region, where a γ-ray signal is expected (signal region);
2. Counting events in the signal region (N_{on});
3. Determining the number of expected background events in the signal region (N_{bg});
4. Determining the number of excess events in the signal region ($N_{excess} = N_{on} - N_{bg}$)
5. Determining the significance of the number of N_{excess}.

The *Hadronness* cut and the size of the signal region are usually optimized on the basis of MC γ-showers. Alternatively, one optimizes the cuts on an independent data sample containing strong γ-ray signal. In this analysis, MC γ-showers were used for the optimization. One distinguishes between so-called *tight* and so-called *loose* cuts. Tight cuts are obtained by optimizing on the best significance of the signal with an addition requirement of a minimum number of γ-events after cuts. Tight cuts are usually applied when searching for new VHE γ-ray emitters. Loose cuts are obtained by widening tight cuts until the significance of the signal drops by more than $\approx$20%. In this way, one gains statistics of the signal without loosing much on the sensitivity. Loose cuts are usually applied to determine the energy spectrum and the light curve of already established γ-ray signals. The size of the signal regions is *Size* (or energy) dependent since *Alpha* and θ^2 are much better

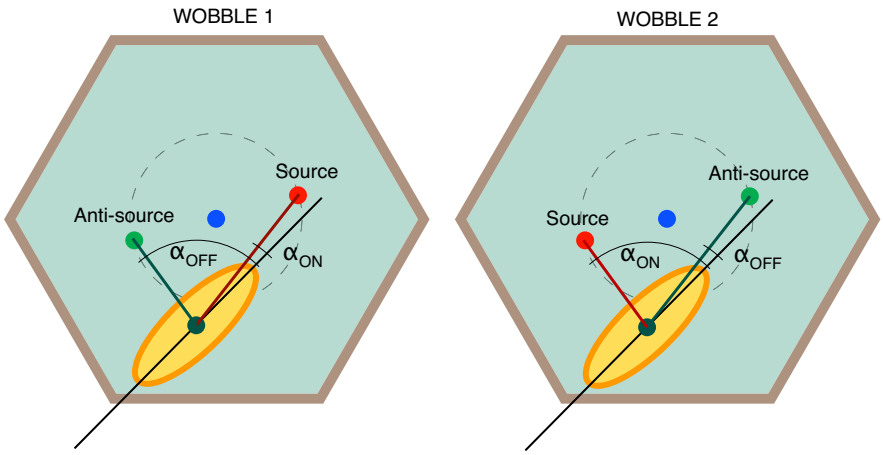

Figure 5.10: Sketch of the signal (Source) and background (Anti-source) regions for the *Alpha*-approach. The image in the WOBBLE 1 data set (left sketch) will be included in the ON-Alpha plot. The event will be excluded from the OFF-Alpha plot because the angle $\alpha_{\rm on} < (\alpha_0 = 10^\circ)$. The image in the WOBBLE 2 data set (right sketch) will be included in the OFF-Alpha plot. The event will be excluded from the ON-Alpha plot because the angle $\alpha_{\rm off} < (\alpha_0 = 10^\circ)$.

defined for higher *Size* values. The acceptance for the MC γ-rays after all cuts is about 40–50% and 70–80% for the tight and loose cuts, respectively.

5.10.1 *Alpha* approach

Definition of ON and OFF regions: In the case of the *Alpha* approach, the signal region is defined in the *Alpha* variable. The ON region is centered at the source position. For the WOBBLE mode data, the OFF region is centered at a position opposite to the source in respect to the camera center. This is the so-called anti-source position. See the sketch in Fig. 5.10 illustrating the source and anti-source positions. The γ-like events from a known source position are expected to have small *Alpha* values. For events with *Size* > 200 ph.e. the signal region in the *Alpha* plot is usually defined as $0 < Alpha < 4$ degrees for tight cuts and $0 < Alpha < 15$ - 20 degrees for loose cuts. An *Alpha* plot for the Crab Nebula data set is shown in Fig. 5.11. A minimum *Size* cut of 320 ph.e. was applied to maximize the sensitivity for this type of presentation. A hadronness cut of $Hadronness<0.17$ has been used. γ-like events with image parameters calculated with respect to the source position are shown by the red crosses (the so-called ON-Alpha plot). The background distribution (the so-called OFF-Alpha plot) is constructed for *Alpha* values calculated with respect to a position, which is on the opposite side of the camera than the source position (anti-source position, OFF plot, shown by the grey filled histogram in Fig. 5.11.). Both distributions, ON and OFF-Alpha plot, are highly correlated since they contain the same events. In

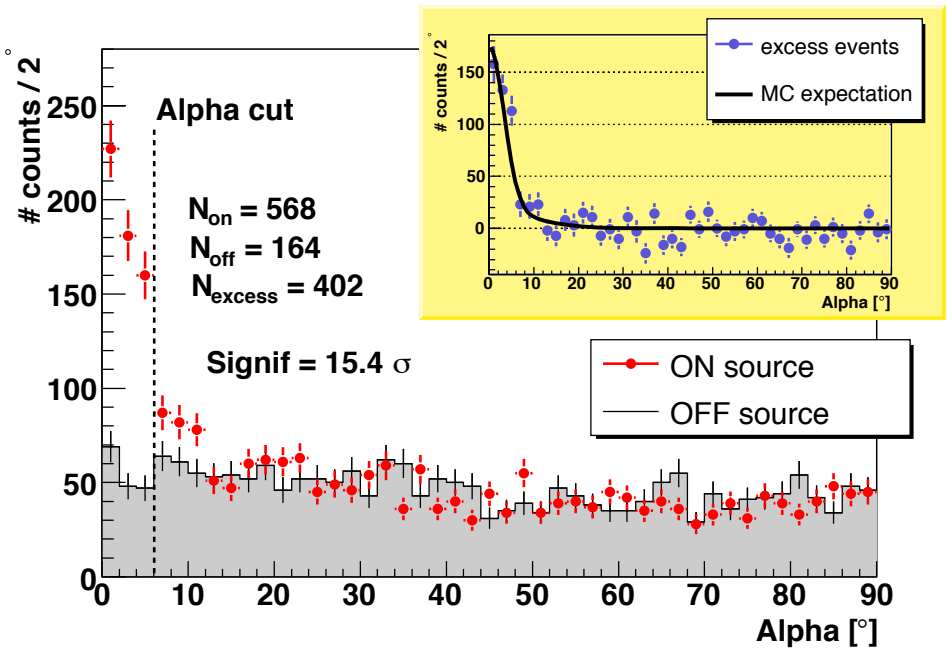

Figure 5.11: *Alpha* plot with cuts: *Size*>320 ph.e. and *Hadronness* < 0.17. Resulting *Alpha* plots for the source position (ON-Alpha plot, red crosses) and for the opposite position in the camera (OFF-Alpha plot, grey histogram) are shown. Applying a cut of *Alpha* = 6° one obtains a significance of 15.4 σ. See text for more explanation. *Insert: Alpha* plot of excess events is shown (blue crosses) overlaid with the MC expectation for a point source (black line).

order to avoid an unwanted contribution from γ-events in the OFF sample and to guarantee the statistical independence between the ON and the OFF samples in the signal region, the following procedure is applied (see Fig. 5.10 for the sketch): events with $Alpha_{\rm ON} < \alpha_0$ (with $Alpha_{\rm ON}$ calculated with respect to the source position) are excluded from the OFF sample, and events with $Alpha_{\rm OFF} < \alpha_0$ (with $Alpha_{\rm OFF}$ calculated with respect to the anti-source position) are excluded from the ON sample. This cut is called *anti-alpha cut*. In the example of the left sketch in Fig. 5.10, the event will be included in the ON-Alpha plot but it will be excluded from the OFF-Alpha plot because the angle $\alpha_{\rm on} < (\alpha_0 = 10°)$. Analogous in the example of the right sketch in Fig. 5.10, the event will be included in the OFF-Alpha plot but it will be excluded from the ON-Alpha plot because the angle $\alpha_{\rm off} < (\alpha_0 = 10°)$. The anti-alpha cut assures that the *Alpha* distributions for ON and OFF events are statistically independent for $Alpha < \alpha_0$.

In order to demonstrate the sensitivity of the analysis, tight cuts are applied to the data set (Fig. 5.11). The anti-alpha cut of $\alpha_0 = 10°$ is also applied, i.e the *Alpha* distributions (ON and OFF) are uncorrelated for $0 < Alpha < 10$ degrees. The difference between ON and OFF *Alpha* plots gives the distribution of excess events and is shown in the insert of Fig. 5.11 (blue points). The excess

distribution is overlaid with the MC γ-ray prediction for a point source (black curve) and agrees with it well. The width of the *Alpha* distribution for MC γ-ray is roughly 3 deg, calculated by a Gaussian fit to the distribution:

$$f(Alpha) \propto \exp\left(-\frac{Alpha^2}{2\sigma^2}\right) \tag{5.5}$$

Significance: The signal region in the *Alpha* plot is chosen to be 6 degrees (marked by a vertical dashed line), corresponding to 70% MC γ-acceptance after cuts. The number of ON events (N_{on}) in the signal region is 568, and the number of expected background events (N_{bg}) is 164. The significance of the signal is calculated using an assumption that both *Alpha* distributions (ON and OFF) have a Poissonian distribution. Then we can calculate the probability that the observed excess is due to a background fluctuation (null hypothesis). This probability can be then converted into a number of standard deviations S for the null hypothesis to be true. Obtaining, for example, for a signal a significance of $S = 3\sigma$ means that a signal, which is as high or higher than the observed one, has a probability of $(100\% - 99.73\%) = 0.27\%$ to be due to a background fluctuation. In the particular case of ON and OFF data samples, we use formula 17 from Li and Ma (1983):

$$S = \sqrt{2}\left(N_{on}\ln\left[\frac{1+\alpha}{\alpha}\left(\frac{N_{on}}{N_{on}+N_{off}}\right)\right] + N_{off}\ln\left[(1+\alpha)\left(\frac{N_{off}}{N_{on}+N_{off}}\right)\right]\right)^{1/2} \tag{5.6}$$

The N_{on} and N_{off} are the numbers of ON and OFF events in the signal region, respectively. The $\alpha = t_{on}/t_{off}$ is the ratio between the effective on-time of the ON and the OFF samples, implying that $N_{bg} = \alpha \cdot N_{off}$. It can be seen from Formula 5.6 the smaller the value of α the higher the obtained significance by the same numbers N_{on} and N_{bg}. The reason for this is that a small α value means a higher statistics on the background and, therefore, a better knowledge of the expected background level in the source region. Thus, a smaller α value makes an analysis more sensitive. In the particular case of the WOBBLE-mode data and the *Alpha* approach, $\alpha = 1$.

Sensitivity: The analysis can also be quantified in terms of its sensitivity. A common sensitivity unit for the different IACTs is the flux, which will be measured with 5σ in 50 hours of observation. This number is normally used to compare different experiments and their potential to detect weak fluxes. It is, however, not common to use Formula 5.6 to compute the sensitivity but instead a Gaussian approximation of it. The resulting number of standard deviations for a given observation time is then:

$$Sens(t) = \frac{N_{ex}}{\sqrt{N_{bg}}} \cdot \sqrt{\frac{\mathrm{t}}{\mathrm{T}}} \tag{5.7}$$

where $N_{ex} = N_{on} - N_{bg}$ is the number of excess events, T is the observation time, and t is the normalization time. I want to stress that this definition does not take into account fluctuations of the uncertainty of the mean number of the background events and gives, therefore, an optimistic sensitivity. Moreover, formula 5.7 overestimates stronger the sensitivity of an experiment with a poorer background estimation compared to an experiment with a better background estimation. In the particular case of the analysis presented here, the observation time T = 1.7 h, and one obtains $Sens(t = 1\,h) = \frac{404}{\sqrt{164}} \cdot \sqrt{t[h]/1.7} = 24.2\sigma\sqrt{t[h]}$. In 50 hours of observation an excess with a significance of $Sens(50\,h) = 24.2\sigma\sqrt{50} = 171\ \sigma$ would be detected from a Crab Nebula like source. Equivalently, in 50 hours of observation a source with a flux level of $5\sigma/171\sigma = 2.9\%$ of the Crab Nebula would be detected with 5σ. This number agrees well with the current claims of the MAGIC sensitivity, in which for the ON mode data set a flux sensitivity of $2.21 \pm 0.05 \pm 0.2\%$ of the Crab Nebula flux is obtained (Albert et al., 2007i).

The description so far refers to data taken in the WOBBLE mode. If the data are taken in the ON-OFF mode, the OFF-Alpha plot is produced using the OFF data sample. There is no need of the anti-alpha cut, but a normalization between ON and OFF sample has to be done. A natural way would be to normalize the two distributions according to the effective observation time in the ON and in the OFF samples. However, due to some differences in the camera efficiencies between different data sets, the normalization is done using the ON-Alpha plot. In this case a normalization region is chosen where no γ-ray events are expected, usually from 30 to 85 degrees. The expected background level N_{bg} in the signal region of the *Alpha* plot is estimated using the number of OFF events in the signal region. In case of a very strong γ-ray signal, the expected background level can even be estimated from the ON data itself, performing a parabolic fit to the *Alpha* plot in the background region (usually from 30 to 85 degrees) and then extrapolating the fit into the signal region. See Paneque (2005) for a detailed discussion on how the fit is performed.

5.10.2 θ^2 approach

Definition of ON and OFF regions: For the data taken in the WOBBLE mode, the preferred signal extraction method is the θ^2 approach. The *Disp* method allows one to reconstruct arrival directions of the γ-candidates on the camera plane. The resolution of the method is about 0.1 degree (slightly depending on the energy). The resolution is called the point spread function (PSF) and is defined as the σ of the Gaussian fit to the θ^2 plot of the MC γ-rays:

$$y(\theta^2) \propto \exp(-\frac{\theta^2}{2\sigma^2}) \tag{5.8}$$

In the WOBBLE mode, the source location is 0.4° off the camera center. This allows one to define several regions in the field of view of the camera, which

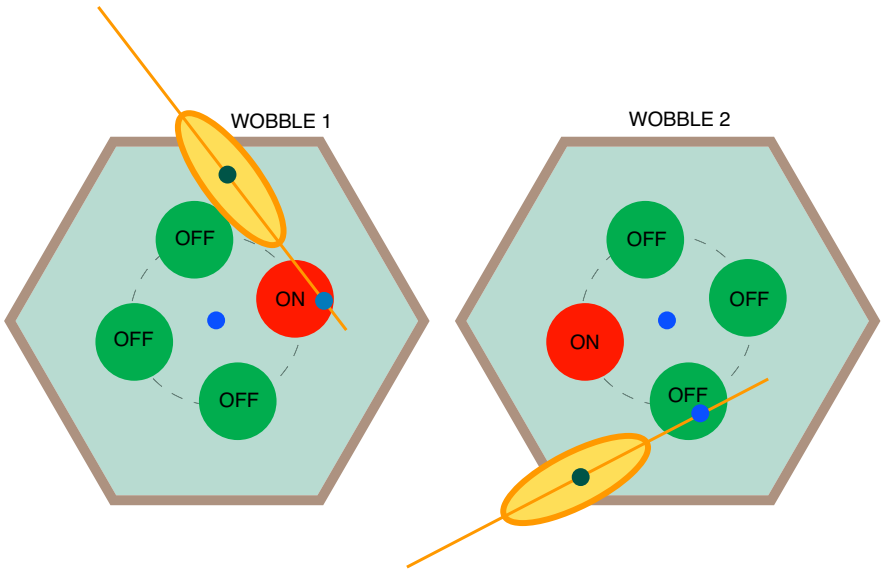

Figure 5.12: Sketch of the signal (ON) and background (OFF) regions for the θ^2-approach. For each WOBBLE position, 1 ON region is defined and 3 OFF regions, symmetrically to the camera center. An image in the WOBBLE 1 data set (left picture) will be included in the ON sample because its estimated arrival direction (using the *Disp* method) is within the ON region. An image in the WOBBLE 2 data set (right picture) will be included in the OFF sample because its estimated arrival direction is within one of the OFF regions.

have the same offset and symmetry with respect to the camera center as the ON source region. In Fig. 5.12 three such OFF regions are defined, for each WOBBLE position. For every event, which survived the γ/hadron separation, the source position is calculated using the θ^2 value. The calculated source position of an event is in camera coordinates (x and y). Now, an ON-θ^2 plot is produced for the source position (red crosses in Fig. 5.13). In addition, one can produce 3 OFF-θ^2 plots, one for each OFF region as defined in Fig. 5.12. Note that the ratio between ON and OFF regions is 1 to 3, improving the estimation of the expected number of background events. The individual OFF θ^2 distributions are added together and scaled by 1/3 (grey histogram in Fig. 5.13) to be compared with the ON source θ^2 plot. Note that by construction, θ^2 values up to $0.08[deg]^2$ for both θ^2 distributions (ON and OFF) are completely uncorrelated, whereas there is a small correlation for values $0.08[\mathrm{deg}]^2 < \theta^2$. The difference between ON and OFF θ^2 distributions is plotted in the insert of Fig. 5.13 (blue points). The distribution is overlaid with the MC γ-ray prediction for a point source (black curve) and agrees with it well.

Significance: Again, in order to compute the significance of the signal and the sensitivity of the analysis, tight cuts are applied. The signal region is defined as $\theta^2 < 0.024\mathrm{deg}^2$, which is indicated by the black dashed vertical line in Fig. 5.13.

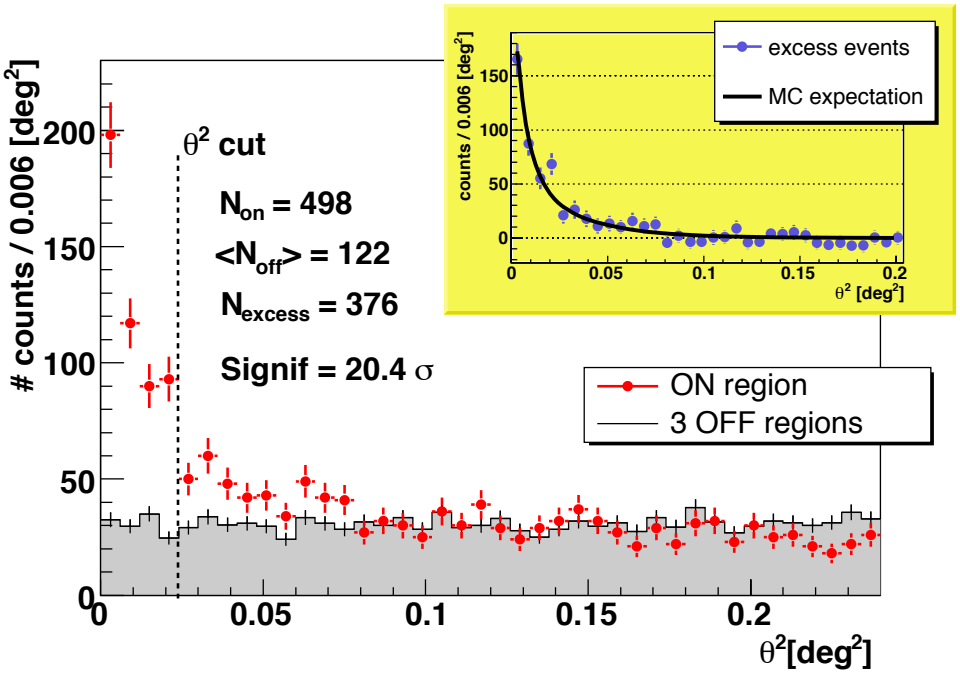

Figure 5.13: θ^2 plot with cuts: *Size*>320 ph.e. and *Hadronness* < 0.17. Resulting θ^2 from ON and three OFF regions are shown. Applying a $\theta^2 = 0.024$ cut one obtains a significance of 20.4 σ. *Insert:* θ^2 plot of excess events is shown (blue crosses) as well as the MC expectation for a point source (black line).

The number of ON events is 498, whereas the number of the estimated background events is 122. Using Equation 5.6 one obtains a significance of $S = 20.4\,\sigma$. Note that $\alpha = 1/3$ for the Equation 5.6 due to differences in the ON and OFF statistics. This is also the main advantage of the θ^2 approach compared to the *Alpha* approach presented above, making the θ^2 more sensitive (compare $S_{\theta^2} = 20.4\ \sigma$ with $S_{\text{alpha}} = 15.4\sigma$) .

Sensitivity: The sensitivity of the analysis is again computed using Equation 5.7 resulting in $Sens(t = 1\,h) = \frac{376}{\sqrt{122}} \cdot \sqrt{1/1.7} = 26.1\sigma\sqrt{t[h]}$. This corresponds to 2.7% of the Crab Nebula flux, which would be detected with 5σ in 50 hours of observation. As one can see, there is basically no difference between the sensitivity numbers of the *Alpha* approach (2.9%) and the θ^2 approach (2.7%), whereas the actual significances differ. I would like to stress again that the calculation of the sensitivities (Equation 5.7) is not correct due to neglecting the uncertainty of the background fluctuations.

5.11 The sky maps

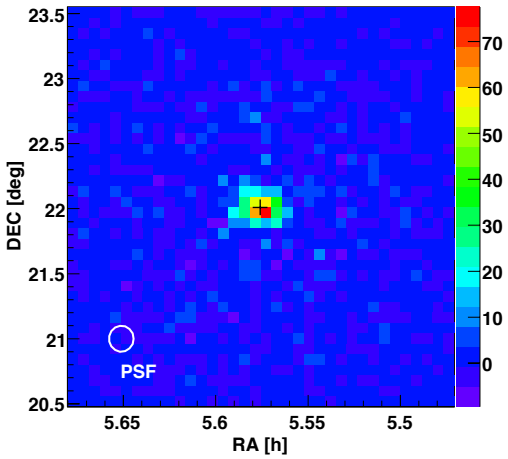

Figure 5.14: Sky map of the Crab Nebula data set. Excess events per bin of 1/12 deg × 1/12 deg are color coded.

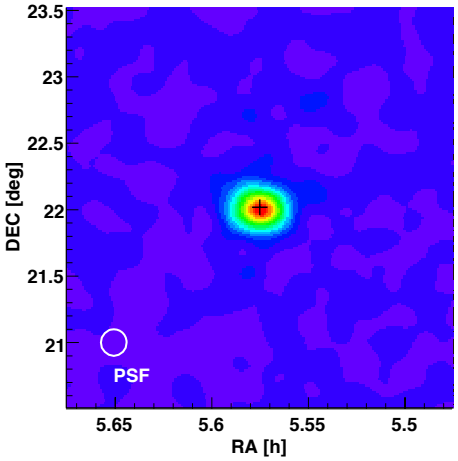

Figure 5.15: The same as Fig. 5.14 but smoothed out with the PSF with a σ = 0.1 deg.

Sky maps are calculated by reconstructing the arrival directions of each γ-like event in camera coordinates, transforming these into sky coordinates, filling the sky coordinates of all γ-like events into a histogram, and subtracting the expected background. Sky maps are produced using the *Disp* method, like for the θ^2 approach, allowing to reconstruct the arrival direction of the primary particle for each event, which survived the γ/hadron separation cuts. For the sky maps it is important that no source dependent parameters are used in the separation in order not to bias certain camera areas.

The background subtraction requires a special attention. The reason is that the camera acceptance for γ-rays is not homogeneous and may also differ between data sets due to different star fields, zenith angles, bad pixels, trigger inefficiencies etc. For WOBBLE data the background estimation can be done from the same data set. This is an important advantage since it allows to take into account the γ-ray acceptance of each individual data set separately. The background estimation works as follows: The arrival direction (X_s, Y_s) in camera coordinates is reconstructed for each γ-like event. The full data set still contains mostly hadron events but also real γ-events. Therefore, the camera is divided into two halves and only events, for which the reconstructed arrival direction is in the half not containing the source position, are used for the background estimation. In this way two 2-dimensional histograms for the background events are created, one for each camera half. In the particular case it means that for the WOBBLE 1 data set, only events with $Y_s < 0$ are kept, because the Crab Nebula position is in the upper part of the camera; while for the WOBBLE 2 data set, only events with $Y_s > 0$ are kept (see Fig. 5.4). The two histograms for the two camera halves

are then normalized to each other either using the observation time difference between the two data sets. The normalization factor is usually close to 1 ($\pm 5\%$) since almost equal amount of time is spent in both Wobble pointings. Let us call the resulting 2-dimensional histogram $CamMapOFF$. The $CamMapOFF$ histogram represents the background acceptance of the camera in camera coordinates for the particular data set. In the next step, for each γ-candidate (A) of the data set, a random event (B) is taken from the $CamMapOFF$ histogram. The arrival direction of the event (B) is projected into the sky coordinates using the arrival time of the event (A). The procedure is repeated 30 times, i.e. for every γ-candidate 30 random background events are projected into the sky coordinates. The resulting 2-dimensional histogram $SkyMapBg$ represents the background acceptance in sky coordinates for the particular data set.[6] Finally, the normalized background model $SkyMapBg$ is subtracted from the distribution of γ-candidates. The resulting distribution of excess events in sky coordinates is shown in Fig. 5.14. The normalization is obtained from a sky map region where no γ-ray source is expected. The excess events in bins of 1/12 deg $\times$ 1/12 deg are color coded. The excess has a roughly Gaussian shape with a PSF of 0.1deg consistent with the one obtained from the θ^2 plot (see Fig. 5.13).

The fit by a Gaussian to the sky map is also used to determine the center of gravity of the emission, with an error on the parameters defining the source position accuracy. For this particular data set, it is

- RA: +5:34:33 $\pm$ 0:0:01
- Dec: +22:0:35 $\pm$ 0:0:12

The errors are statistical only. A systematic uncertainty, caused by the fact that the real pointing of the telescope can be systematically wrong, has to be considered in addition. The systematic error of the pointing accuracy is 0.01 degrees (1 σ value). The catalog position of the Crab Nebula pulsar (in the center of the Nebula) is:

- pulsar RA: +5:34:31.97
- pulsar Dec: +22:0:52.1

Since the PSF is slightly larger than the bin size of the extracted excess events (Fig. 5.14), a smoothing of the sky map is common. Hereby, the excess map is folded with a Gaussian distribution with a σ_{gauss}= PSF = 0.1deg. The

[6]It is worth noticing that the $SkyMapBg$ is not a real background acceptance of the camera in sky coordinates but a model. By construction, the model scrambles the arrival times of the events. However, on average the zenith and azimuth distribution of the background events used for the model is the same as of the data sample. The possible error made in this method is negligible. The reason is that small differences in the camera acceptance due to changes of the zenith angle of observation are small compared to differences in the spatial camera acceptance.

resulting smoothed (also called oversampled) sky map is shown in Fig. 5.15. The smoothing polishes the sky map, averaging over the fluctuations and leaving over (or even highlighting) regions which are above the fluctuation level of the map. This might be especially important for weak signals and helps to identify γ-ray emitters. On the other hand the smoothing also widens the signal, which might cause disadvantages for correlation studies between the VHE γ-ray signal and data from other wavelengths.

5.12 Energy determination and spectrum calculation

The energy estimation is again performed using the Random Forest technique and a MC γ-sample for training. The parameters used for the energy estimation are the same as for the γ/hadron separation. Since the Random Forest is usually a decision tree to distinguish between two possibilities, a following modification had to be made: The MC training sample is divided into many (e.g. 1000) energy bins and probabilities are calculated that a given event belongs to a certain energy bin. The probabilities are then used as weights to assign an energy to the event. The obtained parametrization for the energy estimation is applied to an independent MC γ-sample. The actual migration from the true energy into the estimated energy is called migration matrix. The migration matrix for this MC sample is shown in Fig. 5.16, left plot. Fig. 5.16, right plot shows the quality of the energy reconstruction characterized by the resolution and the bias. The energy resolution is defined by the RMS value from a Gaussian fit to the relation:

$$\frac{\mathrm{E_{estim}} - \mathrm{E_{mc}}}{\mathrm{E_{estim}}} \tag{5.9}$$

The resolution is about 25% between 100 GeV and 10 TeV. The bias of the reconstruction is the Gaussian mean of the relation 5.9. Though the correlation between the reconstructed and the true energy is linear for most of the energies, biases below 150 GeV and above 8 TeV in the estimated energy are clearly seen. At low energies, the estimator seems to overestimate the energy, whereas at very high energies it underestimates the energy. This behavior is typical for all kind of energy estimators for different IACTs and must be corrected for when producing the final energy spectrum. The procedure for correcting the biases is called unfolding and is presented in the next subsection (unfolding).

The differential γ-ray energy spectrum is defined as:

$$\frac{\mathrm{d}F}{\mathrm{d}E}(E) = \frac{\mathrm{d}N_\gamma}{\mathrm{d}E\,\mathrm{d}A_{\mathrm{eff}}\,\mathrm{d}t_{\mathrm{eff}}} \tag{5.10}$$

with the number of excess events N_γ, the effective collection area A_{eff}, and the effective observation time t_{eff}. The effective collection area A_{eff} is the area in which

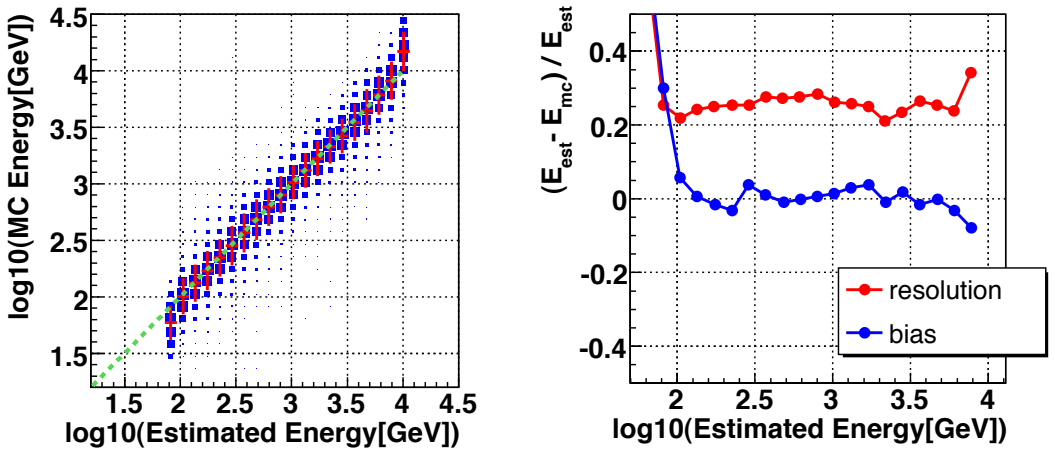

Figure 5.16: Energy reconstruction plots for MC γ-rays after all cuts. *Left plot:* Migration matrix between estimated and true energy. The matrix is normalized to 1 for each bin in the estimated energy separately. A perfect correlation, at which the true energy of γ-rays is equal to their estimated energy, is indicated by the green dashed line. A profile histogram is shown by the red crosses. *Right plot:* The quality of the energy reconstruction defined by the the resolution (red points) and the bias (blue points). Note that the reconstruction gets considerably worse below 100 GeV.

air showers can be observed by the telescope folded by the detection efficiency ϵ after all cuts. The detection efficiency ϵ is determined by the ratio between the number of γ-ray showers surviving the cuts and the number of simulated γ-ray showers.

For the energy spectrum determination, looser cuts are applied compared to the cuts giving the highest significance. The reason is that once the γ-ray signal is established, the total number of excess events and the energy threshold become more important than the significance. Thus, the looser cuts in *Hadronness* are chosen to increase the γ-ray acceptance. The energy thresholds of the analysis is defined as the peak in the differential energy distribution of the MC-γ events after all cuts (see Fig. 5.17). For this particular analysis, the analysis threshold is 178 GeV. The maximum of the distribution is rather flat. The position of the maximum changes slightly with cuts. Thus, the resulting threshold for small zenith angle observations ranges typically between 150 and 180 GeV. These values do not mean that there is no signal below the quoted energy threshold. Depending on the energy spectrum of the source and the strength of the signal, the actual lowest energy, at which a significant excess can still be found, is by a factor 1.5 to 2 lower. In fact, for this particular Crab Nebula data set, the lowest energy bin is from 126 to 158 GeV with an excess of 169 events corresponding to a significance of $3.1\,\sigma$. In the next lower energy bin (between 100 and 126 GeV), the excess is just 45 events with a significance of $1.5\,\sigma$. Please note that the excess is calculated

in bins of estimated (not true) energy because the true energy is not a measurable quantity. However, as we know from the migration matrix (see Fig. 5.16), at lower energies, the estimated energy is systematically higher than the true one. This means that a significant excess was found down to about 100 GeV.

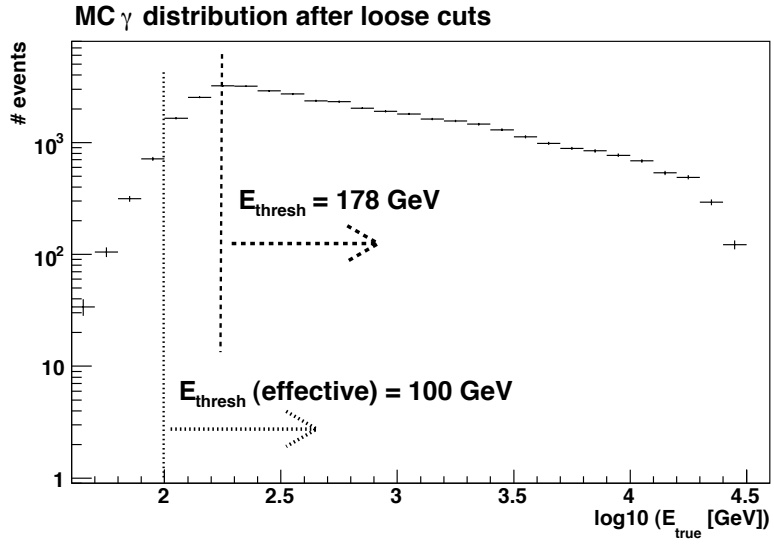

Figure 5.17: Distribution of MC γ-events after loose cuts as they are used for the energy spectrum calculation. The maximum of the distribution defines the energy threshold of the analysis. In this case it is 178 GeV as indicated by a dashed vertical line. An effective analysis threshold corresponding to a lowest extracted significant excess is about 100 GeV (indicated by a dotted vertical line).

The energy spectrum is then calculated in the following way. The number of excess events per estimated energy bin is divided by the total effective observation time t_{eff} and the effective area for this energy bin A_{eff}. The effective area after all cuts is calculated using the test sample of MC γ-rays and is shown in Fig. 5.18. The errors on the spectrum include errors on the number of excess events and the uncertainty of the effective collection area. Note that the error on the effective observation time is the same for all energy bins and is not included in the error bars of the spectrum[7]. The resulting spectrum is shown in Fig. 5.19. Note that the spectrum is calculated in bins of estimated energy, which might differ from the true energy (as discussed before and seen in Fig. 5.16). The calculation of the energy spectrum in bins of true energy, a procedure which is called unfolding, is presented in the next Subsection.

[7]The error on the effective observation time is usually very small compared to the uncertainties of the number of excess events and the effective collection area

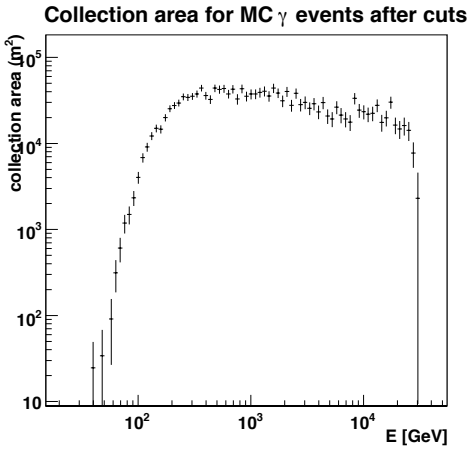

Figure 5.18: Collection area after cuts applied for the energy spectrum determination.

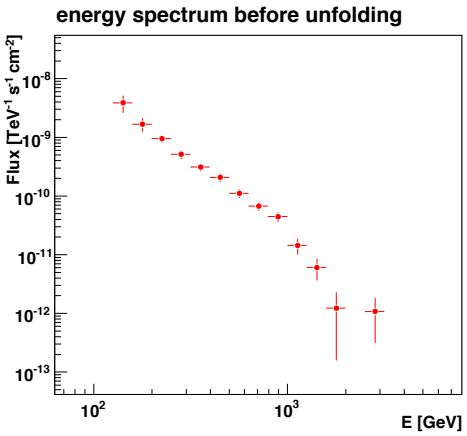

Figure 5.19: Energy spectrum of the Crab Nebula before unfolding.

5.13 Unfolding the energy spectrum

Measurements of physical quantities are often systematically distorted due to the fact that the detectors are not ideal. The distortions are due to biases in the measurements and to the finite resolution of the detectors. A typical task, where this problem appears, is the determination of the energy spectrum of measured γ-rays. The biases occur due to the fact that the true energy is not measured. The distortions due to biases and finite resolution can be written in the form:

$$Y(y) = \int M(y,x)S(x)\mathrm{d}x \quad \text{or} \quad Y_i = \sum_j M_{ij}S_j \quad \text{or} \quad Y = M \times S \qquad (5.11)$$

where y is estimated energy, x is the true energy, M describes the detector response (in this case it is the migration matrix as shown in Fig. 5.16), Y is the measured distribution and S is the true distribution (the one without distortions). The aim is to determine S, given Y and M. There are various approaches to solve this problem. The simplest solution (called deconvolution) is to invert the matrix and is technically correct. However, it is often useless due to large correlations between adjacent bins, which imply large fluctuations of their contents. This fact is the basis of the unfolding methods with regularization. In these methods one considers two additional terms: one term, χ_0^2, expressing the degree of agreement between the prediction $M \times S$ and the measurement Y, and another term, Reg, which is a measure of the smoothness of S. A solution for S is obtained by minimizing the expression

$$\chi^2 = \frac{w}{2} \times \chi_0^2 + Reg \qquad (5.12)$$

for a fixed regularization parameter w. Large values of w, corresponding to no regularization, often produce noisy unfolded distributions that perfectly fit the data. Very small values of w will, on the other hand, overemphasize the regularization, leading to larger deviation from the measurement but a very smooth unfolded distribution. So, the proper choice of w is very important. In the MAGIC software, a variety of methods is implemented which differ in the way regularization is implemented.

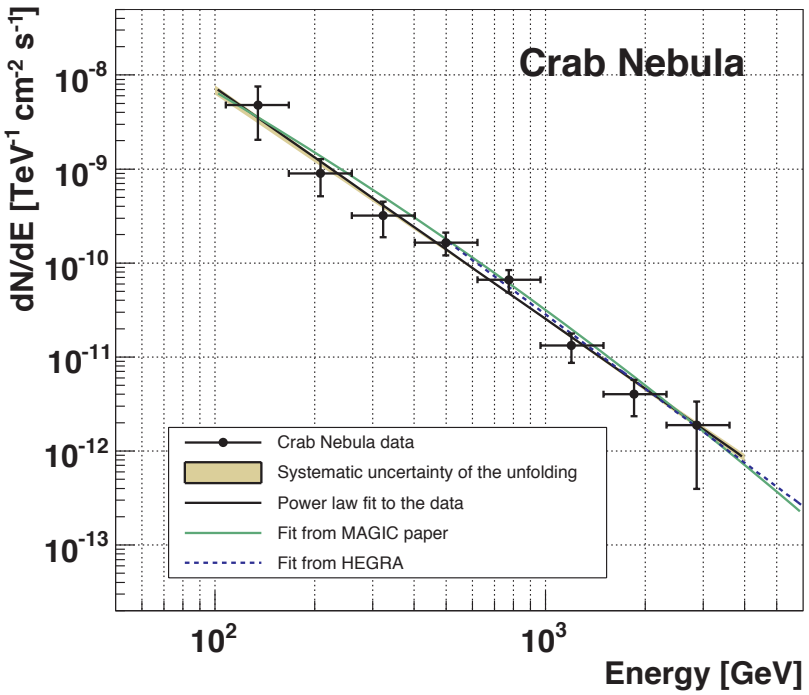

Figure 5.20: Differential energy spectrum of the Crab Nebula. The energy spectrum (black crosses) is obtained using *Tikhonov* method of unfolding. The x-error bars indicate the width of energy bins. A fit by a power law to the data points is shown by the black solid line. The systematic uncertainty using different unfolding methods is shown by the brown area (hardly visible). In addition, the parametrization obtained from a different data set of MAGIC data on the Crab Nebula is shown (green solid line, Albert et al. (2007i)) as well as the flux measured by the HEGRA experiment (blue dashed line, Aharonian et al. (2004b))

Another approach consists in assuming a parametrization of the true distribution S and then comparing $M \times S$ with the measured distribution Y. This is called *Forward* unfolding. The main difference to the previous methods is that an assumption about the true distribution has to be made. Moreover, no explicit

regularization is done in the *Forward* unfolding. On the other hand, the result of the *Forward* unfolding is just the best fit with corresponding errors using a guessed parametrization, but no points scattered around an unknown real distribution can be provided. More details on algorithms, considerations on the choice for w and technical implementation can be found in Wittek (2005); Aliu and Wittek (2006).

Table 5.1: Parameter values from a power law fit to the results of different unfolding methods for the energy spectrum of the Crab Nebula. The power law fit has a form $dN/dE = f_0\,(E/300\mathrm{GeV})^{-\Gamma}$. In addition, the quality of the fit is given in terms of χ^2 divided by the number of degrees of freedom (NDF).

Method	$f_0\,[10^{-10}(\mathrm{TeV\,cm^2\,s})^{-1}]$	Γ	χ^2/NDF
Tikhonov	4.9±0.1	2.46±0.11	5.67/6
Bertero	4.7±0.5	2.43±0.11	7.58/6
Schmelling	5.0±0.1	2.50±0.11	9.51/6
Forward	4.5±0.5	2.39±0.11	12.3/9

Unfolding results are only accepted if the results from the different methods are consistent with each other and if some criteria are satisfied concerning the regularization strength and the χ^2 value. The energy spectrum for the particular data set is unfolded using four different methods: *Tikhonov* (Tikhonov and Arsenin, 1979), *Bertero* (Bertero, 1989), *Schmelling* (Schmelling et al., 1994) and the *Forward* unfolding. Good agreement between all methods is found. In Fig. 5.20 the result of *Tikhonov* is shown. The resulting differential energy spectrum can be well described by a power law function (black solid line in Fig. 5.20) with:

$$\mathrm{d}N/\mathrm{d}E = (4.9 \pm 0.1) \times 10^{-10} \times (E/300\mathrm{GeV})^{-2.43\pm0.11}[\mathrm{TeV}^{-1}\,\mathrm{cm}^{-2}\,\mathrm{s}{-}1] \quad (5.13)$$

This result is in good agreement with the energy spectrum obtained using a 20 hours Crab Nebula data sample (Albert et al., 2007i) as shown by the green solid line in Fig. 5.20. The result obtained by the HEGRA collaboration using a data sample of 400 hours (Aharonian et al., 2004b) above 500 GeV is also shown and agrees well with the presented results, too. A somewhat softer spectral slope obtained by the HEGRA collaboration (this work: $\Gamma = 2.46 \pm 0.11$ compared to HEGRA: $\Gamma = 2.62 \pm 0.02$) can be explained by the different energy ranges measured. In case of HEGRA, the spectrum is measured above 500 GeV, whereas the present result is given above 100 GeV. In fact, one expects a hardening of the energy spectrum of the Crab Nebula towards 100 GeV due to the proximity of the peak position of the IC component of the γ-ray emission. This hardening was also found in Albert et al. (2007i) leading to an estimate of the position of the IC peak (i.e. the slope $\Gamma = -2$) at 77 ± 37 GeV.

Energy spectra obtained by the other unfolding methods can also be well described by a power law fit. The fit parameters are summarized in Table 5.1

together with the corresponding fit quality (χ^2/NDF) and demonstrate the good agreement between different unfolding procedures. The power law fits from different methods are used to estimate the systematic error of the unfolding, which is shown by the brown area in Fig. 5.20. The systematic error of the unfolding is much smaller than other systematic effects (see below) and can be neglected.

As can already be seen from Fig. 5.20, the obtained energy spectrum is in good agreement with the MAGIC publication of the Crab Nebula observations:

$$\mathrm{d}N/\mathrm{d}E = (5.7 \pm 0.2) \times 10^{-10} \times (E/300\mathrm{GeV})^{-2.48\pm0.03}[\mathrm{TeV}^{-1}\,\mathrm{cm}^{-2}\,\mathrm{s}{-}1] \quad (5.14)$$

The flux normalization factor of this parametrization is 15% higher than in the present analysis, which is within the systematic uncertainties of the analysis (20%, see below).

5.14 The light curves

When the γ-flux is determined in time intervals, the so-called light curves is created. The light curve is defined as:

$$\frac{\mathrm{d}F}{\mathrm{d}E}(E,t) = \frac{\mathrm{d}N_\gamma}{\mathrm{d}E\,\mathrm{d}A_{\mathrm{eff}}(t)\,\mathrm{d}t_{\mathrm{eff}}(t)} \quad (5.15)$$

The symbols are the same as in Equation 5.10. Since the effective collection area depends on the zenith angle distribution of the data set, it implicitly depends on the time. Usually the statistics of the signal does not allow to make light curves in the many energy bins for several time intervals. In this case, one defines the light curve of the integral flux above a certain energy E_0:

$$F_{E>E_0}(t) = \int_{E_0}^{\infty} \mathrm{d}E\, \frac{\mathrm{d}N_\gamma}{\mathrm{d}E\,\mathrm{d}A_{\mathrm{eff}}(t)\,\mathrm{d}t_{\mathrm{eff}}(t)} \quad (5.16)$$

Practically, light curves are obtained by making bins in time and calculating the number of excess events in each time bin separately for a given range in estimated energy. The effective collection area is calculated separately for each time bin by using the MC γ-event sample with the zenith angle distribution of the data events in a given time bin. Since the energy range is usually dominated by the events with energies close to the low energy limit (due to a falling power law spectrum) the lower energy limit for the light curve has to be chosen carefully. A safe low energy end is an energy value on the plateau of the collection area, i.e. where the collection area is rather insensitive to small mismatches between the true and the reconstructed energy of the signal events. For this particular data set a value of 200 GeV is chosen (see Fig. 5.18). A significantly smaller value would cause a strong systematic uncertainty due to the steep changing collection area. No unfolding is performed for light curves. It is an additional reason not

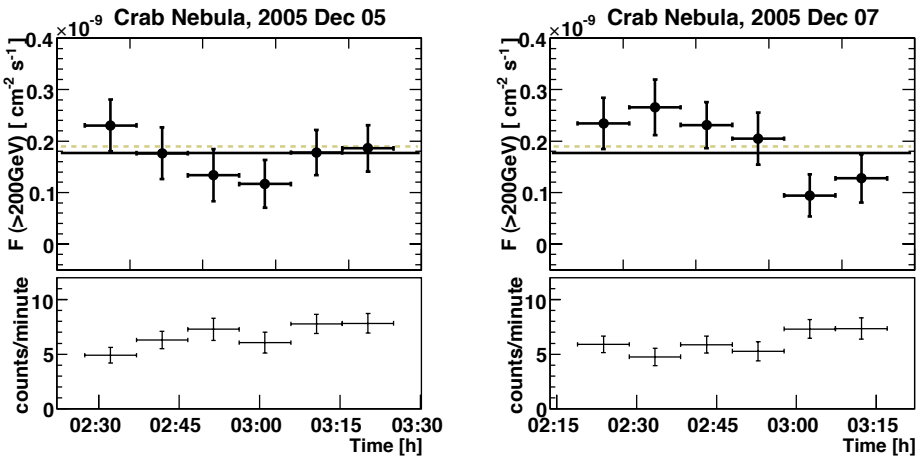

Figure 5.21: *Upper pads:* Light curve for the two nights of the Crab Nebula data set. The integral fluxes above 200 GeV in time bins of 10 minutes. The light curve is fitted by a constant (black horizontal line), which is in a very good agreement with the result based on a bigger data sample (Albert et al., 2007i). *Lower pads:* Corresponding background rate in the signal region after cuts.

to choose a too low energy, at which the linear correlation between the estimated and the true energy is not longer true (see the migration matrix in Fig. 5.16).

The resulting light curves in 10 minute binning for the two observed nights are shown in Fig. 5.21. In the lower panel, the background rates after cuts are shown to demonstrate the stability of the observing conditions and the detector performance. The integral fluxes above 200 GeV are in good agreement with a constant emission. A fit by a constant (black solid line in Fig. 5.21) leads to $\chi^2/NDF = 14.5/11$. The fitted integral flux F is:

$$F(E > 200\,\mathrm{GeV}) = (1.77 \pm 0.14) \times 10^{-10}\mathrm{cm}^{-2}\,\mathrm{s}^{-1} \tag{5.17}$$

This value is in good agreement with the integral Crab Nebula flux measured with the MAGIC telescope using a different data sample (Albert et al., 2007i):

$$F(E > 200\,\mathrm{GeV}) = (1.96 \pm 0.05) \times 10^{-10}\mathrm{cm}^{-2}\,\mathrm{s}^{-1} \tag{5.18}$$

5.15 Analysis of low energy events

The analysis technique presented here is the so-called *classical* one. The classical techniques are based on the reduction of a measured event to a few characteristic parameters (*Size*, *Width*, *Length* etc., see in Section 5.8). The parameters are then used to reconstruct the shower properties in the atmosphere and for the γ-hadron separation. The classical methods are used in other IACT experiments like Whipple, VERITAS, HEGRA or H.E.S.S. These methods are robust, fast,

and have been proven to perform very well for energies above ∼200 GeV. The MAGIC standard software is also based on the classical technique. However, the first years of MAGIC have shown that these tools have difficulties to reconstruct the shower nature below approximately 150 GeV or for images with a total *Size* of 200 ph.e. The reason is mainly that for lower energies the number of radiating shower particles is small, and that the natural differences in γ– and hadron–induced showers are less pronounced. At even lower *Size* values, the differences between image parameters of individual images are dominated by fluctuations in the shower development. In addition, several other backgrounds mimic γ-ray induced images: distant muons and electromagnetic subshowers of hadronic showers. See Section 4.1.4 for details on the backgrounds. One can summarize analysis problems occurring with events containing a small amount of light:

1. At low energies (below 150 GeV), single particle tracks start to be distinguishable. The images are heavily contaminated by shower fluctuations. This means that many γ-induced images look irregular, they do not have a clear elliptical shape and the shape parameters do not provide enough information for γ-hadron separation, position and energy reconstruction.

2. The image from distant muons with large impact parameters from the telescope is a shrank arc, which mimics a small elliptical image like they are from a γ-induced image.

3. Hadronic subshowers can be purely electromagnetic (e.m.) showers, which make an irreducible background if only the the e.m. subshower is observed.

4. At *Size* values below 100 ph.e., air showers produced by cosmic electrons are detected as well as some images originated from a pure light of the night sky fluctuations.

The problem point 2 can be easily overcome using a stereoscopic telescope system, i.e. building a system of several telescopes and recording the same showers in Cherenkov light from different directions (telescopes), as it will be realized with the MAGIC II telescope. Distant muons will produce an image in one of the telescopes only and thus can be easily rejected. The probability that several subshowers from a hadronic shower (point 3) will be detected by different telescopes is also high, and such events can then be rejected. The two remaining problems (1 and 4) cannot be solved with a stereoscopic system and are a matter of investigations. A reconstruction of the shower maximum may overcome the problem number 4. The described in Appendix *model analysis* promises to partially overcome these problems. However, all 4 points make an analysis of a single IACT more complicated, effectively reducing its sensitivity.

There are different approaches to overcome the analysis difficulties described above and improve the results. Naturally, all of them try to extract more information from the measured event and use this additional information for background

reduction and energy reconstruction. The main dilemma is to extract from a measured event as much information as possible but not to be overwhelmed by noise. The other main problem is to define parameters which are sensitive to the remaining small differences between γ– and hadron–induced showers. One of the ideas is that the time information (arrival time of photons in the PMTs) can be used to distinguish between camera pixels containing noise and pixels containing signal from a shower. This so-called time image cleaning allows to decrease the tail cuts during the image cleaning and keep information enclosed in tails of the images. The method improved the suppression of the night sky background fluctuations and reduced the minimum size of analyzed images down to 60 ph.e. However, the γ/hadron separation improved only marginally. Details on the performance of this method can be found in Otte (2007). Another very promising alternative analysis method, called *model analysis*, was developed in the scope of this thesis. Its concept, realization and performance are described in detail in Chapter B.

5.16 Systematic effects and concluding remarks

Apart from statistical errors quoted in this Chapter, the measurement of the γ-ray spectrum, and light curves is affected by systematic errors, most of which are difficult to evaluate. The most important systematic affects are the following:

1. **Atmospheric conditions and atmospheric model.** The MC shower simulation uses the U.S. standard atmosphere and the Elterman model (Elterman, 1964) for the distribution of aerosols and ozone. Atmospherical changes as humidity, temperature, high clouds, haze, calima[8] are not taken into account in the simulation and may lead to an underestimation of the shower energy. The averaged atmospheric values between Summer and Winter change by about 15% the transmission of the atmosphere (Bernlöhr, 2000). Therefore, the subsequent systematic effect on the energy scale is taken to be 15%.

2. **Knowledge of the hardware components of the detector.** Several hardware components are difficult to monitor. Following are the main systematic errors due to hardware components:

   - Reflectivity of the mirrors. The assumed reflectivity is 85%. It critically depends on amount of dust on the mirrors and also worsens with time due to aging. The estimated uncertainty is 5% and affects the energy estimation of the γ-rays.
   - Quality of the optical PSF. The simulated optical PSF has a Gaussian shape with the sigma of 15 mm. The PSF depends critically on the

[8] fine dust or sand blown from the Sahara Desert

accuracy of the active mirror control and the bending model of the telescope. The uncertainty is estimated to be 5% and also affects the energy estimation.

- Photon losses on the camera entrance. The protective plexiglas window at the PMT camera and the Winston cones may suffer from dust. An additional 3-5% systematic error has to be considered.
- Light-to-photoelectron conversion has been estimated to have a systematic error of 5-10%. The conversion is difficult to measure and is dominated by the uncertainty of the light collection efficiency of the first PMT dynode. This error also affects the energy estimation.
- Trigger inefficiencies. Maybe currently the main systematic uncertainty. At energies below 150 GeV the effect is estimated to be 20%. At higher energies it is lower and reaches at ≈ 1 TeV a value of 5%. The trigger inefficiency affects both flux and the energy estimation.

3. **Analysis chain.**

   - The calibration chain using F-Factor method introduces an overall systematic error of 8% (Gaug, 2006). This error affects the energy estimation of the events.
   - Errors in the calculation of the effective on-time. The systematic error can be caused by dead times of the system which are not considered in the analysis. The systematic error is estimated to be 2% and affects γ-fluxes independent of energy.
   - Differences in analysis details (signal extraction, image cleaning, γ/hadron separation method, unfolding) lead to a systematic error of 3% (Otte, 2007).
   - Software bugs. This error is difficult to assess. On this stage of the experiment a guess value of 3% can be considered as conservative.

4. **Monte-Carlo – data agreement.** Possible differences between simulated showers and real showers may lead to an error in computation of effective areas. This can affect both the absolute energy scale and the flux level. The effect is estimated to be 10%.

The overall systematic error on the energy scale is 16%. Depending on the spectral slope of the γ-ray source, the error on the flux differs. Assuming a slope of 2.5, the error on the flux is $\approx$ -30% +50%. For a steeper slope, the effect is larger. Assuming a slope of 4.0, the error on the flux is $\approx$ -50% +100%. It must be stressed that most of the effects lead to an underestimation of the γ-ray energy and/or γ-ray flux. The influence of the systematic errors on the spectral slope is conservatively estimated to be 0.2.

Chapter 6

Observations of Markarian 421

Markarian 421 (Mrk 421, redshift $z = 0.030$) is the closest known and, together with Mrk 501, the best studied TeV blazar. It was the first extragalactic γ-ray source detected in the TeV energy range using IACTs (Punch et al., 1992; Petry et al., 1996). Mrk 421 was also the source with the fastest observed flux variations among TeV γ-ray emitters before the very fast variability of Mrk 501 (Albert et al., 2007g) and PKS2155 (Aharonian et al., 2007b) was found. So far, Mrk 421 showed flux variations of nearly two orders of magnitude and occasional flux doubling times as short as 15 min (Gaidos et al., 1996; Aharonian et al., 2002c). Variations in the hardness of the TeV γ-ray spectrum during flares and correlated with the flux level were reported by several groups (Krennrich et al. (e.g. 2002); Aharonian et al. (e.g. 2005d)). Simultaneous observations in the X-ray and GeV-TeV bands show a significant flux correlation (Krawczynski et al., 2001; Błażejowski et al., 2005).

Mrk 421 was detected and studied at all accessible wavelengths of the electromagnetic spectrum from radio to very high energy (VHE) γ-rays, e.g. extending over $\sim$19 decades in energy. The broad-band spectral energy distribution (SED) shows a typical two bump structure with the first peak in the keV energy range and the second peak at GeV-TeV energies. The SED is commonly interpreted as beamed, non-thermal emission of synchrotron and inverse-Compton scattering from ultrarelativistic electrons, accelerated by shocks moving along the jets at relativistic bulk speed (See Chapter 2 for more details). Worth mentioning that contributions from hadronic production cannot be excluded (Mannheim, 1993; Mücke et al., 2003). A way to distinguish between the different emission models is to close some gaps in the SED, as well as to determine the position of the second peak in the SED and to obtain simultaneous, time resolved data in a broad energy range by performing multiwavelegth campaigns.

6.1 Motivation of the observations

Known to be a strong VHE γ-ray emitter, Mrk 421 was one of the main targets for the MAGIC collaboration to be observed in the commissioning phase of the telescope. Not surprisingly, the first detected γ-ray signal by MAGIC was from Mrk 421. The signal on a 6 σ level was found in a 2 hours data set recorded in February 2004 (D. Paneque, private communication). In Spring–Summer 2004 the Crab Nebula, the standard candle of the TeV γ-ray astrophysics, cannot be observed from La Palma. Therefore, Mrk 421 became the main target to study the performance of the telescope. The source was observed regularly in 2004–2005, and then the data were used to finalize the analysis tools for the MAGIC telescope. Since the source is known to be variable in flux, the stability of the telescope was rather difficult to determine from the detected signal. Nevertheless, one could test the analysis threshold of the MAGIC telescope, i.e. one could determine the lowest energy, at which a γ-ray signal could be detected.

Using the Mrk 421 data I present here, the ability of the telescope to measure energy spectra down to 100 GeV was shown for the first time. Previously, VHE γ-rays from Mrk 421 were measured down to 300 GeV (Piron et al., 2001), i.e. MAGIC explored formerly unknown domain between 100 and 300 GeV. The MAGIC observations were sensitive enough to significantly detect Mrk 421 in the lowest flux state ever on a night-by-night basis. Flux variations on time scales of minutes could be quantified in all measured flux states. The analysis of the data set was published in Albert et al. (2007e), which is currently the most cited MAGIC publication on an extragalactic source.

6.2 The data set

The Mrk 421 data taken between November 2004 and April 2005 were divided into four samples. Due to changes in hardware, data taken before and after February 2005 were treated separately. Most of the data were taken at small zenith angles ($ZA < 30°$) to assure a low trigger energy threshold. Only 1.5 h in December 2005 were taken at $42° < ZA < 55°$ for simultaneous observations with the H.E.S.S. telescope system (Mazin et al. (2005), see Section 6.7). Most of the data were taken in the ON mode. We considered the γ-ray signal from Mrk 421 to be strong enough to make OFF observations dispensable. Instead, the background level was estimated from the ON data, outside the signal region. In April 2005 part of the data were taken in the WOBBLE mode. The Mrk 421 data set consists, therefore, of 4 data samples, which are summarized in Table 6.1. For each data sample a separate Monte-Carlo (MC) set of γ events was simulated, taking into account the zenith angle of observation, the observational mode, and the hardware configuration of the telescope.

The full data set corresponds to 29.0 hours. Runs with problems in the hard-

Table 6.1: Results of the Mrk 421 data using the α approach (see text for details). Samples I+II were recorded in November 2004 - January 2005, while samples III+IV were taken in April 2005.

sample	on time	zenith [°]	mode	E_{thr}[GeV]	N_{on}	N_{off}	N_{excess}	sigma
I	4.63 h	9.3 - 31.2	ON	150	3761	1878 ± 32	1883 ± 69	29.3
II	1.53 h	42.4 - 55.0	ON	260	1086	674 ± 25	413 ± 41	10.1
III	9.30 h	9.2 - 27.5	ON	150	8083	4360 ± 49	3723 ± 102	38.9
IV	10.12 h	9.4 - 32.4	wobble	150	7740	4532 ± 67	3208 ± 111	29.1

ware or unusual trigger rates were rejected in order to ensure a stable performance and good atmospheric conditions. Removing these runs the total observation time decreased to 25.6 h.

6.3 The VHE γ-ray signal

The analysis of the data set was performed with the tools described in Chapter 5. During the entire observation period, Mrk 421 was found to be in a moderate to high flux state, resulting in a clear signal in all four data samples. Fig. 6.1 shows the *Alpha* distribution of the γ-candidates of the combined samples I, II, and III with an energy threshold of $\sim$150 GeV. An excess of about 7000 events was found, which, for the given background, corresponds to an excess of more than 49 standard deviations. The number of excess events and the significances for the individual samples are summarized in Table 6.1.

Fig. 6.3 shows a sky map produced with the *Disp* method (see Chapter5) using samples III and IV. The reconstructed source position from the sky map (Fig. 6.3, indicated by the black cross) is centered at RA=+11h04$'$19$''$, DEC=38°11$'$41$''$. The systematic error of the telescope pointing is 2$'$. The γ PSF is indicated by a white circle in the left bottom corner. The observed extension of Mrk 421 is compatible with the MC expectation of a point source, which can also be seen in Fig. 6.2.

6.4 Light curves and their variability

The integral γ-fluxes above 200 GeV, averaged over each night of observation, are shown in the upper panels of Fig. 6.4. Significant variations of up to a factor of four overall and up to a factor two in between successive nights can be seen. Since sample II has an energy threshold of 260 GeV it is not included in the light curve. The relatively high analysis energy threshold of 200 GeV applied for the light curve ensures that the results are independent of the actual trigger

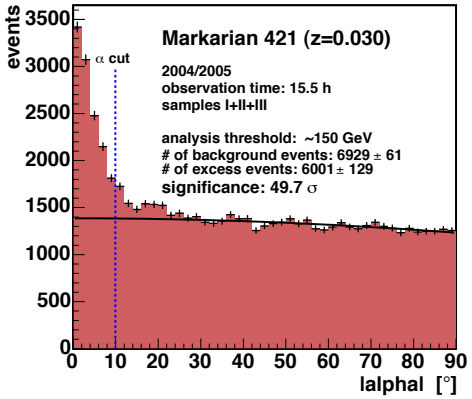

Figure 6.1: *Alpha* distribution for the combined data samples I+II+III with $E_{thresh} = 150$ GeV. A vertical line indicates the *Alpha* cut used to extract excess events. The black curve is a 2nd degree polynomial fit to the *Alpha* distribution between 30 and 90 degrees and is used to estimate the background level between 0 and 10 degrees.

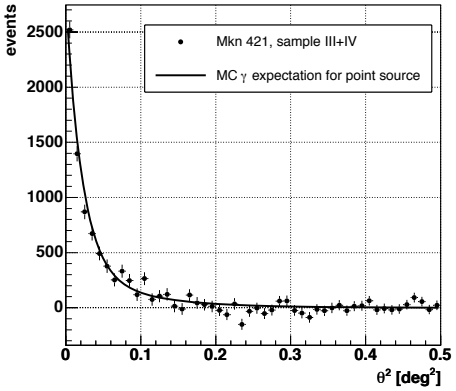

Figure 6.2: θ^2 distribution for the combined data samples III+IV with $E_{thresh} = 150$ GeV after background subtraction. The black line is the MC-γ expectation for a point source.

thresholds during each night. In the middle panels of Fig. 6.4 the corresponding flux in the X-ray band as observed by the All-Sky-Monitor (ASM[1]) on-board the RXTE satellite is shown. In the lower panels of Fig. 6.4 the optical data taken by the KVA telescope[2] on La Palma are shown. The contribution of the host galaxy (appr. 8.0 mJy) has been subtracted. Both the X-ray data and the optical flux show a moderate variability within the observation period.

For the 6 nights in April (MJD 53465 to 53471), the light curve above 200 GeV is shown in Fig. 6.5 in bins of 10 minutes. We also added the background rates for each night in the same binning, in order to demonstrate that the small variation in the excess rates and the daily changes are not caused by detector effects or atmospheric transmission changes. The vertical lines indicate the time in each night at which the observation mode was changed from ON to Wobble. The mean integral energy flux per night, $\overline{\mathrm{F}}$, in units of $10^{-9}\mathrm{cm}^{-2}\mathrm{s}^{-1}$ and the quality of the fit constant are shown in the panels. The horizontal dashed line corresponds to the integral flux of the Crab Nebula above 200 GeV. Combining the findings from the intra-night light curves we conclude that we did not find significant short-term flux variability within individual nights, despite the high sensitivity of MAGIC for such a search. On the other hand, we observe significant

[1] see http://heasarc.gsfc.nasa.gov/xte_weather/
[2] see http://tur3.tur.iac.es/

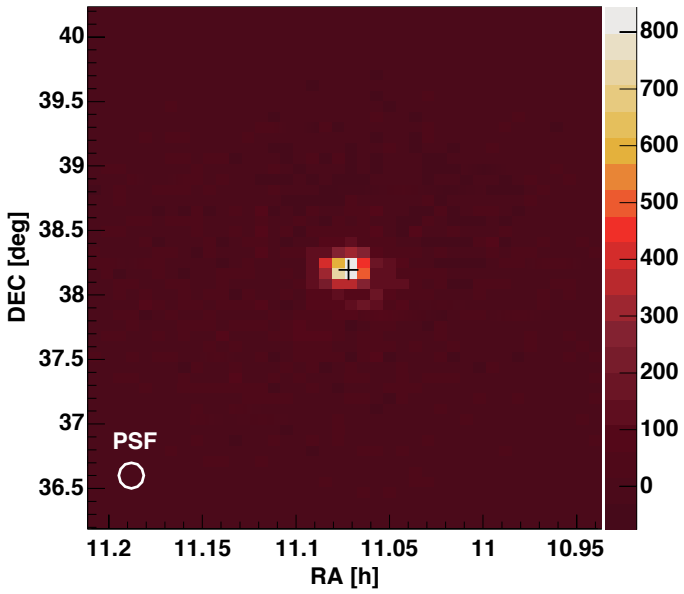

Figure 6.3: Sky map of excess events in the region of Mrk 421 for samples III+IV using the *Disp* method. The black cross indicates the reconstructed source position. Note that the vertical scale is in units of [events / (0.05×0.05 deg^2)].

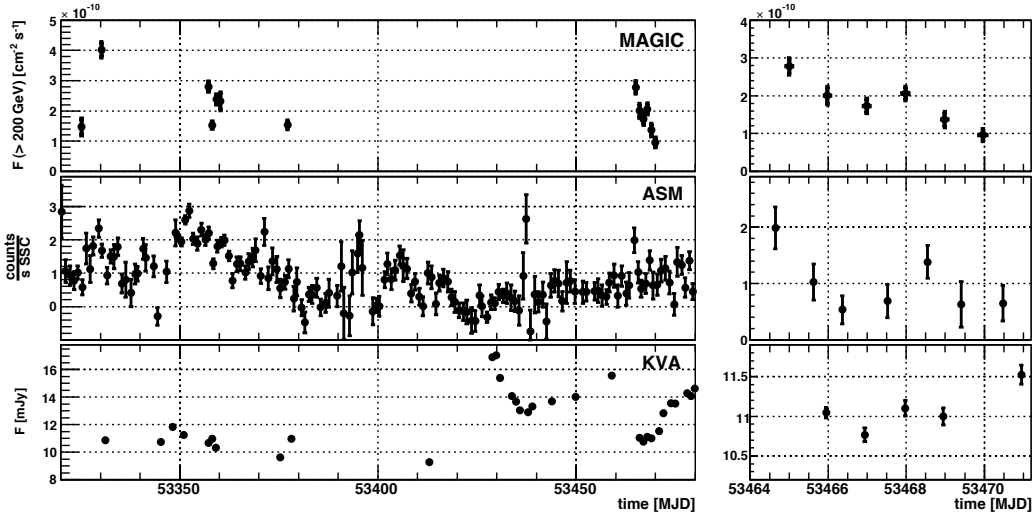

Figure 6.4: Night-by-night light curve for Mrk 421 from November 2004 to April 2005. *Left panels*: data from November 2004 to April 2005. *Right panels*: expanded data for 6 nights in April 2005. *Upper panel*: MAGIC data, night average of Mrk 421 above 200 GeV using samples I+III+IV. *Middle panel*: corresponding day-by-day X-ray counts as observed by the RXTE/ASM. *Lower panel*: Light curve of the optical flux of Mrk 421 as measured by the KVA telescope.

day-to-day variation by up to a factor of two, and differences up to a factor of four in the full sample.

6.5 The energy spectrum

The measured spectrum

For the spectrum calculation, we combined the entire data set because the differences between the fluxes on individual nights are rather moderate (see Fig. 6.4). The resulting averaged differential energy spectrum is shown in Table 6.2 and in Fig. 6.6 by filled grey boxes. The energy spectra extend from around 100 GeV to several TeV. The last spectral point at 4.4 TeV is an 95% upper limit. The error bars shown are statistical only. Systematic errors are estimated to be 18% on the absolute energy scale, which correspond to 44% on the absolute flux level for a photon index of 2.2. The systematic error on the slope is estimated to be 0.2. The attenuation of the VHE photons by intergalactic low energy photons and the determination of the intrinsic spectrum of Mrk 421 are discussed below.

VHE γ-ray absorption by the EBL

The VHE photons from Mrk 421 cross ∼400 million light years distance on their way to Earth. They interact with the low energy photons of the extragalactic background light (EBL, see Section 1.5 and Chapter 9) consisting of redshifted star light of all epochs and reemission of a part of this light by dust in galaxies. The most common reaction channel between VHE γ-rays and the low energy photons of the EBL is pair production

$$\gamma_{\mathrm{VHE}} + \gamma_{\mathrm{EBL}} \rightarrow e^+ e^-, \tag{6.1}$$

a reaction which has its largest cross section when the center of mass energy is roughly 3.6 times larger than the threshold energy of $2\mathrm{m_e c^2}$. The intrinsic (deabsorbed) photon spectrum, dN/dE_i, of a blazar located at redshift z is given by:

$$dN/dE_i \; = \; dN/dE_{obs} \times \exp[\tau_{\gamma\gamma}(E,\, z)], \tag{6.2}$$

where dN/dE_{obs} is the observed spectrum and $\tau_{\gamma\gamma}(E,\, z)$ is the optical depth. The distance to Mrk 421 implies that the optical depth (e.g. Eq. 1.10 in Section 1.3) strongly depends on the shape and absolute photon density of the EBL between 1 and 30 μm wavelength. A rather complicated distortion of the intrinsic spectrum takes place above ∼100 GeV. Although the calculation of the optical depth is straightforward, the spectral energy distribution of the EBL is uncertain (Chapter 3). In Fig. 6.7, the current status of the EBL measurements and the used EBL model (Primack et al. (2005), solid line) are summarized.

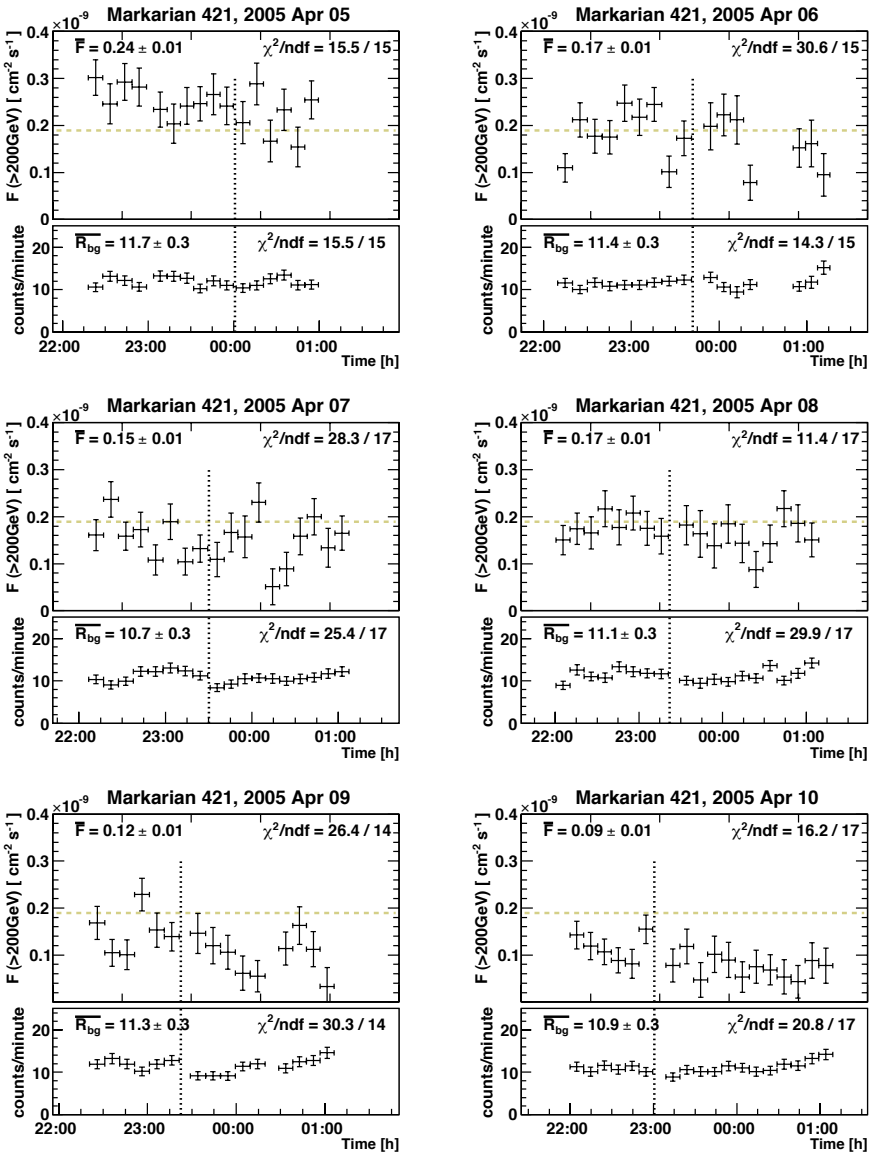

Figure 6.5: Light curve for 6 nights in 2006 April in 10 minutes binning. *Upper panels*: flux above 200 GeV. Mean integral energy flux above 200 GeV, $\overline{\mathrm{F}}$, in units of $(10^{-9}\mathrm{cm}^{-2}\mathrm{s}^{-1})$ and the quality of the fit by a constant are shown in the panels. *Lower panels*: mean background rate $\overline{\mathrm{R_{bg}}}$ per minute after cuts. Note the rising background rate towards the end of each observation slot, related to the rising moon. $\overline{\mathrm{R_{bg}}}$ and the quality of the fit by a constant are shown. The vertical dotted lines indicate the time of the switchover from the ON observational mode to the Wobble mode. The dotted horizontal line indicates the Crab Nebula integral flux above 200 GeV as measured by MAGIC (Albert et al., 2007i).

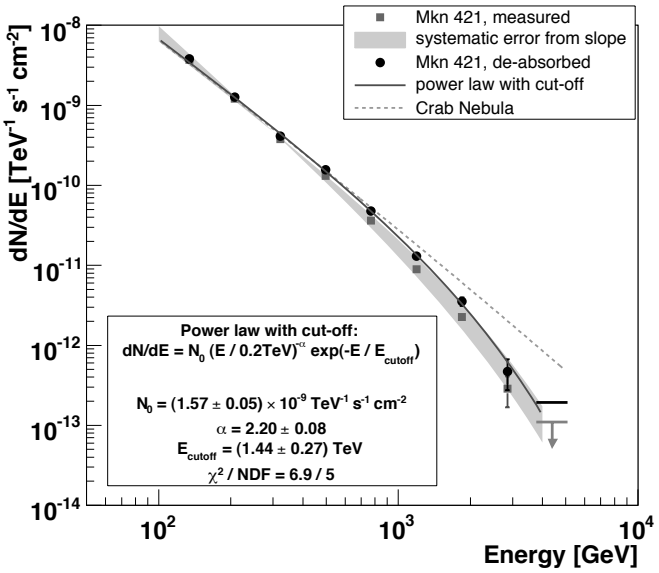

Figure 6.6: Differential energy distribution of Mrk 421 averaged over the whole data sample. The measured energy spectrum is shown by the filled gray squares and the deabsorbed spectrum by the filled black circles. The spectral point at the highest energy is a 95% upper limit. The gray shaded area corresponds to a systematic error from a slope error of ± 0.2 as quoted in the text. The solid black line indicates the best fit to the deabsorbed spectrum by a power law with exponential cutoff; its parameters are listed in the inset. For comparison, the measured Crab Nebula spectrum (Albert et al., 2007i) is shown by the dotted gray line.

The attenuation coefficients $exp(-\tau_{\gamma\gamma})$ are shown as the function of energy of VHE γ-rays in Fig. 6.8. I want to stress that the attenuation coefficients are very similar to the ones published recently by Stecker et al. (2006).

The de-absorbed spectrum of Mrk 421

The measured spectrum and the reconstructed de-absorbed (i.e. corrected for the effect of intergalactic absorption) spectrum are shown in Fig. 6.6. For comparison, the Crab Nebula spectrum is also shown. The de-absorbed spectrum (shown by filled black circles) is clearly curved; its probability of being a simple power law is 1.6×10^{-8}. The de-absorbed spectrum is fitted by a power law with an exponential cut-off: $dN/dE = N_0(E/0.2\,\mathrm{TeV})^{-\alpha}\exp(-E/E_{\mathrm{cutoff}})$, α being the photon index, solid line in Fig. 6.6. The fit parameters are listed in the inlay of Fig. 6.6. The power law with a cut-off describes well the de-absorbed spectrum of Mrk 421, with a photon index $\alpha = 2.20\pm0.08$ and a cut-off energy of $E_{\mathrm{cutoff}} = (1.44\pm0.28)\,\mathrm{TeV}$.

Table 6.2: Averaged measured differential energy spectrum of Mrk 421, derived from the data set presented in the Thesis. The last point is an 95% upper limit.

energy bin [GeV]			differential flux dN/dE
lower bin edge	mean E	upper bin edge	[photons/ (TeV cm^2 s)]
108	134	167	$(3.72 \pm 0.34) \times 10^{-9}$
167	208	259	$(1.21 \pm 0.04) \times 10^{-9}$
259	321	402	$(3.77 \pm 0.15) \times 10^{-10}$
402	498	623	$(1.32 \pm 0.05) \times 10^{-10}$
623	770	965	$(3.63 \pm 0.19) \times 10^{-11}$
965	1192	1497	$(8.95 \pm 0.71) \times 10^{-12}$
1497	1845	2321	$(2.26 \pm 0.27) \times 10^{-12}$
2321	2856	3598	$(2.88 \pm 1.20) \times 10^{-13}$
3598	4429	5579	$< 1.10 \times 10^{-13}$

Table 6.3: Systematic study of the fit parameters on the de-absorbed spectrum of Mrk 421. The fitted function is a power law with an exponential cut-off: $dN/dE = N_0(E/0.2\,\mathrm{TeV})^{-\alpha} \exp(-E/E_{\mathrm{cutoff}})$. We show fit values on the photon index, α, and the cut-off energy, E_{cutoff}, for following assumptions: nominal values (A), a systematic shift by +18% in the VHE energy scale (B), a systematic shift by -18% in the VHE energy scale (C), a systematic shift by +18% in the VHE energy scale and, in addition, 25% more density of the EBL (D), and a systematic shift by -18% in the VHE energy scale and, in addition, 25% less density of the EBL (E). Note that the resulting systematic errors are comparable with the statistical errors.

	α	E_{cutoff} [TeV]
A: nominal	2.20 ± 0.08	1.44 ± 0.28
B: E+18%	2.16 ± 0.08	1.59 ± 0.29
C: E-18%	2.24 ± 0.08	1.26 ± 0.26
D: (E+18%) + (EBL+25%)	2.12 ± 0.08	1.61 ± 0.29
E: (E-18%) + (EBL-25%)	2.20 ± 0.08	1.09 ± 0.20

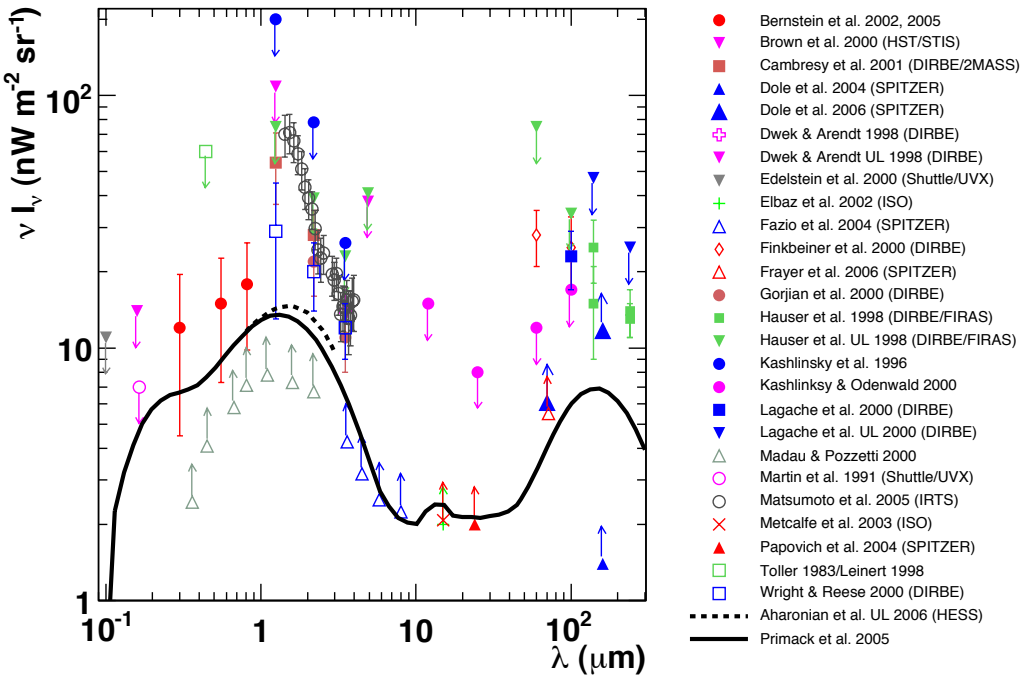

Figure 6.7: Energy density of the extragalactic background light (EBL). Direct measurements, galaxy counts, low and upper limits are shown by different symbols, as described in the legend. The black solid curve is the EBL spectrum as in Primack et al. (2005) for z=0 but upscaled by a factor 1.5 to match low limits derived from the galaxy counts (Elbaz et al., 2002; Metcalfe et al., 2003; Fazio et al., 2004).

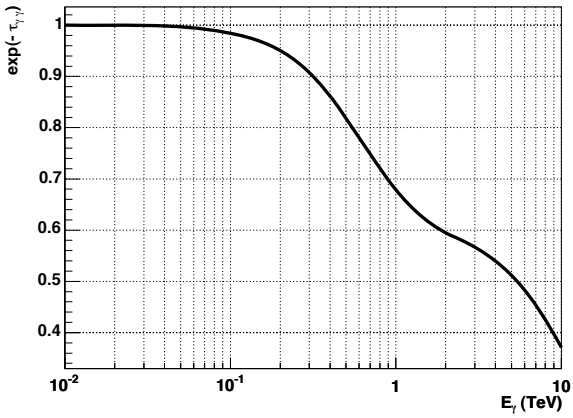

Figure 6.8: Attenuation coefficient $exp(-\tau_{\gamma\gamma})$ for Mrk 421 (z=0.030) using the EBL spectrum as shown in Fig. 6.7.

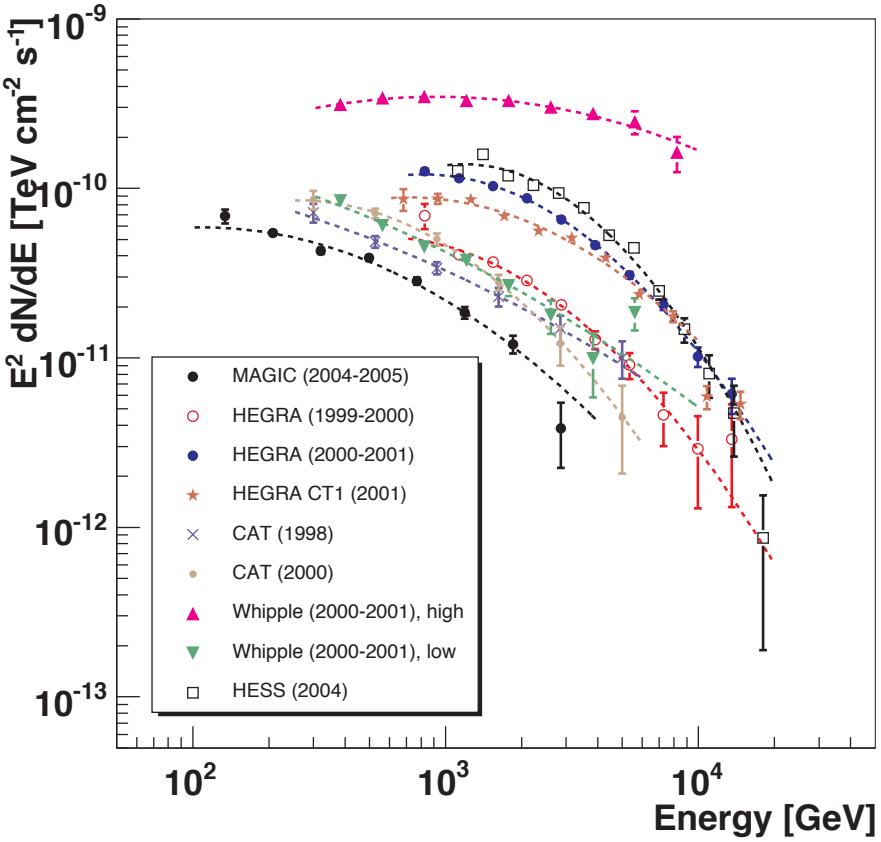

Figure 6.9: Differential energy spectra of Mrk 421 multiplied by E^2 in different activity states from different experiments. The spectra are de-absorbed using the EBL model from Primack et al. (2005), upscaled by a factor of 1.5. A log-parabolic fit is performed (dashed lines) to determine the peak position in the SED (see Fig. 6.11). For clarity, only the highest and lowest flux curves of the published Whipple results are shown. Note that for the MAGIC spectrum the upper flux limit at 4.4 TeV is not shown.

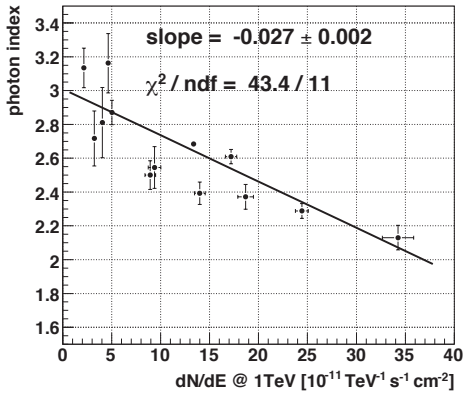

Figure 6.10: Relation between the different flux states at 1 TeV (determined from a power law approximation of the spectra between 700 GeV and 4 TeV) and the fitted photon index of the published data as in Fig. 6.9. A correlation between the flux state and the hardness can be clearly seen.

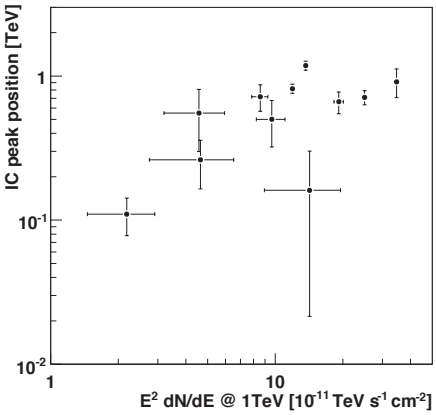

Figure 6.11: Relation between the fitted peak position in the SED and the energy density at 1 TeV for published data as in Fig. 6.9. A clear trend can be observed for the peak position to shift towards higher energies with increased source intensity.

Taking into account the systematic uncertainty of 18% on the absolute energy scale of our measurement and in addition a guessed 25% uncertainty on the EBL level, we find that neither the photon index nor the cut-off energy substantially change (See Table 6.3). The fitted photon index was found to be between 2.12 and 2.24, whereas the cut-off energy was found to be between 1.1 and 1.6 TeV. From this study we conclude that the curvature of the spectrum is source inherent: either at the measured flux level this cosmic accelerator is close to its energy limit, or there exists a source–intrinsic absorption.

6.6 Discussion

6.6.1 Comparison with previous observations of Mrk 421

In Fig. 6.9 we show a compilation of the (de-absorbed) energy density spectra using also several previously published high statistics observations of Mrk 421. For the compilation of Mrk 421 data we used historical data from CAT (Piron et al., 2001), HEGRA (Aharonian et al., 2002c; Schweizer, 2002), H.E.S.S. (Aharonian et al., 2005d), and Whipple (Krennrich et al., 2002)[3]. All measured spectra are

[3]For the Whipple measurements, only spectra in the highest and in the lowest flux state are shown in order not to clutter Fig. 6.9.

de-absorbed using the same EBL model as described in Subsection 6.5. The activity of the source during the MAGIC observations clearly was at the lower flux range end, and our results extend also to energies lower than those previously observed, thus being complementary both in source intensity and energy range. All results are, within errors, consistent with each other, and all show significant deviations from a simple power law, which cannot be explained by attenuation effects. They are, therefore, likely to be source–intrinsic.

From the compilation of the de-absorbed Mrk 421 spectra, it is evident that with an increasing flux state the spectrum becomes harder. In order to verify this, we fitted the spectra by a simple power law ($\mathrm{dN/dE} \propto \mathrm{E}^{-\alpha}$) in the overlapping energy region between 700 GeV and 4 TeV. The resulting photon indices α as function of the fitted flux at 1 TeV are shown in Fig. 6.10. Evidently, with increasing flux the spectra harden. A similar trend (but with lower statistics) was previously observed using data from individual experiments: Whipple data in Krennrich et al. (2002), HEGRA data in Aharonian et al. (2002c, 2003a), and CAT data in (Giebels et al., 2007).

The curvatures observed are indicative for a maximum in the SED, and are most likely due to inverse-Compton (IC) scattering, whose position appears to be dependent on the source flux intensity. We have, therefore, performed a log-parabolic fit for all available data. The log-parabola has the following parametrization:

$$\log 10(\nu F_\nu) = \mathrm{A} + \mathrm{B}\,(\log 10(\mathrm{E}) - \log 10(\mathrm{E}_p))\,,$$

with $\nu F_\nu = \mathrm{E}^2\,\mathrm{dN/dE}$ and E_p being the energy of the peak position. The best fit for the log-parabolic ansatz are shown in Fig. 6.9 by the dashed lines. In Fig. 6.11 we compare the resulting peak positions for the different experiments as a function of their (fitted) energy density at 1 TeV. Evidently, with increasing flux the peak shifts to higher energy values.

The present study is the first comparison of this kind between results of the different experiments. The results of the study show:

- The correlation between flux state and hardness of the spectrum, seen by previous experiments, can be confirmed with a high confidence;
- The correlation between the flux state and the position of the "IC" peak is evident;
- Systematic differences between individual experiments are rather small.

Future intensive observations extending the measurements further down to lower energies should corroborate these results. Such observations are part of the future MAGIC physics program.

6.6.2 A short comment on the light curves

In the observation period between November 2004 and April 2005 we observed night-to-night flux variations up to a factor of 2 and a maximum flux change in the entire set of a factor 4. No short-term flux variations well below 1 hour, as observed during high flaring activity in previous experiments (Gaidos et al., 1996; Aharonian et al., 2002c), were seen, although the sensitivity of MAGIC would allow to detect fast flares in the given flux range. Two equally likely explanations are that either we deal with large fluctuations resulting in the absence of any fast flare during the observation period, or fast flaring is a feature that occurs only when the source is very active. This calls for further high statistics and high sensitivity studies when the source is in its low to moderate flux state.

6.6.3 X-ray / VHE γ-ray and optical / VHE γ-ray correlation studies

The correlation between the γ-ray flux measured by MAGIC and the X-ray flux measured by RXTE/ASM is shown in Fig. 6.12. For the MAGIC flux we take the nightly average above 200 GeV (see also Fig. 6.4). For the X-ray data, we calculate the average of those RXTE/ASM pointings (dwells) which were taken simultaneously with MAGIC data, allowing ± 1 hour extension with respect to the MAGIC data in order to increase X-ray statistics. Fig. 6.12 shows a clear correlation between X-ray and γ-ray data. The linear fit (solid line), forced to go through (0,0), has a slope of $1.4 \pm 0.1\,[\frac{10^{-10}}{\mathrm{cm}^2}/\frac{\mathrm{counts}}{\mathrm{SSC}}]$, and has a χ^2 probability of 54%. The parabolic fit (dashed line) which is also forced to go through (0,0) has the same χ^2 probability of 54%. The correlation coefficient $r = 0.64^{+0.15}_{-0.22}$ (errors correspond to $1\,\sigma$ level) is different from zero by 2.4 standard deviations (taking into account the non-linearity of errors).

In Fig. 6.13 the MAGIC γ-ray flux above 200 GeV is shown together with simultaneous KVA optical data. The latter have been averaged over the MAGIC integration time. One can see a possible γ-ray/optical anti-correlation during the 8 nights of simultaneous observations, however, the correlation coefficient $r = -0.59^{+0.36}_{-0.22}$ is compatible with zero within 1.5 standard deviations.

6.6.4 Comparison with models

Given the temporal correlation between X-ray and γ-ray fluxes, it is reasonable to infer that the VHE γ-ray radiation is dominated by emission resulting from IC upscattering of the synchrotron X-ray photons by their parent population of relativistic electrons. Such correlation can be modeled with a homogeneous synchrotron-self-Compton (SSC) model. The model also predicts a parabolic correlation between X-ray and VHE γ-ray flux states. Based on this model it is possible to constrain the parameter space of the emission region and estimate its

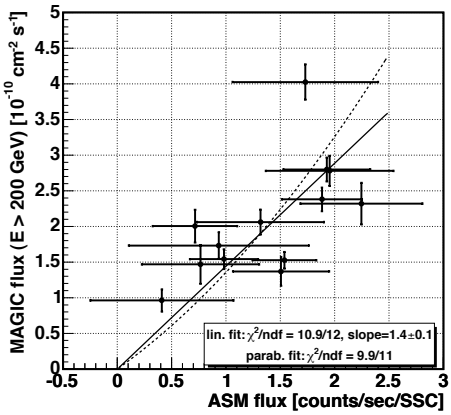

Figure 6.12: Correlation between MAGIC integral flux measurements above 200 GeV and RXTE/ASM counts for 13 nights.

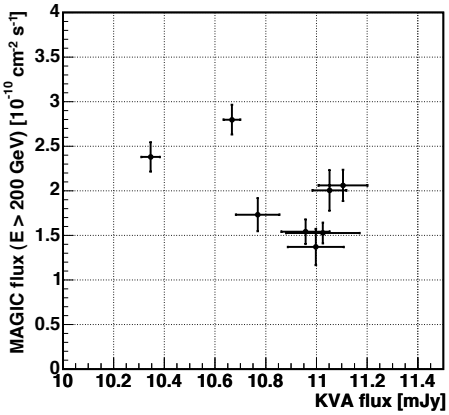

Figure 6.13: Correlation between MAGIC integral flux above 200 GeV and optical flux measured by the KVA telescope for 8 nights.

basic parameters, the Doppler factor, D, and the rest-frame magnetic field, B, of the emitting plasma in the relativistic jet. To this end we follow the procedure first devised by Bednarek and Protheroe (1997) for the Mrk 421 flare of 16 May 1994, subsequently improved by, e.g., Tavecchio et al. (2001); Bednarek and Protheroe (1999); Kataoka et al. (1999); Katarzyński et al. (2003). Application of this method requires precise simultaneous multiwavelength information. Since a synchrotron (X-ray) spectrum simultaneous with the MAGIC observations is not available, we have to resort to previous X-ray observations arguing that similar TeV γ-ray states (IC emission) should correspond to similar X-ray states (synchrotron emission). In fact, similar γ-ray spectra of Mrk 421 have already been observed several times – including the HEGRA observations in April 1998 (Aharonian et al., 1999a) for which simultaneous *Beppo*SAX observations are available (Fossati et al., 2000; Massaro et al., 2004). Here we use the X-ray spectra and parameterization, reported by Massaro et al. (2004) for 21 April 1998. Note that the X-ray flux level between the simultaneous RXTE/ASM data and the BeppoSAX data used here is very similar (see Fig. 6.15).

The low to moderate flux state MAGIC γ-ray spectrum, reported here for energies at $\sim$100 GeV, warrants a better investigation of the crucial energy range where the IC peak is expected to occur than in previous data sets. In cooperation with Wlodek Bednarek and following Bednarek and Protheroe (1997, 1999) we then constrain the allowed parameters of the emission region (D and B) from the ratio of the γ-ray power to the X-ray power, measured at their respective peak emission (see thick curves in the upper panels of Fig. 6.14). The radiation field density and the electron spectrum, co-spatial in the blob, were derived as

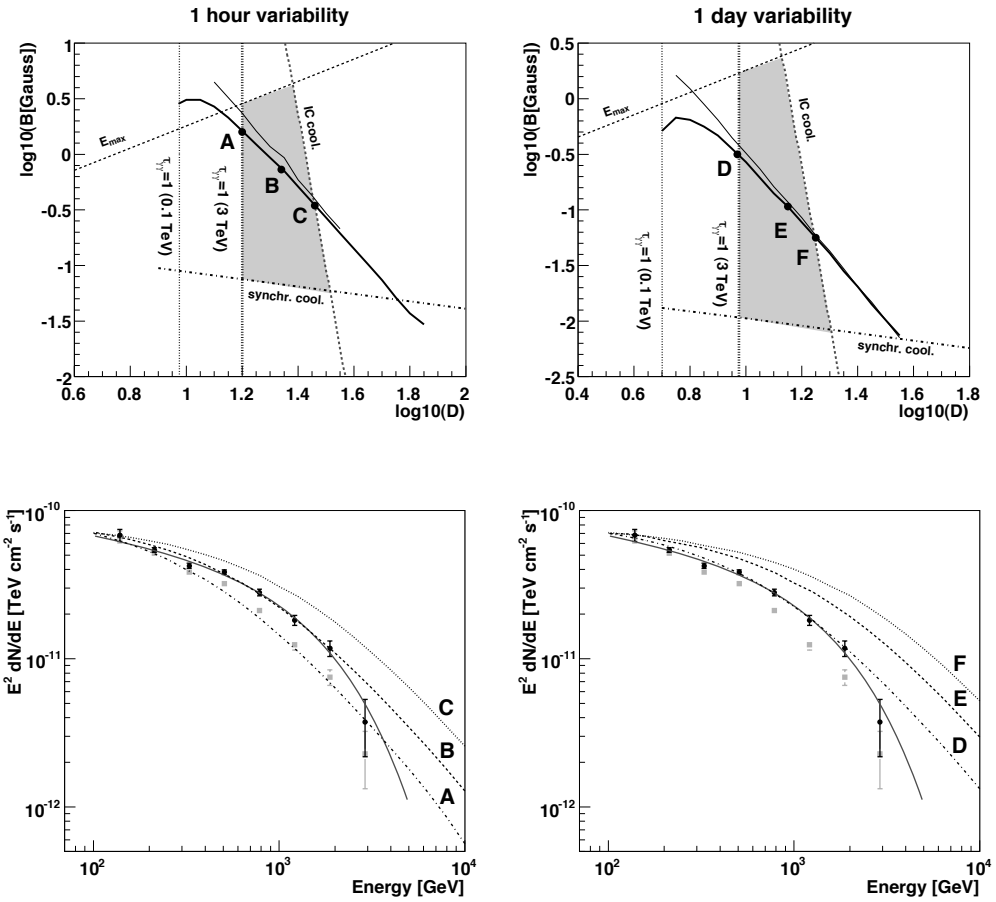

Figure 6.14: Constraints on the parameter space (Doppler factor, D, versus magnetic field strength, B) for the emission region in the jet of Mrk 421 based on the one-zone homogeneous SSC model. From the ratio of the γ-ray to X-ray power during the MAGIC observations of Mrk 421 (measured at the peaks in the synchrotron and IC spectra) the allowed values are limited to the thick curves (assumed IC peak at 100 GeV) or to the thin curves (assumed IC peak at 10 GeV). The left figures correspond to a 1 hour variability, whereas the right figures correspond to a 1 day variability. The physical conditions in the blob are limited by the electron cooling in the synchrotron and IC processes, optical depth for γ-rays, and maximum energy of electrons, as discussed in the text. These constraints are shown by the dashed and dot-dashed lines. The allowed region is limited by these lines and is marked by the grey shaded area. The γ-ray spectra are calculated for the values of the Doppler factor and magnetic field strength marked by A, B, and C (for 1 hr variability), and D, E, and F (for 1 day variability). They are compared with the de-absorbed MAGIC spectrum (shown as full black circles) in the bottom figures. The fit by a power law with an exponential cut-off to the de-absorbed spectrum (as in Fig 6.6) is shown by the black solid line, whereas the measured spectrum is shown by the grey full squares.

a function of D and B for a blob radius assumed equal to the light travel time corresponding to the shortest reported variability time scale (for observational arguments see Takahashi et al. (2000)). We further constrain the allowed parameter space by arguing that the synchrotron and IC cooling time scales should be shorter than the observed variability time scale. These conditions are fulfilled above the dot-dashed lines (for synchrotron cooling) and on the left of the grey dashed line (for the IC cooling) for the 1 hr (upper left panel of Fig. 6.14) and 1 day (upper right panel of Fig. 6.14) variability time scales. The condition that the blob has to be transparent to the VHE γ-rays leads to a further lower bound on D by requiring that the optical depth by pair production has to be lower than unity. The corresponding limits for photon energies of 100 GeV and 3 TeV (which define the energy range of MAGIC measurement) are shown in the upper panels of Fig. 6.14 as thin and thick dotted lines, respectively. One last condition arises from comparing the maximum energy of electrons, determined by the maximum energy of synchrotron photons $\sim$40 keV, with the maximum energy of the detected photons $\sim$3 TeV (see dashed line in the upper panels of Fig. 6.14). These limiting conditions build an allowed region in the D-B plane as marked by the grey shaded area. The allowed parameters of the emission region correspond to the part of the thick full curve inside the region limited by all these lines (see Fig. 6.14). In order to determine the values of D and B more precisely, we now calculate the γ-ray spectra for the points A, B, and C for 1 hr variability, and the points D, E, and F for 1 day variability, and compare the predicted spectrum with the actual de-absorbed spectrum. From the lower panels of Fig. 6.14 it is clear that the best description is provided by the blob with Doppler factor $D \sim$22 and magnetic field $B \sim$0.7 G (the point B) for 1 hr variability, and $D \sim$9 and $B \sim$0.3 G (the point D) for 1 day variability. In order to assess how this result is sensitive on the correct localization of the peak energy in the γ-ray spectrum (which is in fact only limited by the lower energy end of the MAGIC spectrum), we show the allowed parameter space for the γ-ray peak at 10 GeV (see thin full curves in Fig. 6.14). The constraints for the peak at 10 GeV and 100 GeV are almost the same for the parts of the curves inside the allowed region. It is interesting that the emission parameters, as estimated here for the moderate flux state of Mrk 421 (for the 1 day variability time scale), are not very different from those estimated by Bednarek and Protheroe (1997) for the flaring state. This suggest that the flaring state may not be related to the significant change of the blob's Doppler factor and magnetic field strength.

In Fig. 6.15 the broadband SED of Mrk 421 is shown. Large symbols represent averaged data described in this Thesis: optical data from KVA (star), X-rays from RXTE/ASM (full square), γ-rays from MAGIC (full points). The grey curve in the X-rays corresponds to a log-parabolic fit performed by Massaro et al. (2004) on *Beppo*SAX data of Mrk 421 taken on 21 April 1998. The two black curves through the γ-ray spectrum are almost indistinguishable and correspond to the best SSC model parameters for 1-hr and 1-day variability time scales (points B

and D respectively, calculated according to Eq. (13) in Bednarek and Protheroe (1999) who apply the Klein-Nishina cross-section as in 2.48 of Blumenthal and Gould (1970)).

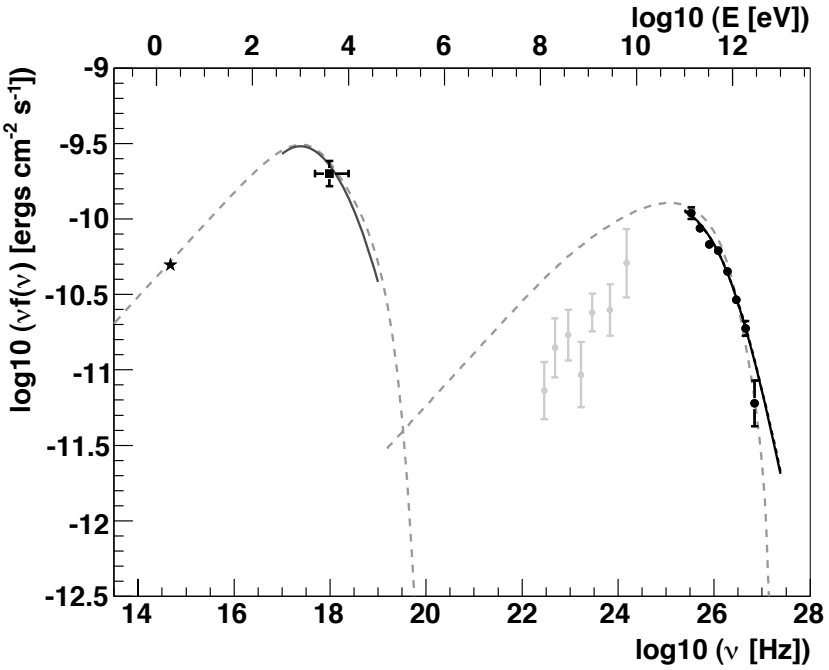

Figure 6.15: The broad-band SED of Mrk 421 from optical wavelengths through VHE γ-rays. Large symbols represent averaged data described in this Thesis: optical data from KVA (star), X-rays from RXTE/ASM (full square), de-absorbed γ-rays from MAGIC (full points). The grey full squares are archival EGRET measurements (Hartman et al., 1999). The grey curve in the X-rays corresponds to the log-parabolic fit taken from Massaro et al. (2004) using *Beppo*SAX (Boella et al., 1997) data of Mrk 421 taken on 21 April 1998. The two black curves through the γ-ray spectrum (almost indistinguishable) correspond to the SSC model parameter sets B and D (see text and Fig. 6.14 for details). The grey dashed line denotes a fit by the SSC model as in Krawczynski et al. (2004), see text for details.

In addition, we apply the SSC code provided by Krawczynski et al. (2004) to our data set. The fitted broad-band SED is shown by the grey dashed line in Fig. 6.15, and the model parameters are listed in Table 6.4. For the fit, we used the simultaneous KVA, ASM and MAGIC data, as well as the archival *Beppo*SAX observations from 21 April 1998 (Massaro et al., 2004). In contrast to the parameters adopted in Krawczynski et al. (2001), we used a smaller Doppler factor (15 instead of 50), resulting in a somewhat larger emitting region (1.1×10^{16} cm instead of 2.7×10^{15} cm), and a higher particle density (0.15 [erg cm^{-3}] instead of

Table 6.4: Fitted SSC model parameters for Mrk 421. The corresponding photon spectrum is shown in Fig. 6.15.

Parameter	Value
spherical blob with:	
Doppler factor	15
magnetic field	0.20 Gauss
radius of emitting region	1.1×10^{16} cm
injected electron spectrum:	
electron energy density	0.15 erg/cm^3
$5 < \log10(E[eV]) < 10.9$	Index 2.31
$10.9 < \log10(E[eV]) < 11.6$	Index 3.88

0.01 [erg cm^{-3}][4]). We note that the fitted values of magnetic field and Doppler factor are within the allowed range as defined above. Remarkably, the archival EGRET data (Hartman et al., 1999) are somewhat below the fit, suggesting an IC peak around 100 GeV.

6.7 H.E.S.S. – MAGIC simultaneous observations of Mrk 421

New generation Cherenkov telescopes cover a wide range of longitudes (137°E to 110°W) allowing continuous observations to follow transient sources. Given the close match in longitude of the MAGIC (17.9°W) and H.E.S.S. (16°E) sites, simultaneous observations at greatly differing zenith angles are also feasible. The measurable energy range can thus be extended beyond what is accessible to individual instruments. The planning and coordination of world-wide observations is challenging and requires close interaction between the different collaborations. First results from a joint H.E.S.S. and MAGIC observation of Mrk 421 in 2004 are presented here. The results were also published in Mazin et al. (2005). The potential of Global Network of Cherenkov Telescopes (GNCT) campaigns for blazar physics and studies of the energy dependent absorption of very high energy (VHE) γ-rays on the extragalactic background light are discussed in Appendix A.6.

Triggered by an increased activity observed in the X-ray band and by observations with the Whipple telescope (H. Krawczynski, private communication) on December 14, 2004 the H.E.S.S. and MAGIC collaborations performed a joint observation of Mrk 421. Due to weather conditions a common observation could only be performed during two nights (December 18 and 19). Moreover, due to observational constrains (such as zenith angle and dark time), the common ob-

[4] 1 erg = 10^{-7} Joule

servational window was only open for 30 minutes on each night. The joint data sample of Mrk 421 encompasses:

1. H.E.S.S. : 25 min, zenith angle range = 65-67°, good weather conditions
2. MAGIC: 25 min, zenith angle range = 47-54°, good weather conditions.

The data have been analyzed independently by both experiments without communicating a preliminary status of the results.

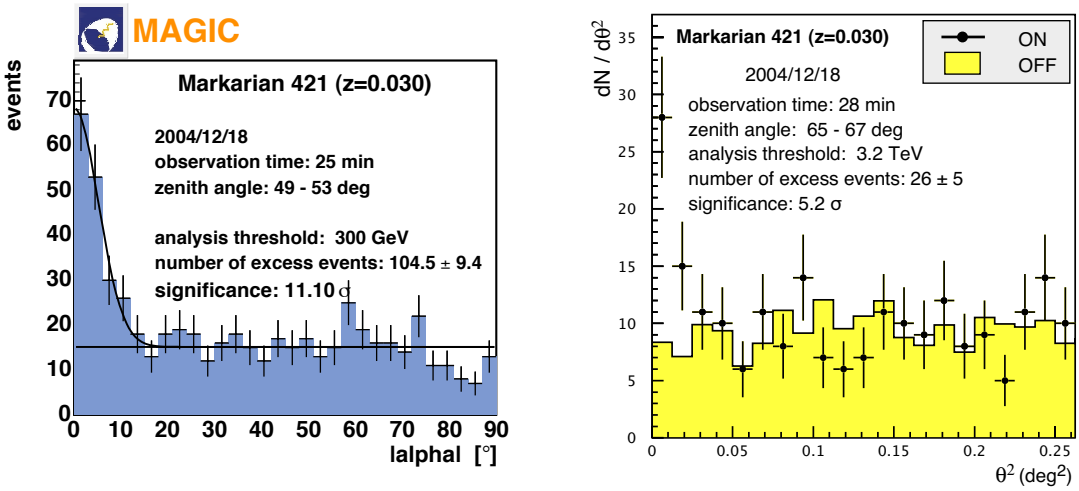

Figure 6.16: *Left: Alpha* distribution of the MAGIC data of the simultaneous data set. *Right:* θ^2 distribution of the H.E.S.S. data of the simultaneous data set.

The results of the analysis of the joint data are shown in Fig. 6.16. A clear detection in both experiments in the simultaneous data set (6 - 10 σ) could be achieved and a reasonable number of photons in the different energy bands was collected. The results are encouraging given the comparably low flux state of the source, the short simultaneous observation time, and the non-optimal zenith angles observed.

The joint energy spectrum is shown in Fig. 6.17. The joint spectrum can be well described by a simple power law with a spectral index $\Gamma = 2.51 \pm 0.11$. The spectrum has not been corrected for the EBL absorption. The excellent agreement between both data in the overlap region is encouraging and prove the potential of joint observations.

6.8 Concluding Remarks

Mrk 421 was observed with the MAGIC telescope during several months in 2004 and 2005. Briefly, I have presented the following:

- first high sensitivity observation down to $\approx 100\,\mathrm{GeV}$;

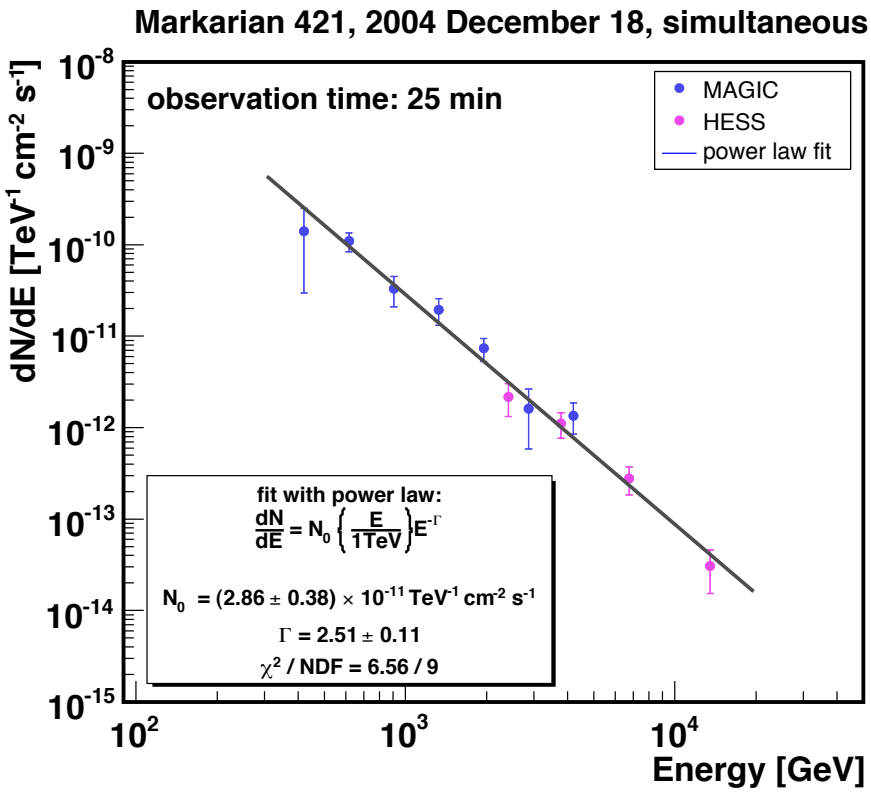

Figure 6.17: The joint H.E.S.S.-MAGIC energy spectrum of Mrk 421. Note the extension of the accessible energy range due to the combination of the two instruments.

- no strong evidence for short flares below 1 hour duration despite sufficient sensitivity;
- flux variation up to a factor 2 between consecutive nights and up to a factor 4 in the entire observation period;
- confirmation of a source–inherent effect resulting in a curved spectrum after de-absorption in case of low to moderate flux intensity;
- a strong correlation between spectral hardness (photon index between 700 GeV and 4 TeV) and flux intensity, obtained by comparison of the de-absorbed energy spectra of various experiments covering different flux levels;
- a clear trend for the (possibly IC) peak position to shift towards higher energies with increased source intensity, obtained by the same comparison;
- confirmation of a significant correlation between X-ray and VHE γ-ray intensity during a state of low to medium intensity;

- a hint that different flaring states result from differences in electron populations (electron spectrum) rather than from significant change of the blob's Doppler factor and magnetic field strength.

I want to add the following conclusions. The flux state was found to be low to moderate, ranging in intensity between 0.5 and 2 Crab units, integrated above 200 GeV. While clear night to night variations were found, the intra-night light curve, binned in 10-minute time intervals, does not show significant variations. I want to stress that MAGIC is sensitive enough to detect variabilities on the 10-minute time scale at such moderate flux level. A clear correlation ($r = 0.64^{+0.15}_{-0.22}$) between X-rays and γ-rays was found, while no clear correlation was seen between optical and γ-rays. This supports the leptonic origin of the γ-rays from Mrk 421. The energy spectrum resulting from the combined MAGIC data, corrected for the extragalactic absorption, suggests the presence of an IC peak at about 100 GeV when the source is in a low / moderate flux state. The spectrum is clearly curved at energies above 1 TeV, and can be fitted by a power-law with an exponential cut-off. The broad-band SED in the observed flux state can be well described by a homogeneous SSC model provided that the emission region moves with a Doppler factor $\sim$9 and its magnetic field strength is $\sim$0.3 G for a 1-day variability time scale. Surprisingly, these parameters do not differ substantially from those estimated for the emission region of Mrk 421 during a strong flare (Bednarek and Protheroe, 1997). The fit with an alternative SSC code of Krawczynski et al. (2001) lead to similar Doppler factor and magnetic field values.

Chapter 7

Discovery of VHE γ-rays from Markarian 180

An optical / VHE γ-ray correlation was never observed before. However, the optical–GeV correlations (seen e.g. in 3C 279 (Hartman et al., 2001)) suggest that at least in some sources, such correlations exist. Using this as a guideline, the MAGIC collaboration has been performing Target of Opportunity observations whenever alerted that sources were in a high flux state in the optical band. See more on observation strategies for MAGIC in Appendix A. In this Chapter I report on the discovery of VHE γ-rays from Markarian 180 with MAGIC. The discovery was accompanied by an optical outburst of the source, and this makes it very tempting to speculate about the connection between optical activity and increased VHE emission. The analysis and the results are published in Albert et al. (2006b).

7.1 Motivation of the observations

The AGN Markarian 180 (Mrk 180, 1ES 1133+704) is a well-known high frequency peaked BL Lac (HBL) at a redshift of $z = 0.045$ (Falco et al., 1999). A general feature of BL Lac objects is that their spectral energy distribution (SED) exhibits the already mentioned two-bump structure (see Chapter 2 for more details). In many cases the second peak of the SED is not observable because of low sensitivity above a few 100 MeV of satellite-borne detectors and too high energy threshold of ground-based γ-ray detectors. In case of Mrk 180, HEGRA (Aharonian et al., 2004a) and Whipple (Horan et al., 2004) observed this object but were only able to derive flux upper limits, and EGRET did not detect the source (Falomo et al., 1994; Hartman et al., 1999).

In the optical, Mrk 180 is characterized by a bright host galaxy $R = 14.17 \pm 0.02$ mag and a much fainter (variable) core $R = 15.79 \pm 0.02$ mag (Nilsson et al., 2003). The variations in total optical brightness are therefore small. The

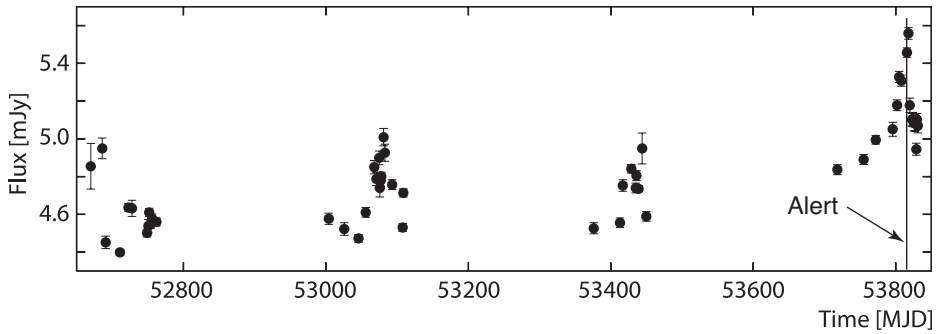

Figure 7.1: The R-band light curve of Mrk 180 extending from January 2003 to end of March 2006 as measured by the KVA telescope. The vertical line indicates the date of the alert. 5 mJy is equivalent to 14.47 mag.

source is observed regularly as part of the Tuorla Observatory Blazar monitoring program (http://users.utu.fi/kani/1m/) with the Tuorla 1 m telescope and the KVA 35 cm telescope (http://tur3.tur.iac.es/). To determine the core flux we had to subtract the flux of the host galaxy and a nearby star within the 5″ aperture radius (together R=14.96 mag resp. 3.2 mJy (Nilsson et al., 2006)).

After Mrk 180 had been detected in the X-rays by *HEAO-1* (Mufson and Hutter, 1981) it was observed by various satellites with fluxes ranging from 6.3 to 22×10^{-12} erg cm^{-2} s^{-1} (Donato et al., 2001) around 1 keV and 5.0 to 9.8×10^{-12} erg cm^{-2} s^{-1} in the 2-10 keV band (Perlman et al., 2005; Donato et al., 2005). The source is monitored by the ASM on-board the RXTE satellite.

The observation of Mrk 180 was triggered by a brightening of the source in the optical on 2006 March 23 by Elina Lindfors. She gave the alert as the core flux increased by 50% from its quiescent level value as determined from over three years of data recording, shown in Fig. 7.1. During the MAGIC observation optical follow-up observations were performed with KVA. The simultaneous MAGIC, ASM and KVA light curves are shown in Fig. 7.2. Around this time Mrk 180 was also observed as part of the AGN monitoring program by the University of Michigan Radio Observatory (UMRAO). The 4.8 GHz flux density was 0.21±0.02 Jy and the 14.5 GHz flux density was 0.22±0.06 Jy from 2006 Jan 1. - Apr. 13 (H. D. and M. F. Aller, private communication). No evidence for flaring was found between January and April 2006.

7.2 The data set

Mrk 180 was observed in 2006 during 8 nights (from March 23 to 31), for a total of 12.4 hours, at zenith angles ranging from 39° to 44°. The observations were performed in the WOBBLE mode (see Section 4.2.2), in which the telescope is pointed alternatively for 20 minutes to two opposite sky positions at 0.4° off the

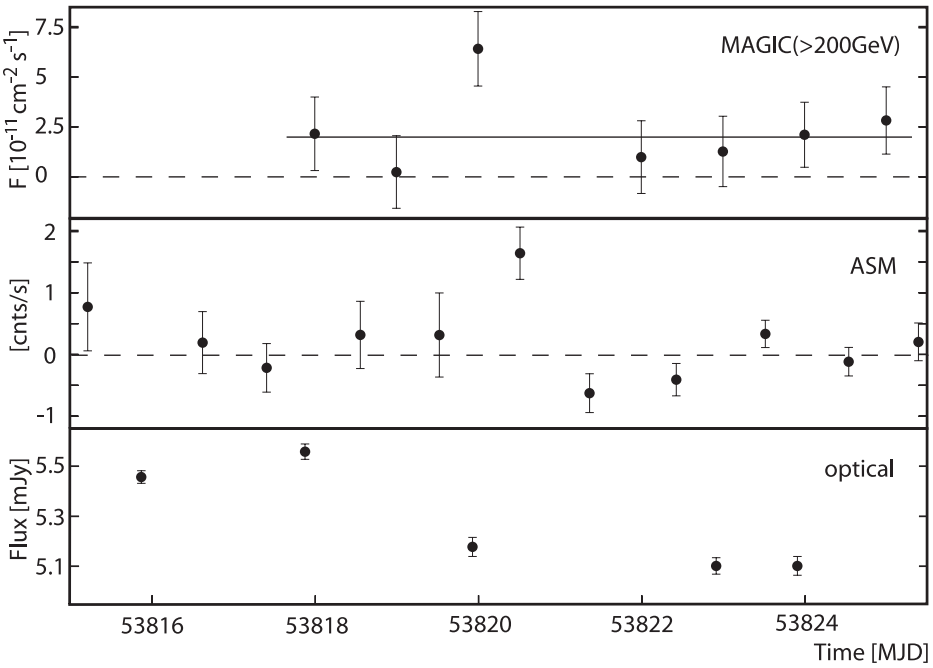

Figure 7.2: Light curve of Mrk 180 for MJD=53815-53825 (March 21 to March 31). Upper panel: VHE γ-rays measured by MAGIC above 200 GeV. Middle panel: ASM count rate. Lower panel: optical flux measured by KVA. The dashed lines show the zero level, the solid line indicates the mean integral flux as measured by MAGIC above 200 GeV.

source. Runs with unusual trigger rates due to detector problems or adverse atmospheric conditions were rejected. The total observation time was thus reduced to 11.1 hours.

The data were analyzed using the standard analysis and calibration programs as described in Chapter 5. For the γ/hadron shower separation the Random Forest method was used (Section 5.9). For the γ-ray signal extraction the θ^2 approach was applied (Section 5.10.2). A final cut of $\theta^2 < 0.024$ is applied to determine the significance of the signal and the number of excess events. The energy of the γ-ray candidates was also estimated using the Random Forest technique. The applied cuts were chosen to be looser than the ones in Fig. 7.3 in order to gain statistics on the γ-ray candidates. Due to the large zenith angle of the observation, the corresponding energy threshold (defined as the peak in the differential energy distribution of the MC-γ events) after cuts was about 200 GeV. Effects on the spectrum determination, introduced by the limited energy resolution of the detector, were corrected using the unfolding according to Section 5.13.

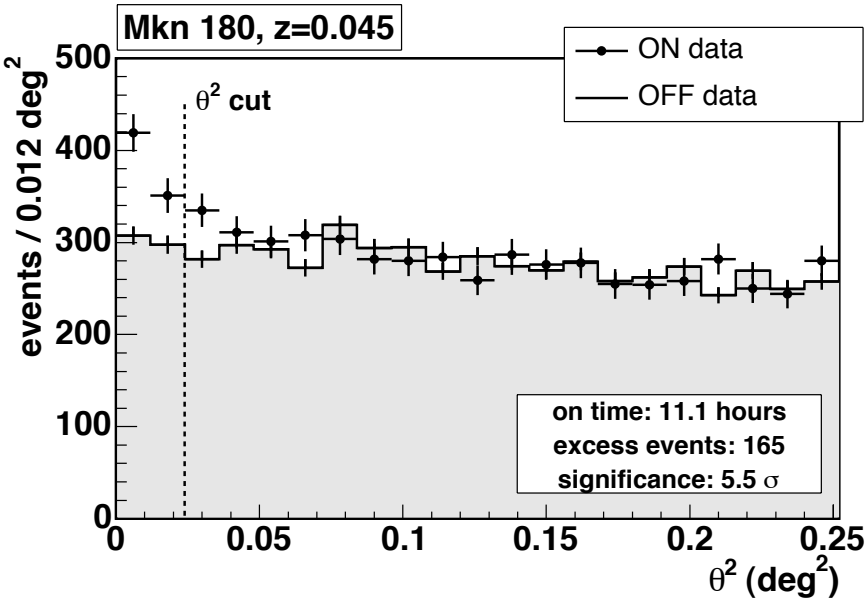

Figure 7.3: The θ^2-distribution for the ON-source data (points) and normalized OFF-source events (grey histogram) for Mrk 180. The vertical dashed line indicates the θ^2 cut used to determine excess events. The total excess of 165 events corresponds to a significance of 5.5 σ.

7.3 The VHE γ-ray signal

The distribution of θ^2 values after cuts is shown in Fig. 7.3. The signal of 165 events over 605.2 normalized background events corresponds to a 5.5 σ excess using Eq. 17 in Li and Ma (1983). The shape of the excess is consistent with a point-like source seen by MAGIC.

7.4 Light curves and their variability

Fig. 7.2 shows the VHE light curve together with the ASM daily averages and the R-band flux data. No evidence for flux variability was found in the MAGIC for $E > 200\,\mathrm{GeV}$. The fit to the nightly integrated flux is consistent with a constant emission ($\chi^2 = 7.1$ for 6 degrees of freedom). The X-ray flux of the source is generally below the ASM sensitivity, but on March 25 a 3 σ excess was observed, which suggests that the source was also active in X-rays. The optical flux reached its maximum in the night MAGIC started the observations (March 23) and began to decrease afterwards.

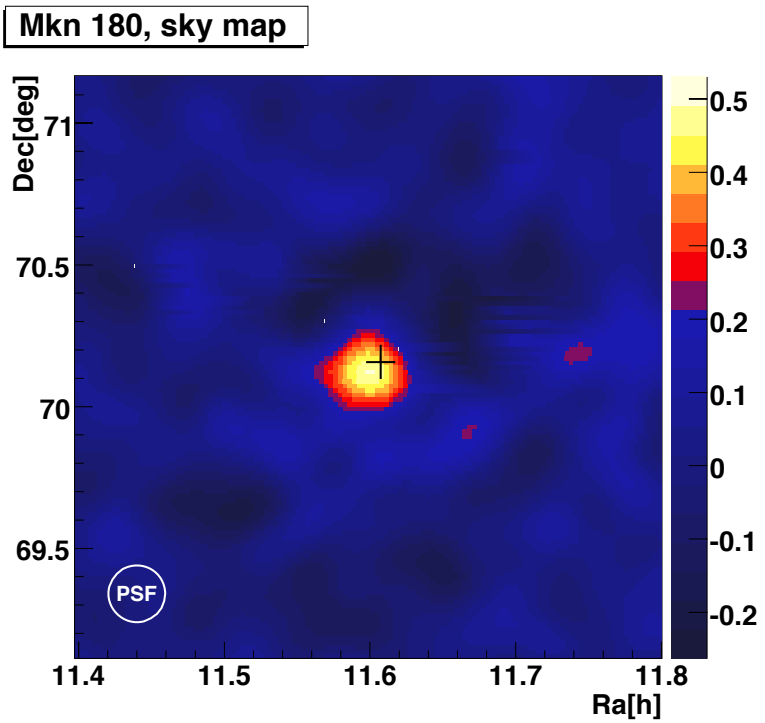

Figure 7.4: Sky map of smoothed excess events in the region of Mrk 180. The catalogue source position is marked by the black cross and coincides with the measured excess within the errors. The sky map is folded with a Gaussian of $\sigma = 0.1\,\mathrm{deg}$, which corresponds to the γ-PSF of the analysis.

7.5 The energy spectrum of Mrk 180

The measured energy spectrum of Mrk 180 is shown in Fig. 7.5. Assuming a power law spectrum we obtained the following parameterization:

$$\frac{\mathrm{d}N}{\mathrm{d}E} = (4.5 \pm 1.8) \times 10^{-11} \left(\frac{E}{0.3\,\mathrm{TeV}} \right)^{-3.3 \pm 0.7} \frac{1}{\mathrm{TeV\,cm^2\,s}}$$

The observed integral flux above 200 GeV is

$$F(E > 200\,\mathrm{GeV}) = (2.25 \pm 0.69) \times 10^{-11} \mathrm{cm^{-2} s^{-1}},$$

which corresponds to $1.27 \times 10^{-11}\,\mathrm{ergs\,cm^{-2} s^{-1}}$ resp. 11% of the Crab Nebula flux measured by MAGIC. The errors are statistical only. We estimate the systematic errors to be around 50% for the absolute flux level and 0.2 for the spectral index. The large systematic flux error is a consequence of the steep slope. See more on the systematic errors in Section 5.16.

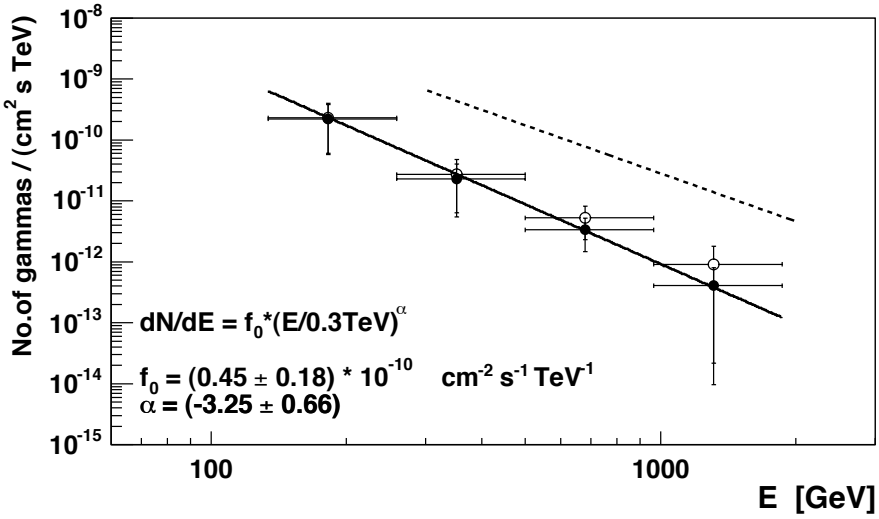

Figure 7.5: The differential energy spectrum of Mrk 180. Full circles: the spectrum measured by MAGIC. Open circles: the de-absorbed energy spectrum (see text). The horizontal bars indicate the size of each energy bin. The black line represents a power law fit to the measured spectrum. The fit parameters are listed in the figure. For comparison, the Crab Nebula energy spectrum as measured by MAGIC is shown (Albert et al. (2007i), dashed line).

7.6 The intrinsic energy spectrum of Mrk 180

The VHE γ-rays from Mrk 180 are partially absorbed by the low energy photons of the evolving extragalactic background light (EBL, see Section 1.5 and Chapter 3 for details). Given the redshift z=0.045 of Mrk 180 the effect is small for photons with energies below 1 TeV. I calculate the optical depth and the resulting attenuation of the VHE γ-rays from Mrk 180 using the number density of the evolving EBL provided by the best fit model of Kneiske et al. (2002). This state-of-the-art model is consistent with the recently derived upper limits on the EBL inferred from arguments on AGN spectra by (Aharonian et al., 2006a) but see also Chapter 9. The attenuation was determined by numerical integration of equation 1.10. The de-absorbed energy spectrum of Mrk 180 is also shown in Fig. 7.5 (open circles). A fit with a simple power law to the de-absorbed spectrum reveals a slope with $\alpha = -2.8 \pm 0.7$.

7.7 Discussion of the results

I have presented the first detection of VHE γ-ray emission from Mrk 180. The discovery was triggered by an optical flare, but no significant variations in the

VHE regime were found. The short observation period and the small signal do not allow to carry out detailed studies. It is therefore not possible to judge whether the detected VHE flux level represents a flaring or a quiescent state of the AGN.

Earlier observations by other experiments have only set upper limits on the VHE γ-ray emission from Mrk 180. HEGRA observed the source for 9.8 hours and derived an upper limit (99% c.l.) at 1.5 TeV of 12% of the Crab Nebula flux (Aharonian et al., 2004a). Whipple observed Mrk 180 during three observation periods for a total of 26.8 hours, and has set a flux upper limit at 300 GeV of 10.8% of the Crab Nebula flux (Horan et al., 2004). Both upper limits are above the flux presented in this paper.

Fig. 7.6 shows the broad-band SED of Mrk 180: the radio, optical and X-ray data are from UMRAO, KVA, ASM, and the NED database. The VHE data from this analysis are compared with the above quoted upper limits. Simultaneous data are noted in black while historical data are noted in grey. The predicted flux by the leptonic phenomenological model of Fossati et al. (2000) (shown as dashed line) is too high, as already emphasized by the non-detection measurements (Aharonian et al., 2004a; Horan et al., 2004). A more detailed synchrotron self Compton (SSC) model from (Costamante and Ghisellini, 2002) (shown as solid line) seems to describe the data more closely. I do not model the simultaneous data with an independent SSC code. The reason is that there are neither simultaneous nor historical X-ray data which would help to determine the Synchrotron peak position. In addition, the VHE γ-ray data do not provide the variability time scale neither the position of the IC peak. The degeneracy is, therefore, very big between possible parameter sets and no particular constraints on the emission mechanism can be derived from this kind of modeling.

The rather steep slope of the VHE spectrum suggests an IC peak position well below 200 GeV, while the non-detection by EGRET gives a lower limit of ~ 1 GeV for the peak position. This is in agreement with the SSC model of Costamante and Ghisellini (2002) suggesting the IC peak position at around 10 GeV. The overall IC luminosity, however, is underestimated in this model: the observed integral flux above 300 GeV is a factor 30 larger than predicted. An explanation for this discrepancy could be the model's underlying assumption of a quiescent state synchrotron spectrum to obtain the IC flux. This could indeed suggest that our measurement was made during a high state.

7.8 Concluding Remarks

The discovery of VHE emission from Mrk 180 during an optical outburst makes it very tempting to speculate about the connection between optical activity and increased VHE emission. Since Mrk 180 has not been observed prior to the outburst with MAGIC and the upper limits from other experiments are above the observed flux level, further observations are needed. See more on a possible

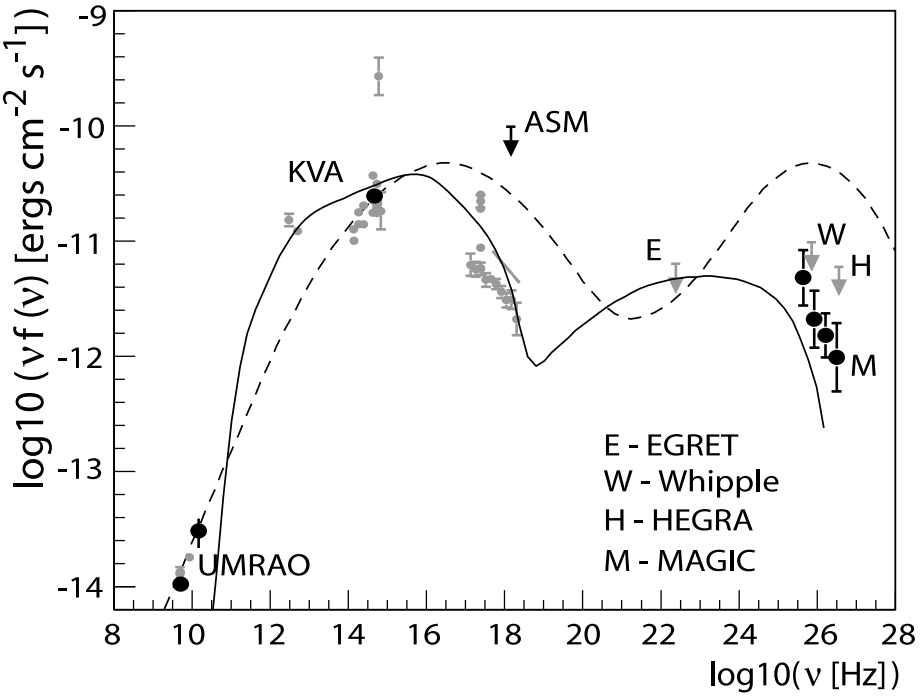

Figure 7.6: The spectral energy distribution of Mrk 180. Simultaneous data (UMRAO, KVA, ASM, and MAGIC) are noted in black. Grey points represent historical data (Giommi et al., 2002; Perlman et al., 2005). The arrows denote the upper limits from ASM, EGRET (Fichtel et al., 1994), Whipple, and HEGRA. The solid line is from Costamante and Ghisellini (2002) and the dashed line is from Fossati et al. (2000) (see text).

optical / VHE emission in the following Chapter.

Chapter 8

Discovery of VHE γ-rays from 1ES 1011+496

Here I report on the discovery of Very High Energy (VHE) γ-ray emission from BL Lacertae object 1ES 1011+496. The observations were triggered like in the case of Mrk 180, Chapter 7, by an optical outburst in March 2007 and the source was observed with the MAGIC telescope from March to May 2007. The discovery was made during the writing phase of the thesis, the results are also published in Albert et al. (2007c).

8.1 Motivation of the observations

1ES 1011+496 is, like Mrk 421 and Mrk 180, a high-frequency-peaked BL Lac (HBL) with a redshift of $z = 0.212$. The source is a strong X-ray emitter and has been also detected by EGRET (Hartman et al., 1999). 1ES 1011+496 is one of the TeV blazar candidates as defined by Costamante and Ghisellini (2002). Previous observations by the HEGRA CT system and the Whipple telescope resulted in upper limits only (Aharonian et al., 2004a; Horan et al., 2004). The non-detection is most likely a consequence of a relatively high energy threshold of these instruments and a large distance of 1ES 1011+496 causing a strong absorption by the EBL (see Section 1.5 and Chapter 3 for details of the EBL). The low energy threshold and a good sensitivity of MAGIC around 150 GeV motivated observations of this VHE γ-ray candidate with MAGIC.

1ES 1011+496 was also observed with MAGIC in March–April 2006, as part of a systematic scan of X-ray bright HBLs, in a lower optical state. The observations resulted in a 3.5σ hint of a VHE γ-ray signal. The analysis of the data are presented in Albert et al. (2007f) and are not part of this thesis. Here I report on the observations of 1ES 1011+496 in 2007 only.

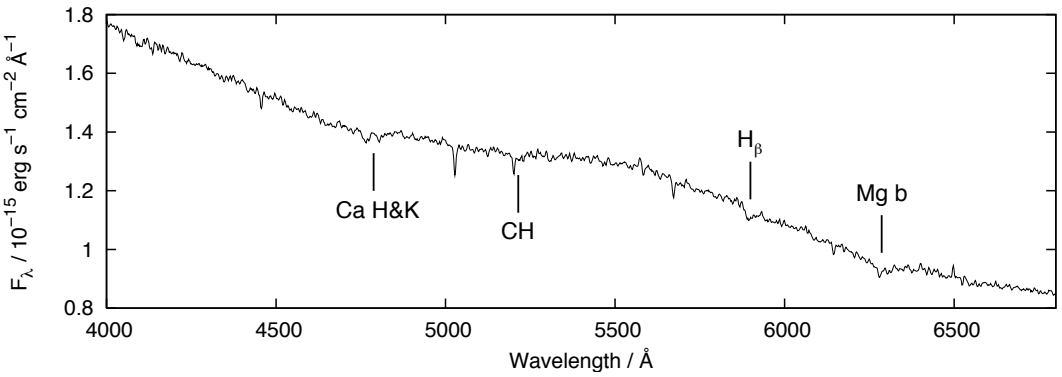

Figure 8.1: Optical spectrum of 1ES 1011+496 obtained with the Multi Mirror Telescope, using the Blue Channel Spectrograph with the 300 line/mm grating, a 1.5" slit, and Loral 3kx1k CCD. Integration time was 30 minutes. Absorption lines of host galaxy (Ca H&K, CH G, H_β and Mg b) are clearly visible and indicate a redshift of $z = 0.212 \pm 0.002$.

8.2 Redshift determination of 1ES 1011+496

Until now the redshift of 1ES 1011+496 has been uncertain as it was based on assumed association with cluster Abell 950 (Wisniewski et al., 1986) leading to a value of $z = 0.200$. Due to a high relevance of the redshift for the modeling of the VHE γ-ray emission, further investigations to determine the distance have been made. Fortunately, an optical spectrum of 1ES 1011+496 of good quality was found in the archival data taken by Eric Perlman with the Multi Mirror Telescope (E. Perlman, private communication). The optical spectrum is shown in Fig 8.1. The instrument used to take the spectrum is the Blue Channel Spectrograph with the 300 line/mm grating, a 1.5" slit, and Loral 3kx1k CCD. With help of Kari Nilsson from the Tuorla Observatory, the following absorption lines from the host galaxy could have been identified in the spectrum: Ca H&K, CH G, H_β and Mg b). The combination of the Doppler-shifted lines allowed to determine the redshift of the source: $z = 0.212 \pm 0.002$. The redshift determined here makes 1ES 1011+496 the most distant source yet detected to emit VHE γ-rays.

8.3 The data set

The MAGIC observations were triggered in 2007 by a high optical state of 1ES 1011+496 on March 12 (Fig. 8.2). The source has been monitored for more than four years with the optical KVA and Tuorla 1m telescopes as a part of the Tuorla blazar monitoring program. In March 2007 it reached the highest flux level ever observed during the monitoring. The core flux, which is the host galaxy subtracted flux level (the host galaxy level is taken from Nilsson et al. (2006) and is 0.49 ± 0.02 mJy), increased by more than 50% from the local minimum of

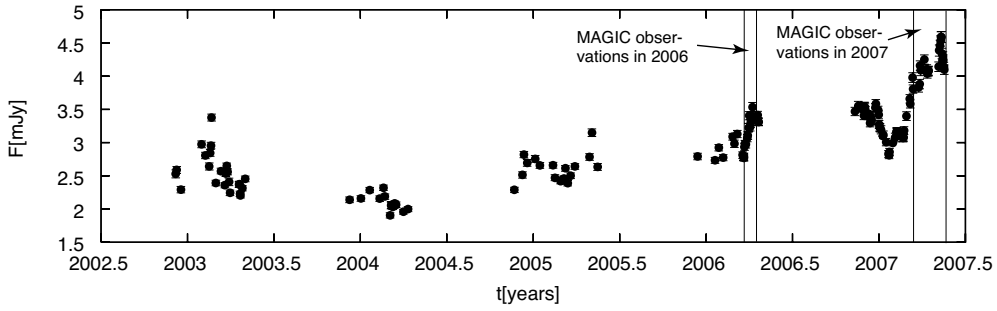

Figure 8.2: The optical R-band light curve of 1ES 1011+496 from Tuorla 1 meter and KVA telescopes. The vertical lines indicate the dates of MAGIC observations in 2006 and 2007. The presented analysis of the MAGIC data includes the 2007 observations only.

the light curve. The high optical state of increased flux continued through the MAGIC observations, even there was an observation gap of 3 weeks (for both the MAGIC and KVA observations) due to bad weather.

1ES 1011+496 is monitored by RXTE/ASM and SWIFT/BAT, but the X-ray flux of the source is below the sensitivity of these instruments and the light curves show no indication of flaring. The source was also observed in Metsähovi Radio Observatory in May 2007. The source was not detected at 37 GHz, which indicates that the source was not in high state in millimeter regime (A. Lähteenmäki, private communication).

After the alert, MAGIC observed the source in March–May 2007. The datataking was delayed due to bad weather. The total observation time with MAGIC was 26.2 hours and the observations were performed at zenith angles ranging from 20° to 37°. The observations were done in the WOBBLE-mode (see Section 4.2.2). After removing runs with unusual trigger rates mostly caused by bad weather conditions, the effective observational time amounts to 18.7 hours.

8.4 The energy spectrum and the light curves

The MAGIC data were calibrated and analyzed using the standard tools as described in Section 5. The distribution of θ^2-values after cuts is shown in Fig. 8.3. The signal of 297 events over 1591 normalized background events corresponds to a excess with significance of $6.21\,\sigma$ using Equation 5.6 for the calculation.

To search for time variability the sample was divided into 14 sub-samples, one for each observing night. Figure 8.5 shows the integral flux for each night calculated for a photon flux above 200 GeV. The energy threshold has been chosen to reduce systematic effects arising from a rapidly decreasing effective area for γ-rays for lower energies. The flux is statistically constant at an emission level of F(>200 GeV)=$(1.58\pm0.32)\cdot10^{-11}$ photons cm^{-2}s^{-1}. In the inset of Figure 8.5,

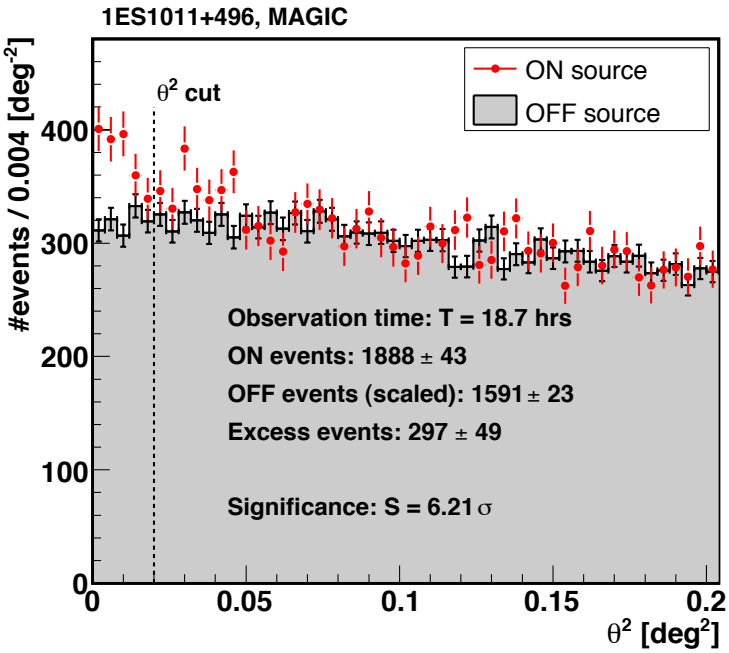

Figure 8.3: Distribution of θ^2 for ON-region data and normalized OFF-region data. The signal region is marked by the dashed line.

I show integral fluxes above 200 GeV on a year-by-year basis. The first point in the inset corresponds to an earlier observation of 1ES1011+496 by MAGIC in 2006, which lead to a hint of a signal (Albert et al., 2007f). This hint can now be interpreted as being due to a lower flux state of the source than measured in 2007.

The differential energy spectrum of 1ES 1011+496 is shown in Fig. 8.6. The spectrum extends from $\sim 120\,\mathrm{GeV}$ to $\sim 750\,\mathrm{GeV}$ and can be well approximated by a power law:

$$\frac{\mathrm{d}N}{\mathrm{d}E} = (2.0 \pm 0.1) \cdot 10^{-10} \left(\frac{E}{0.2\,\mathrm{TeV}} \right)^{-4.0 \pm 0.5} \frac{1}{\mathrm{TeV\,cm^2\,s}}$$

The errors are statistical only. We estimate the systematic uncertainty to be around 75% for the absolute flux level and 0.2 for the spectral index. The observed spectrum is affected by the evolving extragalactic background light (EBL, see Section 1.5 and Chapter 3 for details) as the VHE γ-rays are partially altered by interactions with the low-energy photons of the EBL. Therefore, to obtain the intrinsic spectrum of the source, the observed spectrum must be corrected. The optical depth and the resulting attenuation of the VHE γ-rays from 1ES 1011+496 are calculated using the number density of the evolving EBL provided by the

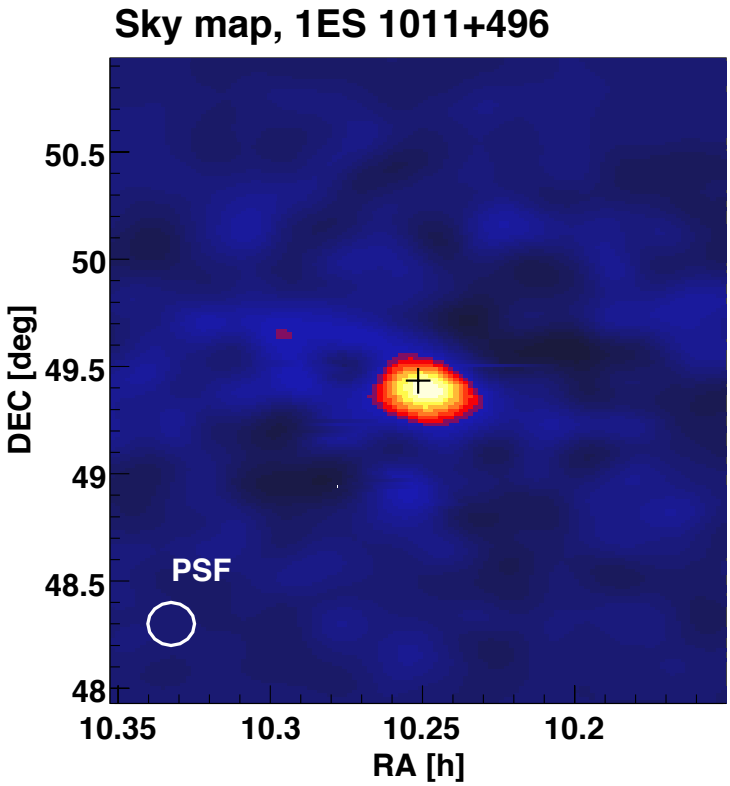

Figure 8.4: Sky map of smoothed excess events in the region of 1ES 1011+496. The catalogue source position is marked by the black cross and coincides with the measured excess within the errors. The sky map is folded with a Gaussian of $\sigma = 0.1$ deg, which corresponds to the γ-PSF of the analysis.

best-fit model of Kneiske et al. (2002). Even after the correction, the slope of the spectrum is $\Gamma_{\rm int} = 3.3 \pm 0.7$ (dashed red line in Fig. 8.6, χ^2 / NDF = 2.55/2), softer than observed for other HBLs in TeV energies and thus not providing new constraints on the EBL density.

8.5 Discussion of the results

I report the discovery of VHE γ-ray emission from BL Lac object 1ES 1011+496. With the redshift of $z = 0.212$, it is the most distant source detected to emit VHE γ-rays up to date. The energy spectrum of 1ES 1011+496 is one of the softest measured VHE γ-ray spectrum so far. Even after the deabsorption the spectrum remains soft with an intrinsic index of $\Gamma_{\rm int} = 3.3 \pm 0.7$. The behavior of the spectrum (soft and no significant excess above $\sim$ 800 GeV) in turn confirms our current understanding of the evolving EBL (e.g. Primack et al. (2005) and

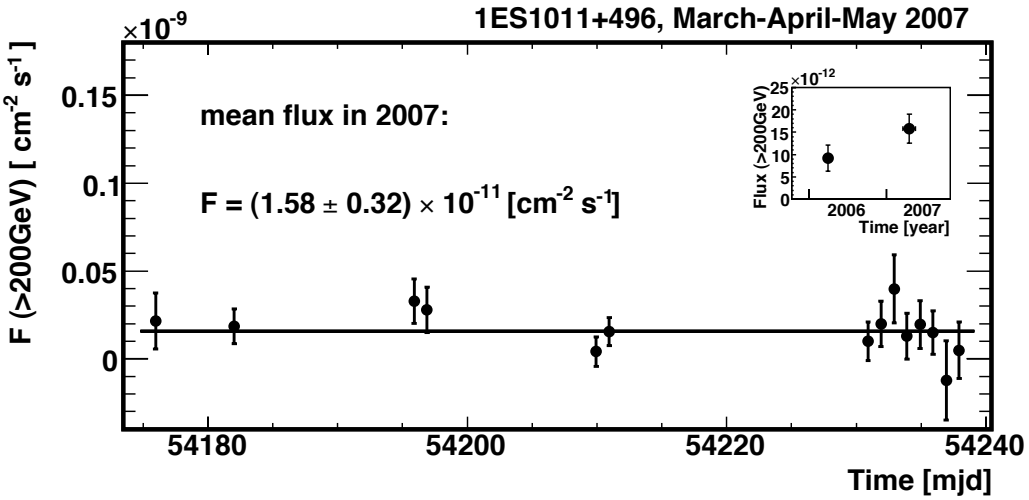

Figure 8.5: The night-by-night light curve of 1ES 1011+496 from 2007 March 17 (MJD 54176) to 2007 May 18 (MJD 54238).

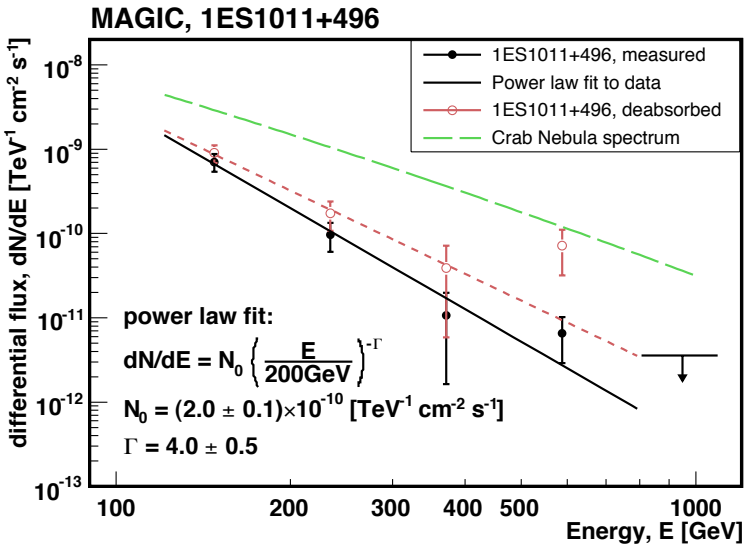

Figure 8.6: The measured spectrum (black filled circles), the power-law fit to the data (solid line), the deabsorbed spectrum (brown open circles), and the fit to the deabsorbed spectrum (dashed red line). The last measured point is a 95% upper limit. In the deabsorbed spectrum, the last spectral point at ≈600 GeV is 1.6 σ above the fit and thus not significant. The Crab Nebula spectrum (green dashed line, Albert et al. (2007i)) is shown for comparison.

Table 8.1: Fitted SSC model parameters for 1ES 1011+496. The corresponding photon spectrum is shown in Fig. 8.7 by the dashed-dotted line.

spherical blob with:	
Doppler factor	20
magnetic field	0.15 Gauss
radius of emitting region	1.0×10^{16} cm
injected electron spectrum:	
normalization of the electron energy density	$2{\times}10^4$ cm^{-3}
electron slope for $8.7 < \log10(\mathrm{E[eV]}) < 10.4$	index 2.0
electron slope for $10.4 < \log10(\mathrm{E[eV]}) < 13.0$	index 5.0

the low model in Kneiske et al. (2002)) and is not in conflict with the recently derived EBL limits by Aharonian et al. (2006a) and in Chapter 9 (Mazin and Raue, 2007).

In Fig. 8.7 we show the Spectral Energy Distribution (SED) of 1ES 1011+496 constructed using historical data (open green circles, from (Costamante and Ghisellini, 2002)) and the quasi-simultaneous optical R-band data (filled red triangle) and the deabsorbed MAGIC spectrum (filled red circles). I also report in green the EGRET flux of the source 3EG J1009+4855, possibly associated with 1ES 1011+496 (Hartman et al. (1992) but see also Sowards-Emmerd et al. (2003) for doubts on this association).

The predicted TeV flux by the leptonic phenomenological model of Fossati et al. (2000) (shown as dashed line in Fig. 8.7) is lower than the observed flux. A more detailed synchrotron self Compton (SSC) model from (Costamante and Ghisellini, 2002) (shown as solid line) is also below the MAGIC measurement. Since the predictions were based on an averaged flux state of 1ES 1011+496, our observation hints to an increased flux state in all wavelengths. The increased optical emission (red triangle) supports this idea.

In collaboration with Fabrizio Tavecchio we model the SED by using an one-zone SSC model (see (Tavecchio et al., 2001) for a description). In brief, the emission region is assumed to be spherical, with radius R, filled with tangled magnetic field with intensity B and relativistic electrons following a smoothed broken power-law energy distributions specified by the limits γ_{min} and γ_{max}, the break at γ_{b} and by the normalization, K. Relativistic effects are taken into account by the Doppler relativistic factor δ.

If the position and the luminosity of the synchrotron and IC peaks are known and an estimate of the minimum variability time scale is available, it is possible to uniquely constrain the model parameters. Unfortunately in this case (like in the case of Mrk 180, Chapter 7) we do not have all the required information and therefore the model parameters reported here are not unique. In particular, we fix the synchrotron peak by requiring that it reproduces the optical flux and

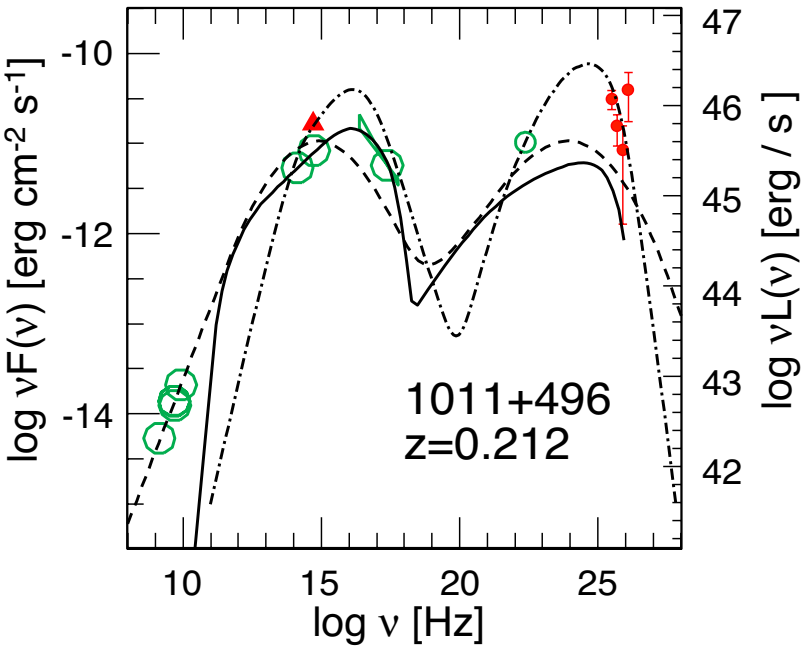

Figure 8.7: The broad-band spectral energy distribution of 1ES 1011+496. The two different fits are done by varying the $\gamma_{\rm min}$ (see text). The other fit parameters are: R=10^{16} cm, δ =20, B = 0.15 G, $\gamma_{\rm max}$ =4e4 and $n_{\rm e}$ =2 10^4 cm^{-3}

the historical X-ray spectrum, while we assume that the IC peak is not too far from the MAGIC threshold: with this choice we minimize the required emitted luminosity, since a lower IC peak frequency would directly imply a larger IC luminosity.

I present here one SSC model, which is shown by the dashed-dotted line in Fig. 8.7. In order to fit the EGRET point, the model requires a high minimum electron energy of E = 0.5 GeV (corresponding $\gamma_{\rm min} = 3 \times 10^3$ in the model) in order to "narrow" both the synchrotron and IC bump (Katarzyński et al., 2006). The other model parameters are summarized in Table 8.1. However, without the limitation set by the EGRET, the minimum electron energy can be relaxed. It is clear that simultaneous GLAST–MAGIC observations of this source could provide important constraints on the model parameters.

1ES 1011+496 has been previously observed with the HEGRA telescope, which reported an upper limit of F(E>1 TeV)$\leq$ $1.8 \cdot 10^{-12}$ photons cm^{-2}s^{-1} (Aharonian et al., 2004a) that is well above the detected flux we found. As already mentioned above, 1ES 1011+496 was also observed by MAGIC, as part of a systematic scan of X-ray bright HBLs, in March–April 2006. Being in a lower optical state (the core flux was $\sim$ 50% lower than that in March–May 2007), the observations showed a marginal signal with 3.5σ significance corresponding to an integral flux of F(>180 GeV)=$(1.26\pm0.4) \cdot 10^{-11}$ photons cm^{-2}s^{-1}, i.e. $\sim$ 40% (Albert et al., 2007f) lower than the detected flux in March–May 2007 (see also

the inset in Figure 8.5). A similar trend was also found for BL Lac (Albert et al., 2007b), where the observations during a lower optical state failed to detect VHE γ-rays. This seems to indicate that there is a connection between the optical high state and the higher flux of VHE γ-ray emission at least in some sources. To further investigate this possibility follow-up observations of the detected objects as well as further observations of other AGN during high optical states are required.

Chapter 9

Constraints On the Extragalactic Background Light

The extragalactic background light (EBL) in the ultraviolet to far-infrared wavelength region carries important information about galaxy and star formation history (see Chapter 3 for details). Direct measurements are difficult, especially in the mid infrared region (see also Chapter 3 for details). I derive here, in collaboration with Martin Raue (Hamburg University), limits on the EBL density from the energy spectra of distant sources of very high energetic γ-rays (VHE γ-rays). The method itself and the achieved results are published in Mazin and Raue (2007) and was included in the highlights in the last International Cosmic Ray Conference in July 2007 (Hinton, 2007; Raue and Mazin, 2007).

The VHE γ-rays are attenuated by the photons of the EBL via pair production, which leaves an imprint on the measured spectra from distant sources. Up to September 2006 (the date of this study), there were 14 detected extragalactic sources of VHE γ-rays, 13 of which are TeV blazars[1]. With physical assumptions about the intrinsic spectra of these sources, limits on the EBL can be derived. In this study I present a new method of deriving constraints on the EBL. Only very basic assumptions about TeV blazar physics are used to derive the limits. Another strong point of the study is that no pre-defined EBL model is used, but instead a large number of generic shapes constructed from a grid in EBL density vs. wavelength. In the study spectral data from all known TeV blazars are utilized, making this the most complete study so far.

I derive limits on the EBL using three individual TeV blazar spectra (Mkn 501, H 1426+428, 1ES 1101-232) and using all spectra combined. Combining the results from individual spectra leads to significantly stronger constraints over a wide wavelength range from the optical ($\sim 1\,\mu$m) to the far-infrared ($\sim 80\,\mu$m). The limits are only a factor of 2 to 3 above the lower limits derived from the source counts. In the mid-infrared the limits are the strongest constraints derived from

[1] I call "TeV blazars" all blazars with a detected emission above 0.1 TeV

TeV blazar spectra so far over an extended wavelength range. A high density of the EBL around 1 μm, reported by direct detection experiments, can be excluded.

This Chapter is organized as follows: In Section 9.1 I summarize the aims and goals of the study, in Section 9.2 I describe the method of using splines and a grid in EBL density vs. wavelength to construct different shapes, in Section 9.3 the TeV blazar spectra are introduced, and in Section 9.4 I describe the criteria, which are imposed on these spectra to derive limits on the density of the EBL. In Section 9.5 results for individual sources and in Section 9.6 the combined results are discussed. Conclusions of the study and an outlook are given in Section 9.7.

9.1 Idea and aim of the study

In the past 2-3 years, many new TeV blazars have been discovered and the established ones were remeasured with higher sensitivity, resulted in a better precision, with the new Imaging Atmospheric Cherenkov Telescopes (IACT) such as H.E.S.S. and MAGIC. It is therefore of high interest whether the new measurements agree with the previous limits on the EBL. Furthermore, to derive limits on the EBL from the data, it is important to scrutinize all available data together to obtain a consistent picture and to maximize the constraints. In this study spectra from all known TeV blazars are used to derive upper limits on the EBL density in a wide wavelength range from the optical to far-infrared. Moreover, a common criticism of the previously derived EBL limits with this method is that the limits are obtained by assuming a certain EBL model and e.g. scaling it, or by exploring just a few model parameters. Since EBL models are complex and different models do not agree in details, the derived limits become very model-dependent. In order to avoid this dependency, we (me and Martin Raue) developed a novel technique of describing the EBL number density by spline functions, which allows us to test a large number of hypothetical EBL shapes. The aims of the study are:

1. Provide limits on the EBL density, which do not rely on a predefined shape or model, but rather allow for any shape compatible with the current limits from direct measurements and model predications.

2. Treat all TeV blazar spectra in a consistent way, using simple and generic assumptions about the intrinsic VHE γ-ray spectra and a statistical approach to find exclusion criteria.

3. Use spectral data from all detected TeV blazars to
   (a) derive upper limits on the EBL density using the individual spectra and then
   (b) combine these results into a single robust limit on the EBL density for a wide wavelength range.

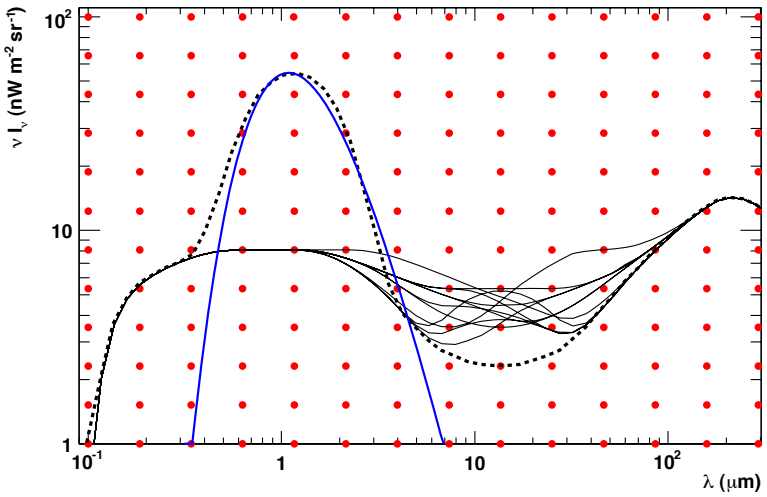

Figure 9.1: Examples for spline shapes resulting from the grid layout, overlaid on the grid points (red filled circles). The dashed black line illustrates the thinnest structure that can be achieved with the grid setup. A Planck spectrum (blue line) is given for comparison. Further examples for shapes are given as solid black lines.

9.2 Grid scan of the EBL with splines

TeV γ-rays traversing the extragalactic radiation fields are absorbed via pair production with the low-energy photons of the EBL: $\gamma_{\mathrm{TeV}}\ \gamma_{\mathrm{EBL}} \rightarrow e^+\ e^-$. Details on the cross section (Heitler, 1960) and the exact calculations can be found in Section 1.5 (see also Dwek and Krennrich 2005 for an overview). Here, I focus on the new technique using splines (as introduced below) in order to examine as many as several million possible EBL shapes.

To calculate the optical depth τ_γ for a TeV-γ ray of energy E_γ emitted at a redshift of z for one realization/shape of the EBL, one needs to solve a three-fold integral over the distance ℓ, the interaction angles between the two photons

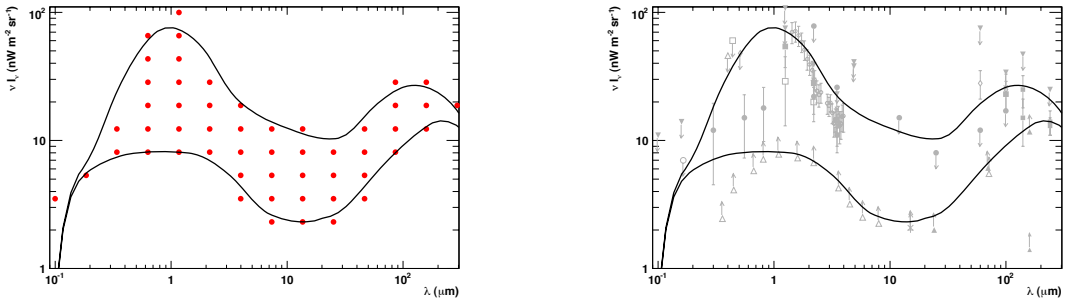

Figure 9.2: *Left:* Grid points (red filled circles) and minimum and maximum shape of the scan. *Right:* Minimum and maximum shape overlaid on the EBL measurements from Fig. 3.4

$\mu = \cos\theta$ and the number density of the EBL photons n_ϵ:

$$\tau_\gamma(E_\gamma,\ z) = \int_0^z \mathrm{d}\ell(\mathrm{z}) \int_{-1}^{+1} \mathrm{d}\mu\ \frac{1-\mu}{2} \int_{\epsilon'_{th}}^{\infty} \mathrm{d}\epsilon'\ n_\epsilon(\epsilon', z)\ \sigma_{\gamma\gamma}(E'_\gamma,\ \epsilon',\ \mu) \tag{9.1}$$

where $\sigma_{\gamma\gamma}$ is the pair production cross section, ϵ the energy of the EBL photon, and E'_γ and ϵ' refer to redshifted energy values.

For the large number of shapes ($\sim$8 million) which are analyzed in this study, a full numerical integration would require an extensive amount of computing power. To avoid this problem, the EBL number density at $z = 0$ is parametrized as a spline

$$n_\epsilon(\epsilon) = \sum_{i=0}^{k} w_i s_{i,p}(\epsilon) \tag{9.2}$$

with

$$\begin{aligned} s_{i,0}(\epsilon) &= \begin{cases} 1 & \text{if } \epsilon_i \le \epsilon < \epsilon_{i+1} \text{ and } \epsilon_i < \epsilon_{i+1} \\ 0 & \text{otherwise} \end{cases} \\ s_{i,p}(\epsilon) &= \frac{\epsilon - \epsilon_i}{\epsilon_{i+p} - \epsilon_i} s_{i,p-1}(\epsilon) + \frac{\epsilon_{i+p+1} - \epsilon}{\epsilon_{i+p+1} - \epsilon_{i+1}} s_{i+1,p-1}(\epsilon)\ . \end{aligned} \tag{9.3}$$

Here p is the order of the spline and is set to $p = 3$ throughout the Chapter, k is the number of supporting points, $\epsilon_1, ..., \epsilon_k$ are the positions of the supporting points of the curve, and $w_1, ..., w_k$ are weights controlling the shape of the curve.

A way to visualize this spline is to add a number of Gaussian-like base functions to lead to a smooth curve, whereby the base functions can be weighted (w_i) to achieve different overall shapes. These base functions are characterized by a position of the center and a certain width, which depends on the order p and the spacing of the supporting points.

By inserting Eq. (9.2) into Eq. (9.1) and then swapping the integration and the summation, one obtains an expression for the optical depth, where the integral can be solved easily for a certain redshift and set of supporting points of the spline. The optical depth can then be calculated by a simple summation, where the shape of the EBL is determined by the choice of a set of weights.

To estimate the numerical uncertainties in the integration of the base functions, the result for τ_γ from the summation is compared to the results from a full integration over the actual EBL shapes for several shapes and spectra used in this study. The deviation for almost all settings is found to be less then 0.5%. Even for extreme cases (high redshift, high EBL density), the deviation is always less than 2%. These small deviations arise from inaccuracies in the numerical integration of the base functions.

The spline parameterization is used to construct a set of EBL shapes using a grid in EBL energy density vs. wavelength. The x-positions of the grid points

(wavelength) are used as positions for the supporting points ϵ_i of the spline. The y-positions of the grid points (energy density) are used as weights w_i.

For the supporting points (x-axis of the grid) ϵ_i, 16 equidistant points are used in $\log_{10}(\lambda)$ ($\lambda = hc/\epsilon$) from 0.1 to 1000 μm. The number and distance of the supporting points, together with the order of the spline, determines the minimum width of the structures, which can be described with the spline. Given the grid setup and the spline of order $p = 3$, the thinnest peak or dip that can be modeled is about three grid points wide (Fig. 9.1). This minimum width is similar to a Planck spectrum from a black body radiation (Fig. 9.1). It is expected that the EBL originates mainly from an overlap of the redshifted spectra of single stars, for which a Planck spectrum is a good first-order approximation, and dust reemission. Thus, an EBL structure thinner than a Planck spectrum is unlikely.

Noteworthy, any extremely sharp and strong cut-offs or bumps can only be described in an approximate way. Such features can arise from the Lyman-α drop-off of massive Population III stars in certain models (Salvaterra and Ferrara (e.g. 2003) and Section 3.5), but they are generally not expected on larger wavelength scales, since they would be smoothed out by redshift. Of course, the upper limits depend on the thickness of the structures modeled, and the choice of minimum thickness has to be physically motivated, as it is in this case.

The weights w_i of the spline (y-axis of the grid) are varied in 12 equidistant steps in $\log_{10}$(energy density) from 0.1 to 100 $\mathrm{nW\,m^{-2}\,sr^{-1}}$. Since the grid point positions are applied directly as weights w_i, the resulting curve does not directly go through the grid points. So for all limits derived in this study, the actual curve has to be considered and not the grid point positions. The use of the grid point positions as weights also results in several shapes lying between two grid points. This is illustrated in Fig. 9.1 for two arbitrarily chosen grid points between 10 and 20 μm.

For the scan, a subset of grid points is selected such that all resulting shapes are within the limits given by the galaxy counts on the lower end and by the limits from the direct measurements and the fluctuation analyses on the upper end. In the 20 to 100 μm regime, a somewhat looser shape is chosen, given the wider spread of the (tentative) measurements (Fig. 9.2). By iterating over all grid points (Fig. 9.2, left plot), one obtaines 8 064 000 different EBL shapes, which will be examined.

The expansion of the Universe and the shifting of the photon's wavelength (energy) due to the Doppler effect are taken into account in Equation 9.1. However, the generic shapes used in this analysis have no redshift dependency, thus evolution of the EBL cannot be taken into account. Neglecting the evolution of the EBL is a valid assumption for nearby sources (e.g. Mkn 501), but for distant sources[2] this can result in an additional error in the order of 10 to 20% depending on the evolution model and redshift (see e.g. Aharonian et al. 2006a). The

[2]the farthest source in the study is 1ES 1101-232, z = 0.186

Table 9.1: TeV blazar spectra used in this study.

Source name	Red-shift	Experi-ment	Energy range (TeV)	Slope $\Gamma \pm \sigma_{\rm st} \pm \sigma_{\rm sy}$	Cut-off (TeV)	Reference
Mkn 421	0.030	MAGIC	0.10 – 3.0	$2.20 \pm 0.08 \pm 0.20$	1.44 ± 0.28	Albert et al. (2007e)
Mkn 421	0.030	HEGRA	0.70 – 18.0	$2.19 \pm 0.02 \pm 0.20$	$3.6^{+0.4}_{-0.3}$	Aharonian et al. (2002c)
Mkn 421	0.030	Whipple	0.35 – 0.90	$2.31 \pm 0.04 \pm 0.05$	——	Krennrich et al. (2002)
Mkn 501	0.034	HEGRA	0.50 – 22.0	$1.92 \pm 0.03 \pm 0.20$	6.2 ± 0.4	Aharonian et al. (1999b)
1ES 2344+514	0.044	Whipple	0.80 – 11.0	$2.54 \pm 0.17 \pm 0.07$	——	Schroedter et al. (2005)
Mkn 180	0.045	MAGIC	0.14 – 1.5	$3.25 \pm 0.66 \pm 0.20$	——	Albert et al. (2006b)
1ES 1959+650	0.047	HEGRA	1.5 – 13.0	$2.83 \pm 0.14 \pm 0.08$	——	Aharonian et al. (2003b)
PKS 2005-489	0.071	H.E.S.S.	0.20 – 2.5	$4.0 \pm 0.4\,(\pm 0.2)$	——	Aharonian et al. (2005c)
PKS 2155-304	0.116	H.E.S.S.	0.20 – 3.5	$3.37 \pm 0.07 \pm 0.10$	——	Aharonian et al. (2005e)
H 1426+428	0.129	HEGRA	0.70 – 12.0	$2.6 \pm 0.6 \pm 0.1$	——	Aharonian et al. (2003d)
H 2356-309	0.165	H.E.S.S.	0.16 – 1.0	$3.06 \pm 0.21 \pm 0.10$	——	Aharonian et al. (2006b)
1ES 1218+304	0.182	MAGIC	0.08 – 0.7	$3.0 \pm 0.4 \pm 0.6$	——	Albert et al. (2006a)
1ES 1101-232	0.186	H.E.S.S.	0.16 – 3.3	$2.88 \pm 0.14 \pm 0.1$	——	Aharonian et al. (2006a)

possible systematic error arising from this assumption will be discussed further in Section 9.7.

For a given optical depth $\tau_\gamma(E_\gamma,\, z)$ one can determine the intrinsic differential energy spectrum using

$$dN/dE_{\rm intr.} \,=\, dN/dE_{obs} \times \exp[\tau_\gamma(E_\gamma,\, z)], \tag{9.4}$$

where dN/dE_{obs} is the observed spectrum. The intrinsic spectrum is then tested on its physical feasibility as described in Section 9.4. This process is repeated for all VHE γ-ray sources (described in the next section) and for all 8 064 000 EBL shapes.

9.3 The used TeV blazar sample

Since the detection of the first extragalactic VHE γ-ray source Mrk 421 in 1992 (Punch et al., 1992), a wealth of new data from this source type has become available. Up to now all detected VHE γ-ray sources belong to the class of active galactic nuclei (AGN) and, with the only one exception of the radio galaxy M 87 (Aharonian et al., 2003c, 2006e), to the subclass of TeV blazars (Horan and Weekes, 2004). AGNs are known to be highly variable sources, with variations of the absolute flux levels in the TeV range by more than an order of magnitude and on time scales as short as 15 min (e.g. Gaidos et al., 1996; Aharonian et al., 2002c). Changes in the spectral shapes have also been observed (e.g. Krennrich et al., 2002; Aharonian et al., 2002c), see also Chapter 2.

In this study we utilize spectral data obtained during the past seven years by four different experimental groups operating ground-based imaging atmospheric Cherenkov telescopes (IACTs): Whipple (Finley and The VERITAS Collaboration, 2001), HEGRA (Daum et al., 1997), H.E.S.S. (Hinton, 2004), and MAGIC.

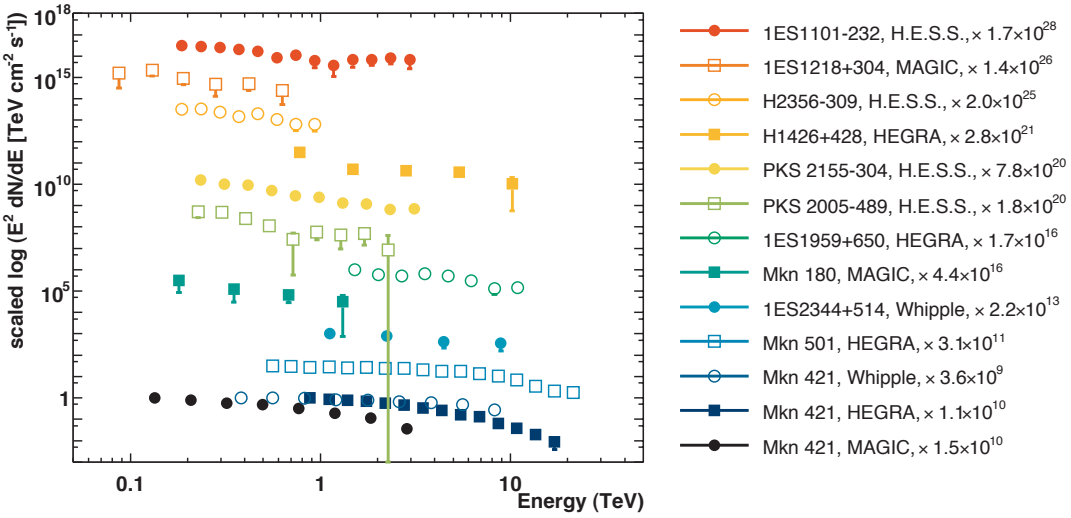

Figure 9.3: TeV blazar sample chosen for this study. From all detected TeV blazars, at least one spectrum is shown with the exception of PG 1553+113 (unknown redshift). The spectra are multiplied by E^2 to emphasize spectral differences and are spread out along the Y-axis and ordered in redshift (closest source at the bottom) to avoid cluttering of the plot. The corresponding scaling factors are given in the legend of the plot.

We select at least one spectrum for every extragalactic source with known redshift. If there is more than one measurement with a comparable energy range, we take the spectrum with the better statistics and the harder spectrum (expected to give stronger constraints, see Sect. 9.4). If different measurements of one source cover different energy ranges, we include both spectra as independent tests. Another possibility would be to combine the measurements from different experiments, as was done before in the case of H 1426+428 (Aharonian et al., 2003d). However, since the sources are known to be variable in the flux level and spectral shape, a combination of non-simultaneous data is not trivial. In addition, in a conservative approach one has to consider the systematic errors reported by the individual experiments, which are around 20%. The method is quite sensitive to the errors of the flux, and this additional error would weaken the results. We therefore do not use combined spectra. The selected TeV blazar spectra are summarized in Fig. 9.3 and Table 9.1. In the case the measured spectrum can be described well by a simple power law $dN/dE \propto E^{-\Gamma}$, only the slope Γ is quoted. Otherwise, the cut-off energy E_{coff} according to $dN/dE \propto E^{-\Gamma} \exp(-E/E_{\mathrm{coff}})$ is also quoted. If no systematic error in the photon index is given in the corresponding paper, we use a value of 0.2 (values in brackets). In Fig. 9.3 the spectra are multiplied by E^2 to emphasize spectral differences and are spread out along the Y-axis and ordered in redshift (closest source at the bottom) to avoid cluttering the plot.

We did not include data from the radio galaxy M 87, which was recently

confirmed as a VHE γ-ray emitter (Aharonian et al., 2006e). M 87 is a nearby source ($z = 0.00436$), so even for high EBL densities the attenuation is weak and would only be noticeable at energies ≥ 30 TeV. Nevertheless, M 87 has a hard spectrum with a photon index of $\Gamma \sim 2.2$ (currently measured up to 20 TeV), so further observations that extend the energy range to even higher energies could make M 87 an interesting target for EBL studies as well.

The cross section $\sigma_{\gamma\gamma}$ of the pair production process has a distinct peak close to the threshold. The maximum attenuation of VHE photons of energy E_γ occurs by interaction with low-energy photons with a wavelength

$$\lambda^{\max}(\mu\mathrm{m}) \approx 1.24\ E_\gamma(\mathrm{TeV}). \tag{9.5}$$

Since the selected spectra cover an energy region from 100 GeV up to more than 20 TeV, the EBL wavelength range for the absorption of VHE γ-rays spans from UV ($\sim$0.1 μm) to the mid IR ($\sim$30 μm). As already pointed out, this region is difficult to measure directly and it is of particular cosmological interest since it might contain a signature of Population III stars.

9.4 Exclusion criteria for the EBL shapes

Table 9.2: Analytical functions that are used to fit the intrinsic TeV blazar spectrum.

#	Description	Abbreviation	Formula $f(E) = dN/dE$	Parameters to evaluate
1	simple power law	PL	$N_0 E^{-\Gamma}$	χ^2, Γ^{PL}
2	broken power law with transition region	BPL	$N_0 E^{-\Gamma_1}\left[1+\left(\frac{E}{E_b}\right)^f\right]^{\frac{\Gamma_1-\Gamma_2}{f}}$	χ^2, Γ_1^{BPL}, Γ_2^{BPL}
3	broken power law with transition region and super-exponential pile-up	BPLSE	$\mathrm{BPL}\times\exp\left(\frac{E}{E_{\mathrm{p}}}\right)$	χ^2
4	double broken power law with transition regions	DBPL	$\mathrm{BPL}\times\left[1+\left(\frac{E}{E_{b2}}\right)^{f_2}\right]^{\frac{\Gamma_2-\Gamma_3}{f_2}}$	χ^2, Γ_1^{DBPL}, Γ_2^{DBPL}, Γ_3^{DBPL}
5	double broken power law with transition regions and super-exponential pile-up	DBPLSE	$\mathrm{DBPL}\times\exp\left(\frac{E}{E_{\mathrm{p}}}\right)$	χ^2

We aim to construct an upper limit on the EBL density using the TeV blazar sample described in Sect. 9.3. In order to achieve this, every EBL shape is examined (as introduced in Sect. 9.2) to see whether the intrinsic TeV blazar spectra, which result from correcting the measured spectra for the corresponding optical depths, are physically feasible[3]. EBL shapes are considered to be allowed

[3]I call an intrinsic energy spectrum "feasible" if its spectral shape does not contradict possible emission scenarios of VHE γ-rays

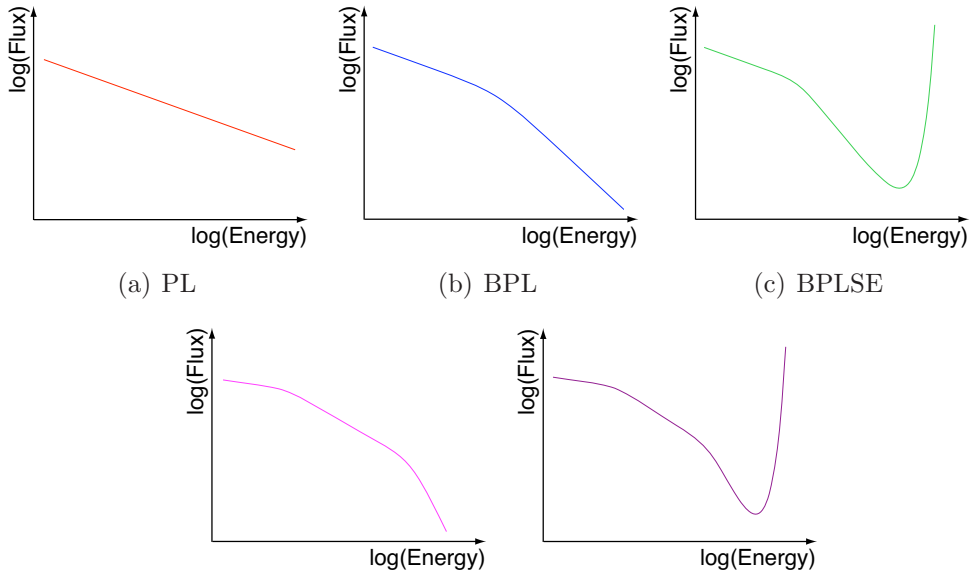

(a) PL (b) BPL (c) BPLSE

(d) DBPL (e) DBPLSE

Figure 9.4: Sketch of the analytical funtions that are used to fit the intrinsic TeV blazar spectra

if the intrinsic spectra of all tested TeV blazars are feasible. As an upper limit we define the upper envelope of all allowed shapes. The envelope is constraining in the wavelength range where it lies below the maximum shape tested in the scan. Otherwise no upper limit is quoted.

There are different ways to examine a TeV blazar spectrum upon its feasibility. In this study we follow very general arguments arising from the shock acceleration scenario of relativistic particles. As discussed in Section 2.4.4, the resulting intrinsic γ-ray spectrum should have the photon index $\Gamma > 1.5$.[4] In an extreme case we deal with a monoenergetic spectrum of VHE relativistic electrons. Then, and this is the most extreme case, a resulting IC photon index can be as small as $\Gamma = 2/3$. We use this limit in the present study, in addition to the standard limit of $\Gamma = 1.5$, to demonstrate the strength of the method.

In the simplest models, it is assumed that VHE photons originate from a single compact region (so-called one-zone scenario). This results in a smooth, convex spectral energy-distribution with two peaks at certain energies in a $\log(\nu F(\nu))$ vs. $\log(\nu)$ representation. Yet there are no obvious arguments against scenarios including some kind of multizone models, which can be naturally realized in the jets of TeV blazars. Then, the measured spectrum of VHE γ-ray emitting sources will be a superposition of several one-zone emission regions. So far, there has been no indication of this in the measured spectra, however, the attenuation of VHE γ-rays by EBL photons could hide such substructures.

[4] assuming the photon spectrum of the form $dN/dE \sim E^{-\Gamma}$

In addition to the constraints on the photon index of the intrinsic TeV blazar spectra, we also argue that a super-exponentially rising energy spectrum with an increasing energy is not realistic. The so-called *pile-up*[5] at high energies was first noticed by Protheroe and Meyer (2000) for the Mkn 501 spectrum, and early attempts to avoid it invoked violation of the Lorentz invariance (Kifune, 1999; Protheroe and Meyer, 2000). On the other hand, Stecker and Glashow (2001) argue that the same Mkn 501 spectrum data can be used to place severe constraints on the Lorentz-invariance breaking parameter. Another possibility for explaining pile-ups would require an ultrarelativistic jet with a very high bulk-motion Lorentz factor $\Gamma_0 > 3 \times 10^7$ (Aharonian et al., 2002f). The pile-ups, however, seem to arise at different energies for different sources, which is not expected in these models. Moreover, the pile-ups can be easily avoided by choosing a sufficiently low level of the EBL density.

Based on the arguments above and including possible multizone emission scenarios, we assume that at least one of the following smooth, analytical functions can describe the intrinsic spectrum satisfactory well: a simple power law (PL), a broken power law with a transition region (BPL), a broken power law with a transition region and a super-exponential pile-up (BPLSE), a double broken power law with two transition regions (DBPL), or a double broken power law with two transition regions and a super-exponential pile-up (DBPLSE). These functions are summarized in Table 9.2 and illustrated in Fig. 9.4.

In case we fail to find such a function, we abandon any further examination of the fit parameters, and a given EBL shape (realization) is not excluded. It is noteworthy that less than 0.06% of all intrinsic spectra of the TeV blazars could not be fitted well by the chosen functional forms, which are described below.

In order to determine a good analytic description, we fit the intrinsic spectrum with the functions listed above, starting with the simplest one (PL). As "good description" we take a fit with a chance probability $P_{\rm Fit} > 5\%$ based on its χ^2 value. The determined fit parameters are examined to be physically meaningful as described below. If the fit has a probability $P_{\rm Fit} < 5\%$, we do not consider the function and examine the next function from the list (Table 9.2, Fig. 9.4). Also if the fit has a chance probability $P_{\rm Fit} > 5\%$, but the determined parameters do not lead to an exclusion of the corresponding EBL shape, we take the next function from the list. The reason is that a function with more free parameters can lead to a significantly better fit. In order to make sure that a more complicated function indeed describes the intrinsic shape better than a simpler one, we use the likelihood ratio test (Eadie et al. 1988, Appendix C). We require at least a 95% probability to prefer a function with a higher number of free parameters. Only if the function is preferred, we examine its fitted parameters and their errors. Spectra with n data points are only fitted with functions with up to $n-1$ parameters. In case of spectra with low statistics, we fix the softness of the break

[5] *pile-up* – here a rapid raise of the energy flux with increasing energy

(f, see Table 9.2) between two spectral indices to an *a priori* chosen value of $f = 4$ to allow for a fit by a higher-order function (e.g. in case of the BPL for H 1426+428).

We finally define the following criteria to exclude an assumed EBL shape:

- At least one of the determined photon indices from the best hypothesis is outside of the allowed range, i.e. $\Gamma^{i,\max} < \Gamma^{\text{limit}}$, where $\Gamma^{\text{limit}} = 1.5$ or $2/3$, and $\Gamma^{i,\max} = \Gamma^i + \sigma_{\Gamma^i} + \sigma_{\text{sy}}$ with Γ^i and σ_Γ the fitted photon index and its error, respectively, and σ_{sy} as the systematic error on the spectral slope (as given for the corresponding measurement).

- The best fit is obtained by one of the two shapes with an exponential pile-up (BPLSE or DBPLSE).

A single confidence level for the derived upper limits on the EBL density cannot be quoted easily: For the test on the photon index we use a $1\,\sigma$ confidence level (as defined for two-sided distributions, including systematic errors). For the likelihood ratio test, we use a $2\,\sigma$ level (as defined for one-sided distributions). Thus, the confidence level for the upper limit ranges from 68% to 95%.

As discussed in this section, the theoretical expectations on the smallest possible photon index Γ^{limit} have a given spread. Thus, we perform two EBL scans, assuming a limit of $\Gamma^{\text{limit}} = 1.5$ for the first case, dubbed *realistic* case, and for the second case, dubbed *extreme* case, a limit of $\Gamma^{\text{limit}} = 2/3$. From here on, we refer to *realistic* and *extreme* scan accordingly.

Since our exclusion criteria consider the effect of an EBL shape solely on the hardness of the spectra of extragalactic VHE γ-ray sources, some shapes might be considered acceptable in our scan, even though other criteria for exclusion could be found (e.g. exclusion based on spectral shape of the EBL, related to the energy density of star and dust emission as discussed in Dwek and Krennrich 2005). In this respect our approach is conservative.

9.5 Results for individual spectra

To present the results for individual spectra in a compact and non-repetitive way, we sort our preselected spectra into three categories. For each category we select one prototype spectrum (following similar criteria to those in Sect. 9.3), for which we give results. The categories considered are:

"Nearby and well-measured". As prototype spectrum we select the Mkn 501 spectrum ($z = 0.034$) recorded by HEGRA during a major TeV flare in 1997. The relatively hard spectrum provides good statistics from 800 GeV up to 25 TeV. Other sources in this category are Mkn 421 and 1ES 1959+650. 1ES 2344+514 and Mkn 180 are at a comparable distance, but the spectra do not have such high statistics. PKS 2005-489 lies somewhere between this

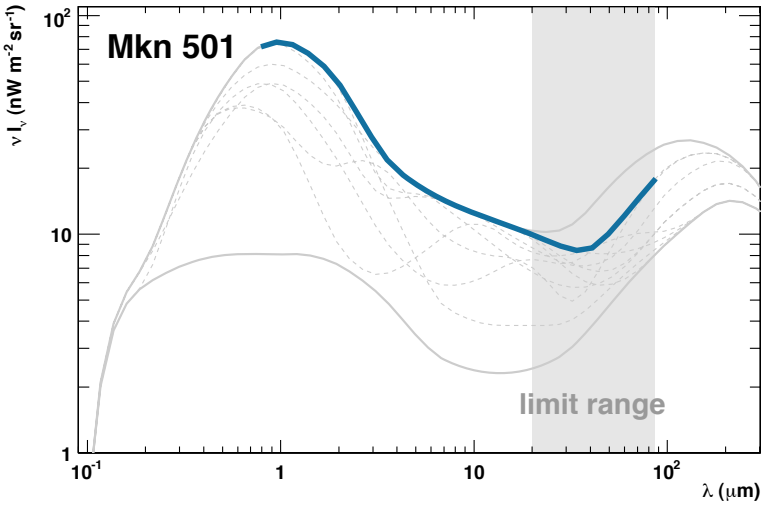

Figure 9.5: Limits on the EBL density from Mkn 501 ($\Gamma_{\rm max} > 1.5$). Grey solid curves are the minimum and maximum shapes of the scan; grey dashed curves are all the highest allowed EBL shapes for Mkn 501; the thick colored curve is the corresponding envelope shape. The grey shaded area marks the wavelength region, in which the envelope shape is constraining the EBL density.

and the following category. Spectra in this category mainly provide limits in the FIR due to a pile-up at high energies.

"Intermediate distance, wide energy range". The prototype for this category is the spectrum from H 1426+428 at a redshift of $z = 0.129$, with energies ranging from 700 GeV up to 12 TeV. PKS 2155-304 is at a comparable distance, and its measured spectrum has a better statistic, but the highest energy point is only at 2.5 TeV; and the spectrum is much softer.

"Distant source, hard spectrum". The most distant TeV blazar discovered so far with a published energy spectrum is 1ES 1101-232 at a redshift of $z = 0.186$. Its spectrum is hard and ranges from 160 GeV to 3.3 TeV. H 2356-309 and 1ES 1218+304 are at similar distances, but the statistics are not as good and/or the spectrum is softer. This makes 1ES 1101-232 the natural choice for a prototype spectrum in this category.

As the limit on the EBL for the individual spectra (and for the combined results in Sect. 9.6 as well), we define the envelope shape of all allowed EBL shapes. In most cases a single EBL shape represents the highest allowed shape only for a small wavelength interval. Consequently the envelope shape consists of a number of segments from different EBL shapes. One exception occurs, if the maximum shape tested in the scan is allowed. In this case the spectrum does not constrain the EBL density. In general, a spectrum constrains the EBL density when the envelope shape lies below the maximum shape tested in the scan.

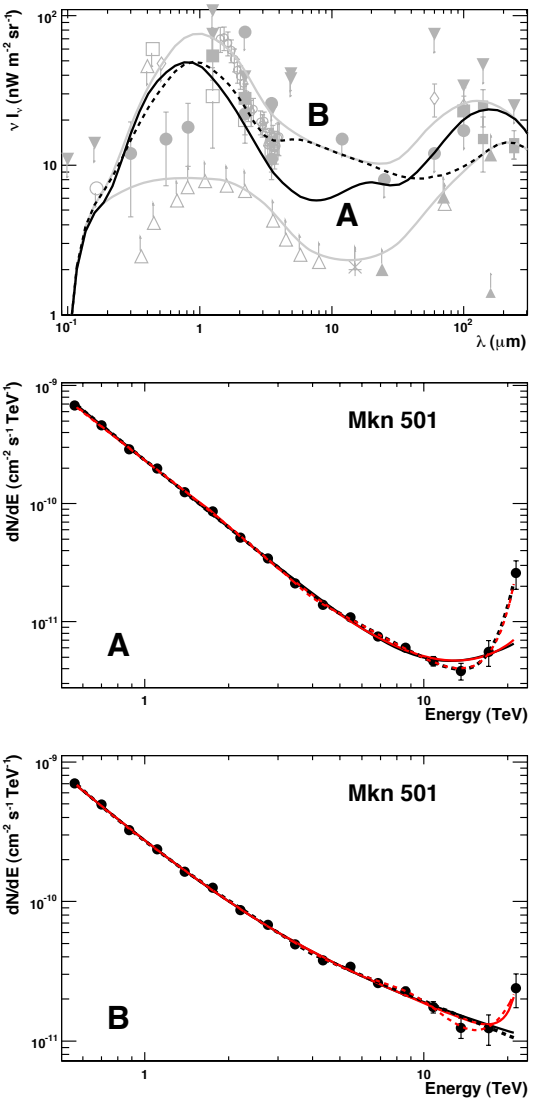

Figure 9.6: Mkn 501 individual results ($\Gamma_{\rm max} > 1.5$). *Upper Panel:* Two examples for the highest allowed shapes (A - solid line; B - dashed line) overlayed on EBL measurements and the minimum and maximum shapes of the scan (grey). *Middle Panel:* Intrinsic spectrum for shape A and fit functions: BPL (solid black line), BPLSE (solid red line), DBPL (dashed black line), and DBPLSE (dashed red line). The fit parameters can be found in Table 9.3. The BPL and BPLSE are not good fits; the DBPL is a good fit and its parameters are within the allowed range; the DBPLSE is not prefered over the BPL and the DBPL. *Lower Panel:* Intrinsic spectrum for shape B and the same fit functions as in the Middle Panel. The fit parameters can be found in Table 9.3. All four functions are good fits. No function is preferred over the BPL.

Given the energy range of the spectra, the limit is only valid for wavelengths $\lambda_{\rm Lim}$:

$$\lambda^{\rm max}(E_{min}) \; < \; \lambda_{\rm Lim} \; < \; \lambda^{\rm thresh}(E_{max}) \tag{9.6}$$

where $\lambda^{\rm max}(E_{min})$ is the wavelength for which the cross section for pair production with the lowest energy point of the VHE spectrum E_{min} is maximized (following Eqn. (9.5)). The variable $\lambda^{\rm thresh}(E_{max})$ is the threshold wavelength for pair production with the highest energy point of the VHE spectrum E_{max}. This wavelength range roughly reflects the sensitivity of the exclusion criteria. There is, of course, some freedom of choice for the wavelength range, given the complexity of the criteria.

In the following three sections the results for the individual prototype spectra for the *realistic* scan with $\Gamma_{\rm max} > 1.5$ are summarized. The results for the *extreme*

Table 9.3: Fit results for the Mkn 501 spectrum using the functions from Fig. 9.5.

	P_{Fit}	Pref.	$\Gamma_{1,\mathrm{max}}$	$\Gamma_{2,\mathrm{max}}$	$\Gamma_{3,\mathrm{max}}$
Shape A					
BPL	0.00	—	(2.13)	(-0.47)	—
BPLSE	0.04	—	—	—	—
DBPL	0.19	yes	2.12	1.62	8.92
DBPLSE	0.40	no	—	—	—
Shape B					
BPL	0.16	yes	2.85	1.77	—
BPLSE	0.23	no	—	—	—
DBPL	0.12	no	(3.91)	(1.42)	(1.05)
DBPLSE	0.24	no	—	—	—

scan with $\Gamma_{\mathrm{max}} > 2/3$ for all prototype spectra are presented in Sect. 9.5.4.

9.5.1 Nearby and well-measured: Mkn 501 (HEGRA)

The envelope shape derived for the Mkn 501 spectrum is shown in Fig. 9.5 in comparison with the maximum and minimum EBL shapes tested in the scan. Although 7 766 674 out of 8 064 000 EBL shapes (96.3%) can be excluded, the effective limit is only constraining in the 20 to 80 μm wavelength region, where it lies below the maximum tested shape. Note that our method is not only testing the overall level of the EBL density but is also sensitive to its structures. Despite the fact that, for the Mkn 501 spectrum, almost all of the tested EBL shapes are excluded, certain types of shapes are allowed, independent of their respective EBL density level. This can be illustrated with an EBL shape, which has a power law dependency $n(\epsilon) \sim \epsilon^{-1}$ or $\nu I_\nu \sim \lambda^{-1}$. Then the optical depth is independent of the energy of VHE photons and the intrinsic TeV blazar spectrum has the same shape as the observed one (Aharonian, 2001). With such a type of shape, an allowed high EBL density level in the MIR can be constructed by choosing a corresponding high density level in the optical/NIR.

The rejection power in the FIR results mainly from the hard intrinsic Mkn 501 spectrum above ∼5 TeV that often can only be described by an exponential or super exponential rise. Two of the limiting shapes, together with the resulting intrinsic spectra and fit functions, are shown in Fig. 9.5 and the corresponding fit results can be found in Table 9.3. In the table, the fit probabilities are given in the column "P_{Fit}". The parameters are put in parentheses, if the corresponding fit has a low probability or it is not preferred over a fit by a function with less free parameters (result of the likelihood ratio test, indicated in the column "Pref"). The fit with a PL function did not meet our acceptance criteria, and the function is omitted from the figure for the sake of legibility. For the two shapes displayed

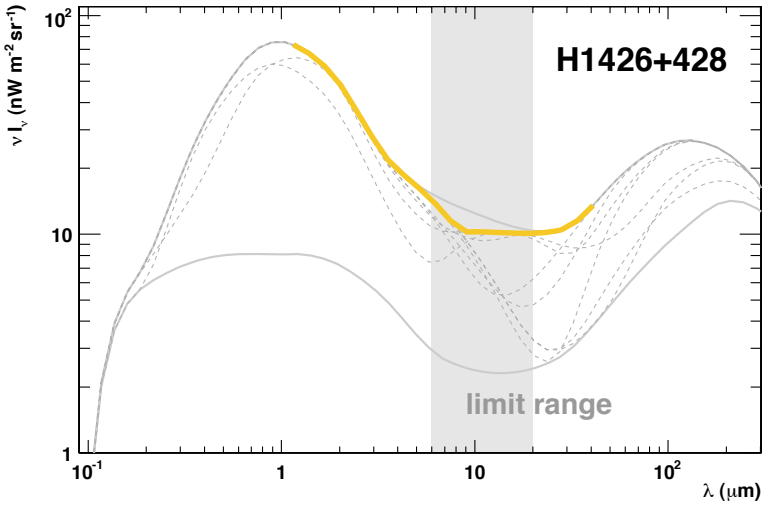

Figure 9.7: Limits on the EBL density from H1426+428 ($\Gamma_{\mathrm{max}} > 1.5$). Grey solid curves are the minimum and maximum shapes of the scan; grey dashed curves are all the highest allowed EBL shapes for H1426+428; the thick colored curve is the corresponding envelope shape. The grey shaded area marks the wavelength region, in which the envelope shape is constraining the EBL density.

here, the pile up at high energies is already visible but not yet significant.

9.5.2 Intermediate distance, wide energy range: H1426+428

Using the H 1426+428 energy spectrum 5 571 772 EBL shapes (corresponding to 69.09% of all shapes) are excluded. The resulting envelope shape is displayed in Fig. 9.7, together with all highest allowed shapes. The limit is constraining from ∼6 to ∼20 μm and the constraints are not very strong. This is illustrated in Fig. 9.8, where two representative highest allowed EBL shapes and the resulting intrinsic spectra are shown, as are the relevant fit functions. Shape A is almost as high as the maximum shape of the scan. Although the intrinsic spectrum is already convex, the relative low statistics of the spectrum even allows for an acceptable fit by a simple PL and results in large errors on the fit parameters for the BPL. Consequently the EBL shape A cannot be excluded. Shape B has a high peak in the O/IR wavelength region but lies below all upper limits in the FIR. The resulting intrinsic spectrum is best described with a simple PL with a maximum slope $\Gamma^{\mathrm{PL}}_{\mathrm{max}} = 1.63 > 1.5$ and is therefore allowed.

9.5.3 Distant source, hard spectrum: 1ES 1101-232

The spectrum from 1ES 1101-232 gives the strongest constraints for all individual spectra, even though slightly fewer EBL shapes (7 706 625, 95.57% of all shapes) are excluded than in the case of Mkn 501. This is due to the different sensitivities

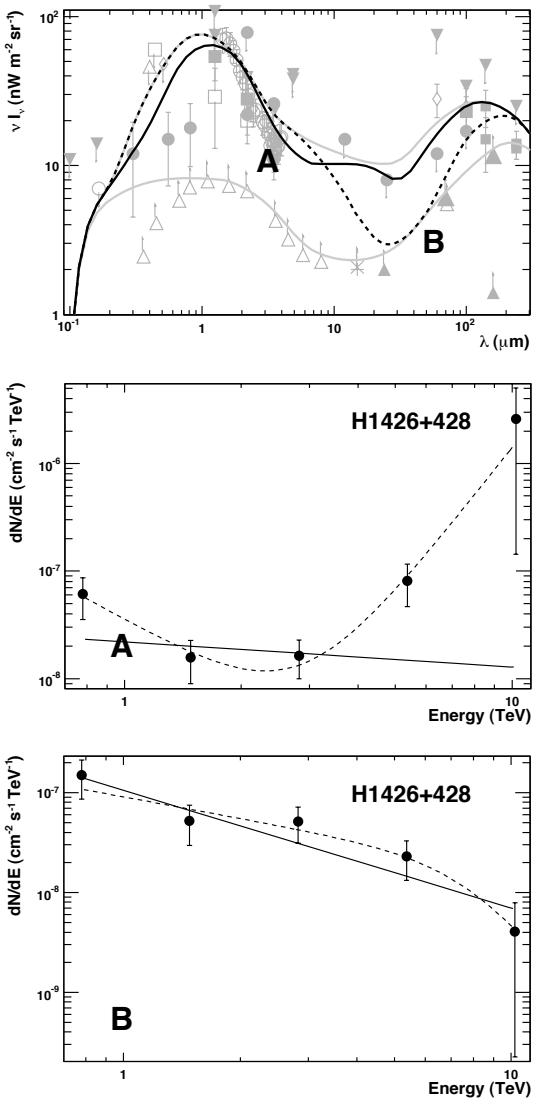

Figure 9.8: H1426+428 individual results ($\Gamma_{\rm max} > 1.5$). *Upper Panel:* Two examples for the highest allowed shapes (A - solid line; B - dashed line) overlayed on EBL measurements and the minimum and maximum shapes of the scan (grey). *Middle Panel:* Intrinsic spectrum for shape A and fit functions. Both PL (solid line) and BPL (dashed line) are good fits; $\Gamma^{\rm PL}_{\rm max} = 0.23 + 1.18_{\rm stat} + 0.2_{\rm sys} = 1.61$, and the BPL fit is preferred over the PL fit ($P_{\rm (BPL\ vs.\ PL)} = 0.97$); $\Gamma^{\rm BPL}_{\rm 1,max} = 2.01 + 1.94_{\rm stat} + 0.2_{\rm sys} = 4.15$ and $\Gamma^{\rm BPL}_{\rm 2,max} = -4.59 + 6.67_{\rm stat} + 0.2_{\rm sys} = 2.28$. *Lower Panel:* Intrinsic spectrum for shape B and fit functions. Both PL (solid line) and BPL (dashed line) are good fits; $\Gamma^{\rm PL}_{\rm max} = 1.18 + 0.24_{\rm stat} + 0.2_{\rm sys} = 1.63$ and the BPL fit is not preferred over the PL fit ($P_{\rm (BPL\ vs.\ PL)} = 0.54$);

in EBL wavelength; the 1ES 1101-232 spectrum is only sensitive up to $10\,\mu$m. The resulting maximum shapes and the envelope shape are shown in Fig. 9.9. The envelope shape constraints the EBL density in the wavelength range from $\sim$0.4 to $\sim$10 μm and clearly excludes the NIR excess claimed by Matsumoto et al. (2005) as being of extragalactic origin. At EBL wavelengths of $\sim$2 μm the limit is consistent with the limit derived by Aharonian et al. (2006a) for the same source with a different technique (see Sect. 9.6). Two representative highest allowed shapes and the corresponding intrinsic spectra are shown in Fig. 9.10. Shape A illustrates the intrinsic spectrum for a high EBL density in the UV/O, while shape B is the maximum shape for wavelengths around 3 μm. For both shapes the examined fit parameters are close to the allowed limits (see caption for values), as expected for the highest allowed shapes.

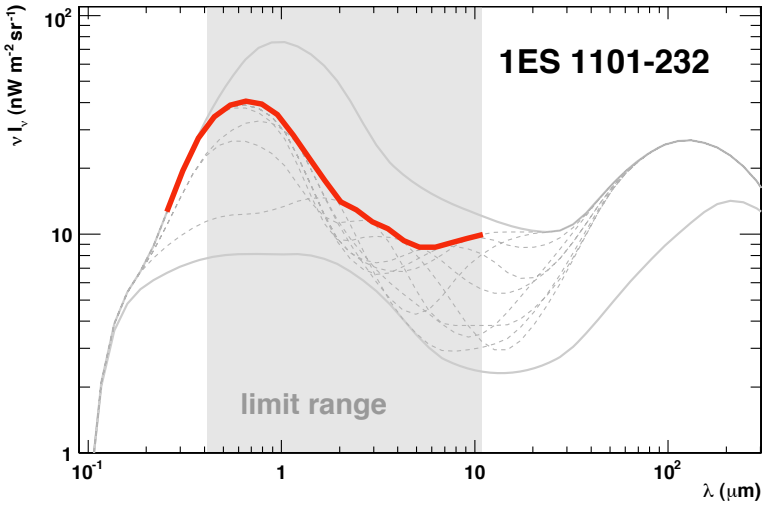

Figure 9.9: Limits on the EBL density from 1ES 1101-232 ($\Gamma_{\rm max} > 1.5$). Grey solid curves are the minimum and maximum shapes of the scan; grey dashed curves are all the highest allowed EBL shapes for 1ES 1101-232; the thick colored curve is the corresponding envelope shape. The grey shaded area marks the wavelength region, in which the envelope shape is constraining the EBL density.

9.5.4 *Extreme* case: $\Gamma_{\rm max}$ up to 2/3 allowed

The upper limits for Mkn 501, H1426+428 and 1ES 1101-232 for the *extreme* allowed case with $\Gamma_{\rm max} > 2/3$ are shown in Fig. 9.11 in comparison to the limits derived for the *realistic* case. In the case of Mkn 501, a similar number of EBL shapes (94.13%) as in the *realistic* scan are excluded, but the effective limit is less constraining (Fig. 9.11, Upper Left Panel). For H1426+428 the limit almost remains at the same level, still close to the maximum shape tested in the scan (Fig. 9.11, Upper Right Panel). For 1ES 1101-232 the limit in the UV/O lies a factor of 1.2 to 1.8 higher than the limit in the *realistic* case (Fig. 9.11, Lower Left Panel). In the wavelength region from 2 to 4μm, the NIR excess claimed by Matsumoto et al. (2005) is now compatible with the limit. In the 1 to 2μ region the limit still lies clearly below the claimed NIR excess.

9.6 Combined results

The number of excluded shapes for all individual spectra for the *realistic* scan are summarized in Table 9.4. One finds that some spectra (namely 1ES 2344+514, Mkn 180, and PKS 2005-489) exclude none of the EBL shapes of the scan. This is mainly a result of the low statistics and limited energy range of the spectra, hence resulting in large errors on the fit parameters. The highest number of excluded shapes and the strongest constraint in the scan result from the previously

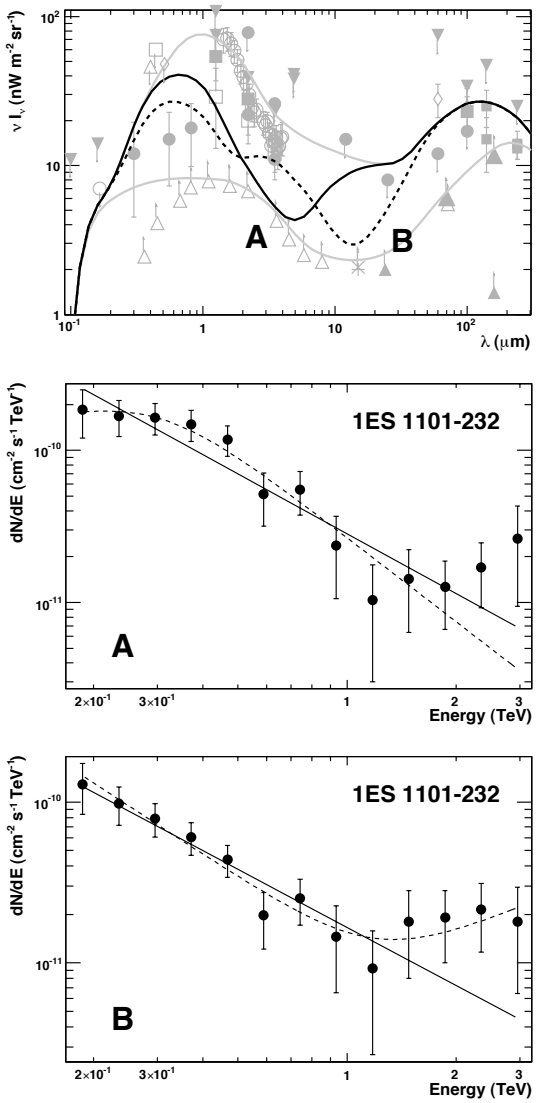

Figure 9.10: 1ES 1101-232 individual results ($\Gamma_{\rm max} > 1.5$). *Upper Panel:* Two examples for the highest allowed shapes (A - solid line; B - dashed line) overlayed on EBL measurements and the minimum and maximum shapes of the scan (grey). *Middle Panel:* Intrinsic spectrum for shape A and fit functions. Both PL (solid line) and BPL (dashed line) are good fits; $\Gamma^{\rm PL}_{\rm max} = 1.31 + 0.13_{\rm stat} + 0.1_{\rm sys} = 1.53$ and the BPL fit is not preferred over the PL fit ($P_{\rm (BPL\ vs.\ PL)} = 0.87$). *Lower Panel:* Intrinsic spectrum for shape B and fit functions. Both PL (solid line) and BPL (dashed line) are good fits; $\Gamma^{\rm PL}_{\rm max} = 1.21 + 0.21_{\rm stat} + 0.1_{\rm sys} = 1.52$ and the BPL fit is not preferred over the PL fit ($P_{\rm (BPL\ vs.\ PL)} = 0.9488$).

presented prototype spectra Mkn 501, H 1426+428, and 1ES 1101-232.

The results of the scan from all TeV spectra are combined by excluding all EBL shapes of the scan, which are excluded by at least one of the spectra.

9.6.1 Combined results of the *realistic* scan

A large fraction of the shapes (98.08%) are excluded by more than one spectra (see Fig. 9.12), which strengthens our results. In total, we exclude 8 056 718 shapes, which leaves us with only 7 282 (0.01%) allowed shapes. The resulting maximum shapes (dashed lines) and the envelope shape for the combined results are shown in the upper panel of Fig. 9.13 in comparison to the results from the individual prototype spectra. In the optical-to-near-infrared the combined limit

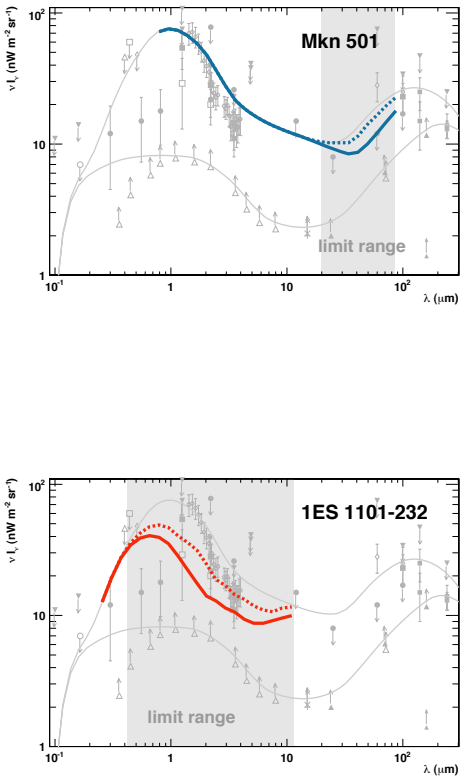

Figure 9.11: Result for individual spectra, comparing the *realistic* case with $\Gamma_{\max} > 1.5$ (thick colored solid line) with the *extreme* case with $\Gamma_{\max} > 2/3$ (thick colored dashed line), overlaid on the EBL measurements and the minimum and maximum shapes of the scan (grey markers and lines). The grey boxes indicate the validity range of the limit for the *realistic* scan as in Figs. 9.5, 9.7, and 9.9. Note that the validity range of the limits from the *extreme* scan are quite similar. *Upper Left Panel:* Results for Mkn 501 (HEGRA). *Upper Right Panel:* Results for H1426+428. *Lower Left Panel:* Results for 1ES 1101-232.

follows exactly the limit derived from the 1ES 1101-232 spectrum. For longer wavelengths, however, the combined limit lies significantly below the limits derived from individual spectra. This is particularly striking in the MIR, where the H 1426+428 spectrum provided only weak limits and the combined limit now gives considerable constraints. This can be understood from the fact that, for a high EBL density in the MIR, a high density in the optical to NIR is needed such that the spectra (Mkn 501, H 1426+428) will not get too hard. These high densities in the optical-to-NIR are now excluded by the 1ES 1110-232 spectrum, which therefore result in stronger constraints in the MIR.

The combined limit for the *realistic* scan in comparison to the direct measurements and limits is shown in the lower panel of Fig. 9.13. In the optical-to-NIR one finds that the combined limit lies significantly below the claimed NIR excess by Matsumoto et al. (2005). It is compatible with the detections reported by Dwek and Arendt (1998), Gorjian et al. (2000), Wright and Reese (2000), and Cambrésy et al. (2001). In the same figure the limit reported by the H.E.S.S. collaboration for 1ES 1101-232 derived with a different technique (Aharonian et al., 2006a) is shown and at wavelengths around 2 - 3 μm it is in good agreement with

Table 9.4: Number of excluded EBL shapes for the *realistic* scan for individual spectra (column 2) as well as the number of the intrinsic spectra, which could not be fitted satisfactorily (column 3).[a]

Spectrum	#Shapes Excluded	#Shapes No Fit
Mkn 421 (MAGIC)	1 756 869 (21.79%)	59 258 (0.94%)
Mkn 421 (HEGRA)	888 575 (11.02%)	0
Mkn 421 (Whipple)	2 287 059 (28.36%)	0
Mkn 501	7 760 733 (96.24%)	1296 (0.43%)
1ES 2344+514	0	0
Mkn 180	0	0
1ES 1959+650	1 086 314 (13.47%)	423 (0.01%)
PKS 2005-489	0	0
PKS 2155-304	4 248 872 (52.69%)	0
H 1426+428	5 571 771 (69.09%)	2 (0.00%)
H 2356-309	4 657 817 (57.76%)	0
1ES 1218+304	19 540 (00.24%)	0
1ES 1101-232	7 706 624 (95.57%)	0

[a] The percentage of these numbers to the number of all shapes (8 064 000) for column 2 and to the number of the allowed shapes for this spectrum for column 3 is also quoted. If the number of shapes is zero, the percentage is omitted.

the limit derived here. For shorter wavelengths our limit lies significantly higher. While for the H.E.S.S. limit comparable exclusion criteria for the spectra were used, a fixed reference shape scaled in the level of the EBL density was used to calculate the EBL limit[6], which presumably causes the differences at smaller wavelengths. In the MIR to FIR our combined limit lies below all previously reported upper limits from direct measurements and fluctuation analysis. For EBL wavelengths greater than 2 μm, the limit lies only about a factor of 2 to 2.5 higher than the absolute lower limit from source counts, leaving very little room for additional contributions to the EBL in this wavelength region. In the FIR it lies more than a factor of ~ 2 below the claimed detection by Finkbeiner et al. (2000).

9.6.2 Combined results of the *extreme* scan

In the *realistic* scan, after combining the results from Mkn 501, H 1426+428, and 1ES 1110-232, adding more spectra does not further strengthen the limit (though marginal more shapes are excluded). Hence, for the *extreme* scan, we only combine the results from these three spectra. The limit for the *extreme* scan

[6] In addition to the fixed shape, several other possible EBL components, like a bump in the UV, were examined (Aharonian et al., 2006a).

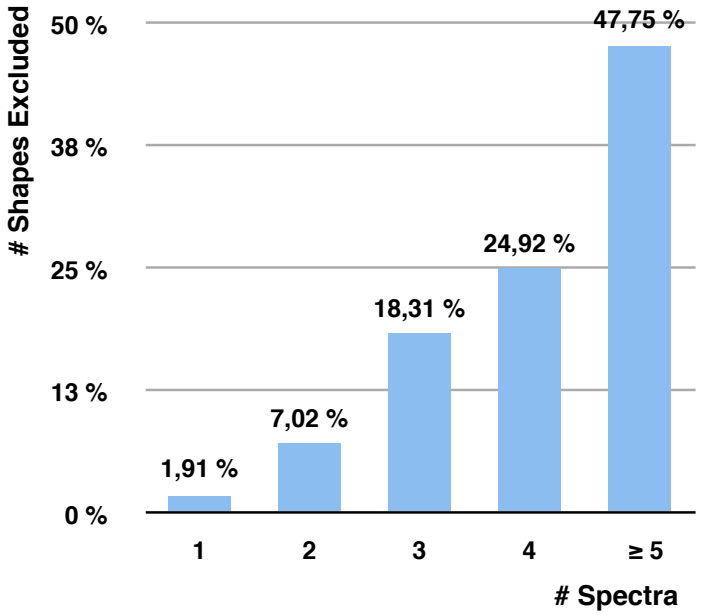

Figure 9.12: Number of excluded shapes as percentage of the total number of shapes vs. the number of spectra, that excluded the shape. A large fraction of shapes (98.08%) is excluded by more than one spectrum.

is shown in Fig. 9.14 in comparison to the limit from the *realisistic* scan. The limit from the *extreme* scan lies for all EBL wavelengths above the limits from the realistic scan and is a factor of 2.5 to 3.5 higher than the lower limits from the source counts. In the optical-to-NIR the combined limit again follows the limit derived from the 1ES 1101-232 spectrum. As stated for the individual spectrum the NIR excess claimed by Matsumoto et al. (2005) for wavelengths above 2 μm is now compatible with the limit, but for shorter wavelengths it is still clearly excluded.

9.6.3 Comparison of combined results with model predictions

In Fig. 9.15 the limits derived in this study are shown in comparison to predictions from EBL models by Kneiske et al. (2002), Stecker et al. (2006), and Primack et al. (2005) (at $z = 0$). The models lie below our *realisitc* limits, only the high model of Kneiske et al. (2002) is slightly higher in the NIR, and the fast evolution model of Stecker et al. (2006) is marginally higher in the MIR. These two models are also excluded when applying the criteria from Sect. 9.4 while the other models are allowed. Noteworthy is that the Primack et al. (2005) and the low model from Kneiske et al. (2002) are below the lower limits derived from galaxy counts in the MIR and FIR.

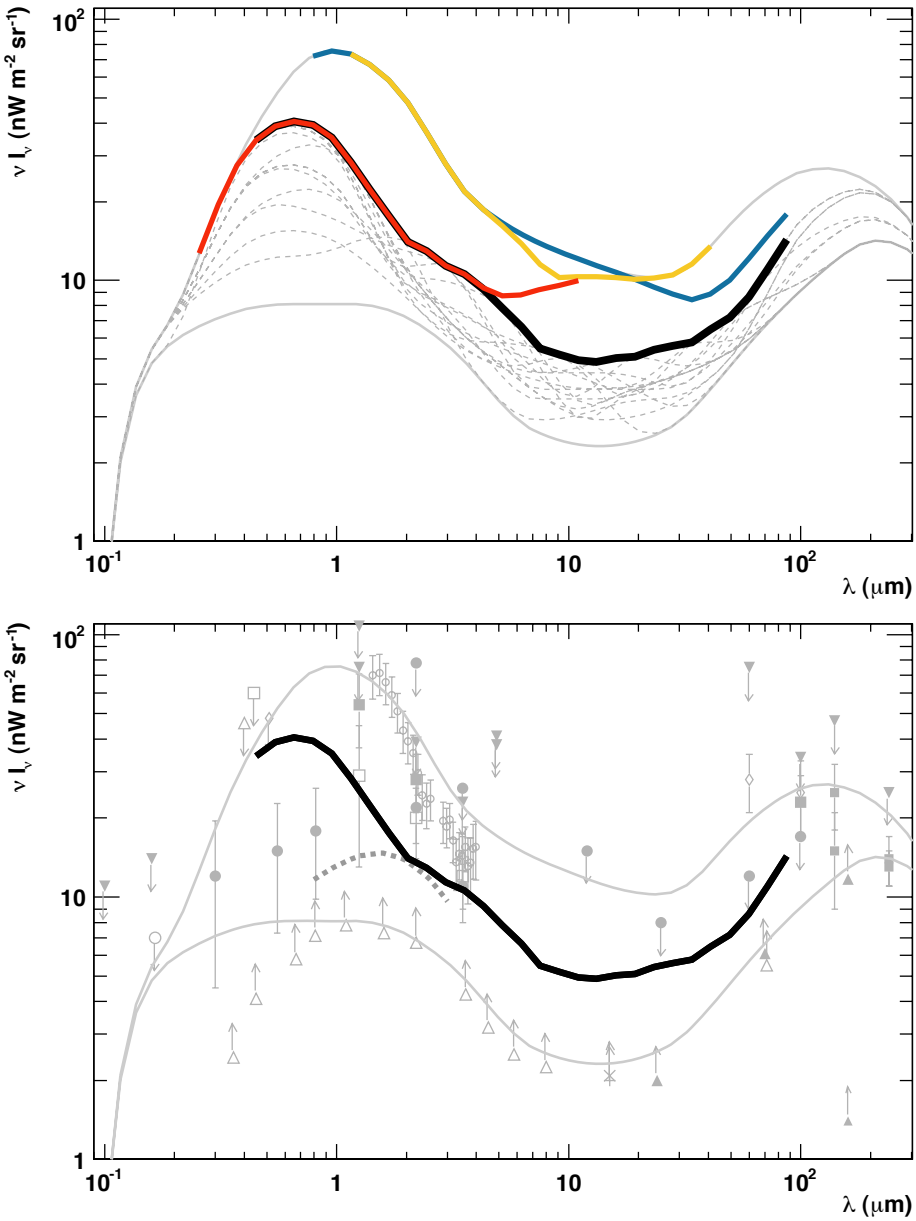

Figure 9.13: Combined results for the *realistic* scan. *Upper Panel:* All highest allowed shapes of the combined scan (dashed grey lines) and the corresponding envelope shape (solid black line) in comparison to the limits for individual spectra: Mkn 501 (solid blue line), H 1426+428 (solid yellow line), and 1ES 1101-232 (solid red line). The minimum and maximum shapes of the scan are also shown (grey lines). *Lower Panel:* The combined limit from the *realistic* scan (solid black line) in comparison to direct measurements and limits (grey marker). The grey dashed curve around 2 μm is the limit derived by Aharonian et al. (2006a).

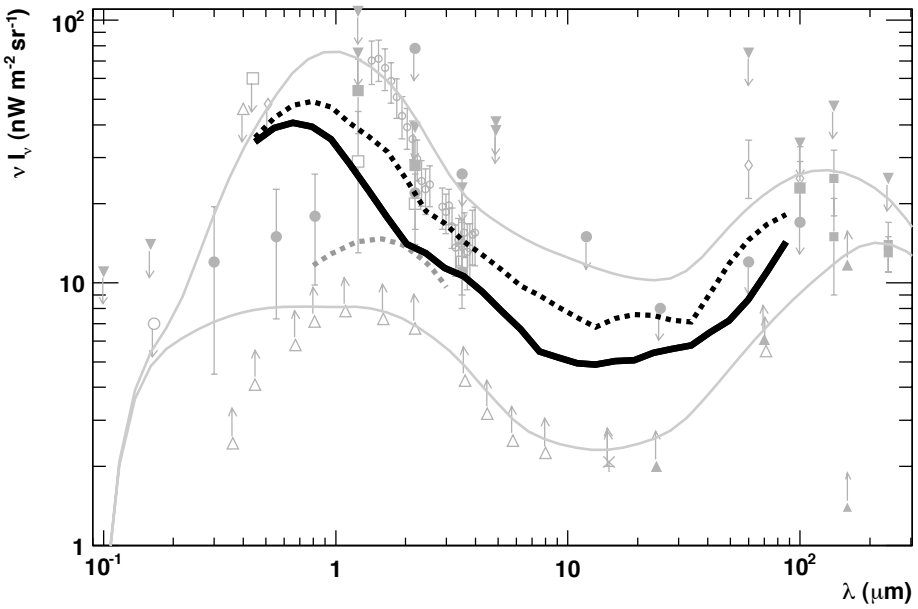

Figure 9.14: Combined results from the *extreme* scan (dashed black line) in comparison to the result from the *realistic* scan (solid black line). Grey lines are the minimum and the maximum shapes tested in the scan. Grey markers are direct measurements and limits.

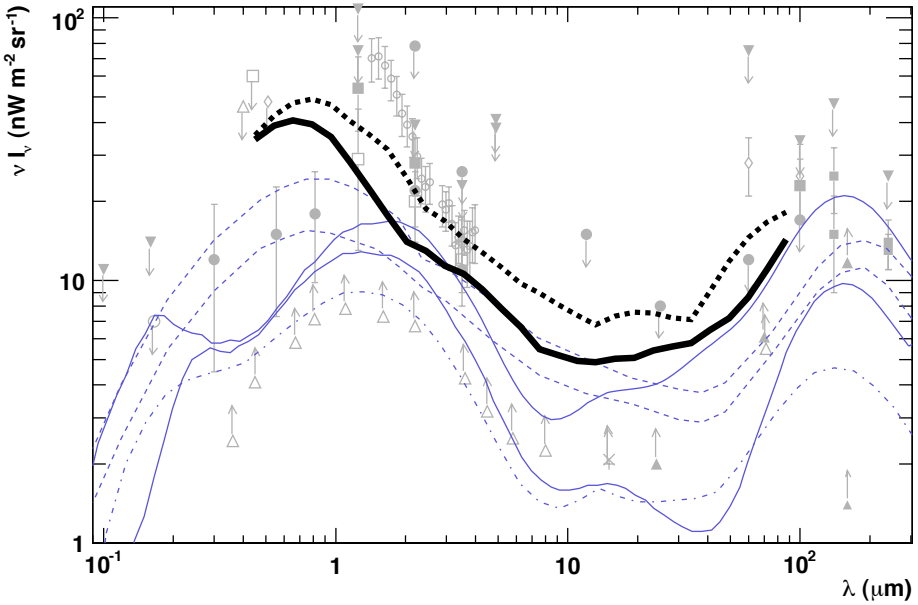

Figure 9.15: EBL limits from the *realistic* (thick solid black curve) and the *extreme* scan (thick dashed black curve) in comparison to different EBL models at $z = 0$ (blue curves): updated version of the Kneiske et al. (2002) high and low models (solid), Stecker et al. (2006) fast and baseline evolution models (dashed), Primack et al. (2005) (dashed dotted).

9.7 Summary and conclusions

In this study we present a new method of constraining the density of the extragalactic background light (EBL) in the optical-to-far-infrared wavelength regime using VHE spectra of TeV blazars. We derive strong upper limits, which are only a factor 2 to 3 higher than the lower limits determined from the source counts. Unlike many previous studies of this kind, we do not use one or a few pre-defined EBL shapes or models, but rather a scan on a grid in EBL density vs. wavelength. This grid covers the wavelength range from 0.1 μm to 1000 μm and spans the EBL density range from the lower limits from the source counts to the upper limits determined from direct measurements and fluctuation analyses. By iterating over all scan points, we test a large set of different EBL shapes (8 064 000 in total). Each EBL shape is described by a spline function, which allows us to calculate the optical depth of VHE γ-rays for this shape via a simple summation instead of solving three integrals numerically. The resolution of the scan for sharp bumps or dips in the EBL is limited by the choice of the grid and the order of the spline.

To test the EBL shapes, we use the measured VHE γ-ray spectra from distant sources, which carry an imprint of the EBL from attenuation via pair production. We included spectra from all known TeV blazars (13 in total), making this the most complete study of this type up to now. All spectra are scrutinized with the same robust algorithm. For each spectrum and each EBL shape, the intrinsic spectrum is calculated and an analytical description of the intrinsic spectrum is determined by fitting several functions. The fit parameters and errors of the functions are subsequently used to evaluate whether the intrinsic spectrum is physically feasible. We use two conservative criteria from the theory of VHE γ-ray emission in TeV blazars. The EBL shape is excluded if (i) a part of the intrinsic spectrum is harder than a theoretical limit or (ii) the intrinsic spectrum shows a significant pile-up at high energies. Since there is some spread in the predictions from theory, we included two independent scans for two theoretical limits on the hardness of the spectrum: (1) the *realistic* case allowing a photon index of $\Gamma > 1.5$ and (2) the *extreme* allowed case with $\Gamma > 2/3$.

We present limits derived from individual VHE γ-ray spectra. The strongest constraints result from the 1ES 1101-232 spectrum in the wavelength range from 0.8 and 10 μm, mainly due to the hard spectrum and its large redshift. An extragalactic origin of the claimed excess in the NIR between 1 and 2 μm (Matsumoto et al., 2005) can be excluded even by the *extreme* scan. This result confirms the results from the recent publication of Aharonian et al. (2006a). In the FIR (20 and 80 μm), strong upper limits are provided by the nearby TeV blazar Mkn 501. H 1426+428, situated at an intermediate distance, provides some constraints on the EBL density in the MIR (between 1 and 15 μm), connecting the upper limits derived from 1ES 1101-232 and Mkn 501. Most of the other spectra provide constraints in certain wavelength ranges, but they are not as strong as the limits from the three mentioned sources.

By combining the results from all spectra, we find that the upper limits become much lower compared to the limits derived for individual spectra, especially in the wavelength range between 4 and 60 μm. In the wavelength region from 2 to 80 μm, the combined limit for the *realistic* case lies below the upper limits derived from fluctuation analyses of the direct measurements (Kashlinsky and Odenwald, 2000) and is just a factor of 2 to 2.5 above the absolute lower limits from the source counts. This makes it the most constraining limit in the MIR to FIR region so far. As expected, the upper limits from the *extreme* scan are less constraining (factor of 2.5 to 3.5 above the lower limit from the source counts), but still substantial for this wide wavelength range.

The derived upper limits can be interpreted in two different ways:

1. The EBL density in the optical-to-FIR is significantly lower than suggested by direct measurements, and the actual EBL level seems to be close to the existing lower limits. It can thus be concluded that experiments like HST, ISO, and Spitzer resolve most of the sources in the universe. This would indicate that there is very little room left for a significant contribution of heavy and bright Population III stars to the EBL density in this wavelength region.

2. The assumptions used for this study are not correct. This would require a revision of the current understanding of TeV blazar physics and models, which has so far been fairly successful in modeling multi-wavelength data from the radio to the VHE for all detected sources.

We estimate that the main contribution to the systematic errors arises from the minimum width of the EBL structures that can be resolved by the scan. Although the choice of the grid spacing, which defines the minimum width of the EBL structures, is physically well motivated, there are arguments that even thinner structures could be realized in nature due to, say absorption effects. We tested a 20% smaller grid spacing, resulting in much less realistic, but still possible, EBL structures, when using the 1ES 1101-232 spectrum. The resulting limits on the EBL are 20 to 30% higher than the ones presented in Section 5.3. We therefore conclude that the overall contribution from the grid setup to the systematic error is at most 30%.

Another contribution to the systematic error originates from ignoring the evolution of the EBL in the method. To estimate the effect of the evolution of the EBL for the most distant sources, we calculate the late contribution to the EBL in the redshift interval between $z = 0$ and $z = 0.2$. Here, we utilize the EBL model by Kneiske et al. (2002) (the recently updated version is used, Kneiske 2006, private communication). We obtain a wavelength dependent contribution, which has a maximum value of 3-4 $\mathrm{nW\,m^{-2}sr^{-1}}$ in the optical to NIR (the relevant wavelength region for the distant sources in our scan). Given that these values

are derived with the extreme assumption that all late emission occured instantaneously at z=0, we estimate the systematic error arising from the EBL evolution to 10% of the derived limits. Note that Aharonian et al. (2006a) estimated an error of <10% for the most distant TeV blazar in our study 1ES 1101-232.

To study the effect of the uncertainties in the absolute energy scale of IACT measurements, we calculate a limit on the EBL utilizing the energy spectra from Mkn 501, H 1426+428, and 1ES 1101-232 shifted by 15% to lower energies (for $\Gamma > 1.5$, *realistic* scan). Since the optical depth is increasing with energy, the energy shift reduces the attenuation of the spectra, especially reducing the effect of a possible pile-up at the highest energies. The difference between the limit derived from the energy shifted spectra and the *realistic* limit is negligible in the optical to NIR ($<6\,\mu$m), while there is a moderate effect in the MIR to FIR on the level of $1-4.5\,\mathrm{nW\,m^{-2}sr^{-1}}$. We therefore conclude that the systematic error in the MIR to FIR ($\lambda > 6\,\mu$m) introduced by the uncertainties in the absolute energy scale of IACT measurements is close to 10–45% of our *realistic* limit.

Adding the individual errors quadratically, we finally conclude that the (very conservative) systematic error on the upper limit is about 32% in the optical-to-NIR and 33 – 55% in MIR to FIR.

The strong constraints derived in this study only allow for a low level of the EBL in the optical to the far-infrared, suggesting that the universe is more transparent to VHE γ-rays than previously thought. Hence, we expect detections of many new extragalactic VHE sources in the next few years. Further multi-wavelength studies of TeV blazars will improve the understanding of the underlying physics, which will help to refine the exclusion criteria for the VHE spectra in this kind of study. The upcoming GLAST satellite experiment, operating in an energy range from 0.1 up to ∼100 GeV, will allow such studies of the EBL to be extended to the ultraviolet-to-optical wavelength region.

Chapter 10

Implication from the EBL: redshift of PG 1553+113

PG 1553+113 is another known BL Lac object, newly detected in the GeV-TeV energy range by H.E.S.S. and MAGIC (Aharonian et al., 2006d; Albert et al., 2007a). The redshift of this source is unknown and a lower limit of $z > 0.09$ was recently estimated using its optical spectrum. The very high energy (VHE) spectrum of PG 1553+113 is attenuated due to the absorption by the low energy photon field of the extragalactic background light (EBL). Together with Florian Goebel (MPI for Physics, Munich) we developed a method to test the redshift of the PG 1553+113 using the measured VHE γ-ray spectrum and our knowledge about the EBL. In brief, we correct the combined H.E.S.S. and MAGIC spectrum of PG 1553+113 for this absorption assuming a minimum density of the evolving EBL. We use an argument that the intrinsic photon index cannot be harder than $\Gamma = 1.5$ and derive an upper limit on the redshift of $z < 0.69$. Moreover, we find that a redshift above $z = 0.42$ implies a possible break of the intrinsic spectrum at about 200 GeV. Assuming that such a break is absent, we derive a much stronger upper limit of $z < 0.42$. Alternatively, this break might be attributed to an additional emission component in the jet of PG 1553+113. This would be the first evidence for a second component is detected in the VHE spectrum of a blazar. This study was published in Mazin and Goebel (2007).

10.1 The case of the blazar PG 1553+113

PG 1553+113 was discovered in the Palomar-Green survey of UV-excess stellar objects (Green et al., 1986). It is classified as a BL Lac object based on its featureless spectrum and its significant optical variability (Falomo and Treves, 1990; Miller et al., 1988). PG 1553+113 is well studied from the radio to the X-ray regime. Based on its broad-band spectral energy distribution (SED), PG 1553+113 is now classified as a high-frequency peaked BL Lac (Giommi et al.,

1995), similar to most of the AGNs detected in the VHE band.

The redshift of PG 1553+113 is essentially unknown. It was initially determined to be z=0.36 (Miller and Green, 1983) but later this claim was withdrawn (Falomo and Treves, 1990). To date no emission or absorption lines have been measured despite several observation campaigns with optical instruments. No host galaxy was resolved in *Hubble Space Telescope* (HST) images of PG 1553+113 taken during the HST survey of 110 BL Lac objects (Scarpa et al., 2000). The HST results were used to set a lower limit of z>0.78 (Sbarufatti et al., 2005) for PG 1553+113 assuming that PG 1553+113 is a typical L-star elliptical galaxy (Stefan Wagner, private communication). A more recent publication claims a lower limit on the redshift of z>0.09 using the ESO-VLT optical spectroscopy survey of 42 BL Lacertae objects of unknown redshift (Sbarufatti et al., 2006). The possibility of a large redshift is of critical importance to VHE observations due to the absorption of VHE photons by pair-production on the extragalactic background light (EBL, see Section 1.5 and Chapter 3 for details). This absorption, which is energy dependent and increases strongly with redshift, distorts the VHE energy spectra observed from distant objects. Note that the most distant objects detected so far at VHE are 1ES 1011+496 ($z = 0.212$, Albert et al. (2007c), Chapter 8) and 1ES 1101-232 ($z = 0.186$, Aharonian et al. (2007d)).

Recently, VHE γ-ray emission from PG 1553+113 was measured by H.E.S.S (Aharonian et al., 2006d) and by MAGIC (Albert et al., 2007a). Both collaborations reported a soft energy spectrum with a differential photon index of $\Gamma = 4.0 \pm 0.6$ and $\Gamma = 4.2 \pm 0.3$ respectively. The VHE data from the two measurements were used independently to derive an upper limit on the redshift of the source of $z < 0.74$. This limit is based on the assumption of a minimum possible level of the EBL and the maximum hardness of the intrinsic VHE spectrum. Although the intrinsic VHE γ-ray spectra of the AGNs are not well known, it can be assumed that the intrinsic photon index of the sources is not harder than $\Gamma_{\rm int}$=1.5. However, there are emission scenarios where the maximum possible VHE photon index is even harder ($\Gamma_{\rm int} = 2/3$, Katarzyński et al. (2006), Section 2.4.4).

Here we use the combined H.E.S.S. and MAGIC spectrum of PG 1553+113 to derive upper limits on its redshift, assuming the two limits on the hardness of the intrinsic photon index ($\Gamma_{\rm int}$=1.5 and $\Gamma_{\rm int} = 2/3$).

In addition, we present an alternative method to estimate an upper limit on the redshift of PG 1553+113 assuming that there is no break in the intrinsic VHE spectrum of the source.

10.2 Assumed minimum EBL

The most likely reaction channel in the interaction of VHE γ-rays with the low energy photons of the EBL is pair production $\gamma_{\rm VHE} + \gamma_{\rm EBL} \rightarrow e^+ e^-$ (see Sec-

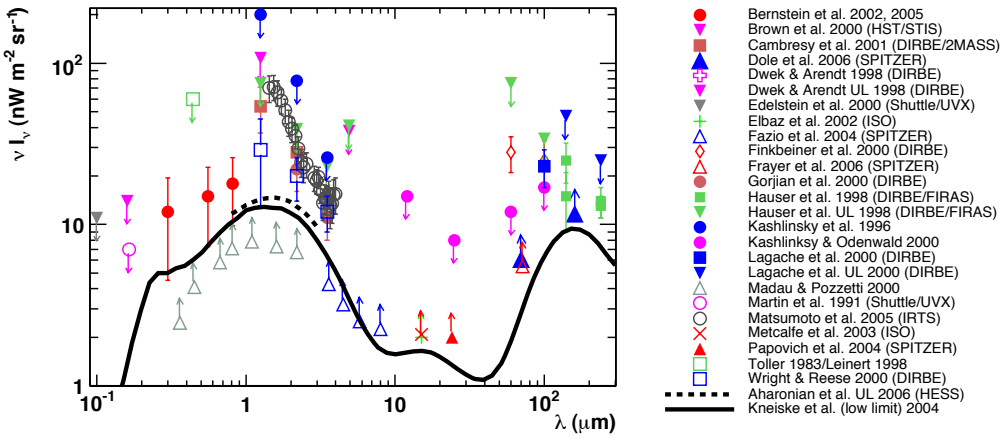

Figure 10.1: Energy density of the extragalactic background light (EBL). Direct measurements, galaxy counts, low and upper limits are shown by different symbols as described in the legend. The dashed black line represents the upper limit set by H.E.S.S. (Aharonian et al., 2007d). The black solid curve is the minimum EBL spectrum taken from Kneiske et al. (2002) for z=0. The model takes evolution of the EBL into account.

tion 1.3). The relevant EBL wavelength range for the absorption of VHE γ-rays spans from UV light (0.1 μm) to far infrared (few 100 μm). This light predominantly consists of redshifted star light of all epochs and reemission of a part of this light by dust in galaxies (for more details see more Chapter 3). The intrinsic (de-absorbed) VHE photon spectrum, dN/dE_i, of a blazar located at redshift z can be determined using:

$$dN/dE_i \; = \; dN/dE_{obs} \times \exp[\tau_{\gamma\gamma}(E,\, z)], \tag{10.1}$$

where dN/dE_{obs} is the observed spectrum and $\tau_{\gamma\gamma}(E,\, z)$ is the optical depth.

In the present study, we want to use the lowest possible realistic level of the EBL in order to derive a minimum redshift, above which a break in the VHE spectrum of PG 1553+113 becomes evident. Several EBL models have been developed, taking into account the evolution of the EBL, which is related to star and galaxy evolution (e.g. Kneiske et al. (2002); Primack et al. (2005); Stecker et al. (2006)). Though different in approach, the models agree in their predictions within a factor of 2. For this study, we use the lower limit model from Kneiske et al. (2002), which is just at the level of the direct lower limits set by the galaxy counts (see Fig. 10.1).

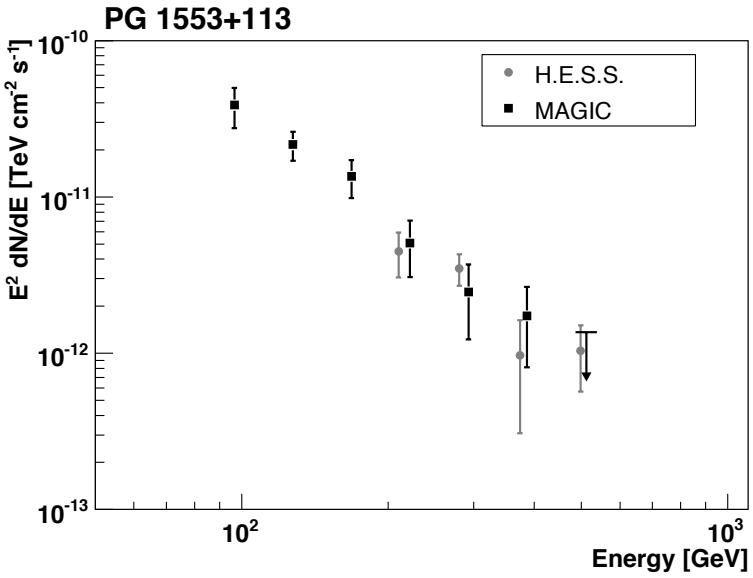

Figure 10.2: Differential measured energy spectrum of PG 1553+113 multiplied by E^2 to show the energy density. The spectrum measured by H.E.S.S. is shown by grey points, whereas the MAGIC spectrum is shown by black boxes. The last point in the MAGIC spectrum is a 95% upper limit.

10.3 Combining the spectra of PG 1553+113 from H.E.S.S. and MAGIC

The differential VHE γ-ray spectra of PG 1553+113 published by H.E.S.S. and MAGIC are shown in Fig. 10.2. The photon fluxes are multiplied by E^2, which is equivalent to a $\nu F(\nu)$ representation. The H.E.S.S. data are shown as grey circles and the MAGIC data by black boxes. For H.E.S.S., the data were taken in spring–summer 2005. In case of MAGIC, it is a combined data set taken between spring 2005 and winter 2006. The last spectral point is a 95% upper limit and will not be used in the further analysis. AGNs are known to be variable sources in flux so that, in general, it is not trivial to combine non-simultaneous data sets. In the present case, however, the agreement between the spectra measured by H.E.S.S. and MAGIC is very good. As a test, we fitted a power law

$$dN/dE = N_0 E^{-\Gamma} \tag{10.2}$$

to the observed spectra in the overlapping energy region between 150 and 600 GeV by fixing the slope (observed photon index Γ) to the value measured by H.E.S.S.: $\Gamma = 4$. The resulting normalization factors are

$$N_0 = (2.01 \pm 0.34) \times 10^{-13}\ \mathrm{phot}/(\mathrm{TeV\,cm^2\,s})^{-1}$$

and

$$N_0 = (2.24 \pm 0.59) \times 10^{-13}\ \mathrm{phot}/(\mathrm{TeV\,cm^2\,s})^{-1}$$

for the H.E.S.S. and MAGIC data, respectively. These numbers differ by 10%, which is small compared to the individual statistical errors. In order to increase the statistical power of the tests described below, we use the combined spectrum of MAGIC and H.E.S.S. data on PG 1553+113. We normalize the spectra by multiplying the H.E.S.S. fluxes by a factor 1.1 to avoid a possible bias in our results. In order to show the effect of the normalization we also perform the same study on a combined spectrum without this normalization.

10.4 Determination of upper limits on the redshift of PG 1553+113

Two different methods are used. The first one assumes that the spectral index of the intrinsic differential photon spectrum is not higher than 1.5 (or, alternatively, 2/3). The second one assumes that the intrinsic photon spectrum has no break in the measured energy region from 80 to 600 GeV.

10.4.1 Maximum intrinsic photon index Γ_{int}

A fit of Eq. 10.3 is performed to the intrinsic spectrum of PG 1553+113. The fitted index Γ_{int} and its error σ_Γ are combined to Γ_{max}, where $\Gamma_{\mathrm{max}} = \Gamma_{\mathrm{int}} + 2 \times \sigma_\Gamma$ corresponding to a 95% confidence level. We note that despite the fact that for $z > 0.42$ (see below) a curved power law gives a significantly better fit to the intrinsic spectrum than a simple power law, the χ^2 value of the latter fit is still acceptable. A redshift z is considered to be unrealistic if $\Gamma_{\mathrm{max}} < 1.5$ or, in case of the extreme scenario, $\Gamma_{\mathrm{max}} < 2/3$.

10.4.2 Presence of a break in the intrinsic photon spectrum

The second method is based on the indication that for larger redshifts ($z > 0.3$) the intrinsic spectrum of PG 1553+113 exhibits a break at about 200 GeV with the intrinsic energy spectrum rising after the break (see Fig. 10.3). Such a break in the intrinsic spectrum of PG 1553+113 cannot be excluded *a priori*. It could be attributed to a second population of γ-ray emitting particles. However, in none of the measured VHE γ-ray spectra of extragalactic sources such a component has been found. Thus, if a spectrum shows a break, either it is the first time a second emitting component is found in a VHE γ-ray spectrum or a lower redshift value z has to be assumed.

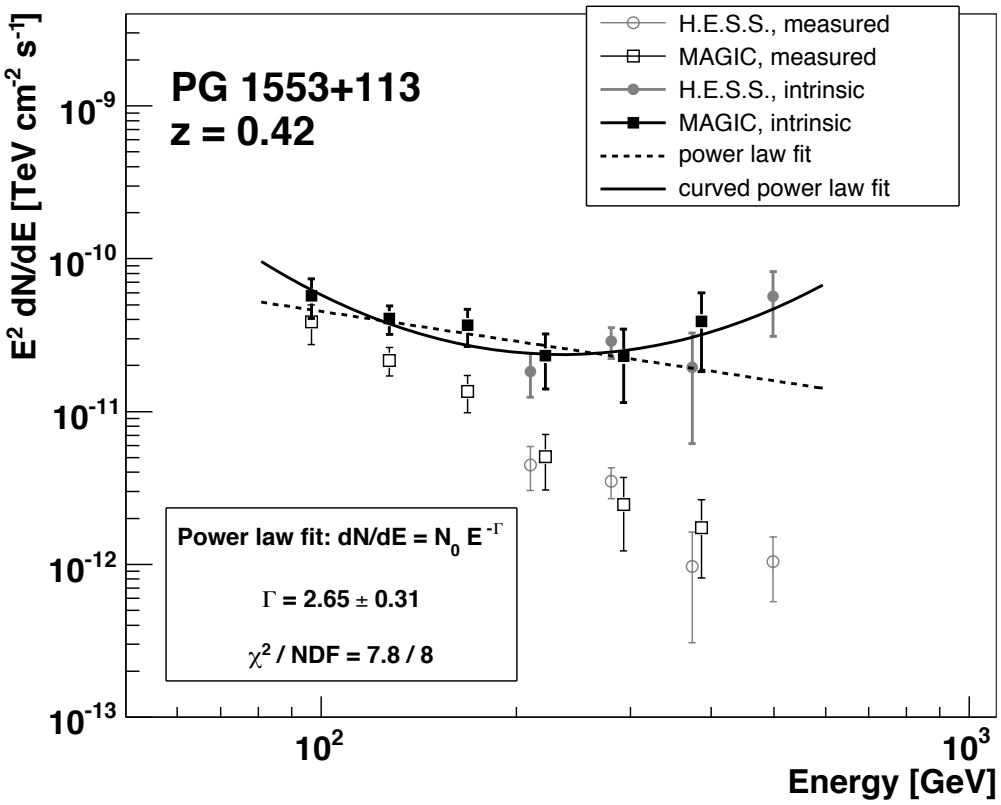

Figure 10.3: Constraint on the redshift of PG 1553+113. *Hollow points*: measured combined (normalized) differential energy spectrum of PG 1553+113 using MAGIC (squares) and H.E.S.S. (circles) data from 2005 and 2006. *Filled points*: intrinsic spectrum of PG 1553+113, using minimum possible density of the evolving EBL and the redshift of $z = 0.42$. *Black dotted line*: power law fit to the intrinsic spectrum; the fitted photon index is listed in the inlay. *Black solid line*: curved power law fit. The probability of the likelihood ratio test is 95.06%, meaning that the fit by a curved power law is to be preferred over the fit by a power law.

To test the presence of a second component (or the presence of a break) in the VHE spectrum of PG 1553+113 we performed a likelihood ratio test (see Appendix C) on the intrinsic spectrum. Two hypotheses are tested. Hypothesis A is a simple power law (2 free parameters):

$$dN/dE = N_0 E^{-\Gamma_{\rm int}} \tag{10.3}$$

Hypothesis B is a curved power law (3 free parameters):

$$dN/dE = N_0 E^{-(\alpha + \beta \, \ln(E))} \,, \tag{10.4}$$

which corresponds to a parabolic law in a $\log(\mathrm{E}^2\,\mathrm{dN/dE})$ vs. $\log(\mathrm{E})$ representation. A parabolic shape is a natural choice to describe the transition region of a break between two spectral components. By fitting the two functional forms (Eq. 10.3 and 10.4) to the de-absorbed spectrum one obtains values of the likelihood functions L_A and L_B. If hypothesis A is true the likelihood ratio $R = -\ln(L_A/L_B)$ is approximately χ^2 distributed with one degree of freedom. One defines a probability

$$P = \int_0^{R_{\rm meas}} p\,(\chi^2)\,\mathrm{d}\chi^2 \tag{10.5}$$

where $p\,(\chi^2)$ is the χ^2 probability density function and R_{meas} is the measured value of R. Hypothesis A will be rejected (and hypothesis B will be accepted) if P is greater than the confidence level, which is set to 95%.

10.5 Break in the VHE spectrum of PG 1553+113?

We examined a wide range of redshifts values z between 0.1 and 0.9 in steps of 0.02. Each time, the corresponding optical depth was calculated and the intrinsic spectrum of PG 1553+113 was determined using the low limit model from Kneiske et al. (2002). The probability of the likelihood ratio test and the intrinsic photon index $\Gamma_{\rm int}$ as a function of redshift z are shown in Fig. 10.4.

The intrinsic photon index $\Gamma_{\rm int}$ as a function of the redshift is shown by the thick blue line in Fig. 10.4. A 2σ confidence belt is drawn as blue shaded area. The result without the normalization between the H.E.S.S. and MAGIC measured spectrum of PG 1553+113 is shown by the dashed blue line with a corresponding 2σ confidence belt as grey shaded area. Assuming that the intrinsic photon index cannot be harder than $\Gamma_{\rm int} = 1.5$, we obtain a redshift limit of $z < 0.69$ with a confidence of 95%. Assuming the maximally hard spectrum as proposed by Katarzyński et al. (2006) with $\Gamma_{\rm int} = 2/3$, we obtain a redshift upper limit of $z < 0.80$.

The intrinsic spectrum was considered to have a break if the likelihood ratio test gave more than 95% confidence. The probability of the likelihood ratio

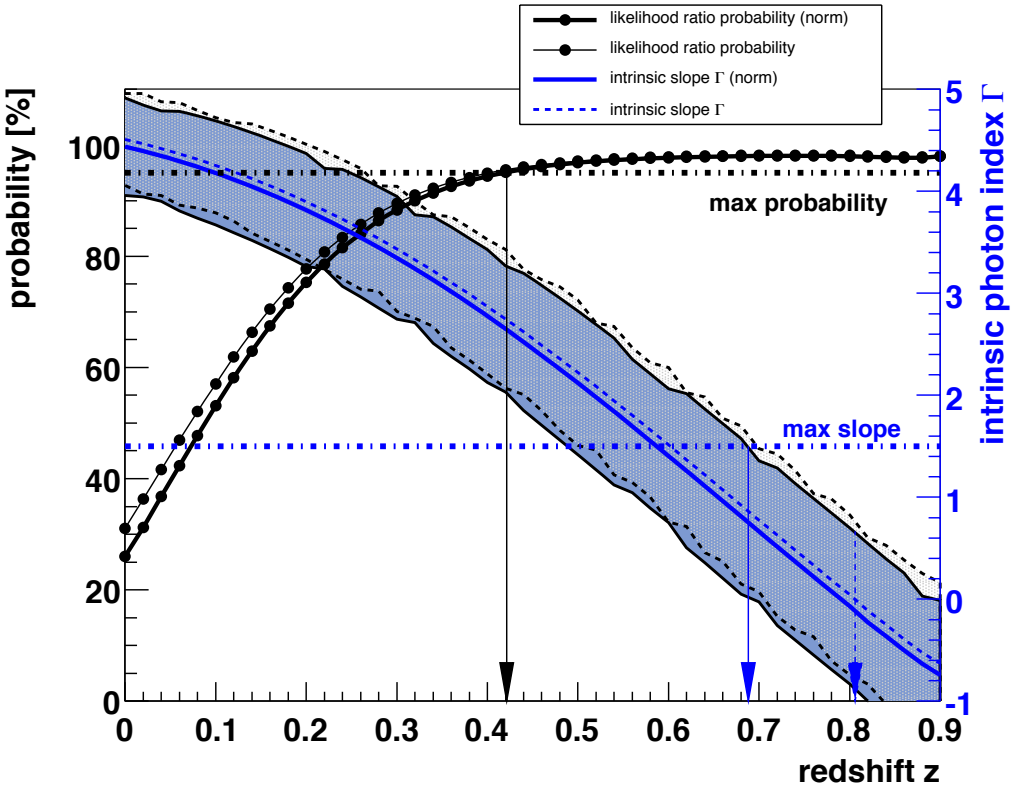

Figure 10.4: Constraints on the redshift of PG 1553+113 (see text for details).
Black points and left Y-axis: probability of the likelihood ratio test (Eq. 10.5). The black arrow indicates the minimum redshift ($z = 0.42$), at which the break in the intrinsic spectrum of PG 1553+113 is evident.
Blue line and right Y-axis: intrinsic photon index $\Gamma_{\rm int}$. Shaded areas correspond to 2 σ confidence belt. The intrinsic spectrum is harder than this for $z > 0.69$, which is indicated by the blue arrow. The extreme case of $\Gamma = 2/3$ leads to an upper limit of $z < 0.80$ as indicated by the dashed blue arrow.

test as a function of the redshift is shown by the black points and thick black line in Fig. 10.4. The smallest redshift, for which the test gave more than 95% confidence, is $z = 0.42$ (see Fig. 10.3). The assumption that there is no break in the intrinsic spectrum of PG 1553+113 thus leads to an upper limit on its redshift of $z < 0.42$. The result without the normalization between the H.E.S.S. and MAGIC measured spectrum is shown by the thin black line. The systematic uncertainty in the derived limits, arising from the applied normalization of 10% between the H.E.S.S. and MAGIC data, is below 10%.

The test for the existence of a break cannot be applied to the H.E.S.S. spectrum alone since the break occurs around the lower end of the energy region of the H.E.S.S. measurement. On the other hand, applying this test to the MAGIC data alone never reaches the required probability of 95% for the existence of the break due to insufficient statistics.

10.6 Discussion of the results

In this study, we combined H.E.S.S. and MAGIC data using their good agreement and used a realistic minimum density of the EBL to reconstruct the intrinsic spectrum of PG 1553+113. We showed that the intrinsic photon index $\Gamma_{\rm int}$ becomes smaller than $\Gamma_{\rm int} = 1.5$ at $z = 0.69$, which can be considered a robust upper limit on the redshift of PG 1553+113. In case of the extreme emission scenario with $\Gamma_{\rm int} = 2/3$, we obtain an upper limit of $z < 0.80$. Moreover, we showed that a break in the intrinsic spectrum at about 200 GeV becomes evident at a redshift of $z = 0.42$. The break can either be interpreted as an upper limit on the redshift of PG 1553+113 or as evidence for a second emission component in the VHE spectrum of the object. The upper limit of $z < 0.42$ implies values of the intrinsic slope indicating that the peak of the high-energy component of the SED lies below few hundred GeV, as typically derived for the closest TeV blazars Mrk 421 and Mrk 501 (in low flux state). We note that increasing the statistics by combining the spectra of MAGIC and H.E.S.S. resulted in a moderate improvement of the redshift upper limit. On the other hand, the second method, which is based on the search for structures in the intrinsic spectrum and which resulted in much more stringent limits, became only feasible using the combined data set.

The knowledge of the distance of PG 1553+113 is crucial for the modeling of the emission processes in the object, especially for combining X-ray and VHE data. In case the redshift of PG 1553+113 is larger than $z > 0.2$ it would not only be the farthest AGN detected in the VHE range so far but also by far the most energetic one. Further campaigns to determine the redshift of PG 1553+113 directly as well as extensive VHE observations are certainly interesting.

Chapter 11

Conclusion and Outlook

In the scope of this thesis I contributed to the field of VHE γ-ray astrophysics and its connection to cosmology. The results profited from the high sensitivity of the MAGIC telescope and especially from its low threshold. For the first time properties of the blazar Markarian 421, an AGN located at the redshift of z = 0.030, have been measured in the energy domain between 100 and 400 GeV. A clear curvature of the energy spectrum indicates that the (possibly inverse-Compton) peak position is at $\approx$100 GeV. The study of the broad-band energy spectrum using the MAGIC and archival data resulted in a support for a leptonic scenario of the γ-ray emission. Within this scenario, a clear hint is found that different flaring states result from differences in electron populations (electron spectrum) rather than from significant change of the blob's Doppler factor and magnetic field strength.

The understanding of the blazar properties and emission mechanisms responsible for the observed variability at all wavelengths is far from being complete. A necessary condition to progress in this field is a detection of more sources emitting VHE γ-rays. In the scope of this thesis, two new blazars, Markarian 180 (z = 0.045) and 1ES 1011+496 (z = 0.212) have been discovered in the VHE γ-ray domain making it to a total of 13 sources in the GeV-TeV catalog of extragalactic sources. In both cases, the discovery was triggered by an optical outburst of the sources, which makes it very tempting to speculate that an optically high state of blazars is related to a VHE γ-ray activity. In case this relation exists, a detection of new extragalactic VHE γ-ray emitters can become easier since optical instruments are much more numerous and sensitive than X-ray satellites, which are usually used to trigger VHE γ-ray observations.

The available measurements of VHE γ-ray spectra of blazars were used to constrain the density of the EBL. With the existing sample of 13 extragalactic blazars detected at VHE, strong limits were derived in the broad wavelength range from the ultraviolet to far infrared. The derived upper limits are the strongest so far and can be interpreted in two different ways:

1. The EBL density in the optical-to-FIR is significantly lower than suggested

by direct measurements, and the actual EBL level seems to be close to the existing lower limits. It can then be concluded that experiments like HST, ISO, and Spitzer resolve most of the sources in the universe. This would indicate that there is very little room for a significant contribution of heavy and bright Population III stars to the EBL density in this wavelength region.

2. The assumptions on the intrinsic blazar spectra used for this study are not correct. This would require a revision of the current understanding of TeV blazar physics and models, which has so far been fairly successful in modeling multi-wavelength data from the radio to the VHE for all detected sources.

However, the GeV–TeV blazar sample is still small and the measured VHE γ-ray spectra are affected by large statistical uncertainties, which prevents one from distinguishing between an EBL imprint and intrinsic features of the sources. Hence, only upper limits on the EBL can be derived. Only with a larger sample of high quality VHE γ-ray spectra and a better understanding of the processes of the VHE γ-ray emission it will be possible to resolve the EBL level. Moreover, using many well-measured energy spectra of VHE γ-ray sources at different redshifts, one can constrain individual EBL contributions in redshift slices. This would be the first experimental measurement of the EBL evolution and an indirect measurement of the star formation rate as a function of the redshift.

Naturally, the next steps in this research field include both future observations of well established GeV-TeV blazars and the search for new VHE γ-ray emitting blazars. Precise measurements of energy spectra and light curves of the established sources in combination with simultaneous observations at other wavelengths will provide details on the jet structure and the acceleration mechanism. In addition, EBL constraints can be substantially improved by more precise measurements of the established GeV-TeV blazars. Especially the energy spectra above 20 TeV are important to constrain the EBL in the far infrared, where no EBL constraints using the current generation of IACTs are provided so far. Another major goal of future observations is the detection of new extragalactic VHE γ-ray sources exploiting the redshift range of these sources. So far the TeV blazar 1ES 1011+496 is the most distant source with a redshift of $z = 0.212$ while it is expected that VHE γ-ray sources with detectable fluxes exist up to a redshift of $z = 1$.

Joint efforts between big collaborations MAGIC, H.E.S.S. and VERITAS are ongoing in order to maxime the potential to detect blazars in flaring state. In addition, future observations of extragalactic VHE γ-ray sources will significantly profit from the new generation of sensitive IACT systems like MAGIC II and H.E.S.S. II starting operations in 2008 and 2009, respectively. Using the stereoscopic observation mode for the MAGIC II system of two telescopes, the sensitivity of MAGIC observations will increase by a factor of roughly 3. Motivated by

the outstanding results of the current ground based IACT experiments, ambitious plans already exist to build an IACT array of many telescopes. This Cherenkov Telescope Array, CTA, aims to increase the flux sensitivity by a factor of 10 and extend the accessible energy range from several 10's of GeV to 100 TeV. Projects like CTA promise a further dynamical development of VHE γ-ray astrophysics exploiting its exceptional physics potential for the next 10–15 years and beyond.

Appendix A

MAGIC strategies for the observation of AGNs

As MAGIC went online in 2003, only six extragalactic VHE γ-ray emitters were established: Mkn 421, Mkn 501, 1ES 1959+650, 1ES 2344+514, H 1426+428, and PKS 2155-304. All of them are HBLs, i.e. low luminosity blazars having the synchrotron peak in X-ray band. In following, I present the strategies to study known and to discover new extragalactic VHE γ-ray sources.

A.1 Monitoring of the bright TeV blazars

During the commissioning phase of the MAGIC telescope in the years 2003–2004, data on established blazars Mkn 421, Mkn 501, and 1ES 1959+650 were collected. Significant signals were obtained from all three sources, which for the first time allowed to study the properties of these sources below 300 GeV (Albert et al., 2006d, 2007e,g). Flux and spectral variabilities in time, correlations with other wavelength data and historical evolution of the source behavior could be studies with a precision which was not possible with previous instruments (see Chapter 6).

After the commissioning phase, the MAGIC collaboration established a long term monitoring program of bright TeV blazars. Currently, Mkn 421, Mkn 501, 1ES 1959+650 are being monitored 40 times per year and source for 20 minutes duration. In addition, whenever the scheduling plan allows it, the two sources 1H1426+428 and 1ES2344+514 (40 times 40 minutes each) should be observed. The sensitivity of MAGIC allows one to detect a signal if the flux level exceeds 50% of the Crab flux at a significance level of 5 sigma within 20 minutes. The monitoring observations are therefore well suited to trigger those multiwavelength campaigns, which are based on a high GeV/TeV γ-ray flux level. In addition, a long term flux level variability and statistics can be studied. The monitoring of the sources above 100 GeV will, among others, help to estimate the statis-

tical significance of possible correlations between observed neutrino events (by Amanda/IceCube) and γ-ray flares (E. Bernardini, internal IceCube/Amanda report). Since the proposed monitoring measurements are independent of any trigger condition they allow the detection of possible orphan flares, i.e. GeV/TeV flares without X-ray counterparts.

The integrated data will allow one to study energy spectra for different flux levels. In particular, since most of the data is expected to be taken during low flux levels, it will increase the hitherto scarce statistics taken during quiescent states.

A.2 Source *hunting* using the blazar sequence

Using the blazar sequence (see Section 2.2.2) as a guideline, the following criteria were used to select a catalog of primary candidates for new sources:

- High X-ray flux (based on Donato et al. (2001)), $F_{1\,\mathrm{keV}} > 2\,\mu$Jy;
- moderate redshift: $z < 0.3$;
- Culmination below 30 deg in La Palma, leading to sources with a declination between -2 deg and +58 deg.

Overall, 13 sources were selected and observed during the first year of operation of the MAGIC telescope. In that campaign the HBL source 1ES 1218+304 was discovered and the other HBL source 1ES 2344+514 was detected in a low flux state but with high significance. For other sources, upper limits on the level of 2 to 10% of the Crab Nebula flux were derived (Albert et al., 2007f).

The blazar PG 1553+113 did not fulfill the criteria above because its redshift was cataloged to be $z = 0.36$. The other criteria (X-ray flux and culmination in La Palma) were very well suited making PG1553+113 to an excellent candidate. Since, in addition, doubts about its redshift of $z = 0.36$ arose, it was proposed to observe it with MAGIC. The combined observations from 2005 and 2006 lead to a co-discovery of PG 1553+113 by H.E.S.S. (Aharonian et al., 2006d) and MAGIC (Albert et al., 2007a).

A.3 Are the powerful LBL emitting at VHE?

The total luminosity of most LBLs is about two orders of magnitude higher then the one of HBLs. In the past, there were two detection claims of an LBLs at VHE: 3C66A ($z = 0.444$, Neshpor et al. (1998)) and BL Lac ($z = 0.069$, Neshpor et al. (2001)). The detections were very much doubtful and could not be confirmed by the more sensitive instruments HEGRA and Whipple, which observed the sources at the same time. Still, powerful LBLs, especially those which are rather

intermediate blazars (i.e. having the synchrotron peak in the UV), are possible candidates for VHE γ-ray emission. Moreover, observing LBLs at VHE probes the blazar sequence (Section 2.2.2). MAGIC observed several LBLs, and the observations resulted in the discovery of a VHE γ-ray signal from BL Lac (Albert et al., 2007b). This is up to now the only LBL found to emit γ-rays at TeV energies and consequences to the blazar sequence are not yet clear.

A.4 The Target of Opportunity (ToO) program

Blazars have extremely variable flux in all energy regimes from radio to TeV regime. The connection between optical flares and GeV-TeV flares is yet to be studied, but the optical–γ-ray correlations seen in 3C 279 (Hartman et al., 2001) might suggest that at least in some sources and for some flares such correlations exists. X-ray – TeV correlations in HBLs have been studied in more detail and often correlations have been found (e.g. Fossati et al. (2004)) although the relationship has proven to be rather complicated. Gamma-ray flares have been detected in the absence of X-ray flares (Holder et al., 2003; Krawczynski, 2004) and vice versa (Rebillot and VERITAS Collaboration, 2003). Still, in many cases it is possible to use the mean X-ray flux (at least over long time scales) as an indicator of source activity, which could result in enhanced emission of GeV-TeV gamma-rays (de la Calle Perez, I. and Bond, I.H. and Boyle, P.J. and others, 2003). In order to study correlations of fast flares the alerts from ASM weather map are very useful. Noteworthy, the ASM has not enough sensitivity to detect X-ray flares of weak X-ray sources. In many cases, an X-ray flare remains undetected unless another powefull X-ray instrument observes the source during the flare. An optical monitoring is easier than in X-rays and provides more often a trigger alert. The goal of optical alerts and alerts based on ASM light curves is to study more time variability correlations: can we see increased GeV-TeV emission, when the source is in a high optical/X-ray state?

Using this as a guideline, the MAGIC collaboration has been performing Target of Opportunity observations whenever alerted that sources were in a high flux state in the optical and/or X-ray band. Whereas X-ray alerts have been issued only for the established TeV blazar Mrk 421, optical alerts have been issued on sources previously unseen in the VHE band. The subsequent MAGIC observations on Mkn 180 and 1ES 1011+496 lead to discovery of these sources above 100 GeV (see Chapters 7 and 8). For other optical alerts (5 in total), no sufficient MAGIC data could be collected due to adverse weather conditions.

The discovery of VHE emission from Mrk 180 and 1ES 1011+496 during an optical outburst makes it very tempting to speculate about the connection between optical activity and increased VHE emission. The same was also found for BL Lac (Albert et al., 2007b), where the observations during the lower optical state failed to detect VHE γ-rays.

Note, however, that the ToO strategy favors leptonic models, which predict strong correlations between the two spectral bumpts in the SED of the blazars. It might well happen that

A.5 Multiwavelength campaigns

The value of simultaneous multiwavelength campaigns cannot be overestimated. Since the blazars are variable in all wavebands, simultaneous data are essential to constrain emission models and to be able to disentangle them. To constrain the models, the following observables are needed: the position and the flux level of the first (probably, Synchrotron) peak, the position and the flux level of the second peak, the spectral shapes around the peak positions, and the variability time scale. With the current generation of X-ray satellites (XMM-Newton, INTEGRAL, Suzaku, RXTE, and Swift) and ground based Cherenkov telescopes (H.E.S.S. MAGIC, VERITAS), an excellent combination is possible to simultaneously measure the SED of blazars, including a precise measurement of the two peaks. Supporting simultaneous measurements in radio and optical can complete the SED measurement, providing valuable information about the first spectral peak. An organization of multiwavelength campaigns is a challenging task because it involves coordination of big collaborations and satellite experiments. I was closely involved in all multiwavelength campaigns of extragalactic sources with MAGIC. Results of the multiwavelength campaign on the HBL objects Mkn 421 and Mkn 501 with the KVA (optical), SUZAKU (X-ray), MGAIC, and H.E.S.S. (VHE) are published in Hayashida et al. (2007).

A.6 Concept of "Global Network of Cherenkov Telescopes"

The idea of "Global Network of Cherenkov Telescopes" (GNCT) was born during this work and is a part of this Thesis. The combination of similar longitude but widely different latitudes of the H.E.S.S. and MAGIC sites allows one to carry out simultaneously small and large or very large zenith angle observations for sources with declination $|\delta| > 20^\circ$ like e.g. Mkn 421 ($\delta = +38^\circ 12' 32''$), Mkn 501 ($\delta = +39^\circ 45' 37''$), PKS 2155-304 ($\delta = -30^\circ 13' 32''$), M 87 ($\delta = +12^\circ 23' 29''$), and H1426+428 ($\delta = 42^\circ 40' 21''$). Observations at low zenith angles allow measurements with a low energy threshold. For large zenith angles the Cherenkov light cone illuminates a large region on the ground. Due to the reduced photon density this results in a higher energy threshold. On the other hand the effective collection area is significantly increased which improves the sensitivity for γ-rays at high energies, where the fluxes are very low. Figure A.1 illustrates the observational situation for two facilities located at positions of MAGIC and H.E.S.S.

Observatories at similar latitude but different longitude (e.g. MAGIC in La Palma and VERITAS in Arizona or H.E.S.S. in Namibia and CANGAROO III in Australia) allow a different observation strategy. Follow-up observations of variable sources effectively allow one to overcome the long gaps in observation time of ground based Cherenkov detectors during day time.

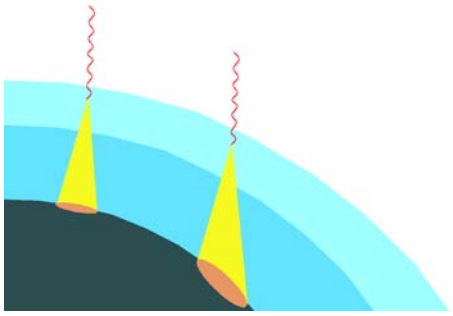

Figure A.1: For two observatories at different latitudes, the showers will be observed under different inclination angles. Observations at high inclination angles result in a large collection area but also a high energy threshold.

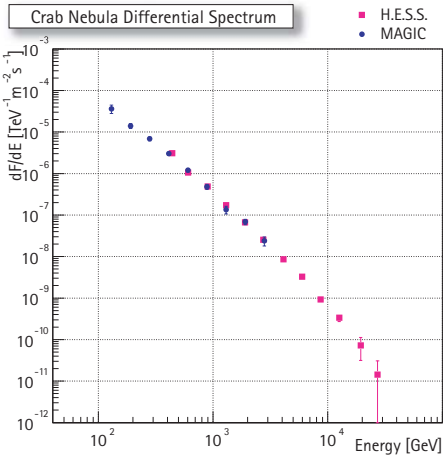

Figure A.2: Combined energy spectrum from the Crab nebula taken around culmination. The large overlap of the energy spectra allows a good cross-calibration (Mazin et al., 2005).

Furthermore, having two observatories at similar latitudes and different longitudes (MAGIC in La Palma and VERITAS in Arizona) allows follow up observations of transient sources, which increases the duty cycle of the ground based Cherenkov detectors.

Carrying out simultaneous observations for bright sources ($F \geq F_{Crab}$), it is also feasible to obtain differential energy spectra between 50 GeV and 50 TeV within a few hours of observation. This means that just with two instruments (MAGIC and H.E.S.S.) one can simultaneously cover 3 decades of energy in a rather short time. In Figure A.2 a combined energy spectrum of the Crab Nebula, the standard candle of VHE γ-ray astrophysics, is shown. Observations of H.E.S.S. contain 10 h of data at mean zenith angle of 45° from 2003/2004. MAGIC data contain 2 hours of data at mean zenith angle of 15° in 2004. Since the Crab Nebula is a strong and stable γ-ray emitter, it is an ideal source to cross calibrate the instruments in the overlapping energy range. Figure A.2 shows a good agreement and indicates a small or the a similar systematic uncertainty of the independent detector calibrations. For variable sources the changes in the spectral index and detailed light curves in three decades of energy can be measured.

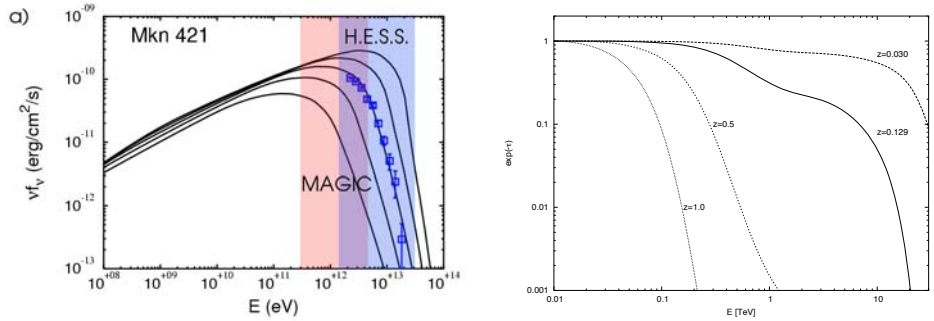

Figure A.3: a) An example for expected broad band spectral variability of Mkn 421. The energy spectrum is the time-average as measured with the H.E.S.S. telescopes at low elevations in April 2004 (Aharonian et al., 2005d). The curves indicate changes of the expected energy spectrum assuming a self-synchrotron Compton model with varying maximum injection energy of the electrons. b) The expected optical depth for different red shifts assuming a model calculation for the extragalactic background light Primack et al. (1999).

Following these ideas, MAGIC, H.E.S.S. and VERITAS collaborations adopted bi-lateral cooperation agreements, including well defined alert criteria for established VHE γ-ray sources and joint observations on targets of opportunity. The first results from a joint H.E.S.S. and MAGIC observation of the HBL object Mkn 421 in 2004 are presented later in Section 6.7. The first steps towards the GNCT are made!

Appendix B

Model Analysis

In this Chapter I present the development and implementation of an alternative analysis method called *model analysis* for the MAGIC telescope. The method uses the entire information recorded in the camera including arriving time of the photons and performs a fit with the expected averaged photon distribution in the camera. In Section B.4 I present results of a performance study using MC data. Preliminary results using data of the same Crab Nebula data sample used in the Chapter 5 are presented in Section B.5.

The model analysis is based on a simple idea to create expected averaged photon distributions from air showers for each energy, sky direction, and impact parameter. The expected photon distributions on the camera plane (hereafter *templates*) are created for γ–induced showers only. Every measured event is then compared with these templates and a fit is used to determine the best template for the particular event. A loglikelihood function containing the charge and the timing of each camera pixel is minimized taking into account fluctuations of the NSB light. The templates contain predicted values even for pixels, which are located substantially distant from the image center and usually have only a small charge. This allows to use an image information, which is normally lost during the image cleaning in the standard analysis (see Section 5.7). The so-called "tails" of the measured events can be used for a better γ/hadron separation and energy determination. In case the fit does not converge or the resulting fit probability is too small, the event is rejected as not being γ–like. In this way, an alternative γ/hadron separation can be performed. Another convenient aspect of the fit is that the fit parameters are direct physical quantities of the air shower, namely: energy of the primary particle, orientation of the shower axis, and impact distance from the telescope. The values determined from the fit can then directly be used for further analysis like determination of the source energy spectrum and the source location.

The idea of the model analysis is not new. Already in 1996, M. Ulrich started developing templates for the HEGRA CT system (Ulrich, 1996). However, the computer power at that time was not enough to produce sufficiently many MC

γ–showers for reliable templates. In parallel, the CAT collaboration developed a similar method based on a semianalytical shower description, which did not need many MC events to produce the templates (Le Bohec et al., 1998). The method was successfully applied to the CAT data and has been proven to be more sensitive for lower energies than the classical approach. With an energy threshold of 250 GeV at low zenith angles, the CAT experiment achieved the lowest energy threshold among the IACTs of the last generation (Piron et al., 2001), and the usage of the model analysis was one of the reasons of this success. Continuing the CAT tradition, the French part of the H.E.S.S. collaboration has implemented the model analysis for the H.E.S.S. data (de Naurois, 2006). Though not published yet, the analysis results obtained from this method yield the lowest threshold and highest detection significance among different H.E.S.S. analysis methods (M. de Naurois, private communication). Motivated by the good experience of the CAT and H.E.S.S. collaborations with this analysis method, we developed the model analysis for the MAGIC telescope.

B.1 Motivation for the model analysis approach

The model analysis has several advantages compared to the classical approach. It mainly takes the NSB fluctuations correctly into account allowing to analyze information in the pixels with a low charge. In the classical (standard) analysis this information is usually lost during the image cleaning procedure. The noise level for each pixel is measured during the pedestal runs and constantly updated (see in Section 4.2.2) and is used to estimate the uncertainty of the measured signal in the pixel. In this way, also the treatment of stars in the FoV is easier: the high signal fluctuations in the affected pixels can be taken into account in the function to be minimized. Hence, no special treatment for stars is needed. The next advantage is that lower energy events can be better reconstructed because the templates predict not only the shape of the image core (normally just a few pixels) but also the tails of the image containing important information. One of the relevant characteristics of an image is the *head-tail* information, i.e. an ability to distinguish on which side along the major axis of the image the impact point of the shower is located. In Fig. B.1, an example of a template is shown. The asymmetric photon distribution along the main axis, defining head-tail information, is clearly visible. In Fig. B.2, the longitudinal and transversal profiles of the expected image for 100 GeV showers at 100 m impact distance are shown. In the longitudinal profile, the striking asymmetry between the head and the tail of the image is clearly visible. We expect the fit to recognize this asymmetry in the measured events even if it is just above or inside the mean noise level. Furthermore, the model analysis provides a completely independent γ–hadron separation. Hadron–like candidates can be separated from the γ–like events by just one cut in the fit probability. In addition, as already mentioned,

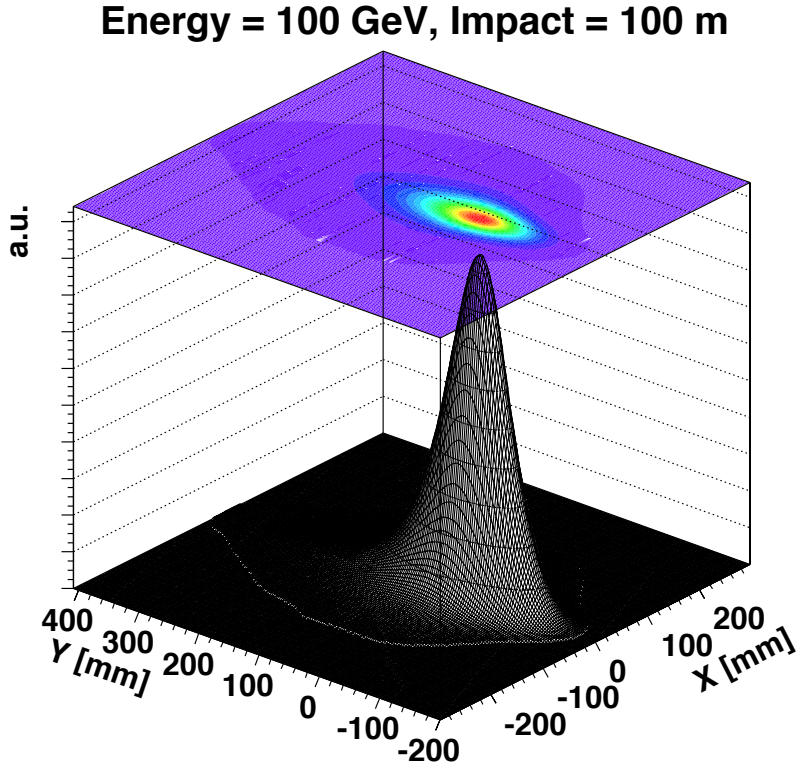

Figure B.1: An example of the templates. Shown is expected averaged photon density in the camera coordinates for γ–ray showers with energy E=100 GeV and impact point I = 100 m. The source position is supposed to in the camera center, i.e. at X=Y=0.

from the fit results one directly obtains an estimation of the physical parameters of the air shower, in particular the orientation of the shower in the atmosphere (and hence the incoming direction of the primary γ–ray) and the energy of the primary γ–ray.

The model analysis may also be used in combination with the classical approach. For instance, for the γ/hadron separation, one may not only want to use the cut in the fit probability but a combination of cuts in image parameters and in the fit probability. Another possibility would be to use the fit probability as an additional parameter for the energy estimation.

Of course, the model analysis also has a few disadvantages, too. The main one is that the fitting of the measured events with templates is a very time consuming procedure. In the current implementation, the model analysis needs about 1 second for 20 events, which is a factor ten slower that the data taking speed. The speed is already optimized by using a fast Marquardt-Levenberg algorithm (Press et al., 1992) and by loading the templates in the program buffer during the fitting. Using the standard standard MINUIT package would result

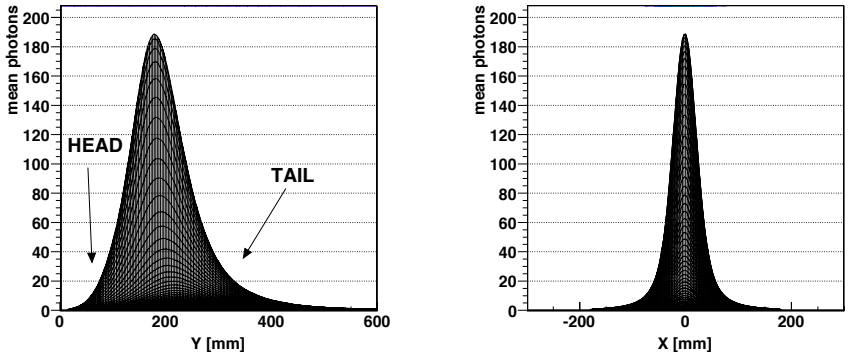

(a) Longitudinal profile (b) Transversal profile

Figure B.2: Profiles of the Cherenkov photon distribution on the camera plane for 100 GeV γ-ray showers at 100 m impact distance from the telescope. An asymmetry between the head and the tail of the image is clearly visible in the longitudinal profile.

in a speed reduction by a factor of 100 to 200. A reading of the templates from disc during each fitting step would result in an additional speed reduction by a factor of 100.

Another disadvantage is time consumption for the template generation. As mentioned above, there are two ways of template generation: based on a semianalytical description of the shower development or based on MC γ–events. We have decided to follow the second option in order to avoid additional tuning between the semianalytical shower description and the real γ–ray showers. However, this is very time consuming because one needs a sufficiently large statistic of γ–ray showers for each parameter set (energy, impact, zenith angle etc.) in order to obtain templates with a negligible statistical uncertainty for the expected values. On the other hand, the template generation has to be done only once. The latest estimation yields that we need about 1 year to produce the templates for the complete range of zenith and azimuth angles.

B.2 Template Generation

In this Section, I give a closer explanation what is meant by templates, how they are generated, and what parameters are used for the fit.

B.2.1 Generation of shower templates

The main idea of the templates generated by MC is rather simple. One simulates many γ–events with the same fixed initial parameters and superimposes the resulting shower images and calculates the mean light intensity at each camera

position. The most straightforward way is to use the complete MC chain for the MAGIC telescope (see Section 5.4) up to FADC signals of the readout electronics. After the simulation, one would average events in terms of the FADC signals and calculate the mean expected signal for each channel. In this way, there would be no need for any approximation (except of those, which are done in the standard MC chain of the MAGIC telescope). However, this way is basically impossible due to the amount of different parameter sets needed. In fact, any rotation of the telescope with respect to a fixed shower in the atmosphere causes the light to hit different PMTs and, therefore, the expected signal in a channel is different.

An alternative was found in terms of the following procedure:

- Standard MC chain is used up to the reflector output, i.e. light distribution of a shower on the camera plane. Showers are simulated for a fixed energy of the γ-rays, and for a fixed zenith and azimuth angles. The same showers are used for 20 different impact points by placing the MAGIC telescope at 20 different positions on a line starting from the shower impact point on the ground, i.e. impact distance 0 m. The maximum impact distance is 240 m. The position of a γ-ray source is chosen to be in the camera center.

- The resulting photon distributions on the camera plane are averaged using a binning, which is much finer than the actual pixel size of the camera. The smearing of the photon distribution with the actual optical PSF of the MAGIC telescope is done just before the averaging. The resulting photon distributions are saved in 2-dimensional histograms. These are the templates.

- When fitting the templates to the data events, the templates are rotated and shifted to match the measured events (see Fig. B.3) and then pixelized to the camera geometry (Section B.3.2).

There are two deficiencies in this procedure. The main one is caused by the fact that the templates are created for a source position in the camera center only. However, the aberration effect (see Section 4.2.1), which is small compared to shower-to-shower fluctuations is negligible. The differences in the the model analysis performance between a source position in the camera center (ON mode) and a source position 0.4 degrees off-center (Wobble mode) are discussed in Subsection B.4.2.

The second deficiency comes from the detector specific noise. I make an assumption that it can be taken into account by a simple parametrization during the fitting procedure. The templates are produced in terms of photon distribution, whereas the data is calibrated in number of photoelectrons. I am using a fixed conversion factor between photons and photoelectrons for all pixels, which might be too simplistic.

Noteworthy, the templates do not contain any NSB and electronic noise, i.e. they consist of shower Cherenkov photons only. This is done in order to obtain

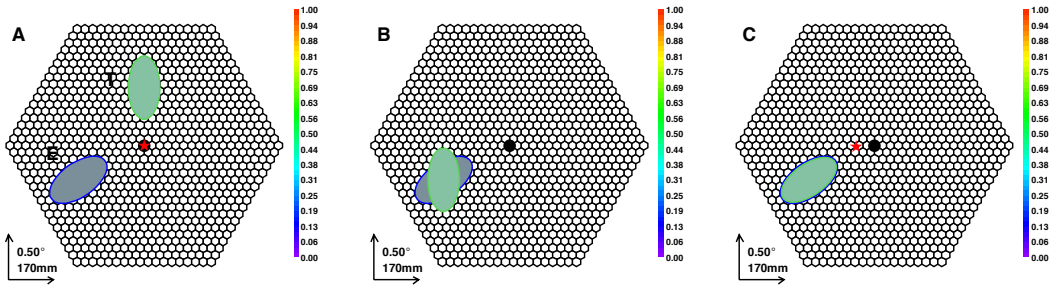

Figure B.3: Sketch illustrating shift and rotation of the template for a given measured event. A: a measured event E (blue ellipse) is to be compared with a template T (green ellipse). The black filled circle represents the camera center and the red star the source position of the template in camera coordinates. B: the template is shifted to the position of the measured image. C: the template is rotated to match the event. The red star represents now the reconstructed source position for a given fit for the template.

templates, which are independent from the noise level of the sky and the electronics. The noise is added later during the fitting procedure using the measured values of the current noise level in the data. In this way, different noise levels in the data can be treated easily and efficiently. The templates include shower fluctuations and photon statistics fluctuations.

B.2.2 Template parameters

The templates are generated as a function of the following parameters:

- energy of the primary γ–ray, E
- height of the shower maximum, $Tmax$
- impact distance from the telescope, I
- zenith angle of the primary γ–ray, Zd
- azimuth angle of the primary γ–ray, Az (not implemented yet)

The energy E of the primary γ–ray and the impact parameter I of the air shower are obviously relevant parameters as well as the zenith angle Zd of the shower. There have been studies about the influence of the Earth's magnetic field on the shower development and hence the importance of the azimuth angle Az of the shower (de los Reyes, 2002; Commichau, 2007). It has been shown that this influence is not negligible mainly due to different number of electrons and positrons in a shower (Hillas, 1982). In order to take this into account, templates are produced with a fixed Az direction of the air showers. Within the scope

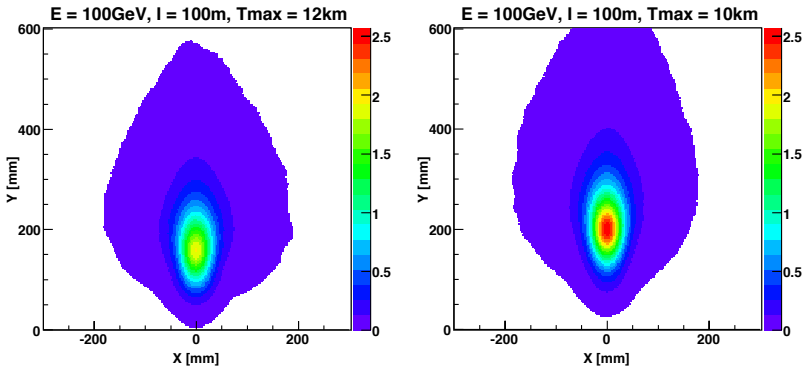

Figure B.4: Templates for 100GeV γ-rays at 100 m impact distance from the telescope. *Left:* template for the second bin in $Tmax$, corresponding to a medium height of 12 km. *Right:* template for the fourth bin in $Tmax$, corresponding to a medium height of 10 km. The source position is located at 0,0 in camera coordinates. Color coded is the numbers of photons per template spacial bin ($3\times3\,\mathrm{mm}^2$). Differences in absolute numbers of expected photons, image shape, and position of the CoG of the image in respect to the source position (here at 0,0) are clearly visible.

of this thesis, the templates are produced for a zenith angle $Zd = 0$ deg only. All following plots and discussions imply $Zd = 0\,\mathrm{deg}$ unless a different value is stated explicitly. Due to the vertical arriving direction of the showers, the azimuth orientation has no influence on the images and the effects of the Earth's magnetic field were not studied.

In addition, the position of the shower maximum ($Tmax$, the height above the sea level, at which the number of shower particles is the largest) has a statistical fluctuation, which is mainly determined by the fluctuations in the first and in the second interaction points (see e.g. Subsection 4.1.1). Different shower heights result in a different angular distance to the center of gravity of the image and, therefore, important for a correct reconstruction of the shower characteristics. In Fig. B.4, one can see the templates for 100 GeV γ-showers for two different $Tmax$ values. Whereas the left template corresponds to roughly 12 km above the sea level, the right template corresponds to the $Tmax$ at roughly 10 km above the sea level. Both templates show a typical 100 GeV γ-ray shower image. Differences in absolute numbers of expected photons, image shape, and position of the CoG of the image in respect to the source position (here at 0,0) are clearly visible.

Due to these substantial changes, averaging over a total range over $Tmax$ values does not reproduce a representative mean image. Therefore, we divide the simulated showers in 5 $Tmax$ bins with similar number of events in each bin (see an example in Fig. B.5). Templates are then produced for each $Tmax$ bin separately.

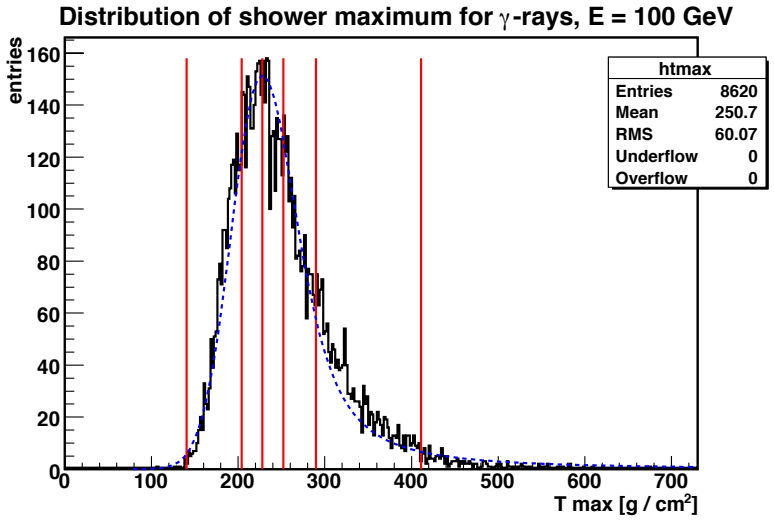

Figure B.5: Distribution of the fitted (inside CORSIKA) shower maximum position in the atmosphere for γ-ray showers with E = 100 GeV and Zd = 0 deg. The $Tmax$ values are show by the black histogram. A fit by a convoluted Landau and Gaussian function is shown by the blue dashed curve. The distribution is divided into 5 bins with a similar statistics per bin as indicated by the red lines. Model templates are produced for each bin separately.

It is certainly not possible to simulate all possible values of energies, impact parameters and zenith angles with sufficient statistics. The simulation is done in a grid of these parameters, and the distances between the simulated values (knots) has been chosen as a compromise between the time needed for a simulation and the level of changes in the templates between the knots. The grid in energy is chosen between 50 GeV and 50 TeV in 40 equidistant logarithmic values. The grid in impact distance has 20 different values, chosen linearly between 0 m to 240 m. The binning in the shower maximum $Tmax$ depends on the energy of the shower. As shown in Fig.B.6, the shower maximum position gets closer to Earth as the energy of γ-rays increases.

B.2.3 Quantities to store

For each template the following 4 quantities are stored for each template pixel i corresponding to an area on the camera plane of $3 \times 3\,\mathrm{mm}^2$:

- $\mu \equiv < Q_i >$: the mean number of photons
- σ_μ: the standard deviation (RMS) of μ
- $\tau \equiv < T_i >$: the mean relative arrival time of photons

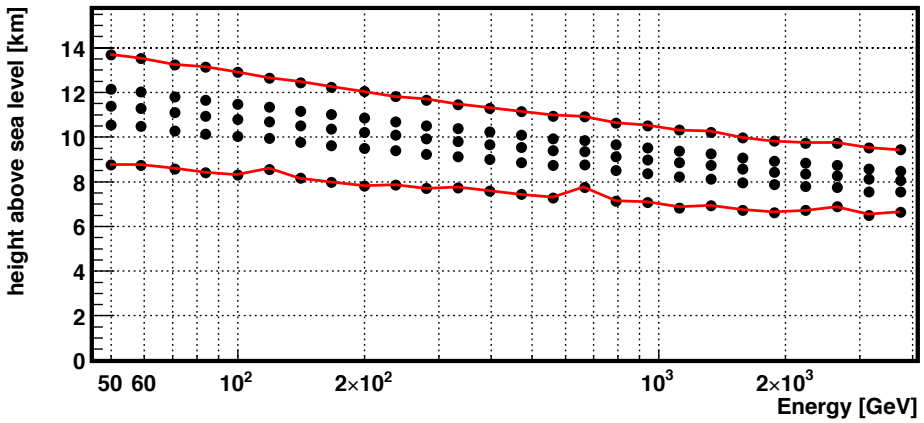

Figure B.6: Distribution of available model templates in energy E and shower maximum $Tmax$. For each energy, 5 bins in $Tmax$ centered at the displayed full points are produced. For a given energy, the lowest and the highest point in $Tmax$ build the possible fitting range in $Tmax$ as marked by the red line.

- σ_τ: the standard deviation (RMS) of τ

The mean expected number of photons for a given pixel μ is the only quantity which is stored in the templates of the previous and existing implementations of the model analysis (CAT and H.E.S.S.). In the templates for MAGIC, not only μ can be stored but also three other quantities. The σ_μ has two contributions, one coming from the Cherenkov photon statistics, the other one is due to fluctuations in the shower development (σ_{fluct}) :

$$\sigma_\mu^2 =< Q_i > +\sigma_{fluct}^2. \tag{B.1}$$

MAGIC offers another measured quantity per pixel i: the relative arrival time of the signal t_i. This can be compared to the mean relative expected photon arrival time in the templates τ. Again, in addition to the mean value, we can also calculate and store a spread of it, σ_τ.

The mean values are not obtained by a simple averaging of the individual γ-ray showers. The reason is that due to intrinsic differences of the shower development, individual images have slightly shifted position in the camera and also the orientation of individual images differs by up to several degrees. In order to produce a representative average, the following procedure is applied: for each image the CoG of the photon distribution and the orientation of the main axis are calculated. Since the simulated source position is in the camera center, all showers should point there. Therefore, the individual images are turned by the angular offset between the calculated and expected orientation of the image. The CoG of all images are also shifted to a common camera point.

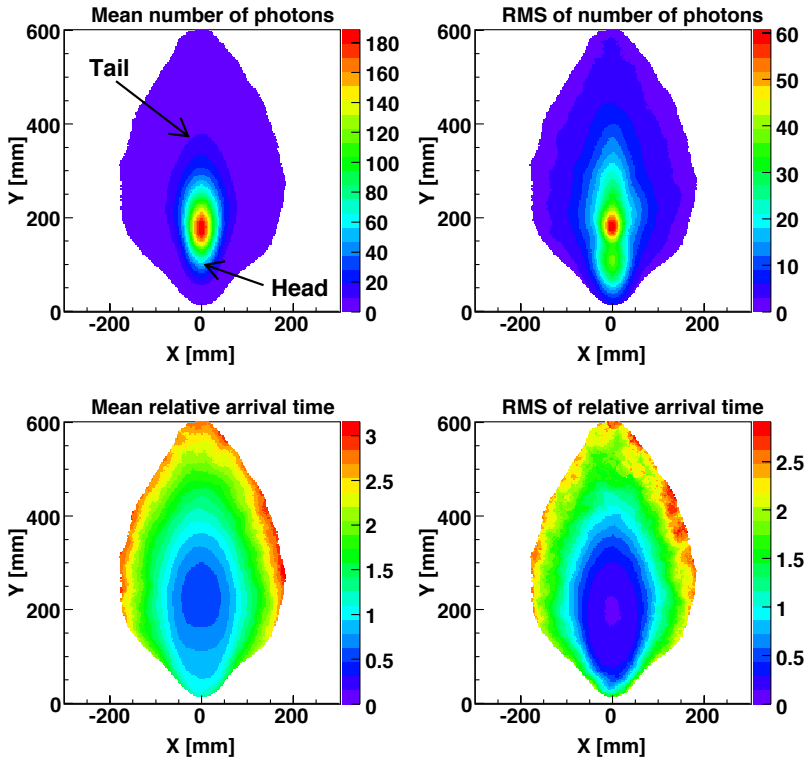

Figure B.7: Stored quantities in the templates. Shown is an example of 100GeV γ-rays at 100 m impact distance from the telescope and third (medium) bin in $Tmax$. *Upper left:* mean number of photons, μ. *Upper right:* RMS of number of photons, σ_μ. *Lower left:* mean expected arrival time, τ. *Lower right:* RMS of expected arrival time, σ_τ. The values per template pixel (3 mm×3 mm) are displayed in color.

After the images are rotated and shifted to a common camera point, the template quantities μ, σ_μ, τ, σ_τ are calculated. In case of τ, a weighted mean with the number of photons in a given pixel is calculated.

An example of a template is shown in Fig. B.7. The template of the four quantities μ, σ_μ, τ, σ_τ is shown in camera coordinates. One can clearly see the head-tail differences in the photon distribution as well as in the time distribution. This template was produced using 2000 showers with an energy of 100 GeV, an impact distance of 100 m and the third (medium) bin in $Tmax$. The values per template pixel are displayed in color.

The dimension of the templates is 3.0 m × 3.0 m centered at the center of gravity of the photon distribution. The dimension of the templates is compared to the size of the MAGIC camera in Fig. B.8, left sketch. The dimension of the templates is chosen to be big enough in order not to truncate high energy images.

The small MAGIC pixels are ≈86 times larger than the template pixel. Mainly due to a technical reason, namely in order to accelerate the fitting procedure, the

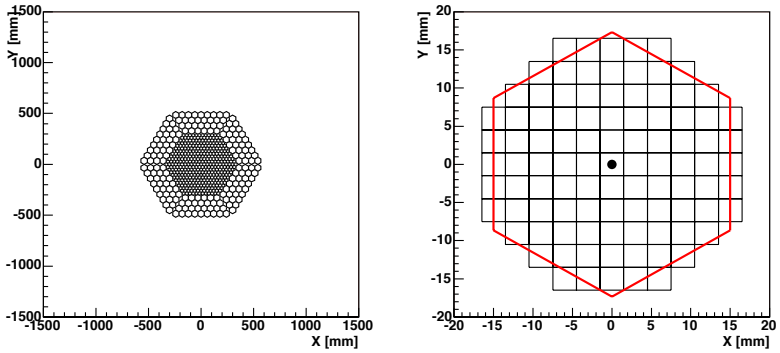

Figure B.8: Sketch illustrating dimension and pixel size of the templates. *Left:* Size of the MAGIC camera ($\approx 1\,\mathrm{m}$ diameter) is compared to the size of the template (3 m wide). *Right:* Size of the small bins of the templates (black squares) is compared to the size of a small MAGIC pixel (red hexagonal). An area of a small MAGIC pixel corresponds to roughly 86 template pixels.

recorded values in a template bin are representative for the area of a small MAGIC pixel centered at that bin. As shown in Fig. B.8, right sketch, the content of the central pixel is the sum of itself and the bin contents from the 96 bins around it. In case of the time information, the weighted average instead of the sum from the 97 bins is calculated. The obtained values are then normalized by the difference between the area of 97 template pixels and the area of a small MAGIC pixel. Due to this construction, the stored values are densities per small MAGIC pixel.

It is also worth noticing that the RMS values are clearly larger than it is expected from a pure Poissonian distribution ($\sigma_N = \sqrt{N}$, where N is the number of photons). This can be explained by the differences in the shower development in the atmosphere between single showers. We assume that the mean expected arrival time and the spread of the mean values (for the number of photons and time) will provide additional help for the γ/hadron separation as well as for the energy estimation. The way these values are used in the construction of the likelihood function is presented in Subsection B.3.1.

B.2.4 Comments on evolution of the templates as a function of shower parameters

The evolution of the images as a function of the γ-ray energy is shown in Fig. B.9. The number of photons is displayed in the upper panels, while the expected relative arrival is displayed in the lower panels. The black ellipse marks the FWHM of the photon signal. Note that the photon signal is displayed in a logarithmic scale. An interesting observation is that the area, at which the signal is above half of the maximum value, i.e. the area within the ellipse, remains

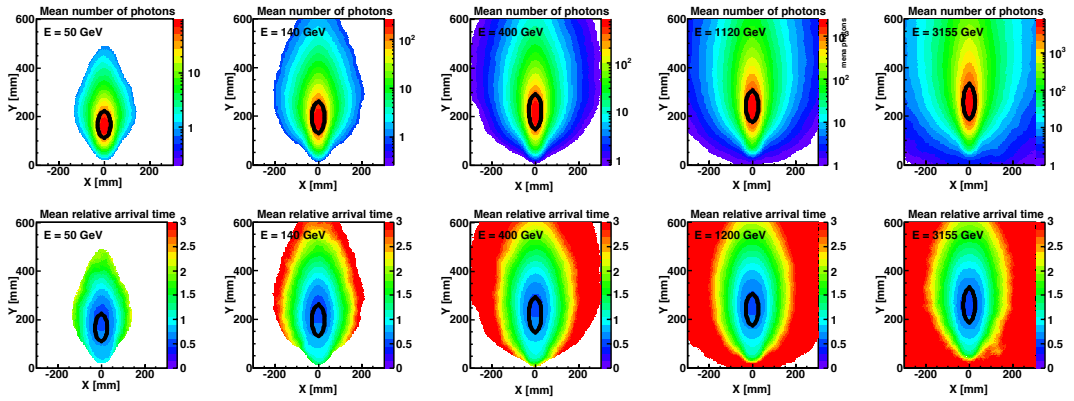

Figure B.9: Templates for expected number of photons and arriving photon times for different energies at 100 m impact distance. Energies shown are: 50 GeV, 140 GeV, 400 GeV, 1. TeV, and 3.15 TeV. The time spread is within 1 ns at the FWHM of the signal (marked by the black ellipse) for all energies. Note that the number of photons is displayed in a logarithmic scale.

almost constant for all energies. Moreover, the spread of arrival times for this inner area is always below 1 ns. The total spread of arrival times increases with increasing energy and reaches 4 ns at 3 TeV.

The evolution of the images as a function of the impact parameter is shown in Fig. B.10. At a fixed energy of 100 GeV, an evolution of the images from the impact distance between 30 m and 160 m is shown. The black ellipse limits again a region, in which the photon signal is above the FWHM value of a given template. One can clearly see that the shape of the image strongly depends on the impact parameter. The time distribution also changes with the impact parameter. Moreover, the time gradient changes along the major axis as a function of the impact distance: while for distances below 100 m photons from the head of the image arrive first, for distances above 120 m photons from the tail arrive first. This means that the time gradient can be used for the head-tail determination. However, because of the change in the time gradient one needs a good estimation of the impact distance of the shower.

B.3 Template fitting

In this Section, I briefly describe the fitting procedure of events (real data or MC) with the templates. After introducing some technical details, I go into details of the fitting and finally present and discuss the performance of the method. Several strategies have been tested during the development phase of the model analysis and the one giving the best performance is presented here. However, some ideas could not be tested due to time constraints in which this thesis had to be finished

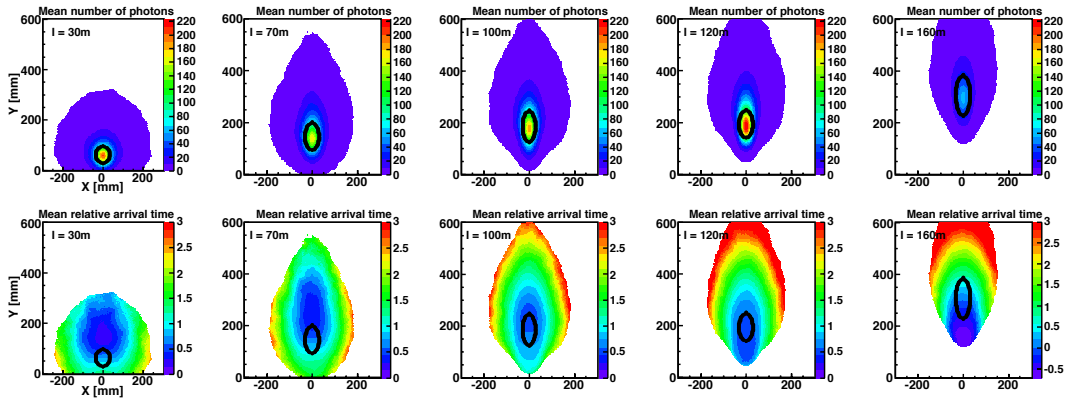

Figure B.10: Templates for expected number of photons and arriving photon times for different impact points for 100 GeV showers. Impact distances shown are: 30 m, 70 m, 100 m, 120 m, and 160 m. The time spread is within 2 ns at the FWHM of the signal (marked by the black ellipse) but the time gradient is nicely visible. The gradient changes sign at around 120 meters impact distance.

and a further improvement of the performance is believed to be possible in future.

B.3.1 Likelihood Function

A correctly constructed function to be minimized during the fit is crucial for the success of the model analysis. In our construction, the following aspects have been considered for the likelihood function:

- The measured quantity per event is the number of photoelectrons per pixel.
- The NSB noise follows the Poissonian statistics.
- The photon statistics of the Cherenkov photons is not Poissonian because of the large shower-to-shower fluctuations. The standard deviation σ_μ of the expected number of Cherenkov photons μ is known by construction of the model templates. We construct a Gauss-term to describe the probability to observe S Cherenkov photons for the expected value μ of Cherenkov photons.
- We fold the Poissonian distribution of the NSB contribution to the measured signal with the Gauss-term for the signal due to Cherenkov photons.

The resulting probability P_i for a pixel i has the form:

$$P(S,\mu)_i = \sum_n \frac{\lambda^n}{n!}\, e^{-\lambda}\, \frac{1}{\sqrt{2\,\pi}\,\sigma_n}\, \exp\left(-\frac{((S+\lambda)-(\mu+n))^2}{2\sigma_n^2}\right) \qquad \text{(B.2)}$$

$$\text{with}\;\; \sigma_n^2 = \sigma_\mu^2 + \sigma_{el}^2 + \sigma_{cal}^2 + n\,(F^2-1)$$

while the following notation is used:

- λ: The mean of the night sky background (NSB) contribution. λ is known from the calibration procedure (see Section 5.2). Moreover, the mean of the NSB contribution, λ, has been subtracted from the measured signals during the calibration. As a result, the reconstructed signals of the pixels containing only noise are distributed around zero.

- The measured signal S has an unknown contribution n due to the NSB photons. The number n in photoelectrons is Poisson distributed around the mean value λ.

- The Gaussian error σ_n has several contributions:

  - the total error of the model (photon statistics and the shower fluctuations), σ_μ
  - electronic noise, σ_{el}
  - calibration error, σ_{cal}
  - fluctuation coming from the photomultiplier tube, $\sqrt{n\,(F^2-1)}$

The overall likelihood function L for an event is then a product of individual probabilities per pixel:

$$L = \prod_i P(S,\mu)_i \tag{B.3}$$

Finally, the loglikelihood function Ln_L is used to be minimized during the fitting routine:

$$Ln_L = -2\,\ln(L) \tag{B.4}$$

Equations B.3, B.3, and B.4 do not include any timing information of the signals. This is already a complete model analysis similar by construction to the one of CAT or H.E.S.S. We hope, however, to improve the reconstruction of the shower properties of the γ-ray candidates as well as the γ/hadron separation by including the timing information into the fitting routine. The implementation is done in the following way:

1. For each pixel, the probability Pt_i to measure a signal at a time t is assumed to be:
$$Pt(t,\tau)_i = \frac{1}{\sqrt{2\,\pi}\,\sigma_T}\,\exp\left(-\frac{(t-\tau)^2}{2\sigma_T^2}\right) \tag{B.5}$$
with mean arrival time τ and width σ_T.

2. The width σ_T has two contributions:

   - error of the model prediction (part of the templates), σ_τ

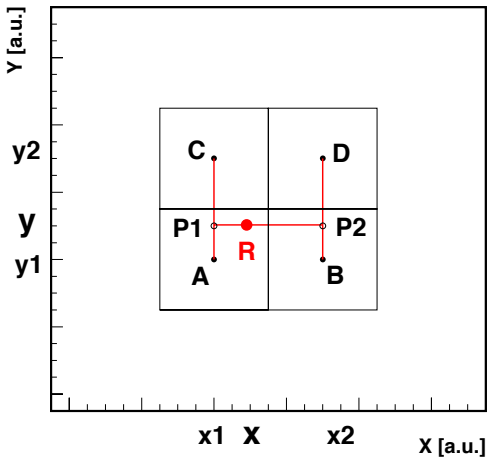

Figure B.11: Pixelization of the templates.
Sketch illustrates how to obtain a value (e.g. number of photons) at a reference location **R**(**x, y**) from a template. The black thin lines illustrate 4 template pixels, centered at the filled black points with contents **A**, **B**, **C**, and **D**. In an intermediate step, values **P1** and **P2** are computed using a linear interpolation along the Y-axis. Then, again via the linear interpolation between **P1** and **P2**, the desired value of **R** is obtained.

- error of the arrival time measurement (part of the calibration), σ_t

so that $\sigma_T^2 = \sigma_\tau^2 + \sigma_t^2$

3. The overall likelihood function L is then analog to Equation B.3

$$L = \prod_i \left(P(S,\mu)_i \, Pt(t,\tau)_i\right) \tag{B.6}$$

The loglikelihood function Ln_L remains as in Equation B.4.

B.3.2 Pixelization and interpolation

The templates are saved in small bins 3 mm × 3 mm as described in Subsection B.2.3. The measured events contain information per pixel according the geometry of the MAGIC camera. In order to compare the events with the templates, the templates are "pixelized", i.e. the template information is translated from the template binning into the geometry of the MAGIC camera. This is done using the following recipe. First, the template is shifted and rotated to match the measured image (see Fig. B.3). Then the template values at the coordinates

of each MAGIC pixel are determined using a linear interpolation between neighboring template pixels (see Fig. B.11). The pixelization of the templates is done at every step of the minimization procedure.

The templates are produced and stored for discrete values of energy, impact distances and shower maximum only. To obtain templates at arbitrary values of E, I, and $Tmax$ an interpolation procedure is needed. For a given values of E, I, and $Tmax$ a linear interpolation of the 8 surrounding templates with values E_1, E_2, I_1, I_2, $Tmax_1$, $Tmax_2$ such that

- $E_1 < E < E_2$
- $I_1 < I < I_2$
- $Tmax_1 < Tmax < Tmax_2$

is performed. The interpolation is performed at any fitting step. From the computational point of view, the interpolation is the most time consuming step in the model analysis. This is due to the time needed to open and close 8 files, which are stored in a compressed way. Storing templates in an uncompressed way would result in a volume of over 30GB, which would allow to perform the model analysis on some few dedicated machines only. An even faster solution would be to load all templates in the buffer in order not to open and close files all the time. However, it is not yet possible to easily access machines with more than several GB memory space. A possible solution is to increase the pixel size of the templates in order to reduce the template volume. As a test, templates with 12 mm×12 mm pixel size instead of 3 mm×3 mm can be loaded easily in machines with 4 GB RAM. A fitting speed of 20 events per second has been achieved while differences in the fit results between the 3 mm×3 mm and 12 mm×12 mm templates are negligible.

B.3.3 Free and fixed parameters and starting values

Overall, 6 parameters are included into the fitting algorithm. The first 3 parameters define the position of the image in the camera: $\overline{X}$, $\overline{Y}$ (position of the CoG of the image), and δ, the orientation angle of the main shower axis in the camera. The other 3 parameters define the physical characteristics of the shower: its energy E, the shower maximum $Tmax$, and the impact distance I from the telescope.

The $\overline{X}$, $\overline{Y}$, and δ are also calculated during the standard calculation of the image parameters (sea Subsection 5.8). The standard analysis is much faster compared to the model fit and, thus, can run as an additional task just before the fit is performed. In Fig. B.12 the relative differences between fitted and calculated values are shown for these three parameters. One can clearly see that the differences are much below 1% level for most of the events. Therefore, in order

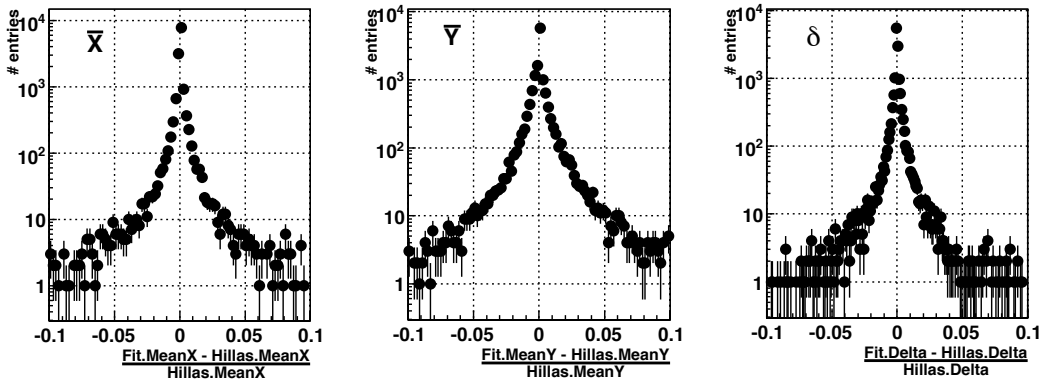

Figure B.12: Relative difference between fitted $\overline{X}$, $\overline{Y}$, δ and the values calculated after the standard image cleaning. Note that the Y-axis is logarithmic and the width of the distributions is much below 1% level though there are wide tails. A MC γ-sample has been used for this study.

to save computation time, the $\overline{X}$, $\overline{Y}$, and δ are fixed during the fit to the values calculated during the standard analysis. For the remaining three parameters, E, $Tmax$, and I, the fit is performed.

The asymmetry between $Head$ and $Tail$ of the image, as clearly seen in the templates, is also aimed to be reconstructed by the fit correctly. Knowledge of the correct $Head$ and $Tail$ assignment for the events removes an ambiguity, at which side along the major axis the real arriving direction is located. Ideally, by reconstructing $Head$ and $Tail$ always correctly, one removes 50% of background events (since the arrival direction for background events is random) by keeping all the γ-events from the source. However, once the starting parameters are chosen for a given $Head - Tail$ assignment, the fit never succeeds to turn by 180 degrees. Therefore, we perform the fit twice: one starting with the orientation closer to the camera center and another one with the opposite orientation. The solution with the better fit result is then used for the further analysis.

For a single telescope analysis, there is a degeneracy in the reconstruction of the energy of a shower, its impact point in respect to the telescope and the position of the shower maximum. The degeneracy arises from the fact that a shower with a smaller energy closer to the telescope can be misinterpreted as a higher energy shower with a larger impact parameter. Decent starting values for the free fit parameters are therefore important for both saving computational time (fast convergence) and a higher probability for the fit to succeed. We use the image parameters calculated during the standard analysis to get starting values. As already mentioned above, $\overline{X}$, $\overline{Y}$, and δ are used directly. In case of the energy of primary γ-rays, the following parametrization is used:

$$\log_{10}(E_{est}) = A + B \cdot \log_{10}(\text{Size/Width}) + C \cdot (\log_{10}(\text{Size/Width}))^2 \, [GeV] \quad \text{(B.7)}$$

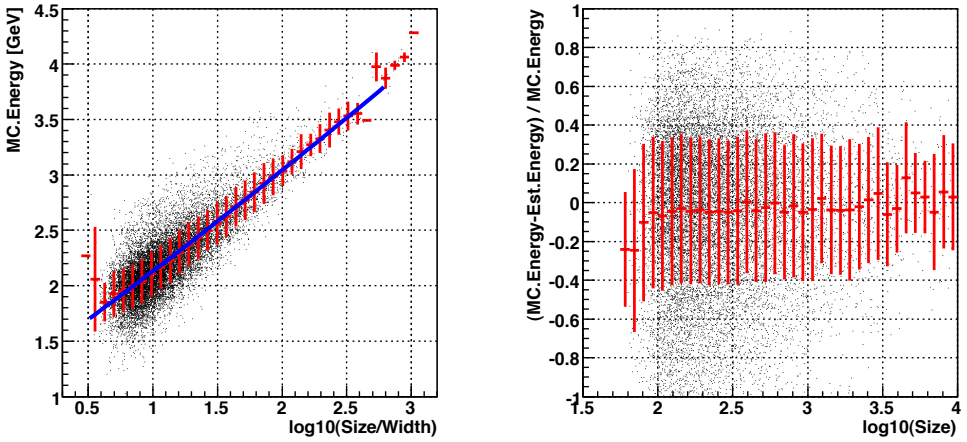

Figure B.13: Estimation of the starting values for the γ-ray energy E using image parameters.
Left plot: estimation of the γ-ray energy as a function of the Size/Width ratio. The red graph is the profile of the distribution and the blue line is the fit to the profile. The parametrization from the fit is used to obtain the starting value for the energy E.
Right plot: Relative resolution of the starting values E compared to the true energy of the MC γ-events as a function of the Size parameter. The spread is 35-40% decreasing slightly with increasing Size.

The parameters A, B, and C are obtained from a subsample of MC γ-events. Fig. B.13 shows the parametrization of the energy as a function of the Size/Width ratio (left plot) and the resulting energy resolution (right plot). As it can be seen from Fig. B.13, the energy resolution is about 35-40% improving at higher Size values. Note that this simple parametrization is used only to obtain the starting values for the model fit.

A starting value for the impact parameter is obtained from one of the following two estimations. In case the source position is known and source dependent parameters can be used in the analysis, the following parametrization is used:

$$\begin{aligned} I_{est} &= A_1 + B_1 \cdot (\text{Dist/Width})\ [m] \quad \text{for Dist/Width} < 10 \\ I_{est} &= A_2 + B_2 \cdot (\text{Dist/Width})\ [m] \quad \text{for Dist/Width} > 10 \end{aligned} \tag{B.8}$$

As it can be seen from Fig. B.14, the impact resolution is about 20-30% and has a bias: At higher impact distances, especially above the hump at 120 m, the values are underestimated. Though at impact distances below 30 m the resolution does not look good either, the effect is rather small due to small absolute values of the mis-reconstruction. Moreover, the statistics of the events below 30 m is low.

In case the source dependent parameters are not used, a *Disp* parametrization

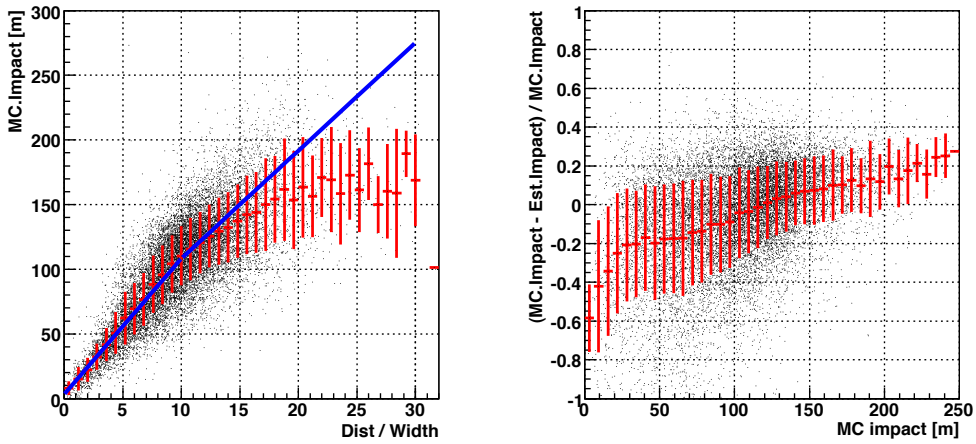

Figure B.14: Estimation of the starting values for the impact distance I using image parameters.
Left plot: estimation of the impact distance as a function of the Dist/Width ratio. The red graph is the profile of the distribution and the blue line is the parametrization used to estimate the impact distance. The parametrization coincides with the to the mean values of the profile for impact values below 120 m. For larger impact values, a steeper parametrization is chosen in order to account for the peak rather than for the mean of the profile distribution. *Right plot:* Relative resolution of the estimated impact distance as a function of the true impact distance of MC γ-events. The RMS is 20-30% for most of the range, whereas there is some bias towards higher impact distances.

is used to estimate the *Dist* parameter:

$$\mathrm{Disp} = \left(1. - \frac{\mathrm{Width}}{\mathrm{Length}}\right) \cdot \left(A_3 - B_3 \cdot \log_{10}(\mathrm{Size}) + C_3 \cdot (\log_{10}(\mathrm{Size}))^2\right); \qquad \text{(B.9)}$$

Then, the Disp is used instead of the *Dist* in Equation B.8 to estimate the impact point. The result of the parametrization and the spread of the estimated values can be seen in Fig. B.15. It can be seen that the Disp parametrization does not work well beyond the hump (above 120 m) and there is a degeneracy in the estimated values. Obviously, the knowledge of the source position improves the estimation of the impact point substantially as it can be seen from the differences between Fig. B.14 and Fig. B.15.

B.3.4 Fitting procedure

The free parameters (energy E, impact point I and the height of the shower maximum $Tmax$) have to remain inside the range for which the templates have been produced. In the current implementation, the following ranges are used:

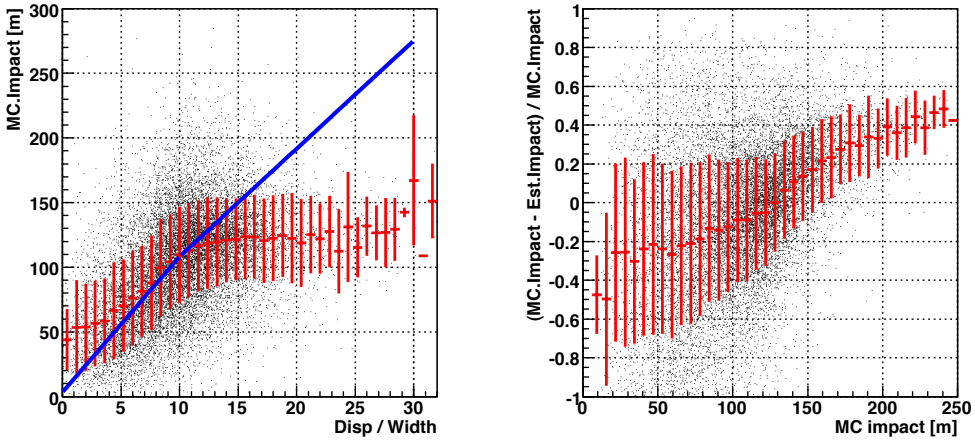

Figure B.15: Estimation of the starting values for the impact distance I using source independent image parameters.
Left plot: estimation of the impact distance as a function of the $Disp/Width$ ratio. The red graph is the profile of the distribution and the blue line is the parametrization used to estimate the impact distance. The used parametrization shown by a blue line is obtained from Fig. B.14. *Right plot:* Relative resolution of the estimated impact distance as a function of the true impact distance of MC γ-events. The RMS is 20-50% and the distribution has a strong bias towards higher impact distances.

- Energy: $50\,\mathrm{GeV} < E < 3750\,\mathrm{GeV}$;
- Impact point: $0\,\mathrm{m} < I < 240\,\mathrm{m}$;
- Height of the shower maximum: depending on energy (see Fig. B.6).

Since $Tmax$ is energy dependent, it is not possible to use fixed limits of $Tmax$ for all energy values. Therefore, the limits are adjusted according to the current estimated energy. In Fig. B.6, the distribution of bins in shower maximum height is shown as a function of energy. Each full circle corresponds to an available template. The interpolation in $Tmax$ is done between these points so that the fitting range in $Tmax$ is given by the lowest and the highest $Tmax$ for each energy as marked by the red line.

The bottle neck of the model analysis is the time needed for the fitting of the events. Therefore, for the success of the model analysis, a fast and efficient fitting algorithm is essential. We have realized this at the very beginning of the development and decided to use the so-called Marquardt-Levenberg method, which is suitable for solving nonlinear models. In the following, I briefly describe the idea, assumptions and the possible problems of the method. More details about the method can be found in Press et al. (1992).

A side note: The Marquardt-Levenberg method was originally developed by Marquardt (Marquardt, 1963) using an earlier idea of Levenberg (Levenberg, 1944) for the χ^2 function assuming a normal distribution of the data. The χ^2 function is a special case of the generalized likelihood function L. In this special case of the normal distribution it is valid:

$$\chi^2 = -2 \ln L \tag{B.10}$$

In order to use the Marquardt-Levenberg method, we constructed the loglikelihood function Ln_L in the same way (compare Equation B.10 and Equation B.4). One can show that the properties of the χ^2 function, which are used for the Marquardt-Levenberg method, also apply for the loglikelihood function Ln_L.

The implemented Marquardt-Levenberg method to find the best template parameters for the events (MC and data) proved to be a factor of about 200 faster than any of the routines from the standard MINUIT package. However, the method performs well if the starting values are not too far from the best ones. In particular, if the starting parameter of the impact distance is wrong by more than 50 meters, only in very rare cases the real values are found. This is a known problem of many local minima in a flat valley of complicated topography. A solution to this problem would be to perform a gross scan in a parameter space and use the best result as a starting point for the minimization.

B.3.5 Integrating into the standard analysis chain

The model analysis is made available in the standard analysis chain as an option. The flow diagram in Fig. B.16 shows the additional tasks in yellow. The event container with the calibrated information per pixel has to be copied in order not to interfere with the standard image cleaning. The standard image parameters are calculated and used to estimate starting parameters of the model fit.

For the convergence of the fit the following criterion is used: the difference between the best loglikelihood value and the second-best is less than $1 \cdot 10^{-5}$. A maximum of 100 fitting steps is set. If the fit does not converge after 100 steps, the fit is declared as “not converged”, but the fit results of the best loglikelihood value are still saved.

There is one complication in case the time information is used in the fitting procedure. The problem is how to treat pixels with very low signals being due to noise. The arrival for those pixels is neither distributed Gaussian nor Poissonian, it is just a flat distribution bounded by the time window of the readout. Another problem arises from those pixels, at which the expected number of photons is zero and hence the expected arrival time is undefined. In order to avoid these complications, we decided to use the time information in the fit only for those pixels, which photon signals are above a certain threshold. For those pixels, the arrival time is well defined and can be well compared to the expected arrival time assuming a normal distribution.

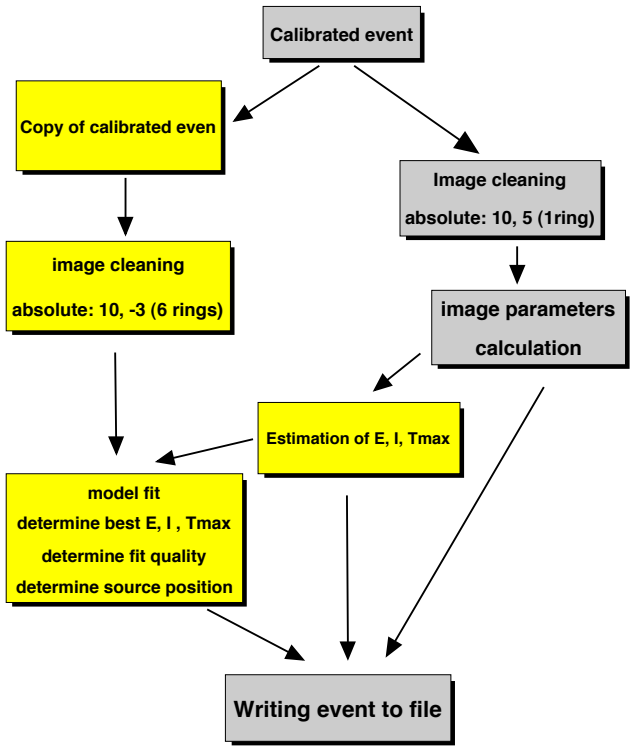

Figure B.16: Incorporation of the model analysis into the standard analysis chain. Standard tasks are marked in grey. New tasks allowing for the model analysis are marked yellow. The final output is written in the same data format with additional event parameters determined by the model fit.

In Fig. B.17, an example of a typical well fitted event is shown. On the left, one can see a MC γ-event after calibration, whereas on the right the best fit is displayed. The real values of the inducing γ-ray are shown on the top of the left plot. The fitted values (shown on the top right) agree with the real ones quite well. The real source position of the event is shown by the black filled circle, whereas the fitted source position is displayed by a yellow star. Both agree quite well too.

B.4 Monte-Carlo results

In the following I present MC studies on the performance of the model analysis. The study has several goals: (1) to show the performance of the method with the best setting, (2) compare the performance of the model analysis between ON and WOBBLE-mode data, (3) show the effect of using timing information, and (4) compare the performance in case the source position is known with the one

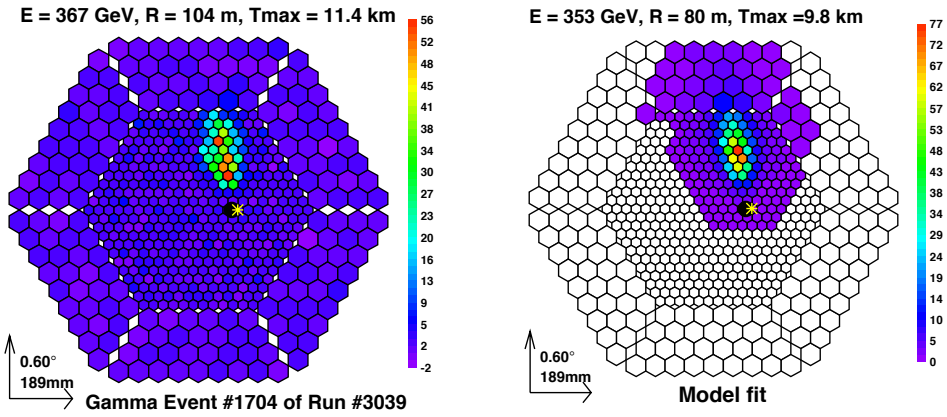

Figure B.17: An example of the fitted event. On the left an MC γevent is shown, whereas the number of photoelectrons per pixel is color coded. On the right, the best fit is shown together with the fitted parameters. The source position of the event is marked by the filled black circle. The reconstructed source position is marked by the yellow star.

where the source position is unknown.

To test the performance of the model analysis, a standard MC γ-ray set was chosen. I chose only MC γ-rays at small zenith angle from 0 to 30 deg because the model templates are produced for the vertical showers only. The MC sample consists of two parts: one with the source position in the camera center (ON mode), the other one with the source position 0.4° off camera center (WOBBLE mode). A minimum cut of 2 neighboring pixels containing at least 10 phe is applied in order to better compare results with the standard analysis, in which the image cleaning 10-5 is used (Section 5.7).

B.4.1 Default setting: WOBBLE mode, timing, known source position

The default setting of the tests for the performance of the model analysis is: (i) WOBBLE mode, (ii) using signal timing, and (iii) known source position. The fact that the source position is known allows using the *Dist* parameter to estimate the impact point of the shower and the energy of the event. The disadvantage of using *Dist* is that sky maps cannot be produced.

The performance plots of the model analysis for the default setting are shown in Fig. B.18. The plots from left to right and top to down:

- (A) Convergence of the fit as a function of the *Size* parameter. The fit converges for more than 98% of the total events. At high *Size* values less events converge but the fraction is still above 80%.

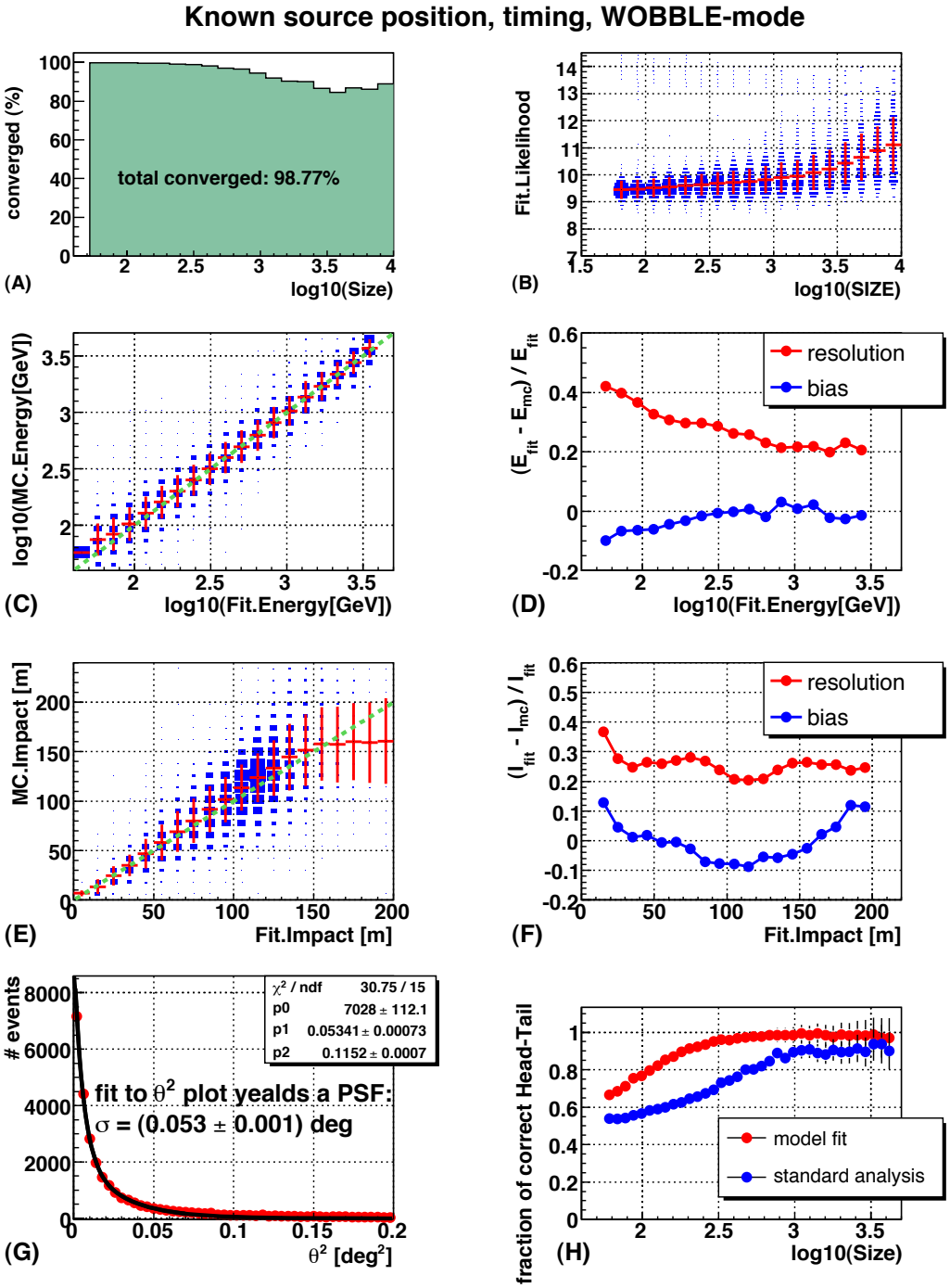

Figure B.18: Performance of the model analysis on MC γ-ray sample. The default setting is shown: WOBBLE mode, using timing, using known source position. See text for details of the plots.

- (B) Loglikelihood value as a function of the *Size* parameter. The entries are normalized to 1 for each bin along the x-axis separately. One can see that the likelihood values slightly depend on the *Size* parameter, which might introduce a bias in the energy reconstruction.

- (C) True (MC) energy as a function of the fitted energy. The entries are normalized to 1 for each bin along the x-axis separately. The green dashed line indicates an ideal correlation between the two quantities. A profile histogram in the bins of fitted energy is shown by the red crosses.

- (D) Energy resolution as a function of the fitted energy. The energy resolution is defined as the RMS value (Gaussian fit) of the relation:

$$\frac{\mathrm{E_{fit}} - \mathrm{E_{mc}}}{\mathrm{E_{fit}}} \tag{B.11}$$

  The bias of the energy reconstruction, i.e. the Gaussian mean fitted to the relation B.11, is also shown.

- (E) True (MC) impact distance as a function of the fitted impact distance. The green dashed line indicates an ideal correlation between the two quantities. A profile histogram in the bins of fitted energy is shown by the red crosses.

- (F) Impact resolution as a function of the fitted impact distance. The impact resolution is defined analog to the energy resolution and is the RMS value of:

$$\frac{\mathrm{I_{fit}} - \mathrm{I_{mc}}}{\mathrm{I_{fit}}} \tag{B.12}$$

  The bias of the impact reconstruction is also shown.

- (G) θ^2-plot. A Gauss-like function is fitted to the distribution of θ^2-values (shown by the black line) leading to a PSF of the method with the indicated width σ.

- (H) Head-Tail assignment of the model fit. The fraction of the correct Head-Tail assignment is shown as a function of the *Size* parameter. The fit result is shown by the red points, the result of the standard (Hillas) analysis is shown by the blue points.

Comments on the energy resolution: The energy resolution is about 40%-19% along the energy range from 50 GeV[1] to 4 TeV, and there is a continuous improvement in the resolution with the increasing energy. The energy resolution is

[1]Note also that the trigger threshold of the MAGIC telescope is about 60 GeV at low zenith angle.

better than the one obtained by the standard analysis (see Fig. 5.16) in the range between 300 GeV to 4 TeV. The reason for the improvement is most probably the cut on the maximum reconstructed impact parameter of the events (here chosen to be $I < 120$ m), which is not used in the standard analysis. It is worth to note that the energy resolution does not break down at γ-ray energies below 100 GeV as it happens in the standard analysis (see Fig. 5.16). A reasonable energy resolution of 35% is possible down to 65 GeV.

Comments on the impact parameter resolution: The impact parameter resolution is about 20%-25% for the range between 30 m and 200 m, which is very good for a single telescope. The impact parameter resolution is the best around the "hump" of the Cherenkov light pool, i.e. in the range between 90 and 130 m from the telescope.

Comments on the θ^2-plot: The width of the θ^2 distribution, σ of the PSF, is another improvement compared to the standard analysis. The value obtained with the model analysis, $\sigma = 0.065 \pm 0.001$ deg, is to be compared with the standard PSF of $\sigma \approx 0.10$ deg.

Comments on the Head-Tail reconstruction: A most impressive improvement is achieved for the correct assignment of the Head-Tail asymmetry. While for the standard analysis only ≈60% of the events with low *Size* values are assigned with the correct Head-Tail orientation, this fraction is above 80% for the model analysis.

B.4.2 ON mode, timing, known source position

The performance of the model analysis for the ON-mode sample using timing and the source position is shown in Fig. B.19. Compared to the WOBBLE mode (Section B.4.1), very similar energy and impact resolutions are achieved. The width of the θ^2 distribution is slightly better than in case of the WOBBLE mode: $\sigma_{WOBBLE} = 0.062 \pm 0.01$ deg vs. $\sigma_{WOBBLE} = 0.065 \pm 0.001$ deg. The Head-Tail assignment is equally good as in case of the WOBBLE mode.

I conclude that the performance in this test in the WOBBLE mode is equally good as in the ON mode. This is particularly important because the templates are produced with the source position in the camera center, thus for a source off center the coma aberration effects are not taken properly into account. Since there is only slight degradation in the width of the θ^2 distribution, the model analysis in its current implementation should perform similarly well for ON and WOBBLE mode data.

B.4.3 WOBBLE mode, no timing, known source position

An important result of the study is how much improvement one gains by using the timing informations of PMT signals. In Fig. B.20 the performance in the WOBBLE mode without using the timing information is shown. The plots have

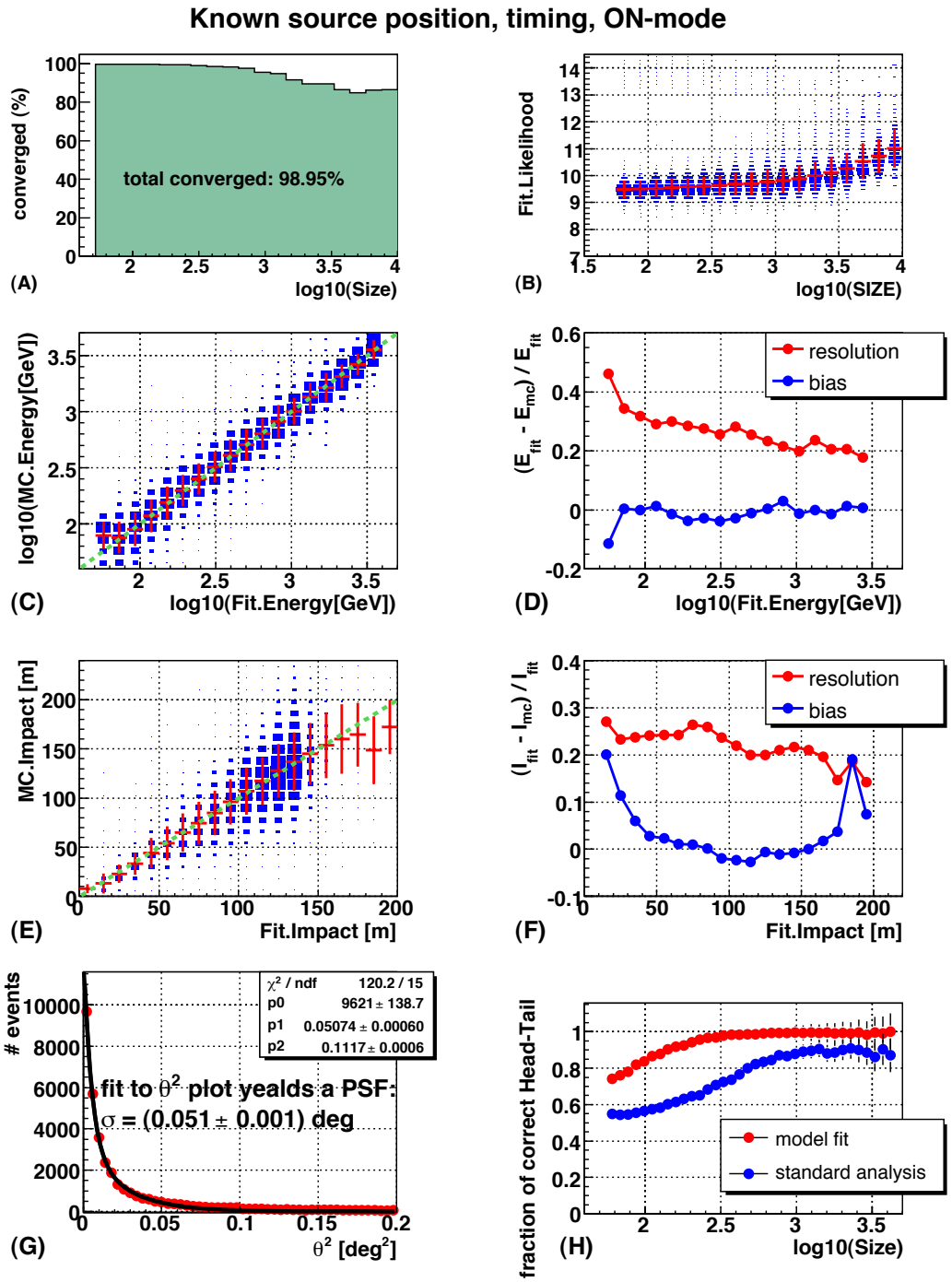

Figure B.19: Performance of the model analysis on MC γ-ray sample. The setting shown corresponds to: ON mode, using timing, using known source position. See Section B.4.1 and Section B.4.2 for details of the plots.

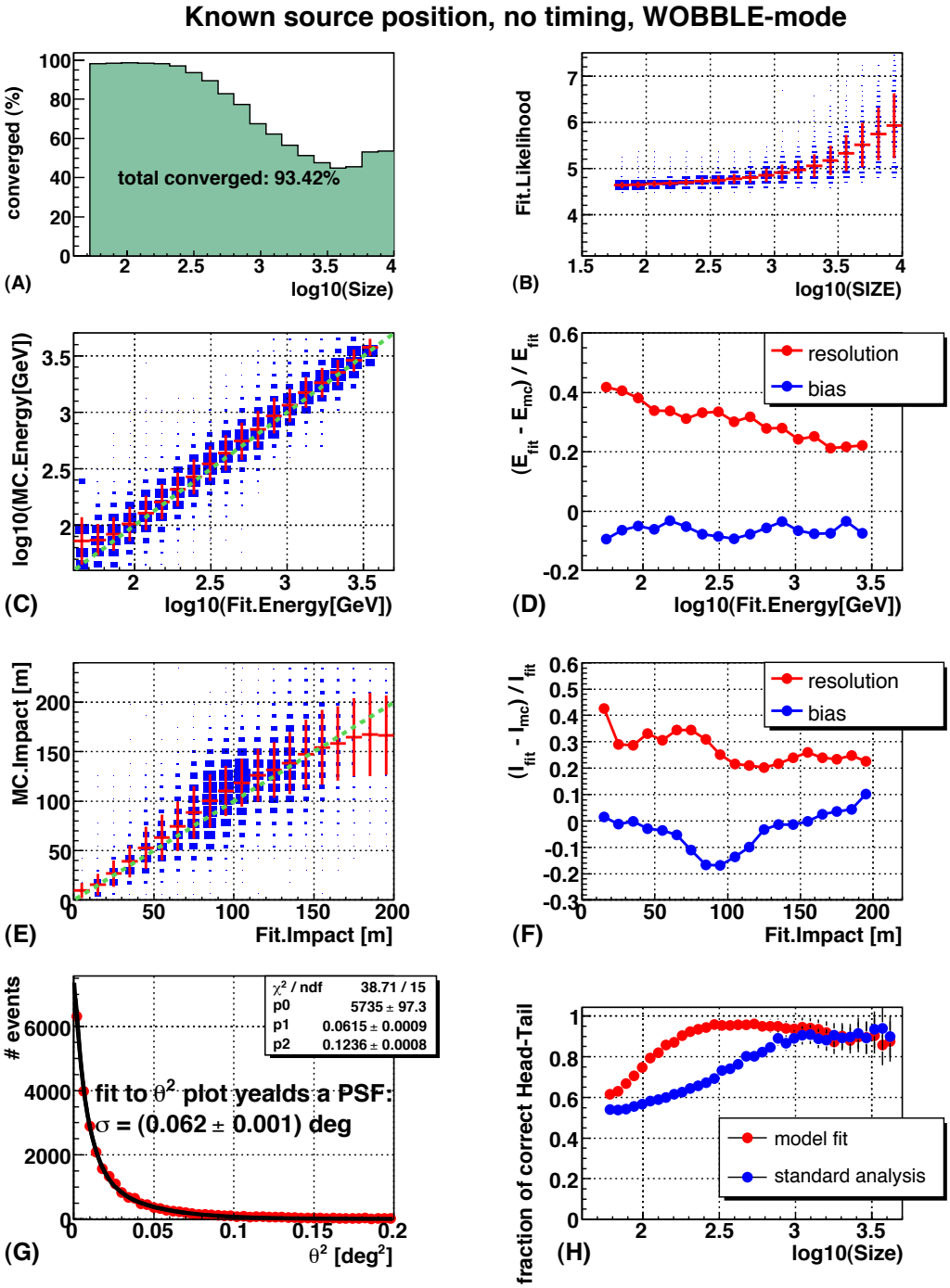

Figure B.20: Performance of the model analysis on a MC γ-ray sample. The setting shown corresponds to: WOBBLE mode, not using timing, using known source position. See Section B.4.1 and Section B.4.3 for details of the plots.

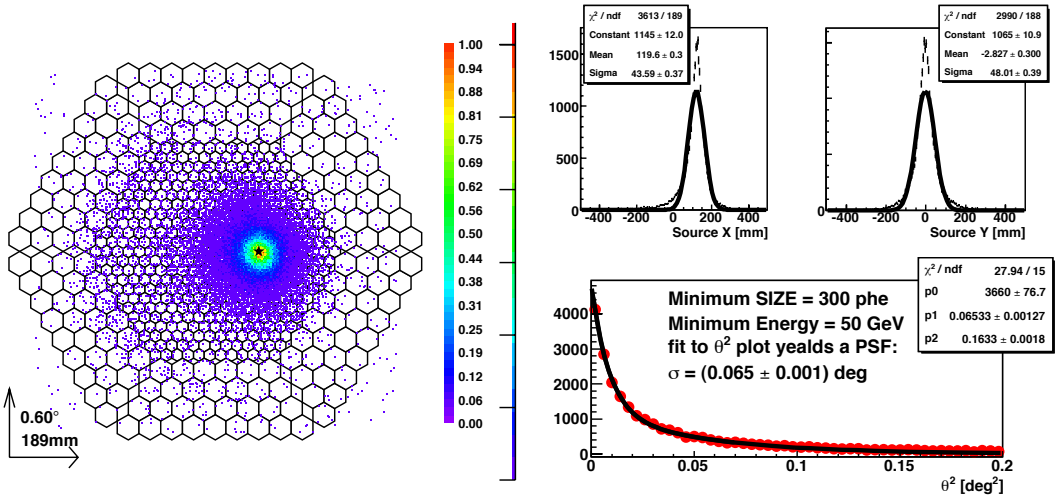

Figure B.21: Source position reconstruction, WOBBLE mode. *Left plot:* camera plot with reconstructed directions of MC events. The true position is marked by the black star. *Right, above plot:* Projections of the reconstructed directions along the X- and Y-axis in the camera. Note that the Y-position is shifted by ≈3 mm down in respect to the true position. *Right, bottom plot:* The θ^2 distribution of the events.

to be compared to Fig. B.18. One can see that the energy resolution becomes worse if no timing information is used. Moreover, the width of the θ^2 distribution increases from $\sigma_{Time} = 0.065 \pm 0.01\,\mathrm{deg}$ to $\sigma_{NoTime} = 0.068 \pm 0.001\,\mathrm{deg}$. In addition, the Head-Tail assignment at high energies is worse than the one by using timing. The fit often does not converge for images with high *Size* parameters (Fig. B.20, plot A). It seems that the timing information helps the fit to converge. However, even without convergence, the fit results look reasonable, which might mean that the convergence criteria can be optimized further.

B.4.4 WOBBLE mode, timing, unknown source position

The position of a γ-ray source is not always available. Also for extended sources it is necessary to perform an analysis without using source-dependent parameters. The only difference in case of the model analysis is that no source dependent image parameters are used to get starting values for E and I (see Section B.3.3, Equation B.9). In Fig. B.21 the source position reconstruction is shown. The width of the θ^2 distribution is $\sigma_{Time} = 0.074 \pm 0.01\,\mathrm{deg}$ and is 15% worse than for the default setting. Still, the accuracy of the source position reconstruction is slightly better than the one of the standard analysis, especially at low energies.

The performance of this setting in respect to other variables is shown in Fig. B.22. One can see that the energy reconstruction is considerably worse than in the case the source-dependent parameters can be used (see Fig. B.18).

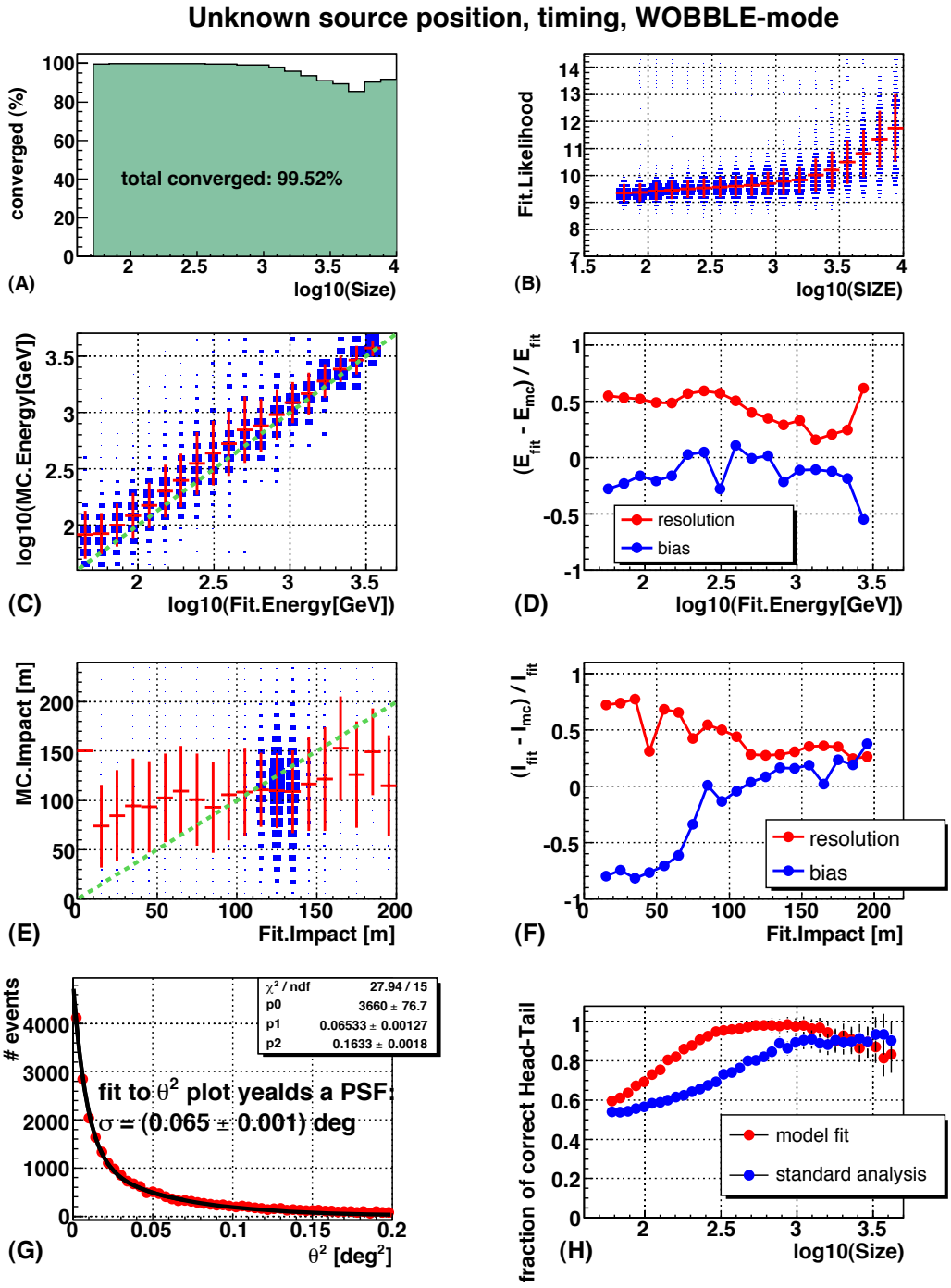

Figure B.22: Performance of the model analysis on a MC γ-ray sample. The setting shown corresponds to: WOBBLE mode, using timing, the source position is unknown. Note that the energy and impact reconstruction are much worse that in case the source position is known. See Section B.4.1 and Section B.4.4 for details of the plots.

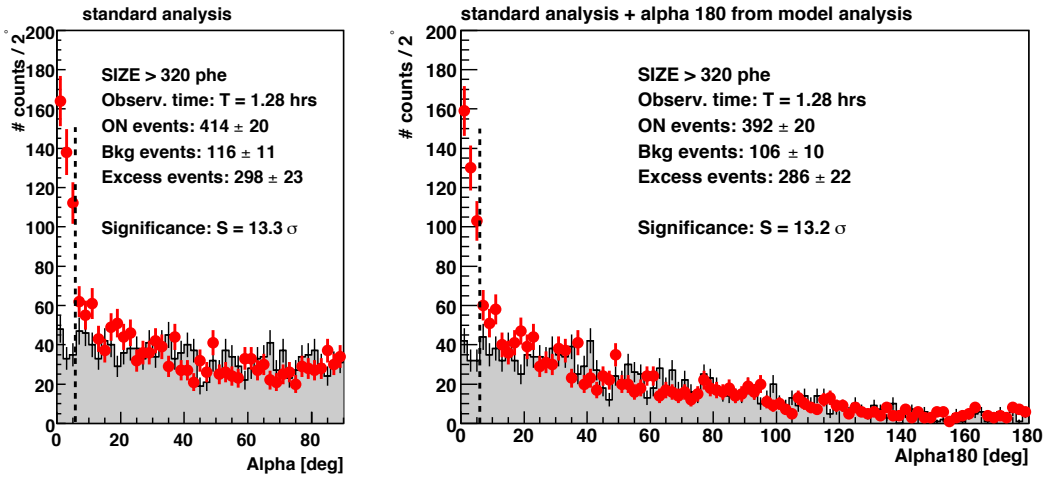

Figure B.23: *Alpha* plots for the Crab nebula above 320 phe. On the left is the result of the standard analysis. On the right, the result of the standard analysis including the Head-Tail assignment from the model analysis.

The reason is that the impact parameter reconstruction basically fails. The only difference to the case where the source position is known (Section B.4.1) is the way how starting values for the fit parameters for impact and energy are obtained. It seems that the model analysis is very sensitive to the starting values. One possible solution to improve the energy and impact reconstruction is to use better starting values, e.g. to use values estimated through the Random Forest method.

B.5 Performance of the method on the Crab Nebula data

The most impressive improvement of the model analysis on the MC sample is the head-tail assignment. To test this improvement on real data, we chose to use a subsample of the Crab Nebula data sample analyzed in Chapter 5. The effective on-time from this subsample accounts to 1.28 h. The effect of the usage of the head-tail assignment from the model analysis is shown in Fig. B.23. The same γ/hadron separation cuts have been applied to the data as for the standard analysis (see Section 5.10.1, Figure 5.11). The left plot in Fig. B.23 shows the result of the signal extraction using the standard analysis. In the right plot, the head-tail assignment from the model analysis is used in addition. The head-tail assignment can be used to define the *Alpha* parameter from 0 to 180 deg (right plot) instead of the usual 0 to 90 deg (left plot). From Fig. B.23 one can

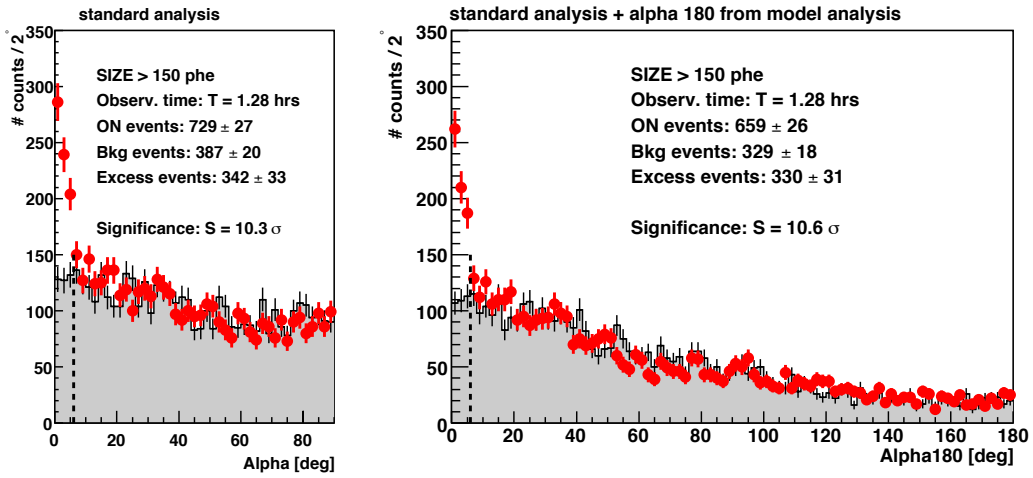

Figure B.24: *Alpha* plots for the Crab nebula above 150 phe. On the left is the result of the standard analysis. On the right, the result of the standard analysis including the Head-Tail assignment from the model analysis.

see that the number of background events (OFF) decreased by ≈9% while the number of excess events decreased by ≈5%. Since the significance of the excess changes with the $\sqrt{N_{bkg}}$, there is basically no change in the significance between the two methods. The reason is that for events with $Size > 320$ phe the head-tail assignment of the standard analysis is quite good, and it has been used for the γ/hadron separation. This is also the reason that the *Alpha* distribution in the right plot of Fig. B.23 has much less events in the background region for *Alpha* >90 degrees than in the background region for 30< *Alpha* <90 degrees.

In order to verify the performance of the model analysis, a lower cut of $Size >$ 150 phe has been applied to the same data set keeping all other cuts the same as above. The resulting *Alpha*-plots are shown in Fig. B.24. A higher significance of the signal is obtained by combining the standard analysis with the Head-Tail assignment of the model analysis. With this lower *Size* cut, the inclusion of the Head-Tail assignment into the *Alpha*-plot reduced the background level by ≈15% whereas the number of excess events was reduced by ≈3.5% only. This improvement of the signal-to-background ratio corresponds to ≈5% increase in flux sensitivity.

The model analysis also reconstructs the Head-Tail asymmetry better for showers outside of the "hump" of the Cherenkov light pool, i.e. showers with large *Dist* parameters ($Dist > 1.2$ deg). In the standard analysis, a sharp cut of $Dist < 1.2$ deg has been applied. As a test, we remove this cut for the *Alpha*180-plot. The resulting *Alpha*180-plot is shown in Fig. B.25, right plot. The left plot in Fig. B.24 and Fig. B.25 are identical corresponding to the result of the

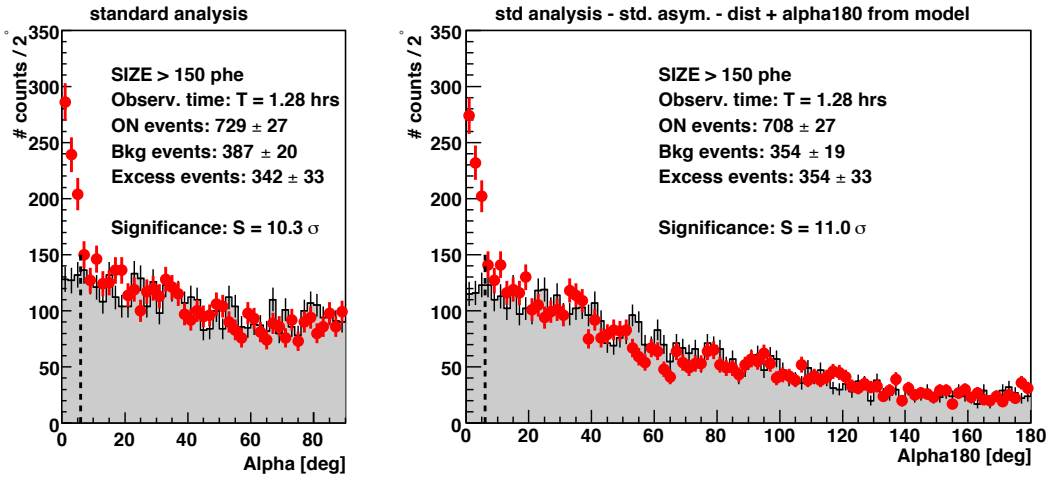

Figure B.25: *Alpha*-plots for the Crab nebula above 150 phe. On the left is the result of the standard analysis. On the right, the result of the standard analysis including the Head-Tail assignment from the model analysis. In addition, no *Dist* cuts have been applied to produce the *Alpha*-plot on the right. The number of excess events as well as the significance increased compared to the result in Fig. B.24.

standard analysis. In the right plot of Fig. B.25 more excess events are obtained than in the standard analysis while the background level is still lower than in the standard analysis. The result corresponds to ≈8% improvement of the sensitivity.

It is expected that the value from the model analysis can be used as a γ/hadron separation parameter to further improve the sensitivity. However, first tests on real data showed that the likelihood value is dependent on the NSB level. This is not unexpected given the construction of the function to be minimized (see Equation B.3). The dependence of the final likelihood values on the NSB level does not mean that the performance of the analysis method depends on the NSB level. This, however, was not tested yet. In turn, for the γ/hadron separation it means that the cuts cannot be easily chosen using the MC data because the NSB level in the standard MC sample is less than in the real data. A production of the MC sample with the NSB level matching the one of the data is ongoing.

B.6 Concluding Remarks

Motivated by a good experience of the CAT Le Bohec et al. (1998) and H.E.S.S. de Naurois (2006) collaborations, we have developed and implemented the model analysis for the MAGIC telescope. Our model analysis is based on the averages of the MC simulated events. For the first time, the timing information of the photons is taken into account. Though tuning and testing of the method is ongoing, the

model analysis already provides an independent analysis chain for the MAGIC data, including γ/hadron separation, a source position reconstruction, an energy estimation, and a Head-Tail assignment.

After the first tests on MC data, we can already show an improvement compared to the standard analysis. A better energy estimation especially for energies below 150 GeV, and a superior head-tail determination are the two major achievements of the method. A further improvement is possible by tuning the templates and optimizing the starting values. It is not yet clear if the model analysis provides a powerful tool for γ/hadron separation and how much it may decrease the energy threshold. In any case we expect an additional improvement of the sensitivity of the experiment by combining the model analysis with the standard one as the first test already showed an improvement in the order of 10% at low energies.

Appendix C

The Likelihood Ratio Test

The likelihood ratio test (Eadie et al., 1988) is a standard statistical tool to test between two hypotheses whether an improvement to a fit quality (quantified by corresponding χ^2 values) is expected from a normal distribution or if it is significant. By fitting two functional forms to the intrinsic spectrum, one obtains values of the likelihood functions L_A and L_B. If hypothesis A is true, the likelihood ratio $R = -\ln(L_A/L_B)$ is approximately χ^2 distributed with N degrees of freedom. N is the difference between numbers of degrees of freedom of hypothesis A and hypothesis B. One defines a probability

$$P = \int_0^{R_{\mathrm{meas}}} p\left(\chi^2\right) \mathrm{d}\chi^2 \tag{C.1}$$

where $p\left(\chi^2\right)$ is the χ^2 probability density function and R_{meas} the measured value of R. Hypothesis A will be rejected (and hypothesis B will be accepted) if P is greater than the confidence level, which is set to 95%.

Bibliography

Abbasi, R. U., Abu-Zayyad, T., Amman, J. F., et al. (2005). Monocular measurement of the spectrum of UHE cosmic rays by the FADC detector of the HiRes experiment. *Astroparticle Physics*, 23:157–174.

Aharonian, F., Akhperjanian, A., Barrio, J. A., et al. (2002a). Limits on the TeV flux of diffuse gamma rays as measured with the HEGRA air shower array. *Astroparticle Physics*, 17:459–475, arXiv:astro-ph/0109145.

Aharonian, F., Akhperjanian, A., Barrio, J. A., et al. (2002b). Search for point sources of gamma radiation above 15 TeV with the HEGRA AIROBICC array. *Astronomy & Astrophysics*, 390:39–46.

Aharonian, F., Akhperjanian, A., Beilicke, M., et al. (2003a). TeV gamma -ray light curve and energy spectrum of Mkn 421 during its 2001 flare as measured with HEGRA CT1. *Astronomy & Astrophysics*, 410:813–821.

Aharonian, F., Akhperjanian, A., Beilicke, M., et al. (2004a). Observations of 54 Active Galactic Nuclei with the HEGRA system of Cherenkov telescopes. *Astronomy & Astrophysics*, 421:529–537.

Aharonian, F., Akhperjanian, A., Beilicke, M., et al. (2004b). The Crab Nebula and Pulsar between 500 GeV and 80 TeV: Observations with the HEGRA Stereoscopic Air Cerenkov Telescopes. *The Astrophysical Journal*, 614:897–913, astro-ph/0407118.

Aharonian, F., Akhperjanian, A. G., Aye, K.-M., et al. (2004c). Very high energy gamma rays from the direction of Sagittarius A*. *Astronomy & Astrophysics*, 425:L13–L17.

Aharonian, F., Akhperjanian, A. G., Aye, K.-M., et al. (2005a). Discovery of the binary pulsar PSR B1259-63 in very-high-energy gamma rays around periastron with HESS. *Astronomy & Astrophysics*, 442:1–10, astro-ph/0506280.

Aharonian, F., Akhperjanian, A. G., Aye, K.-M., et al. (2005b). Discovery of Very High Energy Gamma Rays Associated with an X-ray Binary. *Science*, 309:746–749, astro-ph/0508298.

Aharonian, F., Akhperjanian, A. G., Aye, K.-M., et al. (2005c). Discovery of VHE gamma rays from PKS 2005-489. *Astronomy & Astrophysics*, 436:L17–L20.

Aharonian, F., Akhperjanian, A. G., Aye, K.-M., et al. (2005d). Observations of Mkn 421 in 2004 with HESS at large zenith angles. *Astronomy & Astrophysics*, 437:95–99.

Aharonian, F., Akhperjanian, A. G., Barres de Almeida, U., et al. (2007a). Discovery of VHE γ-rays from the distant BL Lacertae 1ES 0347-121. *Astronomy & Astrophysics*, 473:L25–L28, arXiv:0708.3021.

Aharonian, F., Akhperjanian, A. G., Bazer-Bachi, A. R., et al. (2005e). Multi-wavelength observations of PKS 2155-304 with HESS. *Astronomy & Astrophysics*, 442:895–907.

Aharonian, F., Akhperjanian, A. G., Bazer-Bachi, A. R., et al. (2006a). A low level of extragalactic background light as revealed by γ-rays from blazars. *Nature*, 440:1018–1021.

Aharonian, F., Akhperjanian, A. G., Bazer-Bachi, A. R., et al. (2006b). Discovery of very high energy γ-ray emission from the BL Lacertae object H 2356-309 with the HESS Cherenkov telescopes. *Astronomy & Astrophysics*, 455:461–466.

Aharonian, F., Akhperjanian, A. G., Bazer-Bachi, A. R., et al. (2006c). Discovery of very-high-energy γ-rays from the Galactic Centre ridge. *Nature*, 439:695–698.

Aharonian, F., Akhperjanian, A. G., Bazer-Bachi, A. R., et al. (2006d). Evidence for VHE γ-ray emission from the distant BL Lac PG 1553+113. *Astronomy & Astrophysics*, 448:L19–L23, astro-ph/0601545.

Aharonian, F., Akhperjanian, A. G., Bazer-Bachi, A. R., et al. (2006e). Fast Variability of Tera-Electron Volt gamma-rays from the Radio Galaxy M87. *Science*, 314:1424, astro-ph/0612016.

Aharonian, F., Akhperjanian, A. G., Bazer-Bachi, A. R., et al. (2007b). An Exceptional Very High Energy Gamma-Ray Flare of PKS 2155-304. *The Astrophysical Journal, Letters*, 664:L71–L74, arXiv:0706.0797.

Aharonian, F., Akhperjanian, A. G., Bazer-Bachi, A. R., et al. (2007c). Detection of extended very-high-energy γ-ray emission towards the young stellar cluster Westerlund 2. *Astronomy & Astrophysics*, 467:1075–1080, arXiv:astro-ph/0703427.

Aharonian, F., Akhperjanian, A. G., Bazer-Bachi, A. R., et al. (2007d). Detection of VHE gamma-ray emission from the distant blazar 1ES 1101-232 with HESS and broadband characterisation. *Astronomy & Astrophysics*, 470:475–489.

Aharonian, F. A. (2000). TeV gamma rays from BL Lac objects due to synchrotron radiation of extremely high energy protons. *New Astronomy*, 5:377.

Aharonian, F. A. (2001). TeV blazars and cosmic infrared background radiation. In Gladysheva, O. G., Kocharov, G. E., Kovaltsov, G. A., and Usoskin, I. G., editors, *Proceedings of 27th International Cosmic Ray Conference, Hamburg*, page I250. arXiv:astro-ph/0112314.

Aharonian, F. A., Akhperjanian, A., Beilicke, M., et al. (2002c). Variations of the TeV energy spectrum at different flux levels of Mkn 421 observed with the HEGRA system of Cherenkov telescopes. *Astronomy & Astrophysics*, 393:89.

Aharonian, F. A., Akhperjanian, A. G., Andronache, M., et al. (1999a). Observations of MKN 421 during 1997 and 1998 in the energy range above 500 GeV with the HEGRA stereoscopic Cherenkov telescope system. *Astroparticle Physics*, 350:757.

Aharonian, F. A., Akhperjanian, A. G., Barrio, J. A., et al. (1999b). The time averaged TeV energy spectrum of MKN 501 of the extraordinary 1997 outburst as measured with the stereoscopic Cherenkov telescope system of HEGRA. *Astronomy & Astrophysics*, 349:11.

Aharonian, F. A., Akhperjanian, A. G., Barrio, J. A., et al. (2000). The Energy Spectrum of TeV Gamma Rays from the Crab Nebula as measured by the HEGRA System of imaging Air Cerenkov Telescopes. *The Astrophysical Journal*, 539:317.

Aharonian, F. A., Akhperjanian, A. G., Barrio, J. A., et al. (2002d). TeV gamma rays from the blazar H 1426+428 and the diffuse extragalactic background radiation. *Astronomy & Astrophysics*, 384:L23.

Aharonian, F. A., Akhperjanian, A. G., Beilicke, M., et al. (2002e). An unidentified TeV source in the vicinity of Cygnus OB2. *Astronomy & Astrophysics*, 393:L37.

Aharonian, F. A., Akhperjanian, A. G., Beilicke, M., et al. (2003b). Detection of TeV Gamma-Rays from the BL Lac 1ES1959+650 in its low states and during a major outburst in 2002. *Astronomy & Astrophysics*, 406:L9.

Aharonian, F. A., Akhperjanian, A. G., Beilicke, M., et al. (2003c). Is the Giant Radio Galaxy M87 a TeV Gamma-Ray Emitter? *Astronomy & Astrophysics*, 403:L1.

Aharonian, F. A., Akhperjanian, A. G., Beilicke, M., et al. (2003d). Observations of H1426+428 with HEGRA - Observations in 2002 and reanalysis of 1999&2000 data. *Astronomy & Astrophysics*, 403:523. astro-ph/0301437.

Aharonian, F. A., Timokhin, A. N., and Plyasheshnikov, A. V. (2002f). On the origin of highest energy gamma-rays from Mkn 501. *Astronomy & Astrophysics*, 384:834–847, astro-ph/0108419.

Albert, J., Aliu, E., Anderhub, H., et al. (2006a). Discovery of Very High Energy Gamma Rays from 1ES 1218+30.4. *The Astrophysical Journal, Letters*, 642:L119–L122, astro-ph/0603529.

Albert, J., Aliu, E., Anderhub, H., et al. (2006b). Discovery of Very High Energy γ-Rays from Markarian 180 Triggered by an Optical Outburst. *The Astrophysical Journal, Letters*, 648:L105–L108, astro-ph/0606630.

Albert, J., Aliu, E., Anderhub, H., et al. (2006c). Observation of Gamma Rays from the Galactic Center with the MAGIC Telescope. *The Astrophysical Journal, Letters*, 638:L101–L104, arXiv:astro-ph/0512469.

Albert, J., Aliu, E., Anderhub, H., et al. (2006d). Observation of Very High Energy Gamma-Ray Emission from the Active Galactic Nucleus 1ES 1959+650 Using the MAGIC Telescope. *The Astrophysical Journal*, 639:761–765, arXiv:astro-ph/0508543.

Albert, J., Aliu, E., Anderhub, H., et al. (2006e). Variable Very-High-Energy Gamma-Ray Emission from the Microquasar LS I +61 303. *Science*, 312:1771–1773, arXiv:astro-ph/0605549.

Albert, J., Aliu, E., Anderhub, H., et al. (2007a). Detection of VHE radiation from the BL Lac PG 1553+113 with the MAGIC telescope. *The Astrophysical Journal, Letters*, 654:L119–L122, arXiv:astro-ph/0606161.

Albert, J., Aliu, E., Anderhub, H., et al. (2007b). Discovery of Very High Energy γ-Ray Emission from the Low-Frequency-peaked BL Lacertae Object BL Lacertae. *The Astrophysical Journal, Letters*, 666:L17–L20, arXiv:astro-ph/0703084.

Albert, J., Aliu, E., Anderhub, H., et al. (2007c). Discovery of very high energy gamma-rays from 1ES 1011+496 at z = 0.212. *The Astrophysical Journal*, 667:L21–L24, arXiv:07064435.

Albert, J., Aliu, E., Anderhub, H., et al. (2007d). MAGIC Upper Limits on the Very High Energy Emission from Gamma-Ray Bursts. *The Astrophysical Journal*, 667:358–366, arXiv:astro-ph/0612548.

Albert, J., Aliu, E., Anderhub, H., et al. (2007e). Observations of Markarian 421 with the MAGIC Telescope. *The Astrophysical Journal*, 663:125–138, arXiv:astro-ph/0603478.

Albert, J., Aliu, E., Anderhub, H., et al. (2007f). Systematic search for VHE gamma-ray emission from X-ray bright high-frequency BL Lac objects. *ApJ submitted*, arXiv:07064453.

Albert, J., Aliu, E., Anderhub, H., et al. (2007g). Variable Very High Energy γ-Ray Emission from Markarian 501. *The Astrophysical Journal*, 669:862–883, arXiv:astro-ph/0702008.

Albert, J., Aliu, E., Anderhub, H., et al. (2007h). Very High Energy Gamma-Ray Radiation from the Stellar Mass Black Hole Binary Cygnus X-1. *The Astrophysical Journal, Letters*, 665:L51–L54, arXiv:0706.1505.

Albert, J., Aliu, E., Anderhub, H., et al. (2007i). VHE Gamma-Ray Observation of the Crab Nebula and Pulsar with MAGIC. *ApJ accepted*, arXiv:0705.3244.

Aliu, E. and Wittek, W. (2006). The Unfolding Program in the Standard Analysis Chain, Part1 : How to use it (revised), MAGIC TDAS 06-01. MAGIC internal report.

Antoni, T., Apel, W. D., Badea, F., et al. (2003). The Cosmic-Ray Experiment KASCADE. *Nucl.Instrum.Meth. A*, 513:490–510.

Barrio, J. et al. (1998). The MAGIC Telescope – Design study of a 17 m Cherenkov telescope for Gamma-Astronomy above 10 GeV. MPI-Phe 98-05, http://wwwmagic.mppmu.mpg.de/publications/proposals/.

Bartko, H., Gaug, M., Moralejo, A., and Sidro, N. (2005). FADC Pulse Reconstruction Using a Digital Filter for the MAGIC Telescope. *ArXiv Astrophysics*, astro-ph/0506459.

Bartko, H., Goebel, F., Mirzoyan, R., et al. (2005). Tests of a prototype multiplexed fiber-optic ultra-fast FADC data acquisition system for the MAGIC telescope. *Nucl. Instrum. Meth.*, A548:464–486, astro-ph/0505204.

Bednarek, W. (1997). Gamma-rays from synchrotron pair cascades in blazars? *MNRAS*, 285:69–81.

Bednarek, W. and Protheroe, R. J. (1997). Testing the homogeneous synchrotron self-Compton model for gamma-ray production in MRK 421. *MNRAS*, 292:646, arXiv:astro-ph/9704185.

Bednarek, W. and Protheroe, R. J. (1999). The physical parameters of Markarian 501 during flaring activity. *MNRAS*, 310:577–584, arXiv:astro-ph/9902050.

Berger, M. J. and Seltzer, S. M. (1964). Tables of energy losses and ranges of electrons and positrons. Report NASA Special Publication, National Aeronautics and Space Administration, Washington D.C.

Bernlöhr, K. (2000). Impact of atmospheric parameters on the atmospheric Cherenkov technique. *Astroparticle Physics*, 12:255–268, arXiv:astro-ph/9908093.

Bernstein, R. A., Freedman, W. L., and Madore, B. F. (2002). The First Detections of the Extragalactic Background Light at 3000, 5500, and 8000 Å. I. Results. *The Astrophysical Journal*, 571:56.

Bernstein, R. A., Freedman, W. L., and Madore, B. F. (2005). Corrections of Errors in "The First Detections of the Extragalactic Background Light at 3000, 5500, and 8000 Å. I, II, and III" (ApJ, 571; 56, 85, 107 [2002]). *The Astrophysical Journal*, 632:713–717, astro-ph/0507033.

Bertero, M. (1989). Linear inverse and ill-posed problems. *Advances in Electronics and Electron Physics*, 75:1–120, astro-ph/0507033.

Biermann, P. L., Chirvasa, M., Falcke, H., S., M., and Zier, C. (2002). Single and binary Black Holes and their active environment. In *Proceedings of the 7eme Colloquium Cosmologie*, High Energy Astrophysics from and for Space. arXiv:astro-ph/0211503.

Blandford, R. D. and Konigl, A. (1979). Relativistic jets as compact radio sources. *The Astrophysical Journal*, 232:34–48.

Błażejowski, M., Blaylock, G., Bond, I. H., et al. (2005). A Multiwavelength View of the TeV Blazar Markarian 421: Correlated Variability, Flaring, and Spectral Evolution. *The Astrophysical Journal*, 630:130–141, arXiv:astro-ph/0505325.

Blumenthal, G. R. and Gould, R. J. (1970). Bremsstrahlung, Synchrotron Radiation, and Compton Scattering of High-Energy Electrons Traversing Dilute Gases. *Reviews of Modern Physics*, 42:237–271.

Bock, R. K., Chilingarian, A., Gaug, M., et al. (2004). Methods for multidimensional event classification: a case study using images from a Cherenkov gamma-ray telescope. *Nuclear Instruments and Methods in Physics Research A*, 516:511–528.

Boella, G., Butler, R. C., Perola, G. C., Piro, L., Scarsi, L., and Bleeker, J. A. M. (1997). BeppoSAX, the wide band mission for X-ray astronomy. *Astronomy & Astrophysics, Supplement*, 122:299–307.

Böttcher, M. and Chiang, J. (2002). X-Ray Spectral Variability Signatures of Flares in BL Lacertae Objects. *The Astrophysical Journal*, 581:127–142, arXiv:astro-ph/0208238.

Breiman, L. (2001). Random forests. *Machine Learning*, 45:5.

Bridle, A. H. (1967). The spectrum of the radio background between 13 and 404 MHz. *MNRAS*, 136:219–240.

Brown, T. M., Kimble, R. A., Ferguson, H. C., Gardner, J. P., Collins, N. R., and Hill, R. S. (2000). Measurements of the Diffuse Ultraviolet Background and the Terrestrial Airglow with the Space Telescope Imaging Spectrograph. *AJ*, 120:1153–1159, astro-ph/0004147.

Buckley, J. H., Akerlof, C. W., Biller, S., et al. (1996). Gamma-Ray Variability of the BL Lacertae Object Markarian 421. *The Astrophysical Journal, Letters*, 472:L9.

Calzetti, D., Livio, M., and Madau, P. (1995). *Extragalactic background radiation. A meeting in honor of Riccardo Giacconi*. Space Telescope Science Institute Symposium Series, Proceedings of the Extragalactic Background Radiation meeting, Baltimore, 1993 May 18-20, Cambridge, New York: Cambridge University Press, —c1995, edited by Calzetti, Daniela; Livio, Mario; Madau, Piero.

Cambrésy, L., Reach, W. T., Beichman, C. A., and Jarrett, T. H. (2001). The Cosmic Infrared Background at 1.25 and 2.2 Microns Using DIRBE and 2MASS: A Contribution Not Due to Galaxies? *The Astrophysical Journal*, 555:563.

Catalano, O. et al. (2005). EUSO Instrument: Concept and solutions. In *Proceedings of 29th International Cosmic Ray Conference*, volume 8, page 93.

Catanese, M., Akerlof, C. M., Badran, H. M., et al. (1998). Discovery of Gamma-Ray Emission above 350 GeV from the BL Lacertae Object 1ES 2344+514. *The Astrophysical Journal*, 501:616.

Chadwick, P. M., Lyons, K., McComb, T. J. L., et al. (1999). Very high Energy Gamma Rays from PKS 2155-304. *The Astrophysical Journal*, 513:161.

Cherenkov, P. A. (1934). *Doklady Akademii nauk SSSR*, 2:451.

Chiba, N. et al. (1992). Akeno Giant Air Shower Array (AGASA) covering 100 km^2 area. *Nucl.Instrum.Meth. A*, 311:338–349.

Commichau, S. C. (2007). *Observation of Very High Energy Gamma-Rays from the Galactic Center with the MAGIC Telescope, considering Geomagnetic Field Effects on the Imaging Technique*. PhD thesis, ETH Zurich.

Coppi, P. S. (1992). Time-dependent models of magnetized pair plasmas. *MNRAS*, 258:657–683.

Costamante, L., Aharonian, F., Ghisellini, G., and Horns, D. (2003). The SED of the TeV BLLac 1ES 1426+428 after correction for the TeV-IR absorption. *New Astronomy Review*, 47:677–680, arXiv:astro-ph/0301211.

Costamante, L. and Ghisellini, G. (2002). TeV candidate BL Lac objects. *Astronomy & Astrophysics*, 384:56–71, arXiv:astro-ph/0112201.

Costamante, L., Ghisellini, G., Giommi, P., et al. (2001). Extreme Synchrotron BL Lac Objects – Streching the Blazar Sequence. *Astronomy & Astrophysics*, 371:512.

Dar, A. and de Rújula, A. (2004). Towards a complete theory of gamma-ray bursts. *Phys. Rep.*, 405:203–278, arXiv:astro-ph/0308248.

Dar, A. and Laor, A. (1997). Hadronic Production of TeV Gamma-Ray Flares from Blazars. *The Astrophysical Journal, Letters*, 478:L5, arXiv:astro-ph/9610252.

Daum, A., Hermann, G., Hess, M., et al. (1997). First results on the performance of the HEGRA IACT array. *Astroparticle Physics*, 8:1.

de la Calle Perez, I. and Bond, I.H. and Boyle, P.J. and others (2003). Search for Very High Energy Gamma Rays from an X-ray Selected Blazar Sample. In *Proc. of the 28th ICRC*, volume 5, page 2571.

de los Reyes, R. (2002). *Analysis and simulation of atmospheric Cherenkov telescope data*. Mater thesis, Madrid University.

de los Reyes, R. and Oya, I. (2006). MAGIC data check and on-line analysis program, MAGIC TDAS 0611. MAGIC internal report, Universidad Complutense, Madrid, Spain.

de Naurois, M. (2006). Analysis methods for Atmospheric Cerenkov Telescopes. *ArXiv Astrophysics e-prints*, astro-ph/0607247.

Dole, H., Lagache, G., Puget, et al. (2006). The cosmic infrared background resolved by Spitzer. Contributions of mid-infrared galaxies to the far-infrared background. *Astronomy & Astrophysics*, 451:417–429, astro-ph/0603208.

Domingo-Santamaría, E., Flix, J., Scalzotto, V., et al. (2005). The DISP analysis method for point-like or extended source searches/studies with the MAGIC Telescope. volume 5 of *International Cosmic Ray Conference*, pages 363 – 366.

Donato, D., Ghisellini, G., Tagliaferri, G., and Fossati, G. (2001). Hard X-ray properties of blazars. *Astronomy & Astrophysics*, 375:739–751, arXiv:astro-ph/0105203.

Donato, D., Sambruna, R. M., and Gliozzi, M. (2005). Six years of BeppoSAX observations of blazars: A spectral catalog. *Astronomy & Astrophysics*, 433:1163–1169, arXiv:physics/0412114.

Dube, R. R., Wickes, W. C., and Wilkinson, D. T. (1979). Upper limit on the extragalactic background light. *The Astrophysical Journal*, 232:333–340.

Dwek, E. and Arendt, R. G. (1998). A Tentative Detection of the Cosmic Infrared Background at 3.5 μm from COBE/DIRBE Observation. *The Astrophysical Journal*, 508:L9.

Dwek, E., Arendt, R. G., and Krennrich, F. (2005). The Near-Infrared Background: Interplanetary Dust or Primordial Stars? *The Astrophysical Journal*, 635:784–794, astro-ph/0508262.

Dwek, E. and Krennrich, F. (2005). Simultaneous Constraints on the Spectrum of the Extragalactic Background Light and the Intrinsic TeV Spectra of Markarian 421, Markarian 501, and H1426+428. *The Astrophysical Journal*, 618:657–674, astro-ph/0406565.

Dwek, E. and Slavin, J. (1994). On the determination of the cosmic infrared background radiation from the high-energy spectrum of extragalactic gamma-ray sources. *The Astrophysical Journal*, 436:696–704.

Eadie, W. T., Drijard, D., James, F. E., Roos, M., and Sadoulet, B. (1988). *Statistical Methods in Experimental Physics*. North-Holland Publishing Company; Amsterdam, New-York, Oxford.

Edelstein, J., Bowyer, S., and Lampton, M. (2000). Reanalysis of Voyager Ultraviolet Spectrometer Limits to the Extreme-Ultraviolet and Far-Ultraviolet Diffuse Astronomical Flux. *The Astrophysical Journal*, 539:187–190, astro-ph/0003208.

Elbaz, D., Cesarsky, C. J., Chanial, P., et al. (2002). The bulk of the cosmic infrared background resolved by ISOCAM. *Astronomy & Astrophysics*, 384:848.

Elterman, L. (1964). Parameters for attenuation in the atmospheric wondows for fifteen wavelengths. *Applied Optics*, 3:745–750.

Fabian, A. C. and Barcons, X. (1992). The origin of the X-ray background. *ARA&A*, 30:429–456.

Falcke, H., Apel, W. D., Badea, A. F., et al. (2005). Detection and imaging of atmospheric radio flashes from cosmic ray air showers. *Nature*, 435:313–316, arXiv:astro-ph/0505383.

Falco, E. E., Kurtz, M. J., Geller, M. J., et al. (1999). The Updated Zwicky Catalog (UZC). *PASP*, 111:438–452, arXiv:astro-ph/9904265.

Falomo, R., Scarpa, R., and Bersanelli, M. (1994). Optical spectrophotometry of blazars. *ApJS*, 93:125–143.

Falomo, R. and Treves, A. (1990). PG 1553 + 11 - A bright optically selected BL Lacertae object. *PASP*, 102:1120–1125.

Fazio, G. G., Ashby, M. L. N., Barmby, P., et al. (2004). Number Counts at 3 μm $< \lambda <$ 10 μm from the Spitzer Space Telescope. *ApJS*, 154:39–43, astro-ph/0405595.

Fazio, G. G. and Stecker, F. W. (1970). Predicted High Energy Break in the Isotropic Gamma Ray Spectrum: a Test of Cosmological Origin. *Nature*, 226:135.

Fichtel, C. E. et al. (1994). The first energetic gamma-ray experiment telescope (EGRET) source catalog. *ApJS*, 94:551–581.

Finkbeiner, D. P., Davis, M., and Schlegel, D. J. (2000). Detection of a Far-Infrared Excess with DIRBE at 60 and 100 Microns. *The Astrophysical Journal*, 544:81.

Finley, J. P. and The VERITAS Collaboration (2001). The Whipple Observatory Granite III Upgrade Program. In *International Cosmic Ray Conference*, page 2827.

Fioc, M. and Rocca-Volmerange, B. (1997). PEGASE: a UV to NIR spectral evolution model of galaxies. Application to the calibration of bright galaxy counts. *Astronomy & Astrophysics*, 326:950–962, arXiv:astro-ph/9707017.

Fomin, V. P., Stepanian, A. A., Lamb, et al. (1994). New methods of atmospheric Cherenkov imaging for gamma-ray astronomy. I. The false source method. *Astroparticle Physics*, 2:137–150.

Fossati, G., Buckley, J., Edelson, R. A., Horns, D., and Jordan, M. (2004). Correlated X-ray and TeV variability in Markarian 421. *New Astronomy Review*, 48:419–422.

Fossati, G., Celotti, A., Chiaberge, M., et al. (2000). X-Ray Emission of Markarian 421: New Clues from Its Spectral Evolution. II. Spectral Analysis and Physical Constraints. *The Astrophysical Journal*, 541:166.

Fossati, G., Maraschi, L., Celotti, A., et al. (1998). A unifying view of the spectral energy distributions of blazars. *Monthly Notices of the Royal Astronomical Society*, 299:433.

Frayer, D. T., Huynh, M. T., Chary, R., Dickinson, M., Elbaz, D., Fadda, D., Surace, J. A., Teplitz, H. I., Yan, L., and Mobasher, B. (2006). Spitzer 70 Micron Source Counts in GOODS-North. *The Astrophysical Journal, Letters*, 647:L9–L12, astro-ph/0606676.

Gaidos, J. A., Akerlof, C. W., Biller, S. D., et al. (1996). Very Rapid and Energetic Bursts of TeV Photons from the Active Galaxy Markarian 421. *Nature*, 383:319.

Garczarczyk, M. (2007). *First Observations of the GRB Prompt and Early Afterglow Emission Phase at ≈100 GeV Energy Regime with the 17 m Diameter MAGIC Imaging Atmospheric Cherenkov Telescope*. PhD thesis, Technical University, Munich.

Gaug, M. (2006). *Calibration of the MAGIC Telescope and Observation of Gamma Ray Bursts*. PhD thesis, Universitat Autònoma de Barcelona.

Ghisellini, G., Celotti, A., Fossati, G., Maraschi, L., and Comastri, A. (1998). A theoretical unifying scheme for gamma-ray bright blazars. *MNRAS*, 301:451–468, arXiv:astro-ph/9807317.

Giebels, B., Dubus, G., and Khélifi, B. (2007). Unveiling the X-ray/TeV engine in Mkn 421. *Astronomy & Astrophysics*, 462:29–41, arXiv:astro-ph/0610270.

Giommi, P., Ansari, S. G., and Micol, A. (1995). Radio to X-ray energy distribution of BL Lacertae objects. *Astronomy & Astrophysics, Supplement*, 109:267–291.

Giommi, P., Capalbi, M., Fiocchi, M., et al. (2002). A Catalog of 157 X-ray Spectra and 84 Spectral Energy Distributions of Blazars Observed with BeppoSAX. In Giommi, P., Massaro, E., and Palumbo, G., editors, *Blazar Astrophysics with BeppoSAX and Other Observatories*, page 63.

Goebel, F. (2007). Status of the second phase of the MAGIC telescope. In *30th International Cosmic Ray Conference, Merida, Mexico*. arXiv:0709.2605.

Goebel, F., Bartko, H., Carmona, E., et al. (2007). Upgrade of the MAGIC Telescope with a Multiplexed Fiber-Optic 2 GSamples/s FADC Data Acquisition system. In *30th International Cosmic Ray Conference, Merida, Mexico*. arXiv:0709.2363.

Gorjian, V., Wright, E. L., and Chary, R. R. (2000). Tentative Detection of the Cosmic Infrared Background at 2.2 and 3.5 Microns Using Ground-based and Space-based Observations. *The Astrophysical Journal*, 536:550.

Gould, R. J. and Schréder, G. P. (1967). Opacity of the Universe to High-Energy Photons. *Physical Review*, 155:1408–1411.

Green, R. F., Schmidt, M., and Liebert, J. (1986). The Palomar-Green catalog of ultraviolet-excess stellar objects. *ApJS*, 61:305–352.

Greisen, K. (1966). End to the cosmic-ray spectrum? *Physical Review Letters*, 16:748.

Hartman, R. C., Bertsch, D. L., Fichtel, C. E., et al. (1992). The EGRET high energy gamma ray telescope. In *The Compton Observatory Science Workshop*, page 116.

Hartman, R. C., Bertsch, S. D., Bloom, A. W., et al. (1999). The Third EGRET Catalog of High-Energy Gamma-Ray Sources. *The Astrophysical Journal Supplement*, 123:79.

Hartman, R. C. et al. (2001). Day-Scale Variability of 3C 279 and Searches for Correlations in Gamma-Ray, X-Ray, and Optical Bands. *The Astrophysical Journal*, 558:583–589, arXiv:astro-ph/0105247.

Hauser, M. G., Arendt, R. G., Kelsall, T., Dwek, E., Odegard, N., et al. (1998). The COBE Diffuse Infrared Background Experiment Search for the Cosmic Infrared Background. I. Limits and Detections. *The Astrophysical Journal*, 508:25.

Hauser, M. G. and Dwek, E. (2001). The cosmic infrared backround: Measurements and implications. *Annual Review of Astronomy & Astrophysics*, 39:249.

Hayashida, M., Costamente, L., Horns, D., et al. (2007). Wide-range multiwavelength observations of Northern TeV blazars with Suzaku, MAGIC and HESS. In *30th International Cosmic Ray Conference, Merida, Mexico*.

Heck, D., Knapp, J., Capdevielle, J. N., et al. (1998). Corsika: A monte carlo code to simulate extensive air shower. Wissenschaftliche Berichte FZKA 6019, Forschungszentrum Karlsruhe. http://www-ik3.fzk.de/∼heck/corsika/.

Heitler, M. (1960). *The Quantum Theorie of Radiation*. Oxford, Clarendon.

Hengstebeck, T. (2007). *Measurement of the energy spectrum of the BL Lac object PG1553+113 with the MAGIC Telescope in 2005 and 2006*. PhD thesis, Humboldt-Universitat zu Berlin.

Hess, V. (1912). Observation of penetrating radiation of seven balloon flights. *Physikalische Zeitschrift*, 13:1084.

Hillas, A. M. (1982). Angular and energy distributions of charged particles in electron-photon cascades in air. *Journal of Physics G: Nuclear Physics*, 8(10):1461–1473.

Hillas, A. M. (1985). Cerenkov light images of EAS produced by primary gamma. In Jones, F. C., editor, *19th International Cosmic Ray Conference (La Jolla)*, volume 3 of *International Cosmic Ray Conference*, pages 445–448.

Hinton, J. (2007). Rapporteur talk: Gamma ray astronomy, (OG 2.1 - OG 2.4). In *Proceedings of 30th International Cosmic Ray Conference, Merida, Mexico, http://www.icrc2007.unam.mx*. arXiv:0712.3352.

Hinton, J. A. (2004). The status of the HESS project. *New Astronomy Review*, 48:331–337, astro-ph/0403052.

Holder, J., Bond, I. H., Boyle, P. J., et al. (2003). Detection of TeV Gamma Rays from the BL Lacertae Object 1ES 1959+650 with the Whipple 10 Meter Telescope. *The Astrophysical Journal, Letters*, 583:L9–L12, arXiv:astro-ph/0212170.

Horan, D., Badran, H. M., Bond, I. H., Bradbury, S. M., et al. (2002). Detection of the BL Lacertae Object H1426+428 at TeV Gamma-Ray Energies. *The Astrophysical Journal*, 571:753.

Horan, D., Badran, H. M., Bond, I. H., et al. (2004). Constraints on the Very High Energy Emission from BL Lacertae Objects. *The Astrophysical Journal*, 603:51–61, arXiv:astro-ph/0311397.

Horan, D. and Weekes, T. C. (2004). Extragalactic sources of TeV gamma rays: a summary. *New Astronomy Review*, 48:527–535, astro-ph/0310391.

Horns, D. (2001). Suche nach TeV-Photonen aus intergalaktischen Kaskaden und nach Bose-Einstein-Kondensaten in TeV-Photonen. Dissertation, Fachbereich Physik der Universität Hamburg, dissertation.de.

Horns, D. (2005). TeV γ-radiation from Dark Matter annihilation in the Galactic center. *Physics Letters B*, 607:225–232, arXiv:astro-ph/0408192.

Inoue, S. and Takahara, F. (1996). Electron Acceleration and Gamma-Ray Emission from Blazars. *The Astrophysical Journal*, 463:555.

Jelley, J. V. and Porter, N. A. (1963). Čerenkov Radiation from the Night Sky, and its Application to γ-Ray Astronomy. *QJRAS*, 4:275.

Jimenez, R. and Kashlinsky, A. (1999). Galaxy Evolution, Deep Galaxy Counts, and the Near-Infrared Cosmic Infrared Background. *The Astrophysical Journal*, 511:16–33, arXiv:astro-ph/9802337.

Karle, A., Merck, M., Plaga, R., et al. (1995). Design and performance of the angle integrating Cerenkov array AIROBICC. *Astroparticle Physics*, 3:321–347.

Kashlinsky, A. (2005). Cosmic infrared background and early galaxy evolution [review article]. *Phys. Rep.*, 409:361–438, astro-ph/0412235.

Kashlinsky, A., Arendt, R. G., Mather, J., and Moseley, S. H. (2005). Tracing the first stars with fluctuations of the cosmic infrared background. *Nature*, 438:45–50, astro-ph/0511105.

Kashlinsky, A., Mather, J., Odenwald, S., and Hauser, M. (1996). Clustering of the Diffuse Infrared Light from the COBE DIRBE Maps. I. C(0) and Limits on the Near-Infrared Background. *The Astrophysical Journal*, 470:681.

Kashlinsky, A. and Odenwald, S. (2000). Clustering of the Diffuse Infrared Light from the COBE DIRBE Maps. III. Power Spectrum Analysis and Excess Isotropic Component of Fluctuations. *The Astrophysical Journal*, 528:74.

Kataoka, J., Mattox, J. R., Quinn, J., et al. (1999). High-Energy Emission from the TeV Blazar Markarian 501 during Multiwavelength Observations in 1996. *The Astrophysical Journal*, 514:138–147, arXiv:astro-ph/9811014.

Katarzyński, K., Ghisellini, G., Tavecchio, F., Gracia, J., and Maraschi, L. (2006). Hard TeV spectra of blazars and the constraints to the infrared intergalactic background. *MNRAS*, 368:L52–L56, astro-ph/0603030.

Katarzyński, K., Sol, H., and Kus, A. (2003). The multifrequency variability of Mrk 421. *Astronomy & Astrophysics*, 410:101–115.

Kauffmann, G., White, S. D. M., and Guiderdoni, B. (1993). The Formation and Evolution of Galaxies Within Merging Dark Matter Haloes. *MNRAS*, 264:201.

Kifune, T. (1999). Invariance Violation Extends the Cosmic-Ray Horizon? *The Astrophysical Journal, Letters*, 518:L21–L24, astro-ph/9904164.

Kino, M., Takahara, F., and Kusunose, M. (2002). Energetics of TeV Blazars and Physical Constraints on Their Emission Regions. *The Astrophysical Journal*, 564:97–107, arXiv:astro-ph/0107436.

Kirk, J. G. and Duffy, P. (1999). TOPICAL REVIEW: Particle acceleration and relativistic shocks. *Journal of Physics G Nuclear Physics*, 25:163, arXiv:astro-ph/9905069.

Kirk, J. G. and Mastichiadis, A. (1999). Variability patterns of synchrotron and inverse Compton emission in blazars. *Astroparticle Physics*, 11:45–48.

Kneiske, T. M., Bretz, T., Mannheim, K., and Hartmann, D. H. (2004). Implications of cosmological gamma-ray absorption. II. Modification of gamma-ray spectra. *Astronomy & Astrophysics*, 413:807–815, arXiv:astro-ph/0309141.

Kneiske, T. M., Mannheim, K., and Hartmann, D. H. (2002). Implications of cosmological gamma-ray absorption. I. Evolution of the metagalactic radiation field. *Astronomy & Astrophysics*, 386:1.

Kosack, K. and VERITAS Collaboration (2004). The Large Zenith Angle TeV spectrum of the Crab Nebula and Galactic Center. In *Bulletin of the American Astronomical Society*, volume 36 of *Bulletin of the American Astronomical Society*, page 927.

Kranich, D. (2002). *Temporal and spectral characteristics of the active galactic nucleus Mkn 501 during a phase of high activity in the TeV range*. PhD thesis, Technical University, Munich.

Kranich, D. et al. (2007). Observations of 3c279 with the MAGIC telescope. In *30th International Cosmic Ray Conference, Merida, Mexico, http://www.icrc2007.unam.mx*.

Krawczynski, H. (2004). TeV blazars - observations and models. *New Astronomy Review*, 48:367–373, arXiv:astro-ph/0309443.

Krawczynski, H., Coppi, P. S., and Aharonian, F. (2002). Time-dependent modelling of the Markarian 501 X-ray and TeV gamma-ray data taken during 1997 March and April. *MNRAS*, 336:721–735, arXiv:astro-ph/0204229.

Krawczynski, H., Coppi, P. S., Maccarone, T., and Aharonian, F. A. (2000). X-ray/TeV-gamma-ray observations of several strong flares of Mkn 501 during 1997 and implications. *Astronomy & Astrophysics*, 353:97.

Krawczynski, H. et al. (2003). X-Ray and TeV Gamma-Ray Observations of Very Strong Flares from the TeV Blazars 1ES 1959+650 and Markarian 421. In *Bulletin of the American Astronomical Society*, volume 35 of *Bulletin of the American Astronomical Society*, page 658.

Krawczynski, H., Hughes, S. B., Horan, D., et al. (2004). Multiwavelength Observations of Strong Flares from the TeV Blazar 1ES 1959+650. *The Astrophysical Journal*, 601:151–164, arXiv:astro-ph/0310158.

Krawczynski, H., Sambruna, R., Kohnle, A., et al. (2001). Simultaneous X-Ray and TeV Gamma-Ray Observation of the TeV Blazar Markarian 421 during 2000 February and May. *The Astrophysical Journal*, 559:187–195, arXiv:astro-ph/0105331.

Krennrich, F., Bond, I. H., Bradbury, S. M., et al. (2002). Discovery of Spectral Variability of Markarian 421 at TeV Energies. *The Astrophysical Journal, Letters*, 575:L9–L13, astro-ph/0207184.

Lagache, G. and Puget, J.-L. (2000). Detection of the extra-galactic background fluctuations at 170 μm. *Astronomy & Astrophysics*, 355:17.

Le Bohec, S., Degrange, B., Punch, M., et al. (1998). A new analysis method for very high definition Imaging Atmospheric Cherenkov Telescopes as applied to the CAT telescope. *Nucl.Instrum.Meth. A*, 416:425–437, astro-ph/9804133.

Leinert, C., Bowyer, S., Haikala, L. K., et al. (1998). The 1997 reference of diffuse night sky brightness. *Astronomy & Astrophysics, Supplement*, 127:1–99.

Leitherer, C., Alloin, D., Fritze-v. Alvensleben, U., et al. (1996). A Database for Galaxy Evolution Modeling. *PASP*, 108:996–1017.

Lessard, R. W., Buckley, J. H., Connaughton, V., and Le Bohec, S. (2001). A new analysis method for reconstructing the arrival direction of TeV gamma rays using a single imaging atmospheric Cherenkov telescope. *Astroparticle Physics*, 15:1.

Levenberg, K. (1944). A Method for the Solution of Certain Problems in Least Squares. *Quart. Appl. Math.*, 2:164–168.

Li, T. P. and Ma, Y. Q. (1983). Analysis methods for results in gamma-ray astronomy. *The Astrophysical Journal*, 272:317.

Lindner, A. (1997). Status and new results of the hegra experiment. In *25th International Cosmic Ray Conference, Durban*, volume 5, page 113.

Longair, M. S. (1992). *High Energy Astrophysics. Particles, photons and their detection*, volume 1. Cambridge University Press.

Longair, M. S. (1994). *High Energy Astrophysics. Stars, the galaxy and the interstellar medium*, volume 2. Cambridge University Press.

Lonsdale, C. (1995). See in Calzetti, Livio & Madau, 1995. pages pp. 145–167.

Lucarelli, F., Barrio, J., Antoranz, P., et al. (2007). The central pixel of the magic telescope for optical observations. In *30th International Cosmic Ray Conference, Merida, Mexico, http://www.icrc2007.unam.mx*.

Madau, P. and Pozzetti, L. (2000). Deep galaxy counts, extragalactic background light and the stellar baryon budget. *Monthly Notices of the Royal Astronomical Society*, 312:L9.

Majumdar, P. et al. (2005). Monte Carlo simulation for the MAGIC telescope. In *International Cosmic Ray Conference*, volume 5, page 203.

Malkan, M. A. and Stecker, F. W. (2001). An Empirically Based Model for Predicting Infrared Luminosity Functions, Deep Infrared Galaxy Counts, and the Diffuse Infrared Background. *The Astrophysical Journal*, 555:641.

Mannheim, K. (1993). The proton blazar. *Astronomy & Astrophysics*, 269:67–76, arXiv:astro-ph/9302006.

Mannheim, K. (1998). Possible Production of High-Energy Gamma Rays from Proton Acceleration in the Extragalactic Radio Source Markarian 501. *Science*, 279:684, arXiv:astro-ph/9803241.

Mantsch, P. M. (2005). The Pierre Auger Observatory - progress and first results. In *International Cosmic Ray Conference*, volume 10 of *International Cosmic Ray Conference*, page 115.

Marquardt, D. W. (1963). An Algorithm for Least-Squares Estimation of Nonlinear Parameters. *Journal of the Society for Industrial and Applied Mathematics*, 11:431–441.

Martin, C., Hurwitz, M., and Bowyer, S. (1991). Spectroscopic limits to an extragalactic far-ultraviolet background. *The Astrophysical Journal*, 379:549–563.

Massaro, E., Perri, M., Giommi, P., and Nesci, R. (2004). Log-parabolic spectra and particle acceleration in the BL Lac object Mkn 421: Spectral analysis of the complete BeppoSAX wide band X-ray data set. *Astronomy & Astrophysics*, 413:489–503, arXiv:astro-ph/0312260.

Mastichiadis, A. and Kirk, J. G. (1997). Variability in the synchrotron self-Compton model of blazar emission. *Astronomy & Astrophysics*, 320:19–25, arXiv:astro-ph/9610058.

Matsumoto, T., Matsuura, S., Murakami, H., Tanaka, M., Freund, M., Lim, M., Cohen, M., Kawada, M., and Noda, M. (2005). Infrared Telescope in Space Observations of the Near-Infrared Extragalactic Background Light. *The Astrophysical Journal*, 626:31–43, astro-ph/0411593.

Mattila, K. (1990). Observations of the extragalactic background light. In Bowyer, S. and Leinert, C., editors, *The Galactic and Extragalactic Background Radiation*, volume 139 of *IAU Symposium*, pages 257–268.

Matute, I., La Franca, F., Pozzi, F., et al. (2006). Active galactic nuclei in the mid-IR. Evolution and contribution to the cosmic infrared background. *Astronomy & Astrophysics*, 451:443–456, astro-ph/0601355.

Mazin, D. (2003). Entwicklung einer Methode zur Einschränkung der Energiedichte des extragalaktischen Hintergrundlichtes mit Hilfe der gemessenen TeV-Gamma-Strahlung. Diplomarbeit, Institut für Experimentalphysik, Universität Hamburg.

Mazin, D. et al. (2005). Concept of a Global Network of Cherenkov Telescopes and first joint observations with H.E.S.S. and MAGIC. In *International Cosmic Ray Conference, Pune, India*, volume 4, pages 331–334.

Mazin, D. and Goebel, F. (2007). Break in the Very High Energy Spectrum of PG 1553+113: New Upper Limit on Its Redshift? *The Astrophysical Journal, Letters*, 655:L13–L16, arXiv:astro-ph/0611817.

Mazin, D. and Raue, M. (2007). New limits on the density of the extragalactic background light in the optical to the far infrared from the spectra of all known TeV blazars. *Astronomy & Astrophysics*, 471:439–452, arXiv:astro-ph/0701694.

Meier, D. L., Koide, S., and Uchida, Y. (2001). Magnetohydrodynamic Production of Relativistic Jets. *Science*, 291:84–92.

Meszaros, P. (2006). Gamma-ray bursts. *Reports of Progress in Physics*, 69:2259–2322, arXiv:astro-ph/0605208.

Metcalfe, L., Kneib, J.-P., McBreen, B., et al. (2003). An ISOCAM survey through gravitationally lensing galaxy clusters. I. Source lists and source counts for A370, A2218 and A2390. *Astronomy & Astrophysics*, 407:791–822, arXiv:astro-ph/0305400.

Miller, H. R., Carini, M. T., Gaston, B. J., and Hutter, D. J. (1988). The ultraviolet/optical variability of PG 1553+11. In *ESA Special Publication*, volume 281, pages 303–304.

Miller, H. R. and Green, R. F. (1983). Optical/UV Observations of the BL Lac Object, PG 1553+11. In *Bulletin of the American Astronomical Society*, volume 15, page 957.

Mirzoyan, R., Cortina, J., Martinez, M., et al. (2002). Ultrafast FADC Multiplexer. *IEEE Transactions on Nuclear Science*, 49, 5:2473.

Mirzoyan, R. et al. (1994). The first telescope of the HEGRA air Cherenkov imaging telescope array. *Nuclear Instruments and Methods A*, 351:513.

Mirzoyan, R. and Lorenz, E. (1997). On the Calibration Accuracy of Light Sensors in Atmospheric Cherenkov, Fluorescence and Neutrino Experiments. In *25th ICRC, Durban, South Africa*.

Monnet, G. and D'Odorico, S. (2006). OWL instrument concept studies. In Whitelock, P., Dennefeld, M., and Leibundgut, B., editors, *The Scientific Requirements for Extremely Large Telescopes*, volume 232 of *IAU Symposium*, pages 52–59.

Mücke, A., Protheroe, R. J., Engel, R., Rachen, J. P., and Stanev, T. (2003). BL Lac objects in the synchrotron proton blazar model. *Astroparticle Physics*, 18:593–613, arXiv:astro-ph/0206164.

Mufson, S. L. and Hutter, D. J. (1981). The detection of X-ray emission from the BL Lacertae object Markarian 180. *The Astrophysical Journal, Letters*, 248:L61–L64.

Neshpor, Y. I., Chalenko, N. N., Stepanian, A. A., et al. (2001). BL Lac: A New Ultrahigh-Energy Gamma-Ray Source. *Astronomy Reports*, 45:249–254, arXiv:astro-ph/0111448.

Neshpor, Y. I., Stepanyan, A. A., Kalekin, O. P., et al. (1998). Blazar 3C 66A: Another extragalactic source of ultra-high-energy gamma-ray photons. *Astronomy Letters*, 24:134–138.

Nilsson, K., Pursimo, T., Heidt, J., et al. (2003). R-band imaging of the host galaxies of RGB BL Lacertae objects. *Astronomy & Astrophysics*, 400:95–118.

Nilsson, K., Takalo, L. P., Pasanen, M., Lindfors, E., Berdyugin, A., and Ciprini, S. (2006). Host galaxy subtraction in differential aperture photometry. In Hovatta, T., Nieppola, E., and Torniainen, I., editors, *Proceedings of the 8th ENIGMA meeting*.

Nishiyama, T., Chamoto, N., Chikawa, M., et al. (1999). Detection of a new TeV gamma-ray source of BL Lac object 1ES 1959+650. In *Proceedings of the 26th ICRC, Salt Lake City*, volume 3, page 370.

Nolan, P. L., Arzoumanian, Z., Bertsch, D. L., et al. (1993). Observations of the Crab pulsar and nebula by the EGRET telescope on the Compton Gamma-Ray Observatory. *The Astrophysical Journal*, 409:697–704.

Oña-Wilhelmi, E., Robert, A., Domingo-Santamaria, E., et al. (2007). Observations of the first unidentified TeV gamma-ray source (TeV J2032+4130) with the MAGIC telescope. In *30th International Cosmic Ray Conference, Merida, Mexico, http://www.icrc2007.unam.mx*.

Oser, S., Bhattacharya, D., Boone, et al. (2001). High-Energy Gamma-Ray Observations of the Crab Nebula and Pulsar with the Solar Tower Atmospheric Cerenkov Effect Experiment. *The Astrophysical Journal*, 547:949–958.

Otte, A. N. (2007). *Observation of VHE gamma-rays from the vicinity of magnetized neutron stars and development of new photon-detectors for future ground based gamma-ray detectors.* PhD thesis, Technical University, Munich.

Otte, N. and Majumdar, P. (2006). The Crab nebula in VHE gamma-reays from 60 GeV to 9 TeV, MAGIC TDAS 0608. MAGIC internal report, Max-Planck-Institut für Physik, München, Germany.

Padovani, P. (2007). The blazar sequence: validity and predictions. *Ap&SS*, page 190, arXiv:astro-ph/0610545.

Paneque, D. (2005). *The MAGIC Telescope: development of new technologies and first observations*. PhD thesis, Technical University, Munich.

Paneque, D., Gebauer, H. J., Lorenz, E., and Mirzoyan, R. (2004). A method to enhance the sensitivity of photomultipliers for air Cherenkov telescopes by applying a lacquer that scatters light. *Nucl. Instrum. Meth.*, A518:619–621.

Papovich, C., Dole, H., Egami, E., et al. (2004). The 24 Micron Source Counts in Deep Spitzer Space Telescope Surveys. *ApJS*, 154:70–74, astro-ph/0406035.

Perlman, E. S., Madejski, G., Georganopoulos, M., et al. (2005). Intrinsic Curvature in the X-Ray Spectra of BL Lacertae Objects. *The Astrophysical Journal*, 625:727–740, arXiv:astro-ph/0502298.

Petry, D., Böttcher, M., Connaughton, V., et al. (2000). Multiwavelength Observations of Markarian 501 during the 1997 High State. *The Astrophysical Journal*, 536:742–755, arXiv:astro-ph/0002255.

Petry, D., Bradbury, S. M., Konopelko, A., et al. (1996). Detection of VHE γ-rays from MKN 421 with the HEGRA Cherenkov Telescopes. *Astronomy & Astrophysics*, 311:L13–L16, arXiv:astro-ph/9606159.

Piron, F., Djannati-Atai, A., Punch, M., et al. (2001). Temporal and spectral gamma-ray properties of Mkn 421 above 250 GeV from CAT observations between 1996 and 2000. *Astronomy & Astrophysics*, 374:895–906.

Pohl, M. and Schlickeiser, R. (2000). On the conversion of blast wave energy into radiation in active galactic nuclei and gamma-ray bursts. *Astronomy & Astrophysics*, 354:395–410, arXiv:astro-ph/9911452.

Press, W., Teukolsky, S., Vetterling, W., and Flannery, B. (1992). *Numerical Recipes in C*. Cambridge University Press, Cambridge, UK, 2nd edition.

Primack, J., Bullock, J., Summerville, R., and MacMinn, D. (1999). Probing galaxy formation with TeV gamma ray absorption. *Astroparticle Physics*, 11:93.

Primack, J. R., Bullock, J. S., and Somerville, R. S. (2005). Observational Gamma-ray Cosmology. In Aharonian, F. A., Völk, H. J., and Horns, D., editors, *High Energy Gamma-Ray Astronomy*, volume 745 of *American Institute of Physics Conference Series*, pages 23–33.

Protheroe, R. J. and Meyer, H. (2000). An Infrared Background – TeV Gamma-Ray Crisis? *Physics Letters B*, 493:1.

Punch, M., Akerlof, C. W., Cawley, M. F., et al. (1992). Detection of TeV photons from the active galaxy Markarian 421. *Nature*, 358:477.

Quinn, J., Akerlof, C. W., Biller, S., et al. (1996). *The Astrophysical Journal, Letters*, 456:L83.

Raue, M., Benbow, W., Costamante, L., and Horns, D. (2007). Discovery of Two New TeV Blazars with the H.E.S.S. Cherenkov Telescope System. In *30th International Cosmic Ray Conference, Merida, Mexico, http://www.icrc2007.unam.mx*.

Raue, M. and Mazin, D. (2007). New Limits on the Extragalactic Background Light from the Spectra of all known TeV Blazars. In *30th International Cosmic Ray Conference, Merida, Mexico, http://www.icrc2007.unam.mx*.

Rebillot, P. F. and VERITAS Collaboration (2003). Intensive TeV Gamma-Ray and X-Ray Observations of the Blazar Mrk 421 in December 2002 and January 2003. In *International Cosmic Ray Conference*, volume 5 of *International Cosmic Ray Conference*, page 2599.

Rees, M. J. and Meszaros, P. (1992). Relativistic fireballs - Energy conversion and time-scales. *MNRAS*, 258:41P–43P.

Renault, C., Barrau, A., Lagache, G., and Puget, J.-L. (2001). New constraints on the cosmic mid-infrared background using TeV gamma-ray astronomy. *Astronomy & Astrophysics*, 371:771.

Reynolds, P. T., Akerlof, C. W., Cawley, M. F., et al. (1993). Survey of candidate gamma-ray sources at TeV energies using a high-resolution Cerenkov imaging system - 1988-1991. *The Astrophysical Journal*, 404:206–218.

Riegel, B., Bretz, T., Dorner, D., et al. (2005a). A systematic study of the interdependence of IACT image parameters. In *International Cosmic Ray Conference*, volume 5, page 215.

Riegel, B. et al. (2005b). A tracking monitor for the MAGIC Telescope. In *International Cosmic Ray Conference*, volume 5 of *International Cosmic Ray Conference*, page 219.

Roach, F. E. and Gordon, J. L. (1973). *The Light of the Night Sky*. D. Reidel Publishing Company.

Rowan-Robinson, M. and Crawford, J. (1989). Models for infrared emission from IRAS galaxies. *MNRAS*, 238:523–558.

Salvaterra, R. and Ferrara, A. (2003). The imprint of the cosmic dark ages on the near-infrared background. *Monthly Notice of the Royal Astronomical Society*, 339:973.

Salvaterra, R. and Ferrara, A. (2006). Where are the sources of the near-infrared background? *MNRAS*, 367:L11–L15, astro-ph/0509338.

Sambruna, R., Aharonian, F. A., Krawczynski, H., et al. (2000). Correlated Intense X-Ray and TeV Activity of Markarian 501 in 1998 June. *The Astrophysical Journal*, 538:127.

Sbarufatti, B., Treves, A., and Falomo, R. (2005). Imaging Redshifts of BL Lacertae Objects. *The Astrophysical Journal*, 635:173–179, arXiv:astro-ph/0508200.

Sbarufatti, B., Treves, A., Falomo, R., Heidt, J., Kotilainen, J., and Scarpa, R. (2006). ESO Very Large Telescope Optical Spectroscopy of BL Lacertae Objects. II. New Redshifts, Featureless Objects, and Classification Assessments. *AJ*, 132:1–19, arXiv:astro-ph/0601506.

Scarpa, R., Urry, C. M., Falomo, R., Pesce, J. E., and Treves, A. (2000). The Hubble Space Telescope Survey of BL Lacertae Objects. I. Surface Brightness Profiles, Magnitudes, and Radii of Host Galaxies. *The Astrophysical Journal*, 532:740–815, arXiv:astro-ph/9911147.

Schmelling, M. et al. (1994). The method of reduced cross-entropy. A general approach to unfold probability distributions. *Nuclear Instruments and Methods in Physics Research A*, 340:400.

Schmidt, F. (2007). CORSIKA shower images. Technical report, University of Leeds. http://www.ast.leeds.ac.uk/∼fs/showerimages.html.

Schroedter, M., Badran, H. M., Buckley, J. H., et al. (2005). A Very High Energy Gamma-Ray Spectrum of 1ES 2344+514. *The Astrophysical Journal*, 634:947–954, astro-ph/0508499.

Schweizer, T. (2002). *Analysis of the Large Gamma Ray Flares of Mkn 421 as Observed with HEGRA CT1 on the Island La Palma in 2001*. PhD thesis, Universitat Autonoma Barcelona, Barcelona.

Sikora, M., Begelman, M. C., Madejski, G. M., and Lasota, J.-P. (2005). Are Quasar Jets Dominated by Poynting Flux? *The Astrophysical Journal*, 625:72–77, arXiv:astro-ph/0502115.

Sikora, M. and Madejski, G. (2001). Blazars. In Aharonian, F. A. and Völk, H. J., editors, *American Institute of Physics Conference Series*, volume 558 of *American Institute of Physics Conference Series*, page 275.

Somerville, R. S. and Primack, J. R. (1999). Semi-analytic modelling of galaxy formation: the local Universe. *MNRAS*, 310:1087–1110, arXiv:astro-ph/9802268.

Somerville, R. S., Primack, J. R., and Faber, S. M. (2001). The nature of high-redshift galaxies. *Monthly Notices of the Royal Astronomical Society*, 320:504.

Sowards-Emmerd, D., Romani, R. W., and Michelson, P. F. (2003). The Gamma-Ray Blazar Content of the Northern Sky. *The Astrophysical Journal*, 590:109–122, arXiv:astro-ph/0212504.

Sreekumar, P., Bertsch, D. L., Dingus, B. L., et al. (1998). EGRET Observations of the Extragalactic Gamma-Ray Emission. *The Astrophysical Journal*, 494:523–534, arXiv:astro-ph/9709257.

Stecker, F. W. and de Jager, O. C. (1997). On the Absorption of High-Energy Gamma Rays by Intergalactic Infrared Radiation. *The Astrophysical Journal*, 476:712, arXiv:astro-ph/9608072.

Stecker, F. W., de Jager, O. C., and Salamon, M. H. (1996). Predicted Extragalactic TeV Gamma-Ray Sources. *The Astrophysical Journal*, 473:L75.

Stecker, F. W. and Glashow, S. L. (2001). New tests of Lorentz invariance following from observations of the highest energy cosmic γ-rays. *Astroparticle Physics*, 16:97–99, astro-ph/0102226.

Stecker, F. W., Malkan, M. A., and Scully, S. T. (2006). Intergalactic Photon Spectra from the Far-IR to the UV Lyman Limit for $0 < z < 6$ and the Optical Depth of the Universe to High-Energy Gamma Rays. *The Astrophysical Journal*, 648:774–783, arXiv:astro-ph/0510449.

Superina, J., Giebels, B., Benbow, W., et al. (2007). Discovery of VHE gamma-rays from the BL Lac object PKS 0548-322 (z=0.069) with H.E.S.S. In *30th International Cosmic Ray Conference, Merida, Mexico, http://www.icrc2007.unam.mx*.

Takahashi, T., Kataoka, J., Madejski, G., et al. (2000). Complex Spectral Variability from Intensive Multiwavelength Monitoring of Markarian 421 in 1998. *The Astrophysical Journal, Letters*, 542:L105–L109, arXiv:astro-ph/0008505.

Takahashi, T., Tashiro, M., Madejski, G., Kubo, H., Kamae, T., Kataoka, J., Kii, T., Makino, F., Makishima, K., and Yamasaki, N. (1996). ASCA Observation of an X-Ray/TeV Flare from the BL Lacertae Object Markarian 421. *The Astrophysical Journal, Letters*, 470:L89.

Tamm, I. E. and Frank, I. M. (1937). Coherent radiation of fast electrons in a medium. *Dokl. Akad. Nauk USSR*, 14:107.

Tavecchio, F., Maraschi, L., Pian, E., et al. (2001). Theoretical Implications from the Spectral Evolution of Markarian 501 Observed with BeppoSAX. *The Astrophysical Journal*, 554:725–733.

Tescaro, D. et al. (2007). Study of the performance and capability of the new ultra-fast 2 GSamples/s FADC Data Acquisition System system of the MAGIC telescope. In *30th International Cosmic Ray Conference, Merida, Mexico, http://www.icrc2007.unam.mx*.

Teshima, M. (2007). Gamma ray astronomy, status in 2007 (HE 1.1 - HE 1.5). In *Proceedings 30th International Cosmic Ray Conference, Merida, Mexico, http://www.icrc2007.unam.mx*.

Tikhonov, A. N. and Arsenin, V. J. (1979). Methods of Solution of Ill-posed Problems – M. *Nauka*.

Tinsley, B. M. (1973). Analytical Approximations to the Evolution of Galaxies. *The Astrophysical Journal*, 186:35–49.

Toller, G. N. (1983). The extragalactic background light at 4400 Å. *The Astrophysical Journal, Letters*, 266:L79–L82.

Tonello, N. (2006). *Study of the VHE γ-ray emission from the Active Galactic Nucleus 1ES1959+650*. PhD thesis, Technical University, Munich.

Tsuchiya, K., Enomoto, R., Ksenofontov, L. T., et al. (2004). Detection of Sub-TeV Gamma Rays from the Galactic Center Direction by CANGAROO-II. *The Astrophysical Journal, Letters*, 606:L115–L118, arXiv:astro-ph/0403592.

Ulrich, M. (1996). *Eine neue Bildanalysemethode fuer Abbildende Atmosphaerische Cherenkov Teleskope und die zweidimensionale Richtungsrekonstruktion von TeV-Photonen des Krebs-Nebels*. PhD thesis, Heidelberg University.

Urry, C. M. and Padovani, P. (1995). Unified schemes for radio-loud active galactic nuclei. *Publications of the Astronomical Society of the Pacific*, 107:803.

Wagner, R. M. (2006). *Temporal and spectral characteristics of the VHE gamma-ray emission of four blazars as observed with the MAGIC telescope and a comparative study of the properties of VHE gamma-ray emitting blazars*. PhD thesis, ISBN 978-3-938363-07-2, Technical University, Munich.

Weekes, T. C. (1989). Observation of TeV Gamma Rays from the Crab Nebula using the Atmospheric Cherenkov Imaging Technique. *The Astrophysical Journal*, 342:379.

Weekes, T. C. (2006). Revealing the Dark TeV Sky: The Atmospheric Cherenkov Imaging Technique for Very High Energy Gamma-ray Astronomy. *ArXiv, astro-ph/0606130*, astro-ph/0606130.

White, S. D. M. and Frenk, C. S. (1991). Galaxy formation through hierarchical clustering. *The Astrophysical Journal*, 379:52–79.

Wisniewski, W. Z., Sitko, M. L., and Sitko, A. K. (1986). 1011 + 496 and 1217 + 348: two new candidate BL Lacertae objects. *MNRAS*, 219:299–304.

Wittek, W. (2002). Image parameters, MAGIC TDAS 02-03. MAGIC internal report, Max-Planck-Institut for Physics, Muenchen, Germany.

Wittek, W. (2005). Unfolding (revised), MAGIC TDAS 05-05. MAGIC internal report, Max-Planck-Institut for Physics, Muenchen, Germany.

Wright, E. L. and Reese, E. D. (2000). Detection of the Cosmic Infrared Background at 2.2 and 3.5 Microns Using DIRBE Observations. *The Astrophysical Journal*, 545:43.

Yao, W.-M., Amsler, C., Asner, D., et al. (2006). Review of Particle Physics. *Journal of Physics G*, 33:1.

Zatsepin, G. T. and Kuz'min, V. A. (1966). Upper limit on the spectrum of cosmic rays. *JETP Letters*, 4:78.

Zimmermann, J. (2005). *Statistical Learning in High Energy and Astrophysics*. PhD thesis, MPP-2005-128, LMU, Munich.